APPLICATIONS OF ACTIVE-SOURCE MULTI-COMPONENT SEISMOLOGY TO SUBSURFACE CHARACTERIZATION

by

Samara M. Garvey

A thesis submitted to the Faculty and the Board of Trustees of the Colorado School of Mines in partial fulfillment of the requirements for the degree of Doctor of Philosophy (Computational Seismology).

Golden, Colorado

Date ______________________

Signed: ______________________

Samara M. Garvey

Signed: ______________________

Dr. Jeffrey Shragge
Thesis Advisor

Signed: ______________________

Dr. Matthew R. Siegfried
Thesis Advisor

Golden, Colorado

Date ______________________

Signed: ______________________

Dr. Paul Sava
Professor and Department Head
Department of Geophysics

ABSTRACT

Multicomponent (MC) seismology extends conventional single-component (SC) methods, which typically rely on vertical (Z) receivers or hydrophones, by recording seismic wavefields in three orthogonal directions (Z and two horizontal, H, components). This vector recording captures the 3-D radiation of different wave modes, each with distinct particle motions relative to the propagating wavefield. The unique component sensitivities to the same mode enable a more comprehensive characterization of both the wavefield and the host elastic medium. Despite this potential, active-source MC experiments often reduce analysis to S waves on the H components, assuming near-vertical incidence at the surface. Challenging this restrictive assumption, this dissertation explores H-component recordings of P- and Rayleigh-wave energy and their potential to complement Z-component data for imaging and velocity model building.

This dissertation comprises four studies spanning applications from deep marine exploration to near-surface glaciology. Study 1 investigates reflected P waves on inline H components (HPP data) from exploration-scale ocean-bottom surveys, demonstrating their value in imaging shallow, dipping, and sub-salt structures that complement Z-component P-wave images. Two industry-standard synthetic datasets are used to evaluate HPP illumination and polarization sensitivities through analysis of migrated gathers and partial stacks. Studies 2 and 3 focus on deriving shear velocity (V_s) from Rayleigh-wave dispersion in smaller-scale glacial surveys. Study 2 shows how the elliptical particle motion recorded on Z and radial H components can be summed within a complex system to enhance low-frequency dispersion signal accuracy in layered or noisy glacial settings. This is demonstrated on synthetic models, which include firn-aquifer scenarios, and on field data acquired at Saskatchewan Glacier in Canada. Study 3 validates this approach, showing that the derived complex component (CC) improves inversion accuracy, reduces non-uniqueness, and increases stability. Study 4 motivates that the improved MC signal is best leveraged when combined with adaptive algorithms. This is demonstrated using a transdimensional Bayesian inversion of CC dispersion data, which resolves thermally sensitive V_s layering at Slakbreen Glacier in Svalbard while employing less restrictive priors than deterministic methods. Together, these studies highlight the untapped value of H-component data and offer a platform for utilizing MC seismology at multiple scales.

TABLE OF CONTENTS

ABSTRACT . . . iii

LIST OF FIGURES . . . xi

LIST OF TABLES . . . xxv

LIST OF SYMBOLS . . . xxvi

LIST OF COMMON ABBREVIATIONS . . . xxix

ACKNOWLEDGMENTS . . . xxx

A LESSON FOR THE JOURNEY AHEAD . . . xxxii

DEDICATION . . . xxxiii

CHAPTER 1 INTRODUCTION . . . 1

- 1.1 MC Seismology - Historical Perspective . . . 2
- 1.2 MC Seismology - Current State . . . 5
- 1.3 Scope of Dissertation . . . 8
- 1.4 Key Research Questions . . . 8
  - 1.4.1 Study 1: Contributions of the Reflected P-wave Recorded on the Horizontal Component of Ocean Bottom Node Surveys to Imaging . . . 9
  - 1.4.2 Study 2: Signal Enhancement of Surface Wave Dispersion using Multi-Component Data from Limited-Coverage Glacial Experiments . . . 9
  - 1.4.3 Study 3: Improving Shear-wave Velocity Modeling using Multi-Component Dispersion Data from Limited-Coverage Glacial Experiments . . . 10
  - 1.4.4 Study 4: Maximizing the Value of Multi-Component Seismic Data with Robust Inversion Approaches . . . 10

1.5 Dissertation Structure 11

CHAPTER 2 CONCEPTS OF MULTI-COMPONENT SEISMOLOGY 13

2.1 Description of Wave Modes 13

2.1.1 Body Waves 14

2.1.2 Surface Waves 18

2.1.3 Other Wave Modes 18

2.2 Acquisition Considerations 19

2.3 Processing Considerations 20

2.4 Summary 22

CHAPTER 3 CONTRIBUTIONS OF THE HORIZONTAL OBN COMPONENTS TO P-WAVE IMAGING 23

3.1 Abstract 23

3.2 Introduction 24

3.3 Method and Implementation 26

3.3.1 Numerical Models and Simulations 27

3.3.2 Coordinate System and Framework 29

3.3.3 Migration Algorithm 32

3.4 Results 33

3.4.1 Study 1: Marmousi2 Example 34

3.4.2 Study 2: SEAM Phase 1 Example 37

3.5 Summary of Observations 41

3.6 Discussions and Suggestions for Further Investigation 42

3.7 Conclusions 44

3.8 Data Availability 45

3.9 Acknowledgments 45

CHAPTER 4 SIGNAL ENHANCEMENT OF RAYLEIGH WAVE DISPERSION FROM LIMITED-COVERAGE GLACIAL EXPERIMENTS USING MULTI-COMPONENT DATA 46

4.1 Abstract 46

4.2 Introduction 47

4.3 Theory 50

4.3.1 Assumptions and Notation 50

4.3.2 Rayleigh Waves 51

4.3.3 Layering and Dispersion Effects 56

4.4 Methods and Implementation 58

4.4.1 Design of DC Sensitivity Studies 59

4.4.2 Field Data Implementation 60

4.5 Results: DC Sensitivity Studies 60

4.5.1 Study 1: DC Sensitivity to Data Conditioning 60

4.5.2 Study 2: DC Sensitivity to Acquisition Geometry 68

4.5.3 Study 3: DC Sensitivity to Shallow Complexity 70

4.5.3.1 Combining MC data 75

4.6 Results: Field Experiment on Saskatchewan Glacier 76

4.6.1 Survey Details 76

4.6.2 Data Conditioning 77

4.6.3 Supergather Processing 80

4.6.4 Dispersion Analysis 81

4.7 Discussion 84
4.7.1 Acquisition Design Recommendations 84
4.7.2 Supergathers and Data Conditioning 84
4.7.3 Horizontal-Component Contributions 85
4.8 Conclusions 86
4.9 Data Availability 87
4.10 Acknowledgments 87
CHAPTER 5 IMPROVING SHEAR-WAVE VELOCITY MODELING USING MULTI-COMPONENT DISPERSION DATA FROM LIMITED-COVERAGE GLACIAL EXPERIMENTS 88
5.1 Abstract 88
5.2 Introduction 89
5.3 Theory 93
5.3.1 Forward Problem: Theoretical Dispersion Curves 93
5.3.2 Forward Problem: Experimental Dispersion Curves 94
5.3.3 Inverse Problem: Estimating V_s-Depth Models 97
5.4 Inversion Parameterization 99
5.5 Synthetic Study: Firn-Aquifer Structures 99
5.5.1 Results 103
5.5.2 Key Insights 108
5.6 Field Study: Alpine Glacier 109
5.6.1 Results 113
5.6.2 Key Insights 116
5.7 Discussion 117

5.8 Conclusion 118

5.9 Data Availability 119

5.10 Acknowledgments 119

5.11 Supplemental: Experiments to Validate MASW Inversion Results 120

  5.11.1 Inversion Ill-Posedness 120

  5.11.2 Inversion Hyper-Parameterization 121

  5.11.3 Median Model Representation 122

CHAPTER 6 MAXIMIZING THE VALUE OF MULTI-COMPONENT SEISMIC DATA WITH ROBUST INVERSION APPROACHES 128

6.1 Abstract 128

6.2 Introduction 129

6.3 Comparison of Inversion Methods 131

  6.3.1 Model Parameterization and Prior Assumptions 132

  6.3.2 Data Misfit and Noise Quantification 134

  6.3.3 Evaluation of Candidate Models 135

  6.3.4 Model Space Discretizations and Updates 136

  6.3.5 Implementation and Post-Inversion Analysis 136

6.4 Svalbard Dataset 137

6.5 MASW Results 142

6.6 TDB Results 146

6.7 Interpretation of Slakbreen Glacier Structure 151

6.8 Conclusion 153

6.9 Data Availability 153

6.10 Acknowledgments 154
6.11 Supplemental: Inversion Parameterizations for Slakbreen Experiments 154
  6.11.1 MASW Parameterization 154
  6.11.2 TDB Parameterization 156
CHAPTER 7 CONCLUSION 158
7.1 Oil and Gas Exploration 159
  7.1.1 Contributions of HPP data to Imaging 159
  7.1.2 HPP Sensitivities and Processing Considerations 160
  7.1.3 Suggestions for Future Work 160
7.2 Glacial Seismology 160
  7.2.1 Contributions of CC-Rayleigh-wave Data to V_s-Depth Profiling . . . 161
  7.2.2 CC Sensitivities and Acquisition/Processing Considerations 162
  7.2.3 Suggestions for Future Work 162
7.3 Broader Contributions 163
7.4 Summary and Outlook 163
REFERENCES 165
APPENDIX COPYRIGHT PERMISSIONS FOR CHAPTER 3 179
A.1 Journal Permission 179
A.2 Journal Citation 180
A.3 Co-Author Permissions 180

LIST OF FIGURES

Figure 2.1 Description of wave modes generated in a homogeneous, isotropic medium from different sources: a buried explosive source (a, b), a vertical point source at the free surface (c, d), and a horizontal point source at the free surface (e, f). The left and right columns show propagation along two perpendicular planes for the same source mechanism. Surface Rayleigh and Love waves can be generated by any source due to mode conversion and free-surface reflections; they are included in certain panels for conceptual reference relative to other wave modes. 15

Figure 2.2 Description of radiation patterns of wave modes initiated from (a) an explosive source mechanism, (b, c) a vertical point source, and (d, e, f) a horizontal point source at the free surface above a homogeneous, isotropic medium. Red symbols describe the direction and placement of the source mechanisms. Panels b, c, d, and e are taken from modeling by Jílek, P and Červený (1996), whereas panels a and f are sketched from modeling by Gaiser (2016). Although the details provided in these studies are insufficient to verify whether the same velocity models and assumptions (such as frequency) were used, the vertical-source results between the publications are broadly comparable. Nevertheless, these sketches are intended to be illustrative rather than quantitatively precise. . 16

Figure 2.3 Map view depiction of two common acquisition coordinate frameworks for MC experiments: (a) horizontal components oriented North (N) and East (E), and (b) horizontal components aligned along the source-receiver azimuth (X) and perpendicular to it, counterclockwise (Y), typically in 2-D experiments. Also shown is (c) the radial-transverse ($R-T$) coordinate system, a processing rotation that removes azimuthal sensitivity of polarity and, in horizontal-source experiments, separates polarized SV and SH modes onto the R and T components, respectively. 21

Figure 3.1 P-wave velocity (V_p) and density (ρ) models modified from the Marmousi2 dataset created by Martin *et al.* (2002) are depicted in panels (a) and (b) respectively. Transition layers are removed from the original model which places the seafloor at a depth of 0.512 km. 2-D P-wave velocity (V_p) and density (ρ) models extracted from the SEAM Phase 1 dataset created by Fehler & Keliher (2011) are shown in panels (c) and (d) respectively. Acquisition geometries for the acoustic finite-difference forward modeling of an OBN survey for each model are described in the text. 28

Figure 3.2 Description of coordinate system for OBN acquisition. The table describes the polarity of different waves registered on the positive or negative offsets of the pressure, Z, X, and R components. 30

Figure 3.3 Raw shot gathers from the Marmousi2 experiment for the Z, X, and R components at 3.0 km (a–c), where the stratigraphy is relatively flat, and at 9.3 km (d–f), where the beds are severely tilted and faulted. Yellow and blue arrows (a–c) highlight the direct arrival and the reflection at the top of a gas reservoir, respectively, for each component. For both direct and reflected waves at this location, we observe uniform polarity at all offsets for the Z component and an SOP on the X component, which is corrected by rotation to the R direction. Pink arrows (e and f) highlight comparative dipping bed reflectors: on the X component, no SOP is observed, while on the R component, an SOP is introduced due to rotation. 31

Figure 3.4 CIGs from the Marmousi2 experiment at shot locations 3.0 km (a–c) where stratigraphy is relatively flat and 9.3 km (d–f) where beds are severely tilted and faulted. The H components (X and R) are gained three times the amplitude of the Z component and all gathers have an outer mute of 45 degrees applied. Using the same parameterizations for KPSDM, the PP energy on all components is equally flattened (blue arrows) at both locations. Pink arrows on the 9.3 km CIGs highlight dipping bed reflections which are uniformly illuminated at all offsets on the Z component, but are illuminated differently between the positive and negative offsets of the X and R components. 35

Figure 3.5 Comparison of the RPP ultra-near (a and b) and mid (c and d) partial-offset stacks for both positive (left column) and negative (right column) offsets. All panels are displayed on the same amplitude scale. Yellow arrows highlight left dipping bed reflections which are similarly imaged (disregarding polarity) on the ultra-near stacks but better imaged on the negative mid-offset stacks as a result of the biased HPP illumination to signed-offset. 36

Figure 3.6 Comparison of full (0-45°), signed-offset stacks for ZPP (a and b) and RPP (c and d) data. RPP amplitudes are gained two times that of the ZPP images. RPP illumination has a stronger SOI bias (compare the differences in (c) and (d)) versus the ZPP illumination (compare the minor differences in (a) and (b)). In general, RPP data supplement the ZPP data in critical locations below the salt overhangs and at the base of salt. Yellow arrows highlight the base of salt illumination which is more continuous on the RPP images as opposed to the ZPP images which are more affected by poorly migrated inter-salt multiples. Blue arrows highlight these multiples in regions below the salt and under the salt overhangs. Red boxes #1 and #2 on panel (a) outline the zoomed regions displayed in Figure 3.7 and Figure 3.8 respectively. 37

Figure 3.7 Positive partial-offset stacks zoomed to the right salt flank of the SEAM Phase 1 model. Zoomed region is described in Figure 3.6. Panels a–d show the ZPP ultra-near, near, mid, and far partial-offset stacks respectively and panels e–h show the RPP equivalent stacks. Generally, dotted arrows highlight reflectors that are comparably imaged on both Z and R components whereas solid arrows highlight examples where the RPP illumination is significantly better. Yellow arrows highlight observations related to salt imaging and white arrows highlight observations related to stratigraphy. The bolded yellow arrows mark reflectors along the salt overhang, a notoriously difficult yet reservoir-critical zone, that are better illuminated in the RPP data. Refer to the text for relevant details. 39

Figure 3.8 Negative partial-offset stacks zoomed to the left edge of the main salt body on the SEAM Phase 1 model. Zoomed region is described in Figure 3.6. Panels a–d show the ZPP ultra-near, near, mid, and far offset stacks respectively, and panels e–h show the RPP equivalent stacks. Descriptions of arrow annotations are the same as those used in Figure 3.7. 40

Figure 4.1 Definition of the (a) acquisition coordinate system in horizontal x and y and vertical z directions, and (b) the cylindrical processing coordinate system in outward-positive radial R and vertical Z directions. The transverse, T direction is always counter clockwise from R. I and G annotate the locations of the impact source and receivers in each sketch. . 51

Figure 4.2 Conceptual representation of Rayleigh-wave generation from a vertical impact source I. (a) An incident P wave reflects off an impedance contrast producing up-going reflected P (PP) and S (PS) waves. (b) The up-going PS wave undergoes total internal reflection at the free surface producing a PSS wave and a mode-converted PSP wave. The velocity and horizontal and vertical slownesses are described relative to the free-surface incidence angle. (c) At large angles of incidence, evanescent PSP and PSS waves propagate along the surface out-of-phase thus producing (d) a Rayleigh wave with retrograde elliptical particle motion along the free surface. U_z and U_x are described in terms of the potentials, Φ and Ψ, of the evanescent wavefields. 52

Figure 4.3 Frequency-dependent depths at which Rayleigh-wave particle motion change from retrograde to prograde for a fully saturated soil profile (green) (Yang, 2005)), a Poisson's solid (yellow) (Ammon *et al.,* 2020), and glacial ice (blue) based on parameters estimated for the Saskatchewan Glacier (Stevens *et al.,* 2023). Solid line are analytical solutions (Eqn. (4.5)), and dotted lines are approximated depths (Eqn. (4.6)) for all models. Table 4.1 lists associated material properties. . 54

Figure 4.4 Rayleigh-wave characteristic equation (Eqn. (4.7)) represented as a relationship between V_p/V_s and V_r/V_s (black curve) with reference values for a saturated soil (green cross), Poisson solid (yellow circle), and glacial ice at the Saskatchewan Glacier (cyan square). V_p/V_s estimates of other glacial examples are plotted as vertical lines since V_r/V_s estimates are not mentioned in reference studies. Table 4.1 lists associated material properties. 56

Figure 4.5 Model describing a homogeneous, isotropic, elastic ice layer of 150 m thickness overlying a bedrock half space. Table 4.2 presents the elastic model properties. The idealized acquisition has a dense 1 m receiver spacing and 400 m aperture. The sketched geometry is not to scale and approximates receiver placement for visual reference. 61

Figure 4.6 (a) Raw Z-component shot-gather data with corresponding (b) Z-component and (c) raw R-component shot-gather data with corresponding (d) R-component DP for the two-layer ice-bedrock model (Figure 4.5), with the numerically calculated DC for the fundamental model (black line). Every 10th trace is shown in the shot gathers for display purposes. Dashed red lines on DPs highlight the maximum wavelengths for resolving depths 20 m, 150 m, and 200 m; valid regions for picking experimental DCs for each depth range fall to the right of these lines. The experimental DCs for the Z- (purple) and R- (blue) components are displayed on both DPs. We note the DC complexity particularly for R and sub-10 Hz Z, which are not consistent with the numerical solution. 62

Figure 4.7 Monochromatic depth-sensitivity kernels for the homogeneous-ice over bedrock half-space model (Figure 4.5). Curves are the eigenfunctions (the layered-model equivalent of the third terms of Eqns. (4.1) and (4.2) normalized to $U_z(z = 0) = 1$) and represent the sensitivity of U_z (purple) and U_x (blue) to discrete model depths and wave frequencies. The dotted gray lines show the ice-bedrock interface depth for which only the $5 - 10$ Hz panels show non-zero U_z sensitivity and only $5 - 7$ Hz show non-zero U_x sensitivity. 64

Figure 4.8 Conditioned shot gathers and DPs after removing the direct P-wave arrivals. See Figure 4.6 for descriptions of individual panels. Note the substantial improvement in the continuity of the R-component DP, with the mean Z- and R-component pick discrepancy reduced from 180 m s^{-1} to 40 m s^{-1}. Additionally, the Z- and R-component DCs are more closely aligned to the numerical solution (black line). 66

Figure 4.9 Conditioned shot gather data and DPs after removing the direct P-wave arrival and windowing out noisy near-offset traces to highlight the full Rayleigh-wave character at far offsets. See Figure 4.6 for descriptions of individual panels. We improved sub-10 Hz resolution of the DPs with appropriate data conditioning. 67

Figure 4.10 Two-layer ice-bedrock model described in Table 4.2 with two different acquisition experiments: (a) an aperture of $L = 190$ m (approximately half the length of the example described in Figure 4.5) and a receiver spacing of $\Delta r_x = 1$ m with the zero-offset receiver removed; and (b) an aperture of $L = 390$ m and a receiver spacing of $\Delta r_x = 10$ m. Not drawn to scale with the receiver placement only approximate for visual reference. 69

Figure 4.11 Z- and R-component dispersion panels from the two experiments described in Figure 4.10. We conditioned data by removing the direct P-wave arrival and windowing to capture the full Rayleigh-wave signal at all offsets. (a) Z- and (b) R-component dispersion panels for shorter aperture ($L = 190$ m) experiment with dense ($\Delta r_x = 1$ m) receiver sampling; The resulting dispersion panels are lower resolution compared to the those generated from the ideal acquisition (Figure 4.9). (c) Z- and (d) R-component dispersion panels for longer aperture experiment ($L = 390$ m) with sparse ($\Delta r_x = 10$ m) receiver sampling showing comparably lower data distortion than for the limited aperture case. . . . 70

Figure 4.12 Firn-aquifer model variations for synthetic data generation. (a) “Base” model derived from Helheim Glacier seismic inversion results (Killingbeck *et al.,* 2020) with a 10 m thick aquifer overlain by 20 m of firn and a bedrock half-space imposed at 150 m depth. (b) “Deep Aquifer” model similar to (a) but with the firn layer extended to a depth of 40 m. (c)“Thick Aquifer” model similar to (a) but with the aquifer thickened to 20 m. 71

Figure 4.13 Conditioned Z- and R-component shot gathers for the “base” firn-aquifer model described in Figure 4.12a. Every 20th trace is plotted for offsets from 20 m to 300 m. 72

Figure 4.14 Numerical solutions and experimental DCs of the fundamental mode associated with the three models described in Figure 4.12. (a) Numerical solution of the fundamental DC for base (green), deep aquifer (cyan), and thick aquifer (magenta) models. Z- and R-component DCs for the (b) base, (c) deep aquifer, and (d) thick aquifer models, with experimental picks for Z- (plus symbols) and R-component (cross symbols), the arithmetic average of Z- and R-component phase velocity (grey circles), and the complex component (CC) of Z- and R- components (black cross symbols). Between 8 and 20 Hz, the variability of DCs for the three models suggests that accurate picks in this frequency band are important for mitigating the non-uniqueness of dispersion analysis and inversion. 73

Figure 4.15 Depth sensitivity kernels for discrete frequencies of the three aquifer-firn experiments described in Figure 4.12. (a–g) U_z components. (h–n) U_x components. Depths of the bottom of aquifer are color coded for each model, and the depth of the ice-bedrock interface is shown with a dotted gray line at 150 m. The unique sensitivities of the U_x curves for each model motivate an opportunity for improving MASW inversion accuracy through use of MC data. 74

Figure 4.16 (a) Saskatchewan Glacier location in the Canadian Rocky Mountains, Canada (see inset map). Basemap imagery: Orthorectified 4-band PlanetScope scene accessed via Planet.com (b) Geometry of the active-source seismic experiment conducted in the ablation zone involving a stationary array of nine 3-C geophones (R1-R9) linearly spaced at 10 m to form an array of aperture $L = 80$ m. Source station locations S01-S25, also spaced 10 m apart, are shown as blue Xs. 76

Figure 4.17 (a) Raw Z- and (b) R-component shot-gather data for station S02. The zero-offset trace recorded by the mobile geophone is used to window the continuously recorded data on geophones R1-R9 into shot gathers. V_p and V_r moveout velocities calculated by Stevens *et al.,* (2023) are plotted. Note the missing traces at R2 and R9. Additionally, direct P-wave arrival is weaker on the Z- versus the R-component because of the predominantly horizontal particle motion. Strong Rayleigh wave energy is recorded on both components. 78

Figure 4.18 Raw (a) Z- and (b) R-component DPs for the S02 shot gathers shown in Figure 4.17. Conditioned (c) Z- and (d) R-component DPs corresponding to (a) and (b) after removing the zero-offset traces, muting the direct wave, and infilling missing traces with a zeroed trace. Conditioned (e) Z- and (f) R-component DPs at station S05 and (g) Z- and (h) R-component for station S09. Conditioned (i) Z- and (j) R-component supergather DPs combining S02, S05, and S09 shot-gather data. The conditioned individual shots produce consistent DCs although a beat-like signature is imposed as a result of the zeroed infill trace and no interpolation. The supergather DC infills missing offsets and extends the effective array aperture producing higher-resolution DPs. 79

Figure 4.19 (a) Time-aligned Z-component shot gathers for stations S02 (blue), S05 (pink), and S09 (green) with differing offset ranges (x-axis labels). (b) Supergather produced from stacking the three shots in (a) based on similar offsets thus increasing the effective array aperture to $L = 130$ m and infilling missing offset traces without interpolation. 80

Figure 4.20 (a) Dispersion panel derived from CC supergather from shots 02, 05 and 09. (b) Comparison of experimental dispersion curve picks from CC supergather (dashed black line) and individual Z- and R-components (+ and x symbols, respectively), the arithmetic mean (black dots), and the weighted-mean picks calculated from the internal *MASWaves* algorithm (dark and light purple for Z and R components, respectively). All picks were made on the respective DC panels (Figure 4.18) using the standard picking algorithm in the *MASWaves* software. There is little evidence of dispersion and the experimental picks suggest an average $V_r = 1670$ m s^{-1} between 40 and 165 Hz. 82

Figure 5.1 Description of the Rayleigh-wave displacement-stress vector following the nomenclature of Buchen & Ben-Hador (1996). Note that the eigenfunction, $E(z)$ solely controls the depth dependence within any layer, j. 94

Figure 5.2 Overview of the process used to generate dispersion panels (DPs) from shot-gather seismic data for extracting experimental dispersion curves (DCs). (a) Steps involved in calculating the first exponential term, derived from the complex phase of the frequency-transformed shot-gather. Every 20th trace is shown for clarity in all sub-panels. Sub-panel (a1) shows the input shot gather, $D(x_j, t)$; (a2) the frequency-domain representation of the input shot gather, $D(x_j, f)$; (a3) the extracted phase for each trace, ϕ_j; and (a4) the first exponential term, $\exp(i\phi_j)$. (b) Construction of the second exponential term computed from a range of test phase velocities c_T and frequencies. Sub-panel (b1) shows the computed matrix of $\frac{2\pi f}{c_T}$ for various c_T and f; (b2) the offset-scaled version of this matrix for a representative trace at $j = 50$; and (b3) the second exponential term, $\exp(-i\frac{2\pi f x_j}{c_T})$, shown for $j = 50$. (c) Generating the final DP by (c1) computing the product of the two exponential terms for each offset; and (c2) stacking the result across offset. 96

Figure 5.3 Overview of the deterministic inversion workflow implemented in *MASWaves*, which incorporates Monte Carlo sampling for model updates. For a more detailed description of the algorithm, we refer the reader to Ólafsdóttir *et al.* (2018b). 98

Figure 5.4 DPs for Z, R and CC components for each of the three firn-aquifer models: (a-c) base firn-aquifer model (d-e) deep aquifer model (g-i) thick aquifer model. Z-, R-and CC-component DC_{exp} are represented as plus, cross and dot markers, respectively. DC_{theo} for each of the three firn-aquifer models are plotted as solid curves. Dashed red lines on all DPs highlight the maximum resolvable wavelength of 300 m based on the array aperture. 102

Figure 5.5 (a, c and e) Comparison of the Z-, R- and CC-component data (d_{obs}) for each firn-aquifer model (colored lines) alongside the exact data (d_{theo}) plotted in black. (b, d and f) Shortest Euclidean distance, D, between the point extractions of the Z-, R- and CC-component data and the exact data curve treated as a continuous curve. Points plotted along the exact-data curve are the data points used for the exact-data experiments. Annotated frequencies are those at which the component producing the smallest D switches, usually between the Z and CC components. 103

Figure 5.6 Comparison of the median solutions for (a-d) base, (e-h) deep, and (i-l) thick firn-aquifer models each using the true data (left-most column) and the CC-, Z-, and R-component data in the subsequent columns. . . 104

Figure 5.7 Comparison of the depth sensitivity of the vertical and horizontal Rayleigh-wave particle displacements U_z and U_x (plotted as solid and dashed curves, respectively) for the (a–g) base, (h–n) deep, and (o–u) thick firn-aquifer models, for discrete frequencies ranging from 5 Hz (leftmost column) to 35 Hz (rightmost column). Each kernel is plotted on a background shaded to indicate the material present at that depth. Panels highlighted with red boxes are affiliated with observations where the Z-component data appear more accurate than the CC-component data in Figure 5.5. 106

Figure 5.8 (a) Saskatchewan Glacier location in the Canadian Rocky Mountains, Canada (see inset map). Basemap is orthorectified 4-band PlanetScope imagery accessed via Planet.com. (b) Geometry of the active-source seismic experiment conducted in the ablation zone involving a stationary array of nine 3-C geophones (R1-R9) linearly spaced at 10 m to form an array of aperture $L = 80$ m. Source station locations S01-S25, also spaced 10 m apart, are shown as blue Xs. (c) Description of the offset coverage and array length for shots #1, #2, and a supergather generated from both #1 and #2. 110

Figure 5.9 DPs for Z-, R- and CC-components for four experiments: (a–c) shot gather at location S01; (d–e) shot gather at location S02; (g–i) supergather of shots at locations S01 and S02; and (j–l) supergather of shots at locations S01 through S08. All auto-picks selected by the internal *MASWaves* algorithm are plotted as dots; however only a few of these picks (crosses) are used to represent the DC_{exp} input into inversion. This is primarily based on the expected lower and conservative upper wavelength limits of the experiment based on survey design. In some cases, manual de-selection of picks on the Z and R components was necessary at low frequencies to stabilize the inverse solution. 112

Figure 5.10 Results for two single-shot experiments (at station location 1 and 2) using the Z (left), R (middle), and CC (right) data: (a–c) input dispersion data generated from shot location S01; (d–e) input dispersion data generated from shot location S02; The left subplot of each panel shows the d_{calc} for each model solution that is plotted in the right subplot. The solutions are colored by the dispersion misfit where the misfit to d_{obs} (solid black curve) falls within depth-varying error bounds (dashed black curves). Solutions beyond this range are plotted in gray. Red lines in both subplots indicate the median solution, calculated from models with misfits within the 10th to 90th percentile range. 114

Figure 5.11 Results for two supergather experiments using the Z (left), R (middle), and CC (right) data: (g–i) input dispersion data generated from a low-fold supergather of shots at locations S01 and S02; and (j–l) input dispersion data generated from a high-fold supergather of shots at locations S01 through S08. Refer to Figure 5.10 for descriptions of subplots. 115

Figure 5.12 Results of an inversion test where the exact data is used as input in the inversion (i.e., the numerically calculated DC_{theo} is treated as d_{obs}). (a) Median model solution for 100 runs, with 200 iterations per run (in green), versus the true solution plotted as a dotted black curve. The error bounds are calculated from the solutions ranking between the 10th and 90th percentiles. (b) Top five solutions based on lowest data misfits, which are color-coded by the misfit percentages. We note that the yellow model solution, despite having a low misfit, does not resolve the aquifer layer and, as such, emphasizes the non-uniqueness of the inverse problem. 121

Figure 5.13 Comparison of the median solutions from six inversion runs using (a) CC-, (b) Z-, and (c) R-component dispersion data. The CC component, constructed by combining complementary Z and R data, yields the most accurate estimate of the subsurface structure. See Figure 5.12 for subplot descriptions and line definitions. 123

Figure 5.14 Results (curves colored by data misfit) from six inversion runs using the Z data as input. Although most runs recover a firn aquifer layer, the deeper ice and bedrock layers are poorly resolved. This suggests that although longer-wavelength information necessary for resolving these depths is present in d_{obs}, it does not accurately represent the true dispersion behavior, as can be confirmed by comparing DC_{exp} to DC_{theo} in Figure 5.4. All solutions converge at data misfit values ranging from 0.3% to 0.8%. See Figure 5.12 for subplot descriptions and line definitions. 125

Figure 5.15 Results (curves colored by data misfit) from six inversion runs using the R data as input. Similar to the observations made in the CC-component experiment (Figure 5.16), five out of six runs recover a firn aquifer layer. In this experiment, however, the deeper ice and bedrock layers are poorly resolved, as in the Z-component experiment. Compared to the Z-component results, this is likely due to the d_obs capturing very little long-wavelength (above 150 m) information which stems from the DC_{exp} of Figure 5.4b. All solutions converge at data misfit values ranging from 0.2% to 0.5%. See Figure 5.14 for subplot descriptions and line definitions. 126

Figure 5.16 Results (curves colored by data misfit) from six inversion runs using the CC data as input. Most runs recover a firn aquifer layer, with the exception of run #5, despite the low misfit. Although such anomalous solutions can occur across any of the experiments in this study, they exert minimal influence on the median solution, as seen in both the six- and 100-run results in Figure 5.13. The deep ice V_s structure is generally well resolved across all runs, with most uncertainty concentrated near the ice-bedrock interface and in the bedrock V_s. Still, the median estimates for both parameters are reasonably accurate, albeit with broad uncertainty bounds. All solutions converge at data misfit values between 0.3% and 0.7%. See Figure 5.14 for subplot descriptions and line definitions. 127

Figure 6.1 Key elements of the MASW (green workflow) and TDB (blue workflow) inversions. Both approaches involve proposing a new model m', evaluating whether it should replace the current model m, and, if accepted, using it to generate the next m'. The main distinction lies in the inversion mechanics: the definition of parameter spaces (fixed versus free in (a) and (b), respectively), the method of measuring data similarity (c and d), and the rules for model acceptance, rejection, and updating (e and f). 133

Figure 6.2 Overview of the Slakbreen Glacier seismic experiment. (a) Location of Slakbreen within Svalbard. (b) Site map of the Slakbreen Glacier area with elevation contours (meters) and location of 3-C experiment overlaid on satellite imagery from `https://toposvalbard.npolar.no/`. (c) Layout of the 3-C seismic experiment showing the source-receiver acquisition geometry. 138

Figure 6.3 Raw Z- and R-component shot gathers from shot location 91 (plotted in Figure 6.2c) shown on equivalent amplitude scales. Surface Rayleigh-wave energy (annotated "Ray.") is equally strong on both components, whereas the direct wave (annotated annotated "dir.") appears stronger on R. A weak reflection (annotated "ref.") is also observed on both components. 140

Figure 6.4 (a) Z-, (b) R-, and (c) CC^*-component supergathers constructed from shots 1 to 101 on the western side of the 3-C array (refer to Figure 6.2c). As the CC component is a complex-valued signal, the CC^* gather is visualized by taking the the absolute value of the complex signal and reassigning polarity based on that of the Z-component. All gathers are plotted on equivalent amplitude scales, with specific wave modes annotated on the Z-component gather. The CC representation enhances the Rayleigh-wave signal (black arrows annotated on the CC gather), whereas wave modes that are not recorded with a 90° phase shift between the Z and R components are slightly diminished by the summation. 141

Figure 6.5 (a) Dispersion panel for the CC component, based on a supergather constructed from 101 shot gathers acquired on the western side of the 3-C array. DC_{obs} picks from this panel are plotted in green between 8 and 60 Hz and, for comparison, the equivalent Z- and R-component picks are plotted in blue and purple, respectively. (b) Comparison of all three components DC_{obs} picks transformed to plots of V_r versus wavelength, the representation of the data used as input for inversion. . 142

Figure 6.6 Results of three MASW inversion experiments, shown by row. (a, b) The initial model consists of two ice layers with identical elastic properties over bedrock; in (b) the reversal flag allows a low-velocity layer. (b, c) Both include a low-velocity layer, but the internal ice boundary is shifted from 100 m in (b) to 60 m in (c). Columns show: (1) initial model, (2) observed data (solid black), error bounds (dashed black), calculated data from each iteration (colored by misfit percentage), and the median between the 10th and 90th percentiles (solid red), and (3) model solutions from each iteration (colored by misfit percentage) with the median solution (solid red). 144

Figure 6.7 Results of three MASW inversion experiments using (a) CC-, (b) Z-, and (c) R-component data. All experiments use the same parameterization as experiment #3 in Figure 6.6. See Figure 6.6 for descriptions of the individual plots. The median solution for each of the three predefined layers is shown on the right for each experiment. 145

Figure 6.8 Model solutions of three TDB inversion experiments using the (a) CC-, (b) Z-, and (c) R-component data. All experiments share similar parameterization with the exception of the noise window which was lower for the CC experiment. 147

Figure 6.9 (a) Comparison of median model solutions and the (b,c) CC-, (d,e) Z-, and (f,g) R-component TBD results, where panels, (b), (d), and (f) are the standard deviation of the depth-dependent V_s posterior for each component experiment and (c), (e), and (g) are the depth-dependent posterior distributions of interface solutions for each component experiment. Red horizontal lines indicate depths where the interface posteriors are high for either the CC or Z solutions. The R component posterior is not evaluated due to the unreliability of its complex model solution (Figure 6.8). 148

Figure 6.10 Comparison of DC_{obs} (colored points) with the range of DC_{calc} for all accepted solutions in our experiments using (a) CC-, (b) Z-, and (c) R-component. Prior (uniform) and posterior distributions for noise levels in each of the (d) CC-, (e) Z-, and (f) R-component experiments. Data misfits are comparable across all experiments due to the treatment of noise as a free hyperparameter in the TDB inversion. The CC component exhibits the lowest estimated noise level among the three components. Number of layers in the prior and posterior model distributions for the (g) CC-, (h) Z-, and (i) R-component experiments 150

Figure 6.11 (a) Locations of the two polythermal glacier case studies (Bakaninbreen and Lovenbreen) and the density logged exploration well at Reindalspasset relative to the Slakbreen field site. (b) Comparison of V_p profiles: median solutions from the Slakbreen *CC*- and *Z*-component data, converted assuming $V_p/V_s = 2.0$ for glacial ice (Aster & Winberry, 2017), alongside V_p models from Lovenbreen (King *et al.,* 2008) and Bakaninbreen (Smith *et al.,* 2002). Blue arrows annotate the transition from cold to warmer ice in each solution. 152

Figure A.1 Reuse and Open-Access Policy of the Society of Exploration Geophysicists' Interpretation journal, acquired from `https://library.seg.org/page/policies/open-access`. The highlighted section indicates the permissions for reuse of the published manuscript for inclusion in this dissertation to meet degree requirements. 179

Figure A.2 Email correspondence from Dr. Jim Simmons providing permission for the inclusion of our manuscript published in *Interpretation* within this dissertation. 180

Figure A.3 Email correspondence from Dr. Carlos Calderón-Macías providing permission for the inclusion of our manuscript published in *Interpretation* within this dissertation. 180

LIST OF TABLES

Table 4.1 Elastic properties for different subsurface media examined in our analytical models: a. fully saturated soil profile (Yang, 2005); b. Poisson solid (Ammon *et al.,* 2020); c1. ice layer derived from the Saskatchewan Glacier (Stevens *et al.,* 2023); c2. ice layer derived from the Greenland Ice Sheet (Walter *et al.,* 2015); c3. ice layer derived from Nathorst Land, Spitsbergen (Johansen *et al.,* 2011); d. firn layer derived from the Helheim Glacier, Greenland (Killingbeck *et al.,* 2020). Note that although some case studies report higher-precision values, we have rounded results to the nearest hundredth for consistency. 55

Table 4.2 Two-layer homogeneous ice-bedrock model elastic properties extracted from Stevens *et al.* (2023) 61

Table 5.1 Firn-aquifer model variations for synthetic data generation. (a) “Base” model derived from Helheim Glacier seismic inversion results (Killingbeck *et al.,* 2020) with a 10 m thick aquifer overlain by 20 m of firn and a bedrock half-space imposed at 150 m depth. (b) “Deep Aquifer” model similar to (a) but with the firn layer extended to a depth of 40 m. (c) “Thick Aquifer” model similar to (a) but with the aquifer thickened to 20 m. 100

Table 6.1 Initial model for experiments #1 and #2 in Section 6.5. 155

Table 6.2 Initial model for experiment #3 in Section 6.5. 155

LIST OF SYMBOLS

General Nomenclature

Compressional-wave (P-wave) velocity	V_p
Shear-wave (S-wave) velocity	V_s
Rayleigh-wave phase velocity	V_r
Density	ρ
Vertical (Component)	Z
Radial (Component) - along the source-receiver direction	R
Transverse (Component) - counter clockwise from R direction	T
Depth (or vertical position)	z
Horizontal position	x
Incident P-wave reflected as P-wave	PP
Incident P-wave reflected as SV-wave	PS
Layer thickness	h
Frequency	f
Wavelength: V_*/f	λ
Array length	L
Receiver spacing	Δr_x
Source-receiver offset	d
Time	t

Chapter 3

Horizontal (Component) - general reference to components parallel to the surface	H
Inline (Component) - H component direction oriented along the source acquisition line	X
Crossline (Component) - H component direction perpendicular to the source acquisition line	Y
PP-wave recorded on Z-component	ZPP
PS-wave recorded on Z-component	ZPS
PP-wave recorded on H-component	HPP
PS-wave recorded on H-component	HPS
PP-wave recorded on X-component	XPP
PP-wave recorded on R-component	RPP
Summation of the Pressure- and Z-component data	PZ

Chapter 4

Horizontal particle displacement	U_x
Vertical particle displacement	U_z
Scalar wavefield potential associated with P-waves	Φ
Vector wavefield potential associated with SV-waves	Ψ
Amplitude scaling factor	A
Horizontal slowness	p
Vertical component of Rayleigh wave slowness associated with P-waves: $\sqrt{1/V_r^2 - 1/V_p^2}$	$\hat{\eta}_p$
Vertical component of Rayleigh wave slowness associated with S-waves: $\sqrt{1/V_r^2 - 1/V_s^2}$	$\hat{\eta}_s$

Angular frequency: $2\pi f$	ω
Resonant Frequency	f_0
Depth at which Rayleigh wave particle motion reverses (retrograde to prograde)	h_r
Complex Component: $Z(d,t) + iR(d,t)$	CC

Chapter 5

Theoretical dispersion curves	DC_{theo}
Experimental dispersion curves	DC_{exp}
Phase	Φ
Angular Frequency	ω
Test Phase Velocities	c_T
Calculated data	d_{calc}
Observed data	d_{obs}
Current data misfit	ϵ_{DC}
Trial data misfit	ϵ_{test}

Chapter 6

Current model state	m
Proposed model state	m'
Number of model layers	k
Calculated dispersion curve data	DC_{calc}
Observed dispersion curve data	DC_{obs}

LIST OF COMMON ABBREVIATIONS

One-Component, assumed vertical	1-C
Three-Component	3-C
Four-Component (3-C displacement and pressure data)	4-C
Multi-Component	MC
Single-Component (using one data component)	SC
Compressional Wave	P-wave
Shear Wave	S-wave
Vertical Shear Wave with particle motion parallel to plane of wave propagation	SV-wave
Horizontal Shear Wave with particle motion perpendicular to plane of wave propagation	SH-wave
Dispersion Panel	DP
Dispersion Curve	DC
Multi-Channel Analysis of Surface Waves	MASW
Multi-Component, Multi-Channel Analysis of Surface Waves	MC-MASW
Signed-Offset Polarization (bias) - The observation that some reflections are recorded with opposite polarities on positive and negative offsets	SOP
Signed-Offset Illumination (bias) - The observation that different subsurface features are illuminated differently when comparing positive and negative offsets	SOI
Ocean Bottom Node	OBN
Transdimensional Bayesian Inversion	TDB
Signal-to-noise ratio	SNR
Reversible-Jump Markov Chain Monte Carlo	rj-MCMC

ACKNOWLEDGMENTS

My curiosity has often led me into far more chaos than accomplishment, and in the moments where the latter has occurred, I owe much gratitude to the mentors that have guided me throughout the PhD.

To my advisors, Professors Jeffrey Shragge and Matthew Siegfried, your support and kindness exceeded anything I could have hoped for when I transitioned into your groups midway through my PhD. You both taught me not to fear my curiosity but to hone it. Matt, thank you for helping me build perspective and channel a sense of intellectual patience that balanced my restless curiosity. This lesson has been especially pivotal as I navigated the boundaries of a new field with little prior context. Jeff, thank you for showing me how to deepen curiosity rather than scatter it, letting questions take root and grow into meaningful inquiry. You also provided a much-needed outlet for the chaotic ideas and questions that allowed me to release some unsettled thoughts while still moving forward.

Finally, to Jim (aka J), with whom this journey began. You have always cared more about your students' fulfillment than accreditation, a value not easy to uphold in an academic space constantly pushing for metrics and recognition. I am profoundly grateful that you nurtured my curiosity instead of constraining it, providing the courage and reassurance I needed to explore questions beyond our domain, even when the path was uncertain and meant we would eventually go our separate ways.

To my committee, Professor Paul Sava, Dr. Aaron Girard, Professor Wendy Fisher, and Professor Mike Wakin, thank you for your insights and encouragement throughout this journey. I also extend my gratitude to my colleagues from the Reservoir Characterization Project, the Center for Wave Phenomena, and the Mines Glaciology Laboratory for their collaboration and for fostering an inspiring environment in which to conduct research.

To the students I have had the honor of teaching and learning from, thank you. Across four semesters of Leadership by Design (LBD), two Geophysics field camp sessions, and two semesters of Physics of the Earth, you have shaped my approach to both teaching and science communication, but most importantly, you have shown me the profound value of learning alongside an instructor, where discovery is shared rather than simply received.

In this spirit, I must acknowledge Professor CJ McClelland — your teaching pedagogies continue to resonate with me, deeply shaping the development of my own. You inspire the closing sentiments of this dissertation, reflecting the idea that true advocacy for ‘play’ in academia is embodied by educators like yourself, who go beyond words to generously invest the time in building the playgrounds where students can explore and learn for themselves.

To the GP Gals — Hannah, Elena, Rachel — and to Joanna and Nicholas, we’ve weathered the highs, the lows, and the caffeine-fueled chaos in between. I’ve loved celebrating every milestone — mine and yours — and couldn’t be more grateful for the friendships that came with it.

To my best friends and family, I strive to make you as proud as you make me to be your daughter, sister, aunt, and friend. Thank you for standing by me through the ups and downs, offering support even when my journey was hard to fully understand.

Finally, to Richie and Kane - over the past five years, we’ve moved seven times, lived in three different states, chased many a rabbit, started and completed your master’s degree, collectively cycled through four different jobs, and made far too many late-night trips to Cold Stone than any thirty-something-year-olds should admit to. And of course, there was that small life occasion when we got engaged on the day of one of the greatest World Cup finals we’ll probably ever witness, with both our parents cheering and shouting alongside us, and later married on the beach in Jamaica, surrounded for the first time by all our friends and family from the U.S., Jamaica, and Trinidad. These past five years have been no small feat, and I am deeply grateful for your patience, understanding, and unwavering love throughout the journey. Here’s to our next chapter!

A LESSON FOR THE JOURNEY AHEAD

An unfortunate roadblock throughout my PhD has often been my overactive curiosity, which makes me easily inspired and prone to seeing almost everything as an idea worth exploring. I have learned the hard truth that some ideas are considered “unworthy” in the eyes of academia, because, like any business, the field often measures the quality of research by the productivity of results. This can make the scientific process feel daunting and, at times, uninviting to the curious — even though science is, at its core, rooted in curiosity.

I have, however, continued to find a space for my curiosity in the classroom, where ideas can exist freely and alongside one another. And while I may not know exactly how I will get there, I am certain that I want to be part of creating environments that foster open inquiry and moreover equip learners with the tools and frameworks to explore ideas critically. I pursue this not merely for the joy of curiosity itself, but also for the forward momentum it fuels — propelling both individuals and research communities toward deeper exploration and more meaningful work. Academic and professional spaces designed in this way invite learners of all ages and backgrounds to explore with mutual respect and foster a level of knowledge transfer that, in my view, remains a bottleneck in the flow of science.

Guided by this appreciation for curiosity and accessible intellectual playgrounds, the work that follows aims not only to explore specific research questions but also to gently challenge how ideas are organized and understood, offering scholars from diverse backgrounds an opportunity to think critically and differently about the topics presented. It is my hope that this strategy offers you both insight and, more importantly, inspiration for your own journey.

To Richie and Kane

For the Team

CHAPTER 1

INTRODUCTION

Seismic waves propagate through the Earth in three dimensions, with each directional component of the wavefield carrying distinctive information about the subsurface through which it traverses. In active-source seismic experiments, the goal is to improve subsurface characterization by using a controlled seismic energy source and recording a sufficiently comprehensive portion of the wavefield. We can then infer subsurface structure and elastic properties (i.e., compressional, P- and shear, S- wave velocities, and density) by working backward from the recorded wavefield, a process known as seismic inversion. The completeness and quality of the acquired data are critical for accurate subsurface characterization, as they help constrain the solution space in inversions and improve the resolution and reliability of the resulting subsurface models.

Multi-component (MC) seismic surveys advance the objectives of active-source experiments by capturing the vectorial nature of the seismic wavefield. This is achieved through the use of multi-directional sources, multi-component receivers, or a combination of both (Stewart, 2009). In contrast, single-component (SC) methods typically use vertically oriented SC receivers along with point-impact or explosive sources, resulting in a more limited dataset. Generally, by exploiting the complementary information recorded on different directional components, MC surveys can better constrain subsurface properties that remain ambiguous in SC recordings (Hardage *et al.*, 2011).

The contributions of this dissertation are best understood in the context of how active-source MC seismology has evolved and been applied across a range of domains. The following sections will expand on this background, but, in brief, the earliest applications of active-source MC seismology was in oil and gas exploration to capture secondary, S-wave energy (shear waves in which particle motion is perpendicular to the wave propagation direction) as a complement to the primarily targeted primary, P-wave data (compressional waves in which particle motion is parallel to the wave propagation direction) (Tatham *et al.*, 1991). This S-wave acquisition was mainly achieved using three-component (3-C) geophones, recording displacement typically along the vertical and two orthogonal, horizontal directions (Tatham *et al.*, 1991). Although these MC experiments recorded other wave modes with informative vector sensitivities, the clear advantages of S-wave acquisition for elastic-property characterization shaped a relatively narrow perception of the utility of MC experiments. However, MC seismology encompasses a broad strategy of leveraging the vector sensitivities of different wave modes for characterizing subsurface features (Hardage *et al.*, 2011; Stewart, 2009). This principle underpins a range of modern seismic experiments that have grown more complex due to challenging subsurface targets and complex acquisition designs, though they are not often explicitly recognized as MC methods. Examples include ocean-bottom node (OBN) surveys (e.g., Caldwell, 1999), that commonly combine pressure and vertical displacement information to extract reflected P-wave data, as well as efforts involving (elastic) full waveform inversion (e.g., Solano & Plessix, 2023). Motivated by this broader understanding of MC seismology, this dissertation examines the utility beyond conventional S-wave analysis. Specifically, this work explores how P- and surface-wave modes (explained in detail in Chapter 2) captured on the horizontal components of MC receivers (3-C and OBNs) enhance subsurface characterization compared to SC analysis approaches.

1.1 MC Seismology - Historical Perspective

Since the 1800s, earthquake seismologists have used MC data by recording particle motion in three orthogonal directions to detect and locate seismic events (Rodgers, 1968). In contrast, active-source MC seismology in fields such as oil and gas exploration, geotechnical engineering, and environmental science faces distinct challenges, as the experimental objectives of active experiments differ from those of passive seismology. By using controlled sources—often repeatable and directional—and recording the wavefield in multiple orientations, active-source MC methods aim to improve subsurface characterization beyond what is possible with traditional SC approaches, which typically rely on vertical receivers (1-C) and explosive sources.

The earliest review of active-source MC seismology was published by Tatham *et al.* (1991); here, I summarize their account of developments up to 1970. Although MC concepts in earthquake seismology date back to the 1800s, the use of 3-C geophones in active-source experiments did not begin until the 1950s. This development was motivated by initial observations of SV waves (S-waves in which the perpendicular particle motion is in the vertical plane) in 1-C checkshot surveys from the 1940s, which were used to estimate an S-wave velocity.

During the 1960s, interest shifted toward SH waves (S-waves in which the perpendicular particle motion is in the horizontal plane) based on the assumption that their decoupling from P waves could yield simpler seismic records with higher resolution that ultimately improved imaging (Tatham *et al.*, 1991). This shift led to the invention of horizontal sources in the 1970s, coinciding with advances in rock physics that revealed additional benefits to mapping changes in S-wave velocities (Tatham *et al.*, 1991).

Despite numerous production-scale MC experiments that were underway toward the end of the 1970s, the majority of publications from this era did not explicitly refer to these surveys as “multicomponent”. The earliest mentions of the term in the context of vertical seismic profiling (VSP) experiments appear in Karus *et al.* (1975) and Majer (1978). By the 1980s, the term gained broader use in VSP studies, where its advantages were more pronounced compared to the production-scale reflection surveys.

Although early reflection-based MC experiments achieved limited success (Chopra & Stewart, 2010), the proliferation of MC datasets following the 1970s industry upsurge enabled and motivated continued research, introducing new applications of S waves – such as fracture characterization using shear-wave polarization analysis in 9-C surveys (Alford, 2005) – and inspiring theoretical concepts like elastic wavefield imaging (Kuo & Dai, 1984).

However, insufficient computational infrastructure to fully support elastic workflows and large MC data volumes (Yang, 1982), along with the complexity of processing multiple S-wave modes (Chopra & Stewart, 2010), prevented broader adoption of these methods. The 1986 oil price collapse tempered any remaining momentum for MC exploration as widespread staffing reductions led to a shortage of subject expertise and economic constraints (Chopra & Stewart, 2010; Hardage *et al.*, 2011).

The "new wave" of active-source MC seismology in the 2000s, as anticipated by Davis *et al.* (1997) and echoed in subsequent publications (Tatham, 2002; Waggoner & Kristiansen, 2003), was driven by a combination of reduced land acquisition costs enabled by MEMS (Micro-Electro-Mechanical Systems) sensors (Stewart, 2009), the deployment of 4-C (pressure and 3-C displacement) seafloor receivers (Li & Zhang, 2011), and a broader resurgence in industry activity. A 2001 poll from a workshop on the future of MC seismic methods conducted by the Society of Exploration Geophysicists (SEG) (Waggoner & Kristiansen, 2003) identified the most probable applications as improvements in imaging (e.g., below gas clouds or in areas of poor P-wave reflectivity), drilling hazard identification (e.g., pore pressure and stress characterization), and reservoir mapping (e.g., lithological and fluid characterization, and monitoring). While most of these potential applications were proposed on the basis of exploiting S-wave content, some improvements in P-wave imaging, particularly beneath challenging geological features (e.g., basalt, chalk, and salt), were based on enhanced P-wavefield illumination provided by 4-C seafloor surveys compared to traditional 1-C streamer surveys (Tatham, 2002). Around the 2010s, this "new wave" was solidified by a surge in scholarly output on MC seismic technology, which included three review papers (Farfour & Yoon, 2016; Li & Zhang, 2011; Stewart, 2009), two special sections in SEG journals (Chopra & Stewart, 2010; Hardage *et al.*, 2014), and a dedicated SEG book (Hardage *et al.*, 2011) and short course (Gaiser, 2016) on the topic.

1.2 MC Seismology - Current State

Almost a decade has passed since the most recent of these notable contributions, motivating a reassessment of the current state of MC seismic research. Historically, there has been no single, universally accepted definition of MC seismology, since the term "multicomponent" did not originate from a single practitioner, but instead emerged gradually over several decades. This lack of a clear, unified definition complicates efforts to evaluate MC seismology's current impact and value in the industry.

Early descriptions framed MC experiments as related to the additional S-wave recording, such as "the use of concurrent, combined shear (S)- and compressional (P)-wave seismology" (Tatham *et al.*, 1991) or "In multicomponent seismic, we seek to also utilize shear waves (S waves) to explore the subsurface" (Waggoner & Kristiansen, 2003). About a decade later, the term broadened in scope. As examples, Chopra & Stewart (2010) described MC methods as "a superset of conventional seismic technology", Li & Zhang (2011) referred to them as "the seismic method for recording and analyzing multiple modes of the particle motion of a seismic wave", and Hardage *et al.* (2011) emphasized the need for "a vector-based approach" to seismic processing. Though not always explicitly stated, each of these later definitions implies that more than one type of motion must be recorded in order to investigate the multi-dimensional wavefield.

Synthesizing these notions, we may define active-source MC seismology as:

> The practice of analyzing the vector components of the seismic wavefield, for any/all wave mode(s), measured along a single direction of wave propagation defined between a given source–receiver pair.

Such experiments are enabled by surveys that employ more than one directional source and/or record multiple components of particle motion at the receiver. To be explicit, experiments in which the source orientation is varied but SC receivers are used are still considered MC experiments, since the impact of source directivity can be evaluated along a single direction of wave propagation. For example, emerging marine vibrator technology (Alfaro *et al.*, 2023; Laws *et al.*, 2019) may provide opportunities to exploit source directivity aspects of MC surveys in offshore experiments.

Under this definition of MC seismology, 2-D and 3-D surveys are not inherently “multicomponent”, although one could argue that they exploit aspects of wavefield directionality through variations in offset or azimuth. This is because such surveys rely on sampling across different source–receiver geometries rather than measuring multiple components of particle motion along a single propagation path. For example, 3-D streamer acquisition using an explosive source and hydrophone receivers is, by this definition, rightly not considered “multicomponent”.

This definition does, however, encompass modern experiments, including those that explicitly target S-wave content, as well as those that focus on other wave modes such as P waves (e.g., in 2-C pressure and vertical-displacement seafloor experiments) or surface waves (e.g., in 3-C near-surface surveys). It also includes experiments that capture and analyze the vector seismic wavefield, which are now more computationally feasible (Arrowsmith *et al.*, 2022; Igel, 2017). Examples include MC elastic reverse time migration (ERTM) (e.g., Yan & Sava, 2008) to improve S-wave imaging, and MC elastic full waveform inversion (EFWI) (e.g., Cho *et al.*, 2022; Solano & Plessix, 2023), which ultimately seeks to bypass intermediate P- and S-wave velocity estimation and directly construct subsurface images.

In these MC experiments, vector-based relationships between different component data are not only leveraged for interpretative workflows such as joint amplitude versus offset inversions using the P and SV waves from the vertical and horizontal components, respectively (e.g., Tura *et al.*, 2022), or shear-wave polarization analyses for fracture detection using the orthogonal horizontal components (e.g., Alford, 2005; Omar, 2018), but also play a central role in processing workflows. These include techniques such as separating upgoing and downgoing wavefields using pressure and vertical components (e.g., Seher *et al.*, 2022) or sensor orientation correction using vertical and horizontal components (e.g., Dellinger *et al.*, 2002; Gaiser, 1998).

Although the historical development of active-source MC seismology is closely tied to oil and gas exploration, several themes carry over into its modern use across other domains. These include: (1) broad recognition that MC experiments are especially valuable for measuring the S-wavefield energy, thereby improving accuracy in resolving subsurface structure and mapping elastic material properties. This is evidenced by numerous active-source MC studies exploiting S-wave sensitivity of surface waves (e.g., in glaciology (e.g., Tsoflias *et al.*, 2008) and geotechnical engineering (e.g., Park *et al.*, 1998)) and from studies of reflected body waves in glaciology (Agnew *et al.*, 2023), geotechnical projects (e.g., Guan *et al.*, 2021; Vardy *et al.*, 2017), and mineral exploration (e.g., Li *et al.*, 2024; Snyder *et al.*, 2009); (2) the limited adoption of horizontal sources, though successful applications exist in offshore and onshore geotechnical experiments (Stokoe & Rosenblad (1999) and Häusler *et al.* (2018), respectively), in an environmental landslide-hazard study (Pertuz & Malehmir, 2023), and in a mining exploration project characterizing gravel deposits (Harris *et al.*, 2009); (3) increased prevalence of 3-C studies through the use of MEMS sensors, which enable broader offsets, denser spatial sampling, and improved recording of a wider range of wave modes, as highlighted in Barzegar *et al.* (2022)'s review of this technology's application in geotechnical engineering; and (4) growing interest in full-waveform methods. For example, in glaciology, full-waveform inversion is being used to improve characterization of englacial features such as ice-slabs in firn layers (Pearce *et al.*, 2021) and basal conditions (Babcock & Bradford, 2014). Modern challenges in these domains mirror those faced by the oil and gas industry in the 1980s, including limited domain expertise and cost and logistical constraints that restrict data acquisition and processing capacity.

1.3 Scope of Dissertation

The scope of this dissertation research spans MC seismic applications from deep-marine, oil and gas exploration to near-surface glacial characterization. In marine oil and gas exploration, traditional SC surveys (usually using vertical-component geophones or hydrophones) are large-scale and high-resolution, often providing sufficient evidence to motivate and de-risk drilling programs. In this setting, MC experiments must clear a high bar to demonstrate added value, which to date has primarily come from elastic methods as well as specialized processing flows. These opportunities, supported by substantial industry resources (both financial and computational), provide strong motivation for continued experimentation with MC datasets. In contrast, the value of MC data in glaciology can be more compelling as surveys are typically smaller and often rely on shorter or less dense 2-D arrays where data quality and resolution may be limited. In this context, the threshold for demonstrating the value of MC data is lower, since even modest contributions, such as improvements in signal-to-noise ratio, can justify experimentation. Both domains therefore present promising avenues for novel MC applications, particularly because the added cost and time of deploying 3-C receivers (or OBNs in deep-marine exploration) are incremental relative to SC systems.

1.4 Key Research Questions

This dissertation focuses on the utility of active-source MC seismic experiments beyond conventional S-wave analysis. The central aim is to address key gaps in understanding how additional modes recorded on the horizontal (H) components of MC receivers in 2-D experiments can complement subsurface characterization methods that traditionally rely solely on vertical (Z)-component data. This is demonstrated through four studies: the first focuses on reflected P waves recorded on the H components (HPP data), while the remaining three examine surface Rayleigh waves recorded on the H component aligned radially (R) with respect to the source location.

1.4.1 Study 1: Contributions of the Reflected P-wave Recorded on the Horizontal Component of Ocean Bottom Node Surveys to Imaging

This study is motivated by advances in marine acquisition with OBN surveys and the growing interest in full-wavefield imaging. In most 4-C surveys, the H components are primarily used to target S-wave data for reservoir characterization or monitoring. However, these same H components also record portions of reflected P-wave energy. Although this HPP signal is inherently included in full-waveform methods, its specific benefits remain poorly understood. The study is thus guided by two key questions:

1. Which subsurface environments are most likely to benefit from HPP illumination?
2. What acquisition and processing factors are most critical to optimizing the effectiveness of HPP data in seismic imaging?

1.4.2 Study 2: Signal Enhancement of Surface Wave Dispersion using Multi-Component Data from Limited-Coverage Glacial Experiments

This study is motivated by small-scale active-seismic glacial experiments aimed at deriving near-surface S-wave velocity (V_s) models, which are essential for mapping ice thickness and understanding glacial flow dynamics. V_s modeling using surface Rayleigh waves can benefit from MC experiments as the elliptical particle motion of these waves is partially recorded on both Z and R components of 3-C geophones. Combining these datasets can enhance the dispersive signal of Rayleigh waves, which is linked to V_s variations with depth. Glacial conditions can limit survey design, which may reduce signal quality and the depth of investigation in dispersion analysis. MC experiments can help overcome these challenges with little additional effort or cost beyond SC surveys, making them a highly impactful method in such settings. To date, dispersion analysis approaches have been applied only to a limited extent in glaciology. This study therefore first contrasts general data acquisition and processing methods developed for geotechnical studies in order to adapt them to glacial settings, before addressing the primary objective of assessing the utility of MC experiments. The specific research questions are:

1. What are the minimum acquisition setup requirements for sufficiently recording and extracting Rayleigh-wave dispersion in glacial ice environments?
2. How can data conditioning of a limited-offset, sparse 2-D survey be optimized for Rayleigh-wave dispersion analysis in glacial ice environments?
3. Can MC data improve the accuracy of Rayleigh wave dispersion signal?

1.4.3 Study 3: Improving Shear-wave Velocity Modeling using Multi-Component Dispersion Data from Limited-Coverage Glacial Experiments

This study extends from the previous work, shifting focus to the inversion solution as the natural next step after visualizing and picking dispersion signatures. The research questions center on two challenges: non-uniqueness of the inverse solutions in glacial environments that produce similar dispersion curves, and inversion stability in the presence of noise and, data flaws e.g. missing trace information. Accordingly, this study asks:

1. To what extent does combining Z- and R-component data reduce non-uniqueness in shear-wave velocity models derived from dispersion estimates in glacial settings?
2. How does including R-component data influence inversion stability compared to using only Z-component data?

1.4.4 Study 4: Maximizing the Value of Multi-Component Seismic Data with Robust Inversion Approaches

Building on insights from Studies 2 and 3, where R components provided complementary and at times unique information to Z-component Rayleigh-wave data, this study emphasizes the importance of robust inversion strategies to fully exploit MC information. A trans-dimensional Bayesian (TDB) inversion framework is applied to surface-wave dispersion data as a velocity model building approach that allows complexity of model solutions (i.e., number of layers) to be defined by the data rather than set beforehand by the user. The emphasis is on testing how MC data influence the performance of this algorithm by assessing both the fidelity of recovered models and the resilience of solutions given field data noise. The research questions addressed are:

1. Does the TDB inversion strategy using the MC data yield more geologically meaningful velocity structures than SC approaches?
2. How can the TDB posterior results of velocity-depth profile, number of layers, and noise improve interpretation of the englacial and subglacial features?

1.5 Dissertation Structure

Because this dissertation spans multiple application domains, Chapter 2 begins with a review of key concepts in MC seismology, recognizing that familiarity with terminology and underlying assumptions may vary between disciplines. The exposition in this chapter is designed to facilitate knowledge transfer across domains, which is essential for navigating discipline-specific obstacles and bridging gaps in conceptual understanding.

Studies 1 through 4 are presented in Chapters 3 through 6, respectively. Study 1 (Chapter 3) is a synthetic investigation that leverages two well-known oil and gas industry marine models to explore the utility of P waves recorded on H components for imaging. This work was published in the SEG journal INTERPRETATION (Garvey *et al.*, 2025). Studies 2 and 3 (Chapters 4 and 5) employ synthetic glacial models and a field dataset from the Saskatchewan Glacier (Stevens *et al.*, 2023) to examine the value of Rayleigh waves recorded on H components for near-surface V_s modeling. Both studies are in preparation for submission to the Journal of Glaciology. Study 4 (Chapter 6) pivots to a field dataset from the Slakbreen glacier in Svalbard (acquired as part of an Arctic Seismic Exploration course at the University Centre in Svalbard) and exemplifies how the sensitivities of MC records of surface-wave dispersion is better leveraged using a stochastic inversion as opposed to the deterministic approach introduced in Study 3, Chapter 5.

Chapter 7 summarizes the main conclusions from the individual studies and distills pedagogical insights on the value of MC subsurface characterization across diverse fields and industries. This chapter also outlines directions for future work, including extending MC inversion and imaging approaches to more complex field settings, exploring additional wave modes, and developing improved acquisition and processing strategies to further enhance the value of MC data.

CHAPTER 2

CONCEPTS OF MULTI-COMPONENT SEISMOLOGY

In this chapter, I briefly review concepts that are particularly relevant in multi-component (MC) seismology and underpin the studies that follow. The sections provide a foundational understanding of wave-mode propagation relative to source directivity, acquisition considerations for MC experiments, and general considerations for processing frameworks that ensure wave-mode data remain consistent and interpretable across recording components. Although these concepts are not new, they are included to make the dissertation accessible to practitioners across different fields, including those without formal seismology training, to facilitate appreciation of the value of the work and its relevance to their own areas of expertise.

2.1 Description of Wave Modes

This section introduces the main seismic wave modes, grouped by where and how they propagate: through a medium (body waves), along an interface (surface or interface waves), or guided by boundaries such as layering (guided waves). Within each classification, wave modes are further categorized by their particle motion relative to the direction of wave travel. I also link these wave modes to the type of seismic source from whence they originated. The source mechanism also influences the radiation pattern and phase of the initiated wave modes (Gaiser, 2016). The radiation pattern describes how the amplitude of a seismic wave varies with direction from the source, whereas the phase reflects the timing or relative motion of the wave energy as it propagates through the medium. Together, these characteristics are important for understanding how each component in MC experiments records the same wave modes and, in turn, how they can be combined. For body-wave descriptions, I comment on radiation patterns only briefly and direct readers to several key references depending on their interests. For a comprehensive overview, including 3-D plots of radiation patterns associated with specific controlled-source mechanisms, see Appendix B of Gaiser (2016). Readers interested in the sensitivities of these radiation patterns to source design parameters, such as source depth or frequency, including those for surface waves, are referred to Jílek & Červenỳ (1996). For analytical derivations, Miller & Pursey (1954) provided expressions for point vertical and horizontal sources oriented along the direction of wave propagation, and Cherry Jr (1962) extended the analysis to horizontal sources generating wave modes with particle motion orthogonal to the propagation direction.

The discussion below assumes a homogeneous, isotropic medium in which no mode conversions occur except for at the free surface. In heterogeneous media wave modes initially excited by a given source can be partitioned into other modes as they propagate through regions with varying elastic properties. As a result, the particle motion recorded at a receiver may include contributions from modes not directly generated at the source.

2.1.1 Body Waves

Consider an infinitely large homogeneous block in which an explosive source is detonated at the center. This source mechanism, defined as a "center of dilation" by Jílek & Červenỳ (1996), is *omni-directional* in that it initiates energy uniformly in all directions (Gaiser, 2016) (Figure 2.2a). This type of energy, which displaces the medium in the direction of wave propagation, is defined as *compressional waves.* The associated particle motion relative to this wave mode's propagation is illustrated along two ray paths, each on two perpendicular planes, in Figure 2.1a–b. Because this wave mode is the fastest seismic waves, the associated energy arrives first at receivers in seismic experiments and are known as primary waves, or *P waves.*

Although the theoretical radiation pattern from an omni-directional source in a homogeneous medium is spherical, it is also influenced by burial depth (Jílek & Červenỳ, 1996). When such sources are placed at shallow depths (i.e., less than half the initiated P-wave wavelength), interactions with the free surface produce wave-mode conversions that distort the otherwise spherical radiation pattern. This depth sensitivity is examined by Jílek & Červenỳ (1996) for explosive source mechanisms as well as for "single force point sources", which are *directional* in the sense that the seismic wavefield is generated by an initial displacement force along a single direction.

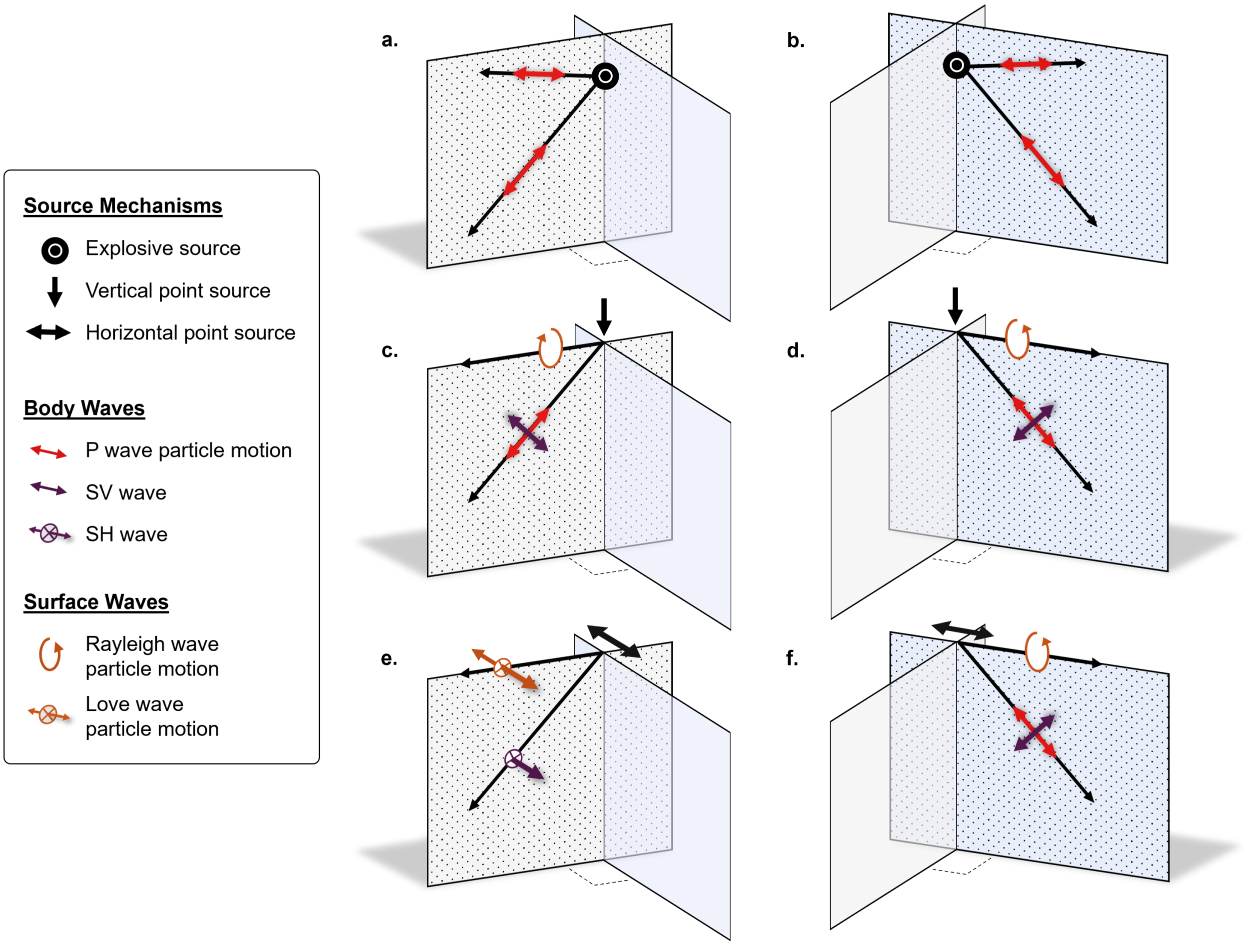

Figure 2.1 Description of wave modes generated in a homogeneous, isotropic medium from different sources: a buried explosive source (a, b), a vertical point source at the free surface (c, d), and a horizontal point source at the free surface (e, f). The left and right columns show propagation along two perpendicular planes for the same source mechanism. Surface Rayleigh and Love waves can be generated by any source due to mode conversion and free-surface reflections; they are included in certain panels for conceptual reference relative to other wave modes.

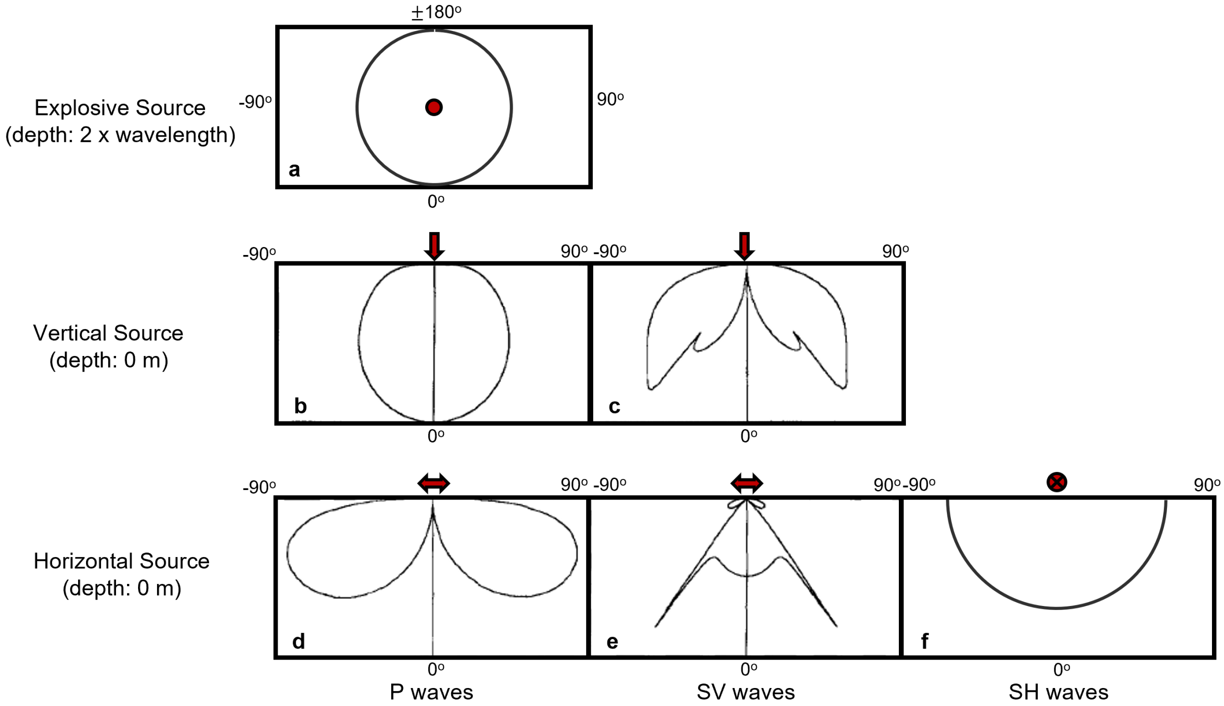

Figure 2.2 Description of radiation patterns of wave modes initiated from (a) an explosive source mechanism, (b, c) a vertical point source, and (d, e, f) a horizontal point source at the free surface above a homogeneous, isotropic medium. Red symbols describe the direction and placement of the source mechanisms. Panels b, c, d, and e are taken from modeling by Jílek & Červenỳ (1996), whereas panels a and f are sketched from modeling by Gaiser (2016). Although the details provided in these studies are insufficient to verify whether the same velocity models and assumptions (such as frequency) were used, the vertical-source results between the publications are broadly comparable. Nevertheless, these sketches are intended to be illustrative rather than quantitatively precise.

If the source mechanism is directional, such as a vertical or horizontal point force source (e.g., using a sledgehammer and plate or a vibroseis trucks), then secondary (S) waves are also generated, radiating outward from the source location but arriving later than the P waves (Hardage *et al.*, 2011). In pure *S waves*, particle motion is perpendicular to the ray path, which is why they are also called *shear waves.* Depending on the plane of particle displacement relative to the ray path (i.e., the polarization), shear waves are further classified as SV or SH waves which have distinct radiation patterns (Aki & Richards, 2002).

When S-wave particle motion lies in the plane of wave propagation, they are termed *SV waves* (Aki & Richards, 2002). These can be generated by either vertical or horizontal point forces oriented along the plane of wave propagation (Figure 2.1c, d, and f) with each creating unique radiation patterns for both the SV and coupled P waves (Gaiser, 2016; Jílek & Červenỳ, 1996).

For a vertical point source, the amplitude of the P-wave radiation pattern is strongest in the vertical direction and falls to zero at 90° (i.e., no lateral propagation; Figure 2.2c). These P waves propagate with zero-phase across all azimuths and angles (Gaiser, 2016). SV-wave energy is zero in the vertical direction and generally increases with angle from vertical, except for a sharp null at ∼35° (Figure 2.2c). Below this angle, SV waves propagate with a 90° phase shift relative to the P wave, with opposite polarization (180° difference) on either side of the source azimuth (Gaiser, 2016). At ∼35°, SV-wave energy vanishes due to interaction with evanescent P-wave energy generated at the free surface (Cherry Jr, 1962). Beyond this angle, SV energy reappears with ±90° phase, diminishing toward the horizontal, where it propagates with zero phase (and 180° in the opposite azimuthal direction).

For a horizontal point force source polarized in the plane of wave propagation (Figure 2.1f), P-wave energy is strongest at ±60° from the vertical and vanishes along the vertical and horizontal axes (Figure 2.2d). In this case, it is the P wave, not the SV wave, that exhibits opposite polarization on either side of the source (Gaiser, 2016). Conversely, SV waves maintain a constant zero phase on either side of the source out to ∼35° from the vertical (Gaiser, 2016), which is where their energy is maximal (Figure 2.2e). Beyond this angle, the SV-wave phase changes in a more complex manner, ultimately flipping to a negative phase around 40°–50° and decreasing further as it approaches lateral propagation.

When S-wave particle motion is perpendicular to the plane of wave propagation, the waves are referred to as *SH waves* (Aki & Richards, 2002). SH waves are generated solely by horizontal point forces (Figure 2.1e) and radiate uniformly outward, maintaining positive polarization at all propagation angles (Gaiser, 2016) (Figure 2.2f).

2.1.2 Surface Waves

Surface waves are seismic waves that travel along and near the Earth's surface rather than through its interior (Ammon *et al.*, 2020). There are two main types of surface waves based on particle motion: Rayleigh and Love waves. Surface waves generally have larger amplitudes than body waves near the surface and propagate more slowly than S waves in the near surface (Foti *et al.*, 2014).

Rayleigh waves exhibit elliptical particle motion in the vertical plane of wave propagation and can be excited by omni-directional, vertical (Figure 2.1c–d), or horizontal force point sources (Figure 2.1f) (Foti *et al.*, 2014). They emerge from the interaction of SV waves with the free surface (where shear and normal stresses vanish), which converts to both P and SV wave motion. Where incidence angles on the free surface are large enough, the converted modes become evanescent and the combination of P- and SV-wave evanescent energy at the surface forces a coupling of vertical and horizontal motions into the characteristic elliptical pattern (Ammon *et al.*, 2020).

Love waves, in contrast, have particle motion in the horizontal plane perpendicular to the direction of propagation (Ammon *et al.*, 2020), similar to SH waves. Their existence depends on vertical heterogeneity (a layered medium), which provides the pathway for mode conversion into SH energy that becomes trapped and guided to generate Love waves in the near surface (Foti *et al.*, 2014). It is important to note that, in principle, Love waves can be generated by any source mechanism. The particle motion shown in Figure 2.1e is included to illustrate the relative motion of the Love wave compared to the SH body wave.

2.1.3 Other Wave Modes

Love waves belong to the broader class of *guided waves*, which describes waves generated and confined by two or more boundaries. These may include a low-velocity layer bounded by the free surface and the layer base such as in Love-wave generation (Foti *et al.*, 2014), or two material interfaces. Higher-frequency surface (or other interface) waves, referred to as *higher-order modes*, are considered guided waves because their energy is trapped within the boundaries rather than propagating freely through the entire medium like the fundamental, lowest-frequency mode. As a result, guided wave velocities are dispersive, depending on wave frequency content.

Similar to guided waves, interface wave types also arise from vertical heterogeneity in the subsurface. *Interface waves* generally travel along boundaries. For example, *Scholte waves* are interface waves that propagate along fluid–solid interfaces, such as the seafloor (Foti *et al.*, 2014). They behave similarly to Rayleigh waves (also considered an interface wave; Sheriff, 2002), exhibiting elliptical particle motion resulting from the coupling of P- and SV-wave energy at the fluid–solid media boundary. Interface waves typically travel at velocities lower than the slowest body wave, usually the *S wave*, in the adjacent media.

2.2 Acquisition Considerations

MC data, like other seismic experiments, are influenced by source mechanism and strength, receiver coupling, source spacing, receiver density, aperture (source–receiver distance), and noise. These factors, however, are uniquely amplified when targeting modes other than P waves or when using horizontal (H) component data (Gaiser, 2016; Hardage *et al.*, 2011).

For example, converted phases (e.g., P-to-S targeted in 3-C surveys), typically require longer have lower amplitudes than primary P reflections (Foti *et al.*, 2014). If the source is too weak, these phases may fall beneath the noise floor, particularly on the horizontal channels, which are more prone to cultural noise, ground roll, and tilt-induced noise from poor sensor orientation (Gaiser, 2016). Other notable source-design considerations for MC experiments include, but are not limited to, vibrator sweep linearity, frequency content, and Earth coupling. Additional details on this topic can be found in Chapter 2 of Gaiser (2016), Chapter 2 of Hardage *et al.* (2011), and Section 3.4 of Foti *et al.* (2014).

Additionally, where wave modes other than P waves are targeted in MC experiments, higher spatial and temporal resolution and extents are often required due to their lower propagation velocities (Foti *et al.*, 2014; Gaiser, 2016). Denser spatial sampling can also improve the separation and isolation of target wave-modes, for example, between fundamental and higher-order surface-wave modes (Foti *et al.*, 2014).

Careful attention to source and receiver orientations, as well as meticulous documentation of these orientations, is a critical yet often underemphasized aspect of MC data acquisition, particularly in smaller-scale, non-industry experiments. In an MC seismic experiment, the source and receiver configurations are chosen to enhance or isolate the wavefield components that are most sensitive to the subsurface properties of interest. Three-component geophones are commonly oriented to capture vertical (Z) particle motion and two horizontal directions. The most standard procedure is to orient one horizontal arm east (E) and the other north (N), with Z vertical (Figure 2.3a). Another common approach, particularly in 2-D surveys, is to align the geophones with an X axis parallel to the source–receiver line, with the Y axis defined counterclockwise to X (Figure 2.3b). In either coordinate system, each component records a mixture of wave modes depending on the source–receiver azimuth relative to the receiver orientation.

Regardless of the selected coordinate system, orientations should remain consistent throughout the survey, and geophone locations and orientations must be properly documented. Errors in acquisition detail or misalignment can lead to mistakes in wavefield separation and polarization analysis (Daves & Simmons, 2018). If polarized sources are used, their orientation should be aligned with the chosen coordinate system; it is equally important that source orientation be accurately documented.

2.3 Processing Considerations

The acquisition coordinates described above record unique combinations of all wave modes and exhibit unique polarization sensitivities due to variations in source–receiver azimuth. To mitigate these effects, seismic data are commonly preprocessed in radial–transverse (R–T) coordinates (Figure 2.3, c). In this framework, the R direction is defined along the source–receiver azimuth, and the T direction is oriented 90° counterclockwise with respect to R (Gaiser, 1999). In this coordinate system, P- and SV-wave energy, which exhibit particle motion within the plane of wave propagation, are concentrated on the R component (Gaiser, 1999). When horizontal sources are used, rotation to R–T also separates the SV and SH components, with SV mapped onto the radial and SH onto the T component (Omar, 2018; Simmons & Backus, 2001).

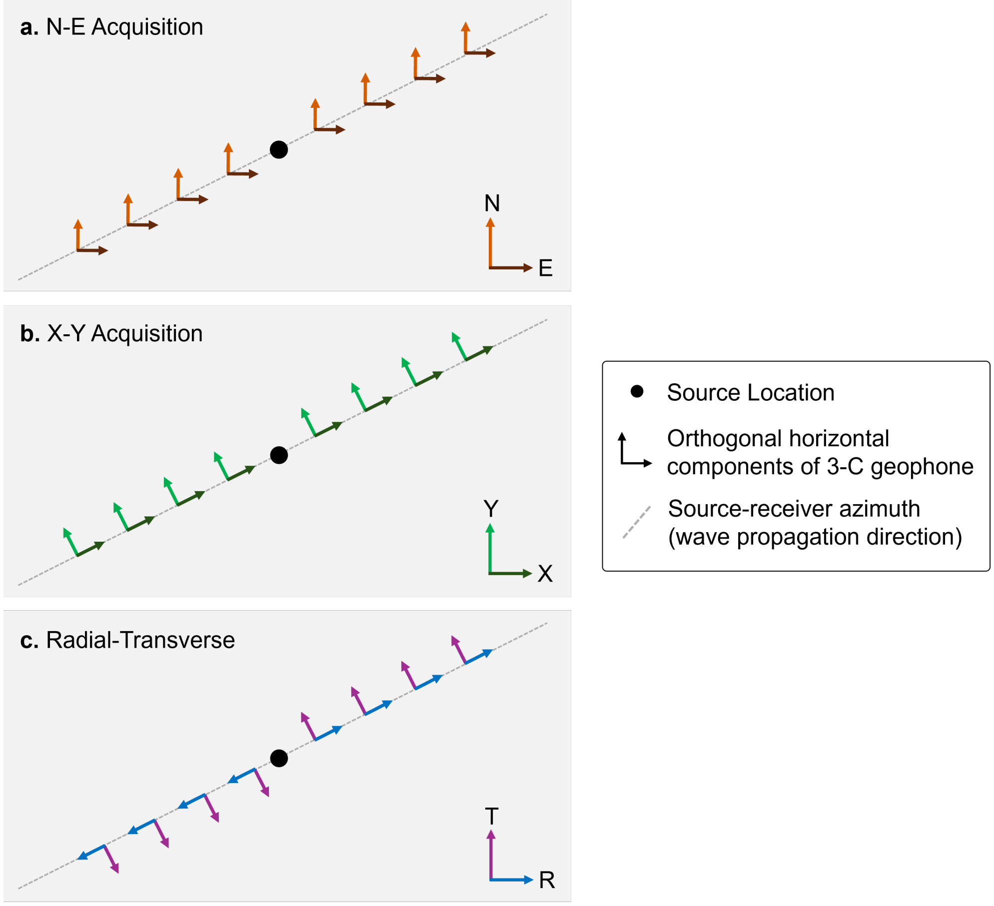

Figure 2.3 Map view depiction of two common acquisition coordinate frameworks for MC experiments: (a) horizontal components oriented North (N) and East (E), and (b) horizontal components aligned along the source-receiver azimuth (X) and perpendicular to it, counterclockwise (Y), typically in 2-D experiments. Also shown is (c) the radial-transverse ($R - T$) coordinate system, a processing rotation that removes azimuthal sensitivity of polarity and, in horizontal-source experiments, separates polarized SV and SH modes onto the R and T components, respectively.

Processing MC data is inherently complex (Chopra & Stewart, 2010); for a comprehensive treatment of specific workflows, the reader is referred to Hardage *et al.* (2011). A central principle is consistency across components. Distortions in amplitude or polarization on even one component can bias interpretation because MC analyses depend on cross-component comparisons. Quality-control procedures should therefore be applied uniformly to all three components, not just the vertical.

After data conditioning in the R–T coordinate system the data can be manipulated depending on interpretation objectives. For example, data can be stacked along azimuth and amplitude or velocity variations evaluated in the R–T system to assess horizontal transverse isotropy (Omar, 2018). Alternatively, other coordinate rotations may be required, such as those applied in S-wave splitting analyses (Gaiser, 2016; Lou *et al.*, 2001).

2.4 Summary

MC experiments have a long and dynamic history in industry data collection and analysis, with researchers exploiting them during downturns and practitioners implementing research findings during upturns or with the introduction of emerging technologies. This established a broad foundation of ideas for leveraging MC experiments, though emphasis has been on converted S waves since the mid 20th century. More recently, improvements in acquisition technology and computational capacity – which support higher-fidelity data and experiments with unique geometries – have enabled broader vector-based concepts and advantages in MC seismology to be fully incorporated into modern seismic experiments, arguably making the approach a standard part of seismic practice, rather than a distinct category. Revisiting the fundamental elements of MC seismology is, however, an important exercise, enabling researchers to pivot from established practices and ensure that new technologies are applied thoughtfully rather than constrained by outdated assumptions. Returning to the core principles ensures that the design, acquisition, and interpretation of MC data are well-positioned to leverage what makes these experiments uniquely powerful for understanding the subsurface.

CHAPTER 3

CONTRIBUTIONS OF THE HORIZONTAL OBN COMPONENTS TO P-WAVE IMAGING

Modified from a paper published in *Interpretation* Volume 13, Issue 3*

S. Garvey[1], J. Simmons[1], and C. Calderón-Macías[2]

3.1 Abstract

Horizontal (H) components of ocean bottom node surveys are acquired at no additional cost to the extensively analyzed vertical (Z) and pressure components. Despite this, H components are seldom processed for reflected converted compressional (P) to shear waves (PS-waves), and less so for reflected P waves (PP) due to a perceived lack of value relative to the added processing cost. Recent advancements in elastic migration methods have sparked interest in the H components given a clear rationale for enhancing PS imaging and interpretation through joint migration. Conversely, the potential benefits of the PP energy observed on the H components (HPP data) are less understood. We investigate the foundational characteristics of HPP data and its contribution to P-wave imaging using idealized acoustic synthetic datasets, free of PS-data and surface-related multiples. HPP illumination varies with respect to bed structure (e.g., dips and depth) like traditional Z component P-wave (ZPP) data but is more sensitive to acquisition geometries. Specifically, we present observations of polarization and strong illumination biases to signed-offsets which motivate a need for strategic handling of HPP data in processing flows. Using partial-offset stacks, we demonstrate that HPP data enhances traditional ZPP imaging most effectively for shallow dipping beds and beneath salt overhangs where

---

*See Appendix A for permissions and citation

[1] Department of Geophysics, Colorado School of Mines, Golden, CO 80401, U.S.A.

[2] TGS, Houston, TX, U.S.A.

inter-salt multiples complicate the ZPP image. Our results elucidate the broader need for studying the sensitivities of all component data prior to joint processing, and more specifically present new understandings of how HPP data can be optimally employed to reduce the uncertainties of traditional ZPP imaging.

3.2 Introduction

Ocean-bottom node (OBN) surveys in offshore exploration, compared to traditional surface streamer surveys, have the operational advantage of allowing for the acquisition of longer offsets and richer azimuth sampling, both of which aid in velocity model building and imaging of complex geologic settings (Huang *et al.*, 2023; Mei *et al.*, 2019). Additionally, the advantages of acquiring PS-wave information, dominantly recorded on the horizontal (H) components have played a role in the growing interest in OBN surveys. This is driven by the increased feasibility of elastic propagation in imaging which requires leveraging the complete wavefield recorded on all components of OBN data. Studying the sensitivity of each component (pressure, vertical (Z), and H) to all wave modes is an important first step to understanding possible advantages or pitfalls in the use of multi-component (MC) data required for elastic workflows.

H components of OBN surveys are often used in preprocessing procedures for example, in sensor orientation which uses all components (e.g., Dellinger *et al.*, 2002; Gaiser, 1998) and for specialized applications such as simultaneous source deblending (Jennings & Ronen, 2017) that use signal polarization as additional statistics for source separation. In terms of interpretation, noteworthy applications of the H components leverage the PS signal where sufficiently recorded in specific geologic conditions. Examples include gas cloud imaging (Nahm & Duhon, 2003), shear wave splitting for fracture characterization (Lou *et al.*, 2001), hydrocarbon validation using joint inversion (e.g., Cafarelli *et al.*, 2006; Damasceno *et al.*, 2021) and, shear wave velocity model building using full waveform inversion (e.g., Dhelie *et al.*, 2022; Masmoudi *et al.*, 2021; Vigh *et al.*, 2014). In sparse OBN surveys, PS-wave interpretation can be hampered by poor subsurface illumination caused by a coarse sampling of the receivers and potentially lower signal-to-noise (e.g., Ata *et al.*, 2013; Casasanta & Gray, 2015; Holden *et al.*, 2016).

Reflected P-wave (PP) energy recorded on the H components (HPP data) has been largely overlooked. In addition to the drawbacks associated with sparse acquisition previously mentioned, there are at least two historical factors that have likely discouraged analyzing HPP data. First is the expectation that the PP signal is dominantly polarized in the Z direction due to the mostly positive velocity gradient in the subsurface. This hypothesis is possibly valid in flat layered geology but in structurally complex regions which have historically been surveyed with short offset, narrow azimuth acquisitions, the observed lack of HPP data is likely due to the limited aperture. Zhao (2008) presents several 3-C acquisition case studies (albeit on land) where HPP signal can be observed on the H component shot gathers. We refer the reader specifically to Figures 1 and 8 in Zhao (2008). Similarly, the OBN acquisition presented in Zhang *et al.* (2021)'s field study reveals strong HPP energy on the MC shot gathers. Both field-data publications focus on the value of the PS information recorded on the H components (HPS data) and treat the HPP data as coherent noise. Along this vein, when targeting only the HPP data, the HPS data translates as coherent noise. This is the second factor limiting the exploitation of HPP data, as it is potentially masked by the strong PS signal. Despite this, Liu & Simmons (2025)'s brief presentation of HPP images generated from an elastic simulation of the SEAM II Barrett model, is a motivating example for our investigation. This study is focused on identifying and understanding the distinctive behavior of HPP data, and as such, we strategically do not model the shear modes. Although our preliminary acoustic experiment simplifies MC field data considerably, it effectively characterizes geological scenarios where using the HPP data could yield substantial benefits.

In practice, P-wave imaging procedures may begin with summing the pressure and Z components (i.e. PZ summation) for separating the up- and down-going energy at the ocean floor (Seher *et al.*, 2022), and for removing shear wave energy (Yang *et al.*, 2020).

The downgoing wavefield is particularly beneficial for near-surface imaging when mirror migration methods are implemented (Wang *et al.*, 2010). These PZ summations require assumptions in scaling the energy of the Z component data, based on the emergence angle, such that the unwanted wave modes cancel out (Soubaras, 1996). Thus, although the pressure component arguably detects P waves from all angles, the downgoing wavefield used in imaging and interpretation emphasizes the events detected on the Z component. This rationale motivates our experimental decision to not simulate free-surface effects. That is, acknowledging that PZ summation focuses working datasets to P-waves on the Z component (ZPP data), we model the upgoing wavefields and focus our analysis on the Z and H components. It is worth mentioning that given this upgoing-only wavefield simulation, the insights into ZPP versus HPP data presented in this study apply to 3-component land data as well.

The paper begins by introducing the 2-D synthetic models used to simulate the idealized acoustic, OBN datasets. The choice of the Kirchhoff prestack depth migration algorithm for imaging is then justified, with details provided on the parameterization and handling of OBN geometries. Each case study is analyzed individually, with the analysis centering on the use of partial stack images to evaluate the characteristics and contributions of HPP versus ZPP illumination. This is followed by a summary of the generalized characteristics of HPP data, offering new insights into the handling and utilization of H component data, which are further discussed before concluding remarks are presented.

3.3 Method and Implementation

Here, we describe the details of each synthetic model along with the coordinate system and migration algorithm employed. We also explain the motivations behind key methodological choices.

3.3.1 Numerical Models and Simulations

We simulate OBN acquisitions on two familiar industry models - the shallow water, faulted setting of the 2-D Marmousi2 model (Martin *et al.*, 2002) and a 2-D section of the deepwater, salt model published by SEG SEAM (Fehler & Keliher, 2011). The Marmousi2 model is a 17.0 km x 3.5 km cross-section representative of the North Quenguela Trough in the Cuanza Basin, Angola. We show the P-wave velocity and density models for this case study in Figure 3.1a and Figure 3.1b respectively. It is an elastic extension of the acoustic Marmousi model and allows for easy extension of this work with elastic simulations. To simulate a best-case scenario for HPP imaging, the Marmousi2 model was modified to replace the shallow transition layers at the seafloor with a water layer. The ocean bottom data were thus recorded on the new seafloor at a depth of 0.512 km. The grid and cell sizes of the model are 4250 x 875 and 4 m x 4 m respectively.

The SEAM Phase 1 model is analogous to a complex salt domain in the Gulf of Mexico and the extent of the 2-D cross-section is 17.5 km x 7.0 km. The P-wave velocity and density models for this case study are shown in Figure 3.1c and Figure 3.1d respectively. The grid and cell sizes of the model are 1751 x 1401 and 10 m x 5 m respectively. Compared to the Marmousi2 model, the seafloor depth varies from 500 m to 1000 m. OBN geometries for both models were simulated by placing receivers every 25 m at the water-solid interface. Sources were characterized by a symmetric, 15 Hz Ricker wavelet and were spaced 25 m at a constant depth of 10 m in the water column.

To highlight the kinematics of the HPP data, we forward model the acoustic wave equation without implementing the standard free-surface condition to forestall the generation of PS-waves and surface-related multiples. We simultaneously model the pressure, Z- and H-displacement wavefields by solving a system of coupled first-order equations (respectively describing the vector displacement and scalar pressure fields) using a forward-marching, staggered in time finite-difference scheme implemented with the *Devito* software package (Louboutin *et al.*, 2019; Luporini *et al.*, 2020).

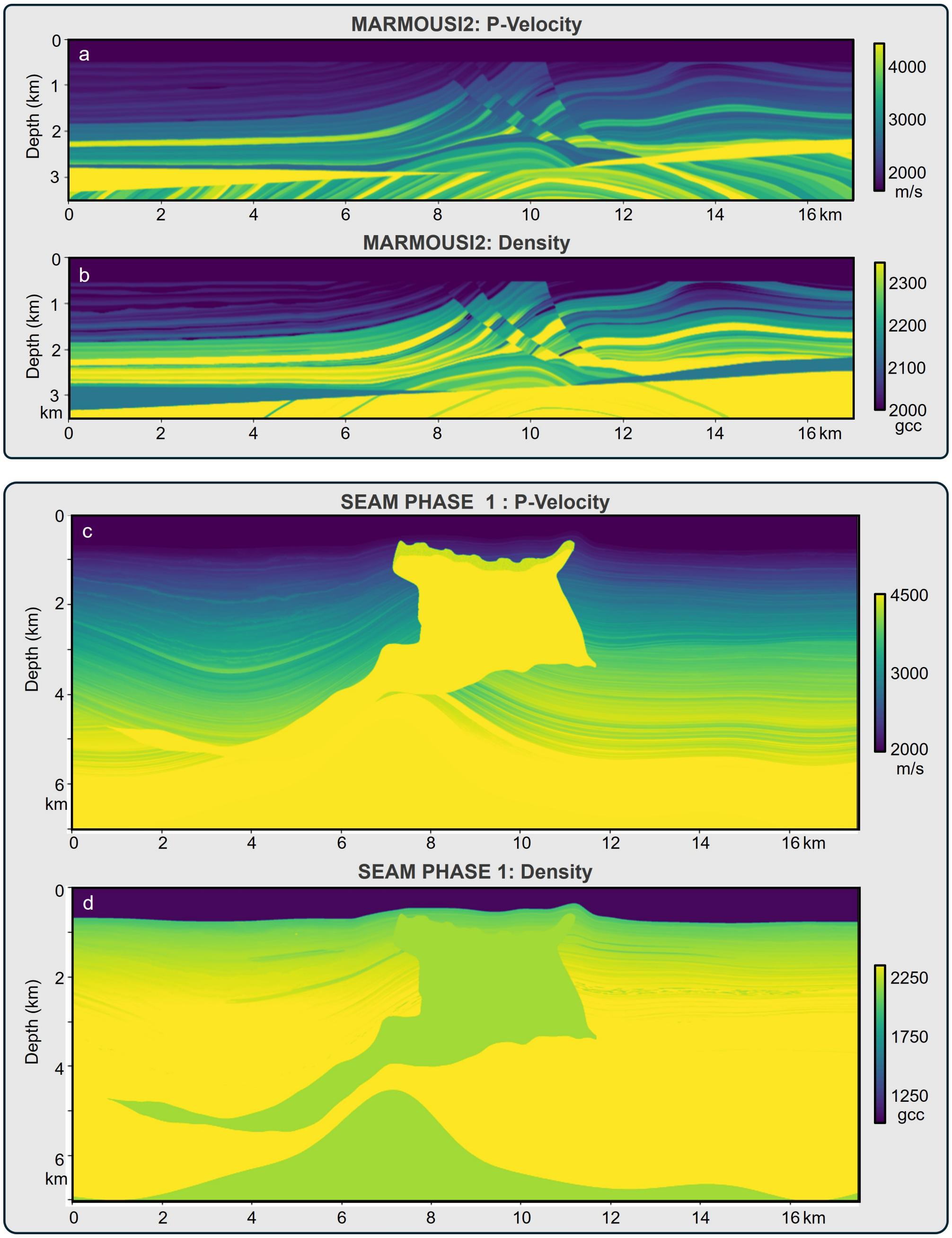

Figure 3.1 P-wave velocity (V_p) and density (ρ) models modified from the Marmousi2 dataset created by Martin *et al.* (2002) are depicted in panels (a) and (b) respectively. Transition layers are removed from the original model which places the seafloor at a depth of 0.512 km. 2-D P-wave velocity (V_p) and density (ρ) models extracted from the SEAM Phase 1 dataset created by Fehler & Keliher (2011) are shown in panels (c) and (d) respectively. Acquisition geometries for the acoustic finite-difference forward modeling of an OBN survey for each model are described in the text.

3.3.2 Coordinate System and Framework

At any receiver, the detected signal's polarity depends on both the coordinate system convention and subsurface properties i.e. layer geometries and elastic properties. We assume an acquisition coordinate system in which the positive Z and X directions point upward and to the right, respectively. Assuming a horizontally-layered Earth model with OBN acquisition (Figure 3.2), an upgoing reflected wave is detected as a positive displacement in Z whereas a downgoing direct wave is detected as a negative displacement in Z. Receivers located to the right of the source are designated as positive-offset receivers, while those to the left are considered negative-offset receivers. For particle motion recorded along the X direction, positive-offset receivers detect positive displacements in X and negative-offset receivers detect negative displacements. This reversal of horizontal particle motion at zero-offset is realized as opposite polarities on the recorded X-component shot gathers and is hereon referred to as a 'signed-offset polarization bias' (SOP bias).

We show an example of the Z and X-component shot gathers at 3.0 km on the Marmousi2 model (Figure 3.3a–b) where the stratigraphy is fairly flat. All energy observed on these gathers are P-wave due to the acoustic forward modeling. For the flat layered stratigraphy at near offsets, this PP energy is dominantly recorded on the Z component, and at far offsets, the energy is distributed onto both the Z and X components. As expected by the coordinate system definition, the direct wave (yellow arrow) is recorded with negative polarity on all offsets of the Z component gather and the negative offsets of the X component gather. On the positive offsets of the X component, this direct wave is recorded with positive polarity. The strong signal at 0.8 s (blue arrows) is a reflected P-wave from the top of a gas reservoir and should have a negative amplitude because of the negative impedance contrast. This reflection is recorded as negative polarity on all offsets of the Z component and on the positive offsets of the X components. On the negative offsets of the X components, the recorded signal has a positive polarity.

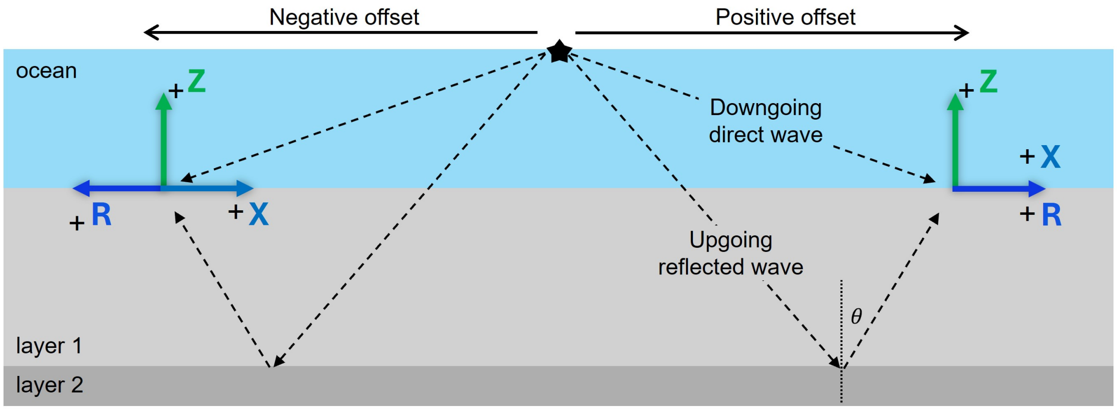

		P	Z	X	R
Downgoing Waves e.g. Direct	Positive Offset	-	-	+	+
	Negative Offset	-	-	-	+
Upgoing Waves e.g., Reflections	Positive Offset	-	+	+	+
	Negative Offset	-	+	-	+

Figure 3.2 Description of coordinate system for OBN acquisition. The table describes the polarity of different waves registered on the positive or negative offsets of the pressure, Z, X, and R components.

The use of a radial-transverse (R-T) horizontal coordinate system successfully removes this SOP bias for reflectors parallel to the recording surface. The R direction for any source-receiver pair points along the source-to-receiver azimuth (Gaiser, 1999). Figure 3.3c shows the result of this rotation at 3.0 km. The direct wave and reflected gas-pocket signal are detected as positive and negative polarities respectively regardless of signed-offset. Where subsurface layers are dipping, the conversion to the R-T system imposes a SOP bias. This is observed on the shot gathers at 9.3 km of the Marmousi2 model where the layers are severely tilted and faulted. In Figure 3.3d–f, we show the Z, X and R shot gathers and annotate the X and R components with pink arrows to highlight the SOP observations.

Stacking across signed offsets in either the X or R directions, can potentially distort or cancel signal depending on the target bed geometry. As rotation to R-T is a standard practice, our initial analyses include a cross-examination of both the X- and R-component data where the synthetic 2-D data is rotated to the R direction prior to migration.

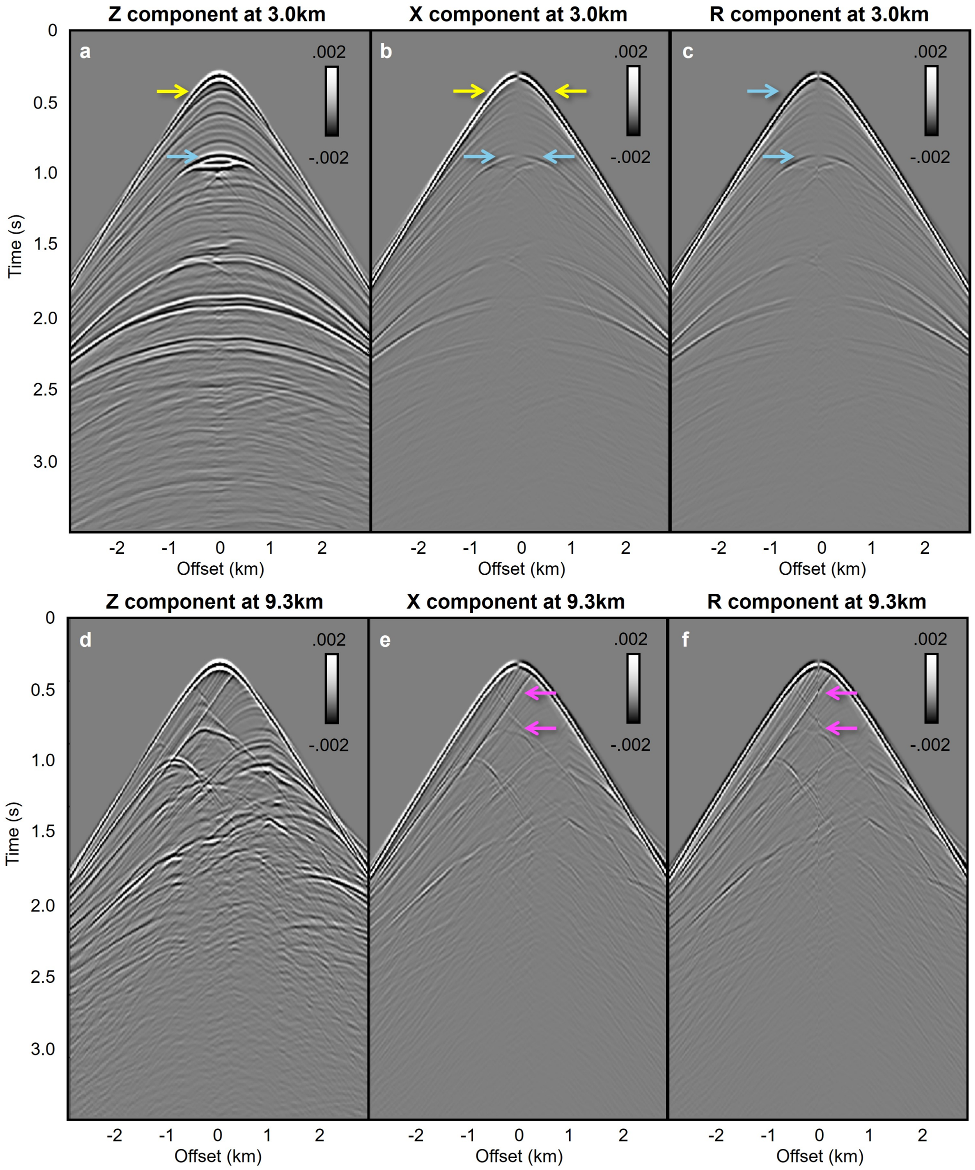

Figure 3.3 Raw shot gathers from the Marmousi2 experiment for the Z, X, and R components at 3.0 km (a–c), where the stratigraphy is relatively flat, and at 9.3 km (d–f), where the beds are severely tilted and faulted. Yellow and blue arrows (a–c) highlight the direct arrival and the reflection at the top of a gas reservoir, respectively, for each component. For both direct and reflected waves at this location, we observe uniform polarity at all offsets for the Z component and an SOP on the X component, which is corrected by rotation to the R direction. Pink arrows (e and f) highlight comparative dipping bed reflectors: on the X component, no SOP is observed, while on the R component, an SOP is introduced due to rotation.

3.3.3 Migration Algorithm

The selection of a migration algorithm can be streamlined into choices between ray-based versus wavefield-based, and vector-based versus scalar-based migrations. Ray-based migrations such as Kirchhoff prestack depth migration (KPSDM) are computationally inexpensive compared to wavefield-based approaches such as reverse time migration (RTM). Furthermore, obtaining 'true' relative amplitude gathers is more efficient and straightforward with KPSDM compared to RTM. For these trivial reasons, KPSDM remains an industry standard in most geologic regimes or at the very least, employed in fast-track processing in regions with complex subsurface structures. Another benefit to ray-based approaches is the ease of migrating distinct wave modes controlled by the input travel time field estimations i.e. scalar wavefield migration (Bucha, 2021). While this distinctive imaging is possible in wavefield-based migrations, the severe cross-talk of unwanted wave-modes often require wavefield separation (effectively migrating each wavefield with a scalar algorithm e.g. Yan & Sava (2009)) or an advanced imaging condition (treating the problem as a vector-based joint migration e.g. Hou & Marfurt (2002) and Rocha & Sava (2018); Yan & Sava (2008)). Vector-based migrations of elastic data often utilize the MC datasets and produce separate P- and S-wave images. These vector approaches may be implemented in both ray-based or wavefield-based migrations (Hokstad, 2000). The interest in vector-based, elastic reverse time migrations (ERTM) in structurally-complex, marine environments is increasing due to more activity in ocean-bottom surveys which facilitate PS-wave acquisition. This is motivated by the need for time-lapse studies of reservoir conditions requiring both P- and PS-wave information. Although the H components are valued for the PS-wave data in joint processing workflows, it is poorly understood how the HPP data impact vector-based migrations of P-wave data. Thus, we use a scalar-based KPSDM such that the P-wave information on each component was separately imaged and the independent contributions of ZPP versus HPP data can be assessed. We continue the discussion of migration algorithms in the 'Suggestions for

Further Investigation' section considering the results presented.

The specific KPSDM code used (written by Liu (1993) and found in Seismic Unix (SU) (Stockwell Jr, 1999)) is based on Bleistein *et al.* (1987)'s integral formulation which is kinematically accurate for direct pure-mode and converted-wave modes (Bleistein, 1986). Our analysis emphasizes subsurface reflection point illumination differences of the ZPP and HPP images and not on reflection amplitude differences. All components were migrated with the same ray tracing and migration parameterizations. The code was modified to utilize two distinct travel time fields for sources and receivers having different elevation datums. This modification makes the Kirchhoff code directly suitable for ocean-bottom geometries. Source-side and receiver-side travel time tables for input to the KPSDM were calculated using a 2-D paraxial ray tracing algorithm (Liu, 1993). We performed ray tracing on a smoothed version of the true P-wave velocity models for both case studies. Turning rays were not migrated. Maximum offsets recorded for the Marmousi2 and SEAM Phase 1 models were 3000 m and 5000 m respectively and a migration aperture equal to these maximum recorded offsets was used for both case. Prior to stacking, data were migrated into common image gathers (CIGs) at 0.1 km offset bins with a 45° outside mute and mild bandpass filter.

3.4 Results

We first explore the Marmousi2 example using the Z, X, and R components, making observations from shot gathers, comparisons between positive and negative offset stacks, and analyses of near- versus far-offset responses. To examine these observations in more detail and assess their transferability, we then investigate the SEAM Phase 1 example using signed, partial-offset stacks, focusing on comparisons between ZPP and RPP interpretations.

3.4.1 Study 1: Marmousi2 Example

The Marmousi2 model provides a convenient opportunity to begin analyzing HPP illumination for flat versus tilted stratigraphy. Figure 3.4 presents the Z, X and R CIGs at the two shot gather locations shown in Figure 3.3 (upper and lower rows). At both locations, the migrated PP reflections on the X and R CIGs are flattened similar to that of the Z component (blue arrows). The SOP bias observed in the X and R component shot gathers in Figure 3.3 persists in the CIGs — at 3.0 km, rotation to R corrects the X-component SOP bias, whereas at 9.3 km, the rotation instead introduces an SOP bias.

A closer examination of the 9.3 km CIGs reveals a signed-offset illumination (SOI) bias on the H components (both X and R) which were not immediately obvious on the shot gathers. Specifically, some steeply dipping beds that are uniformly illuminated across all offsets on the Z component exhibit differences in amplitude and resolution between positive and negative offsets on the X and R components (refer to pink arrows in Figure 3.4d–f). This SOI bias, which exists on some reflections regardless of horizontal coordinate system, underscores the importance of understanding how images and interpretations differ between positive- and negative-offset stacks of the H component data. In the remaining analyses of this work, we focus on the R components for reasons outlined in the 'Coordinate System Framework' section.

Partial-offset stacks are generated with the following angle ranges: 0° - 10° ultra-near, 10° - 20° near, 20° - 30° mid, 30° - 45° far. These angles (θ in Figure 3.2) are computed as the emergent angles assuming flat model layers. Figure 3.5 compares partial-offset stacks of the RPP data, specifically ultra-near versus mid-offset stacks in the most structurally complex area of the model. At ultra-near offsets, dips are similarly illuminated on both positive and negative offset stacks (Figure 3.5a and Figure 3.5b respectively) while at the respective mid offsets (Figure 3.5c and Figure 3.5d), the SOI bias is stronger. These observations are annotated with yellow arrows noting that on mid offset stacks, the left-dipping events are better imaged on the negative offset stack.

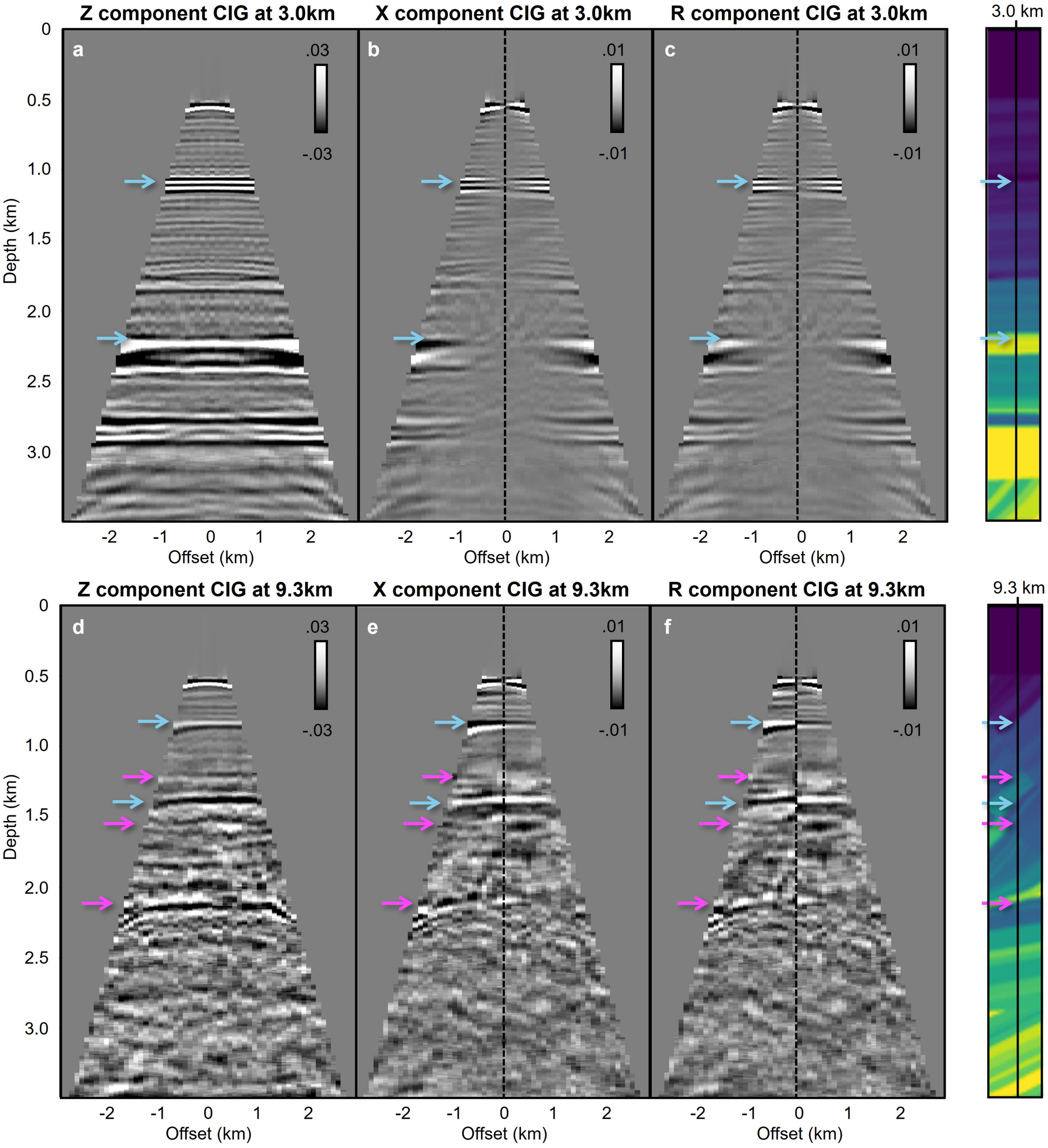

Figure 3.4 CIGs from the Marmousi2 experiment at shot locations 3.0 km (a–c) where stratigraphy is relatively flat and 9.3 km (d–f) where beds are severely tilted and faulted. The H components (X and R) are gained three times the amplitude of the Z component and all gathers have an outer mute of 45 degrees applied. Using the same parameterizations for KPSDM, the PP energy on all components is equally flattened (blue arrows) at both locations. Pink arrows on the 9.3 km CIGs highlight dipping bed reflections which are uniformly illuminated at all offsets on the Z component, but are illuminated differently between the positive and negative offsets of the X and R components.

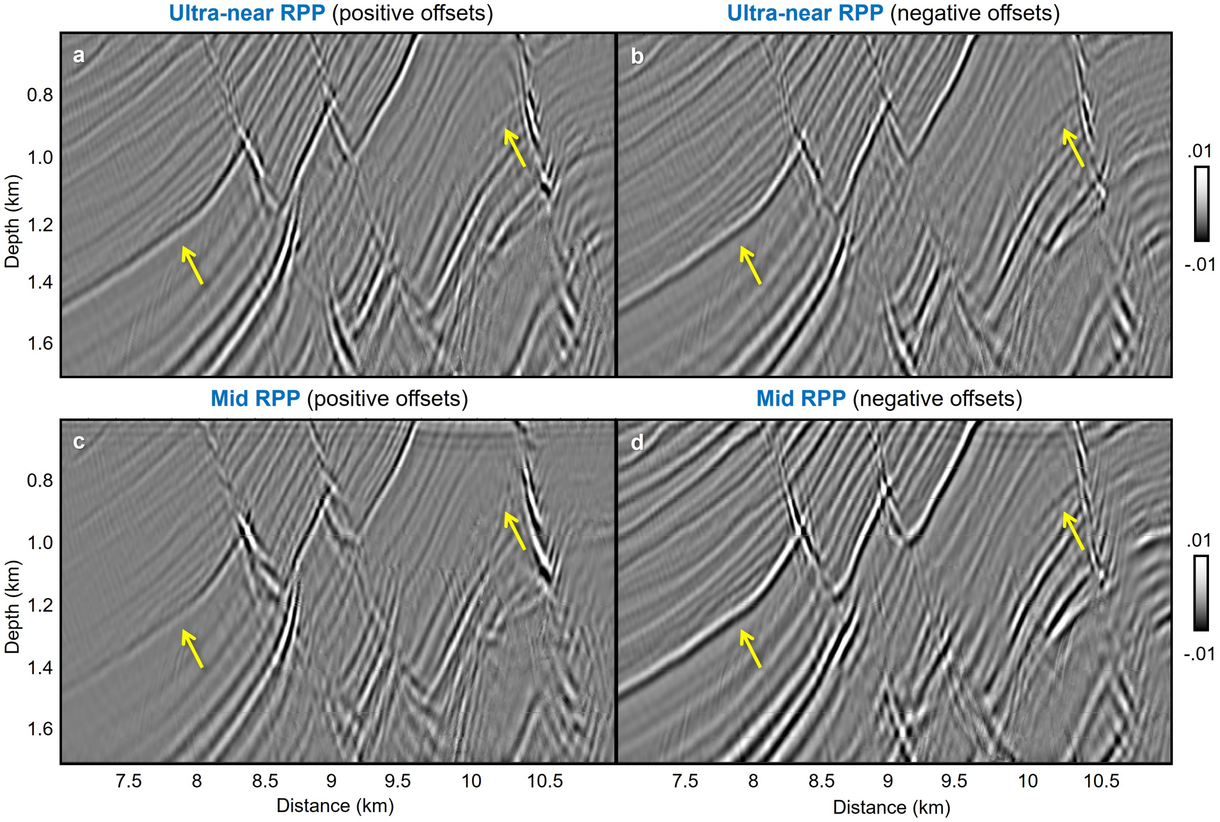

Figure 3.5 Comparison of the RPP ultra-near (a and b) and mid (c and d) partial-offset stacks for both positive (left column) and negative (right column) offsets. All panels are displayed on the same amplitude scale. Yellow arrows highlight left dipping bed reflections which are similarly imaged (disregarding polarity) on the ultra-near stacks but better imaged on the negative mid-offset stacks as a result of the biased HPP illumination to signed-offset.

Our analysis of the Marmousi2 synthetic OBN data reveals two key findings about H component records, independent of the chosen coordinate system: (1) polarization and (2) illumination varies systematically between positive and negative offsets, depending on subsurface geometry. Notably, receivers positioned downdip relative to a given reflector capture stronger HPP energy, highlighting the importance of partial-offset HPP stacks when imaging uniform dips. To explore how this data can complement traditional ZPP interpretation, we now turn to a salt imaging study—a common industry challenge in the pursuit of salt-juxtaposed reservoirs.

3.4.2 Study 2: SEAM Phase 1 Example

Imaging subsalt and salt flanks in marine environments are often difficult because of sparse illumination. The SEAM example investigates the value of HPP illumination to resolving such subtle salt-edge features using partial-offset images generated using the same angle ranges as in the Marmousi2 example. Figure 3.6 compares the full, signed-offset stacks of the migrated SEAM ZPP and RPP data.

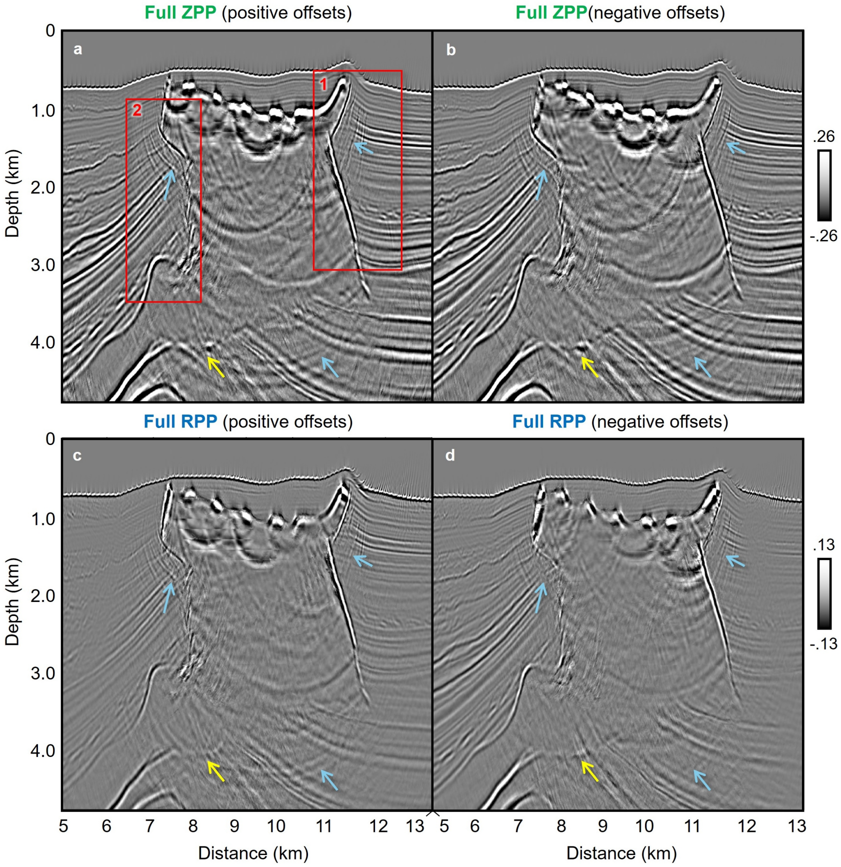

Figure 3.6 Comparison of full (0-45°), signed-offset stacks for ZPP (a and b) and RPP (c and d) data. RPP amplitudes are gained two times that of the ZPP images. RPP illumination has a stronger SOI bias (compare the differences in (c) and (d)) versus the ZPP illumination (compare the minor differences in (a) and (b)). In general, RPP data supplement the ZPP data in critical locations below the salt overhangs and at the base of salt. Yellow arrows highlight the base of salt illumination which is more continuous on the RPP images as opposed to the ZPP images which are more affected by poorly migrated inter-salt multiples. Blue arrows highlight these multiples in regions below the salt and under the salt overhangs. Red boxes #1 and #2 on panel (a) outline the zoomed regions displayed in Figure 3.7 and Figure 3.8 respectively.

Although the migration did not incorporate turning ray information necessary for imaging a continuous base of salt, the RPP images show a more focused base of salt reflector wherever it is illuminated in comparison to the corresponding ZPP images (yellow arrow annotations). This is partly attributed to the strong interference of poorly migrated inter-salt multiples on the ZPP images (blue arrows on Figure 3.6a and Figure 3.6b). Although some multiples are observed on the RPP images (blue arrows on Figure 3.6c and Figure 3.6d), they are relatively weak compared to the primary reflections.

Similar to the Marmousi2 observations, the SOI bias are more pronounced in the RPP data (compare Figure 3.6c versus Figure 3.6d) than in the ZPP data (compare Figure 3.6a versus Figure 3.6b). We also note that negative offset RPP data best illuminates left-dipping sediment layers (on the left side of the salt body in Figure 3.6d) and vice versa for right-dipping sediment layers (on the right side of the salt body in Figure 3.6c), and that multiple contamination on RPP differs between signed-offset images.

In deepwater settings, prolific hydrocarbon reservoirs are often trapped against salt flanks and beneath salt overhangs. Figure 3.7 examines the imaging of the right flank with positive, partial-offset stacks (red box #1 on Figure 3.6a) and Figure 3.8 examines the left flank with negative, partial-offset stacks (red box #2 on Figure 3.6a).

The regions where RPP illumination enhances areas of poor ZPP salt flank imaging vary across the dataset. For example, the right dipping salt flank (annotated on a few panels in Figure 3.7 with dotted yellow arrows) is similarly and continuously imaged on all ZPP and RPP partial-offset images however, the shallow salt edge (solid yellow arrow annotations), benefit more from RPP illumination than ZPP (particularly at mid to far offsets). Additionally, in some instances, the overhang reflector is better focused on the RPP image compared to the corresponding ZPP image. Such examples on Figure 3.7f and Figure 3.8e are annotated with thick yellow arrows and in particular, the continuity of the overhang on the RPP image in Figure 3.8e is a convincing example of the relevance of the RPP illumination to imaging even at near offsets.

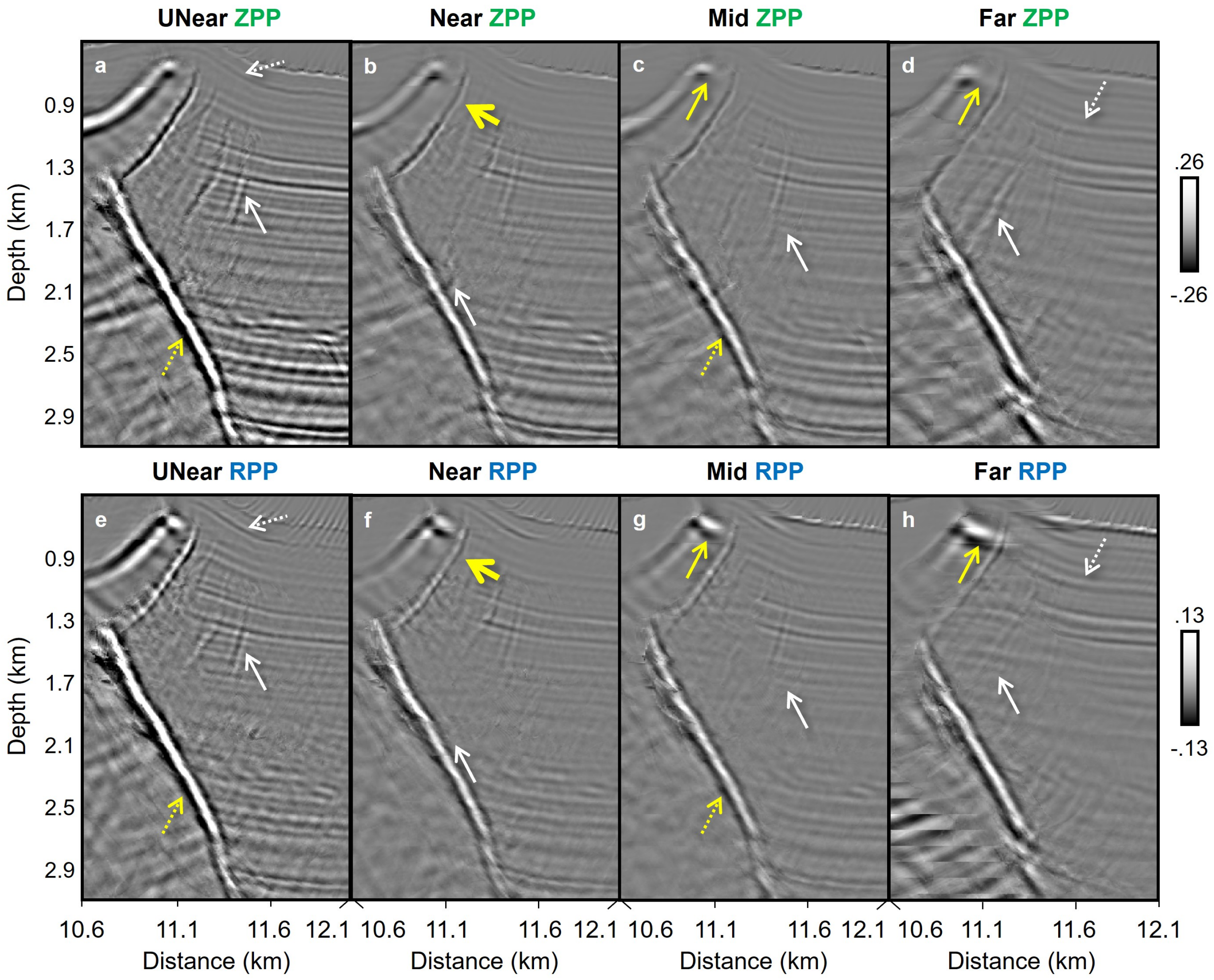

Figure 3.7 Positive partial-offset stacks zoomed to the right salt flank of the SEAM Phase 1 model. Zoomed region is described in Figure 3.6. Panels a–d show the ZPP ultra-near, near, mid, and far partial-offset stacks respectively and panels e–h show the RPP equivalent stacks. Generally, dotted arrows highlight reflectors that are comparably imaged on both Z and R components whereas solid arrows highlight examples where the RPP illumination is significantly better. Yellow arrows highlight observations related to salt imaging and white arrows highlight observations related to stratigraphy. The bolded yellow arrows mark reflectors along the salt overhang, a notoriously difficult yet reservoir-critical zone, that are better illuminated in the RPP data. Refer to the text for relevant details.

Similar to the discontinuous salt flank imaging, the imaging of dipping beds that are weakly illuminated on ZPP can be supplemented by the RPP illumination of these reflectors. Dotted white arrows on Figure 3.7 and Figure 3.8 highlight a few such reflectors at all offsets.

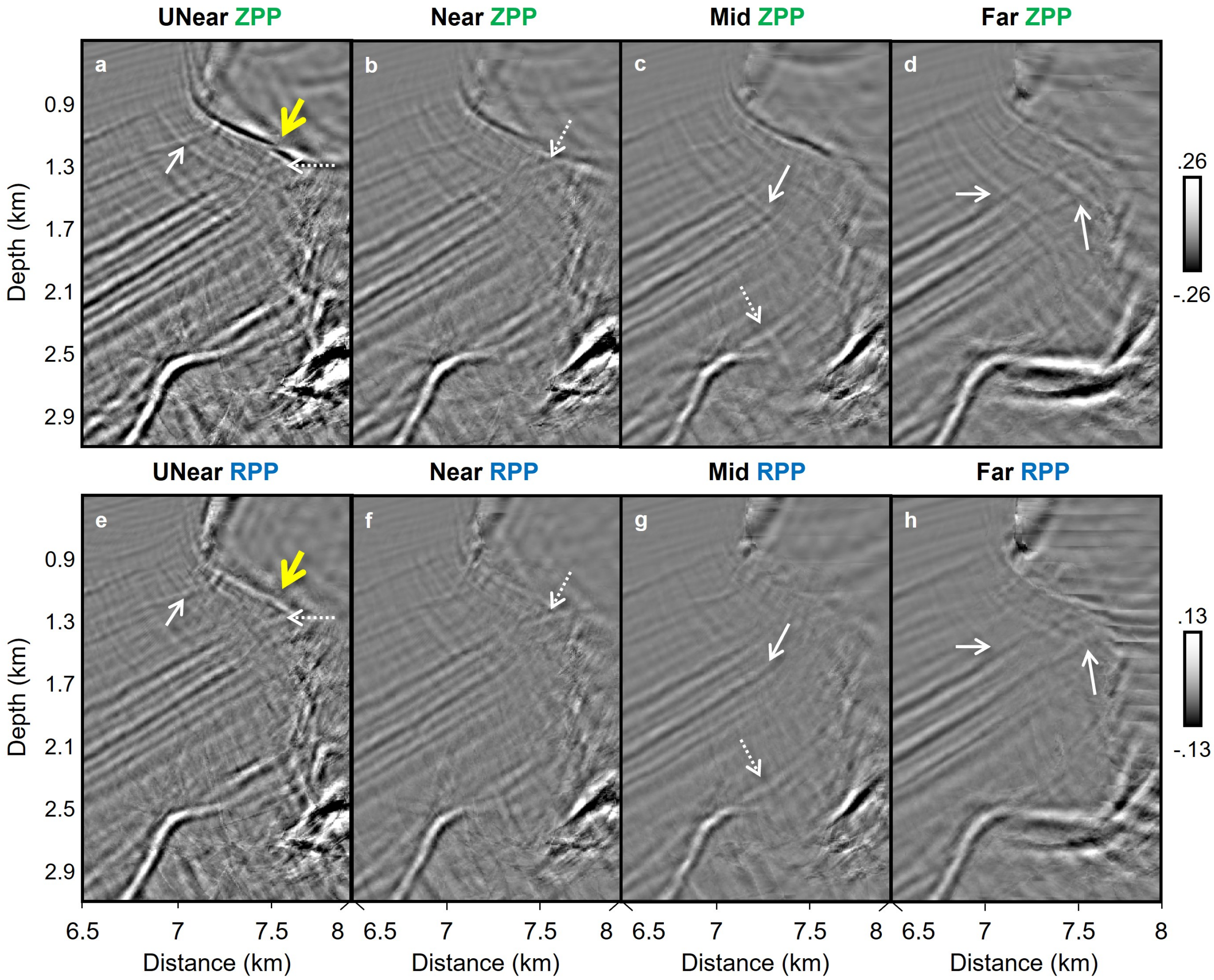

Figure 3.8 Negative partial-offset stacks zoomed to the left edge of the main salt body on the SEAM Phase 1 model. Zoomed region is described in Figure 3.6. Panels a–d show the ZPP ultra-near, near, mid, and far offset stacks respectively, and panels e–h show the RPP equivalent stacks. Descriptions of arrow annotations are the same as those used in Figure 3.7.

Under the salt overhangs, solid white arrows annotate unique observations where the inter-salt multiples contaminate the ZPP images more than the RPP data. An additional noteworthy observation is that in some scenarios where these inter-salt multiples are recorded on the R component, they are inverted polarity to the recorded polarity on the Z component. For example, compare the highlighted multiple in Figure 3.7a versus Figure 3.7e. Assuming that the SOP biases can be remedied with a vector-based migration, then stacking the ZPP and RPP data can provide several benefits to salt basin imaging which include improving the illumination of steeply dipping reflectors (such as salt flanks and salt-juxtaposed beds) and suppressing multiple interference under overhangs. Using both the ZPP and RPP data potentially improves the resolution of salt-sediment interfaces which improves the interpretation of potential trapping and sealing mechanisms critical for accurate hydrocarbon prospecting.

3.5 Summary of Observations

We observe that the reflected P-wave data recorded on the H component contains sufficient signal that after migration, illuminates dipping reflectors differently, but complementary, to the Z component illumination. The strength of the HPP signal is a function of target depth and dip relative to receiver depth and offset. When P-wave signal is strongest on the H component, it is weakest on the Z component and there is potential benefit to jointly analyzing or combining both components. From both studies, we generalize the following observations regarding the reflected P-waves:

(A) RPP polarities of dipping beds are biased to signed-offset (SOP bias) i.e. a dipping interface will be detected with opposite polarities on the negative- versus the positive-offset receivers, which leads to potentially destructive inference in stacking across signed-offsets.

(B) HPP illumination of dipping beds are biased to signed-offset (SOI bias) regardless of coordinate system (X or R). More specifically, beds dipping in the source-to-receiver (offset) direction are best illuminated by receivers positioned on the downdip side of the source.

(C) HPP illumination of the subsurface varies with depth and dip of bed (related to the emergence angle of the reflected wave), and absolute source-receiver offset

(a) In the simple Marmousi2 study, these relationships are discernible: Shallow, dipping beds are best illuminated at near offsets on both signed-offset H components

(b) In the complex SEAM Phase 1 salt study, these relationships are less intuitive and the strength of HPP sub-salt and salt-flank imaging vary possibly due to velocity complexity.

3.6 Discussions and Suggestions for Further Investigation

Evaluating the sensitivities of the H components to individual wave modes is crucial for the efficient implementation of joint imaging and analysis of MC data. Our synthetic experiments provide evidence of the value of HPP data, even at small offsets, to imaging shallow and/or complex subsurface structures. This not only has a potential impact on resource mapping e.g., in deepwater salt field or shallow gas hydrate (Backus *et al.*, 2006) exploration but also on shallow hazard mapping for well-planning or other geotechnical seafloor projects.

The choice of acoustic experiments has allowed us to establish a fundamental understanding of HPP data in isolation from other wave modes. Repeating these analyses on elastic datasets or with free-surface effects are natural progressions of this work. Based on our observations of strong biases in HPP illumination towards signed-offsets, we anticipate similar biases in the case of free-surface multiples and PS-waves in elastic media. The use of KPSDM in this study presents both advantages and limitations. KPSDM is widely used for its efficiency and adaptability, however its reliance on a ray-based imaging model limits proper migration to only single-point reflection events. In regions with strong velocity contrasts and/or complex 3D structural geology, KPSDM of multiple reflections and refractions can result in artifacts. While these limitations may introduce uncertainties in the interpretation, they do not diminish the significance of our key observations. The systematic SOP and SOI biases remain fundamental aspects of the recorded HPP

wavefield, independent of the imaging method. It is possible, however, to resolve these biases by accounting for the direction of emerging particle motion relative to the receiver directions. Exploring such imaging methods could help assess the robustness of these findings.

Correcting the SOP concerns (associated with item A in the summarized observations) would allow for comparison of amplitudes in the ZPP and HPP images. This has been discussed and exemplified in Kirchhoff migration applications of 3D VSP data (e.g., Dillon, 1990; Gherasim *et al.*, 2005) and multi-channel teleseismic receiver functions (e.g., Bostock, 2002; Millet *et al.*, 2019). Implementation of vector-based migrations such as the vectorial-based Kirchhoff migrations as presented by Kuo & Dai (1984) or RTM using the energy-norm imaging condition by Rocha *et al.* (2016) can also account for these amplitude variations with emergence angle. A comparison of these vector-based migrations on separated signed-offset data has the potential to produce better images by capitalizing on the signed-offset biases of the HPP data.

Regarding multiples, our results have demonstrated weaker inter-bed salt multiples on HPP compared to ZPP. It is thus important that these strong ZPP multiples are sufficiently attenuated prior to joint migration otherwise the contributions of the HPP data in critical regions, such as under salt overhangs and along flanks, may be masked by the cross-talk related to these coherent noise events. In instances where inter-bed multiples are discernible on RPP data, there is potential to leverage the observation of opposite polarities between ZPP and RPP to identify and suppress these undesirable modes. We hypothesize that surface-related multiples would also weakly impact HPP data, as they tend to propagate more vertically. Where such multiples are recorded on the HPP data, there may be an opportunity to perform a summation of pressure, Z, and H component data to achieve a more accurate wave mode separation which requires estimations of emergence angles (Schalkwijk *et al.*, 2003).

For velocity model building (VMB), although not in the scope of this work, it is apparent from the results presented that using reflected P-wave energy captured in the H component could benefit the P-wave VMB particularly for shallow geology. Solano & Plessix (2023) have demonstrated the value of a joint elastic full waveform inversion (EFWI) using both the Z and pressure components, versus individual inversions of either component. Although the pressure component is omnidirectional, the joint inversion benefits from the SNR of the unidirectional Z component P-wave records. The higher SNR reflected P-wave signal from the H component can similarly benefit EFWI workflows. Another plausible method to improving VMB is including the residual moveout picks of the P-signal from the HPP migrated gathers to the conventional picks from the Z component. With no considerable cost, this potentially improves P-wave model updating without the need for addressing noise in the pre-stack data before migration. Cho *et al.* (2022) addressed the utility of the H component for the shallow shear VMB in salt fields of the Gulf of Mexico. A potential research opportunity following from our results is investigating the PS-signal recorded on the Z component and exploring its value to shallow shear VMB which suffers from sparse receiver acquisition.

3.7 Conclusions

P-wave energy measured on H components has been mostly neglected in MC surveys. We analyze this HPP data for image improvements evidenced by enhanced focusing and continuity of reflectors versus using a single Z component dataset. Using 'best-case' acoustic simulations of OBN acquisitions on widely used industry marine models, we demonstrate the added value of HPP illumination, particularly for imaging shallow and dipping subsurface geometries. We make critical observations about signed-offset polarization and illumination biases in HPP data compared to ZPP data, with these effects becoming more pronounced at steeper dips and shallower depths. HPP images complement and reduce the uncertainty of the ZPP interpretation of shallow, steeply dipping beds or salt flanks, and intriguingly in regions below salt overhangs where inter-salt multiples complicate the ZPP image. Results shown have potential implications for model building methods, and in particular for the incorporation of components in tomography and FWI approaches. Including free-surface multiples and converted waves in more complex simulations is a necessary succession of this research which will address the complexities in MC imaging of field data.

3.8 Data Availability

The open-source tools Devito (for forward modeling) and Seismic Unix (for data processing and migration) can be accessed at their respective websites: https://www.devitoproject.org and https://wiki.seismic- unix.org/start. Additionally, the synthetic models used in this study are publicly accessible. The Marmousi2 model is hosted at https://wiki.seg.org/wiki/AGL Elastic Marmousi, while the SEAM Phase 1 model is available at https://seg.org/seam/open-data. For the simulated OBN data and processing scripts, interested parties can request access from the corresponding author.

3.9 Acknowledgments

We would like to thank the sponsors of the Reservoir Characterization Project for their financial support and fruitful discussions. We extend our sincere thanks to our reviewers, including Dr. Gaiser and Dr. Liu, for their insightful feedback and constructive comments.

CHAPTER 4

SIGNAL ENHANCEMENT OF RAYLEIGH WAVE DISPERSION FROM LIMITED-COVERAGE GLACIAL EXPERIMENTS USING MULTI-COMPONENT DATA

S. Garvey[1], M. Siegfried[1], J. Shragge[1], L. Zoet[2], D. Hansen[2], and N. Stevens[3]

4.1 Abstract

Seismic ice velocity estimates provide quantitative constraints on glacial systems including ice thickness, englacial structure, and bedrock topography. Detailed velocity modeling using active-source seismic surveys on glaciers, however, is often challenged by sub-optimal survey acquisition design due to complex field logistics. This study explores new potential of such surveys for characterizing potentially heterogeneous seismic ice velocities by leveraging dispersive Rayleigh-wave responses recorded on three-component (3-C) receivers. We use synthetic models to study survey design, data conditioning, and improvements provided by multi-component data for dispersion analysis that inform estimates of vertical velocity profiles. We employ these learnings to optimize the accuracy of dispersion curves derived from a limited aperture, 3-C dataset acquired on the Saskatchewan Glacier in the Canadian Rocky Mountains. Our experiments suggest that when working with a limited number of geophones practitioners should: prioritize array length over finer receiver spacing; use shot points to infill receiver gaps; preprocess shot-gather data to emphasize Rayleigh waves; and use supergathers to enhance signal-to-noise ratio and extend effective array aperture prior to building dispersion panels. Finally, we extract novel value from 3-C dispersion analysis by combining vertical- and

---

[1] Department of Geophysics, Colorado School of Mines, Golden, CO 80401, U.S.A.
[2] Department of Geoscience, University of Wisconsin–Madison, Madison, WI 53706, U.S.A.
[3] Pacific Northwest Seismic Network, University of Washington, Seattle, WA, U.S.A.

horizontal-displacement data to reduce uncertainty and improve picked dispersion curve accuracy.

4.2 Introduction

The structure and material properties of ice masses and underlying bedrock are key parameters that control ice flow (e.g., Bennett, 2022). Active-source seismic methods, which operate at low (sub-200 Hz) frequencies (Podolskiy & Walter, 2016), allow for deep subsurface investigations (e.g., at the ice-bedrock interface and internal bedrock layering) by using a controlled source of acoustic waves, which are sensitive to variations in compressional- (P) and shear- (S) wave velocities and density of the elastic medium. This method has been leveraged to map subglacial structures across multiple glacier types (typically using reflected or refracted wave data), such as at Rutford Ice Stream in West Antarctica (Smith, 1997) and the Taku (Zechmann *et al.*, 2018) and Lemon Creek (Veitch *et al.*, 2021) Glaciers in Alaska. Active-source seismic methods are also able to resolve englacial heterogeneity in elastic properties where recorded frequencies are sufficiently high. Examples include mapping a 40 m deep englacial conduit at Rhonegletscher with a dominant frequency of 100 Hz (Church *et al.*, 2019), mapping debris layers at Sourdough rock glacier in Alaska (Kuehn *et al.*, 2024) with a 100 Hz dominant frequency, and building a seismic-velocity profile through the upper 80 m of firn at Korff Ice Rise in West Antarctica using a dominant frequency of 200 Hz (Agnew *et al.*, 2023).

Typically, a two-dimensional (2-D) seismic survey is sufficient for estimating elastic velocities from which bedrock topography and ice thickness, h, can be calculated. When source-receiver offset distances are long relative to the bedrock depth (i.e., $> 3\times$), refracted P-wave energy can be used to constrain P-wave velocity models (V_p) at depth (e.g., Redpath, 1973). For more limited-offset surveys, Rayleigh waves that propagate along the surface of the Earth and are strong reliable signals (e.g., Socco & Strobbia, 2004) can be used to constrain S-wave velocity (V_s) depth profiles (Crice, 2005). Active-source experiments on glaciers are often offset-limited due to the logistical challenges of operating on ice (Aster & Winberry, 2017), which suggests that Rayleigh wave methods should be well suited for glacial experiments.

There are two common approaches for deriving elastic model properties from Rayleigh waves: (1) the horizontal-vertical spectral ratio (HVSR) method, which exploits the elliptical particle motion of this wave; and (2) the multi-channel analysis of surface waves (MASW), which exploits the dispersive nature of the wave (i.e., the change in wave propagation velocity with frequency).

The HVSR approach calculates h from the resonant frequency (f_0) of ambient Rayleigh-wave energy recorded on a seismic array in conjunction with a V_s estimate that is typically derived from P-waves recorded on a co-located active-seismic survey and an empirical V_p/V_s ratio. We refer the reader to Picotti *et al.* (2017) and Preiswerk *et al.* (2019) for seminal applications of HVSR in glacier settings. Stevens *et al.* (2023), for example, applied this workflow to a combined dataset acquired on the Saskatchewan Glacier in the Canadian Rocky Mountains, using an "accepted" $V_p/V_s = 1.95$.

The HVSR method assumes a layer-over-half-space model from which the upper layer thickness, h, can be estimated as $h = \frac{V_s}{4f_0}$ (Ibs-von Seht & Wohlenberg, 1999). The HVSR method has caveats that limit its applicability in complex environments like those found in firn-aquifer systems. In these settings, HVSR's core assumptions — lateral homogeneity and the validity of h estimates based on a layer-over-half-space system (Koller *et al.*, 2004) — are often violated. This underscores the need for applying alternative velocity model-building approaches that explicitly avoid homogeneity assumptions and reduce or eliminate the need for empirical relationships.

MASW is one such velocity modeling approach which avoids uncertainties arising from the homogeneity assumptions of the HVSR method and exploits Rayleigh-wave dispersion in layered media. Developed by Park *et al.* (1999), MASW is widely used in geotechnical engineering (e.g., Crice, 2005) where dispersion caused by near-surface layering is expressed as the change in Rayleigh-wave phase velocity V_r as a function of frequency f (and consequently depth, z). As opposed to HVSR, MASW is commonly implemented on low-energy, active-source experiments and analyzes higher-frequency surface waves with shallower penetration depths. At Sourdough Rock Glacier, Alaska, Kuehn *et al.* (2024) employed 12 vertical-component (1-C) geophones at 5 m spacing and generated accurate seismic velocity estimates of the upper 5 m of the ice column. At Spitsbergen in the Norwegian Arctic, the MASW method was used to constrain meltwater at a deeper ice-bed interface (down to 200 m) by inverting multi-mode dispersion curves (Tsuji *et al.*, 2012). This required a longer receiver array (1500 m) in which they used 60 1-C geophones deployed at 25 m spacing.

MASW is a relatively straightforward workflow, made accessible through open-source software such as *MASWaves* (Ólafsdóttir *et al.*, 2018b). However, it demands careful implementation and interpretation of inversion schemes and results due to the inherent non-uniqueness of solutions (Foti *et al.*, 2018). In glacial settings, the ill-posed nature of the inverse problem is further amplified by logistical surveying constraints, such as being limited to a small number of receivers or low-impact sources in weight-limited field expedition. This has motivated some practitioners to implement more advanced inversion approaches, such as the transdimensional Bayesian inversion applied at Helheim Glacier, Greenland (Killingbeck *et al.*, 2020).

In this study, we aim to address the ill-posedness of MASW for the typical limited-aperture receiver arrays in glaciological applications by exploring how optimized survey design, enhanced data preconditioning, and the use of three-component (3-C) instruments can reduce observational uncertainty and thereby improve the effective depth of investigation. We begin with an overview of Rayleigh-wave theory relevant to MASW, followed by three synthetic studies that each examine sensitivities of MASW to data conditioning, acquisition geometry, and subsurface complexity. In all case studies, we simulate and analyze multi-component (MC) datasets and develop an MC-MASW approach which accounts for their complementary contributions. Finally, we apply

MC-MASW to an aperture-limited dataset acquired on the Saskatchewan Glacier in the Canadian Rocky Mountains (Stevens *et al.*, 2023). We conclude by offering key recommendations for MC data acquisition, preprocessing, and Rayleigh-wave dispersion analysis in glacial investigations.

4.3 Theory

This section reviews Rayleigh wave theory using potential wavefields (P- and S-waves) rather than the displacement wavefields commonly presented in textbooks. Although displacement-based formulations are widely used for their practical application in matrix methods for solving the wave equation (Aki & Richards, 2002), our approach follows Lay & Wallace (1995) and provides insight into the underlying principles of our MC approach to Rayleigh wave analysis.

4.3.1 Assumptions and Notation

We focus on the 2-D problem in the x–z plane of wave propagation, restricting the development to isotropic, linear elastic solids. Extending these studies to account for anisotropy is a natural progression of this work, particularly given that ice is generally considered anisotropic. We assume an acquisition field coordinate system in which the vertical z and horizontal x directions are positive downward and to the right, respectively (Figure 4.1a). Wavefield displacements in the z and x directions are respectively denoted U_z and U_x. Without loss of generality, we assume that the free-surface interface occurs at $U_z = 0$ m.

Horizontal-component geophone data are rotated into a cylindrical coordinate system centered about the source point with horizontal radial-transverse (R–T) components to isolate the azimuthal dependence of recorded particle displacement (Gaiser, 1999). The R and T components for any source-receiver pair respectively point along and perpendicular to the source-to-receiver azimuth (Figure 4.1b). Here, we limit our analysis to R-component data.

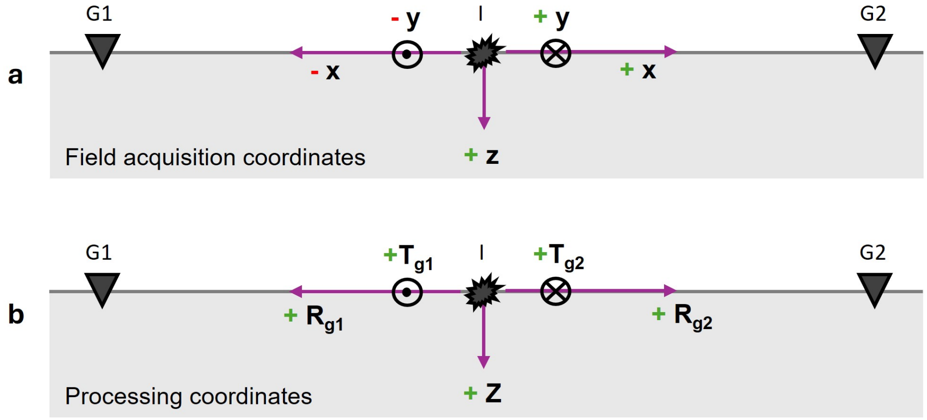

Figure 4.1 Definition of the (a) acquisition coordinate system in horizontal x and y and vertical z directions, and (b) the cylindrical processing coordinate system in outward-positive radial R and vertical Z directions. The transverse, T direction is always counter clockwise from R. I and G annotate the locations of the impact source and receivers in each sketch.

4.3.2 Rayleigh Waves

Rayleigh waves exist in the near surface of an elastic medium due to the interference of elastic body waves (specifically, the P-SV wave system with S-wave particle motion polarized in the plane of wave propagation) and their conversions at the free surface (here, the air-ice interface) (Lay & Wallace, 1995; Liner, 2012). These two wave modes are coupled: when either wave interacts with a boundary with discontinuous material properties, the resulting reflection, refraction, and transmission effects occur in addition to wave-mode conversion (Figure 4.2a). Figure 4.2b illustrates this mechanism for an incident reflected PS wave striking the free surface at an angle j. Interaction of this wave mode with the free surface produces a twice-converted P wave (PSP) and a converted SV wave (PSS), that are respectively reflected at angles j and i and propagate with velocities V_p and V_s of the first layer.

Rayleigh waves are generated when the SV wave meets the free surface where surface tractions vanish at (and beyond) a critical angle. The incident SV wave is converted into a refracted P wave (propagating along the surface) and a 90° phase-shifted, post-critical reflection of SV wave energy (with near-vertical particle motion that grazes the surface) (Lay & Wallace, 1995). The respective wave-mode interactions with the free surface generate evanescent P- and SV-waves (Figure 4.2c). The resulting P- and SV-wave displacements are described by the gradient of the scalar potential, Φ, and the curl of the vector potential, Ψ, respectively.

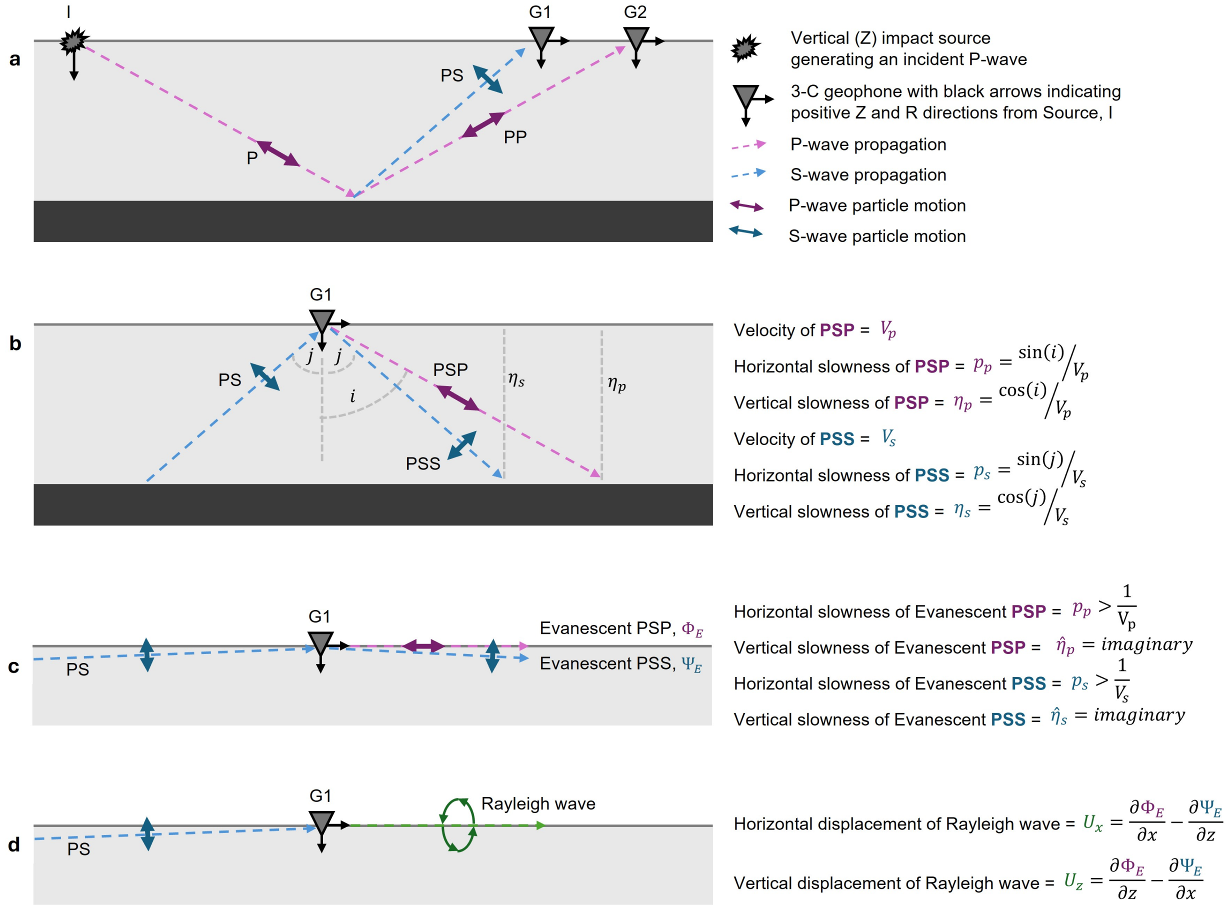

Figure 4.2 Conceptual representation of Rayleigh-wave generation from a vertical impact source I. (a) An incident P wave reflects off an impedance contrast producing up-going reflected P (PP) and S (PS) waves. (b) The up-going PS wave undergoes total internal reflection at the free surface producing a PSS wave and a mode-converted PSP wave. The velocity and horizontal and vertical slownesses are described relative to the free-surface incidence angle. (c) At large angles of incidence, evanescent PSP and PSS waves propagate along the surface out-of-phase thus producing (d) a Rayleigh wave with retrograde elliptical particle motion along the free surface. U_z and U_x are described in terms of the potentials, Φ and Ψ, of the evanescent wavefields.

The simultaneous existence of these two out-of-phase modes generates a Rayleigh wave with elliptical particle motion (Lay & Wallace, 1995) that propagates along the surface (Figure 4.2d). Rayleigh-wave vertical (U_z) and horizontal (U_x) displacements are represented by sums of spatial derivatives of Φ_E and Ψ_E. For a homogeneous Earth system, the equations associated with Figure 4.2d are expanded as:

$$U_x = -A\omega p \sin\left(\omega(px-t)\right)\left[\mathrm{e}^{-\omega\hat{\eta}_p z} + \frac{1}{2}\left(\frac{{V_r}^2}{V_s^2} - 2\right)\mathrm{e}^{-\omega\hat{\eta}_s z}\right], \tag{4.1}$$

and

$$U_z = -A\omega p \cos\left(\omega(px-t)\right)\left[V_r\hat{\eta}_p \mathrm{e}^{-\omega\hat{\eta}_p z} + \frac{1}{V_r\hat{\eta}_s}\frac{1}{2}\left(\frac{{V_r}^2}{V_s^2} - 2\right)\mathrm{e}^{-\omega\hat{\eta}_s z}\right]. \tag{4.2}$$

The displacements are a product of three terms: (1) amplitude terms dependent on the angular frequency ω, the horizontal slowness p of the Rayleigh wave, and a scaling constant A; (2) time-dependent terms describing harmonic plane-wave motion along the x direction; and (3) terms specifying amplitude decay with depth z dependent on vertical slownesses $\hat{\eta}_p$ and $\hat{\eta}_s$ defined by

$$\hat{\eta}_p = \sqrt{\frac{1}{V_r^2} - \frac{1}{V_p^2}} \tag{4.3}$$

and

$$\hat{\eta}_s = \sqrt{\frac{1}{V_r^2} - \frac{1}{V_s^2}}. \tag{4.4}$$

The time-dependent terms are described by orthogonal *sine* and *cosine* functions that produce elliptical particle motion because of generally larger displacements in U_z compared to U_x. At the free surface, the sense of elliptical particle motion is retrograde; however, this changes to prograde at depth h_r where the third term of Equation (4.2) becomes zero causing $U_x = 0$. The depth h_r can be analytically calculated as

$$h_r = \frac{\ln\left(1 - \frac{V_r^2}{2V_s^2}\right)}{\omega\left(\hat{\eta}_s - \hat{\eta}_p\right)}, \tag{4.5}$$

or approximated based on the dominant wavelength (Ammon *et al.*, 2020), $\lambda = V_r/f$, as

$$h_r \approx \frac{1}{5}\lambda. \tag{4.6}$$

To validate that this general expression holds for glacial ice, we compare equations (4.5) and (4.6) for three models — a saturated soil profile (Yang, 2005), a Poisson solid (Ammon *et al.*, 2020), and glacial ice referenced from Saskatchewan Glacier (Stevens *et al.*, 2023). The velocities of each model are listed in rows a, b and c1 in Table 4.1 and resulting plots are shown in Figure 4.3. The similarity between the true and approximate solutions suggests that Eqn. (4.6) is a reasonable estimate for the three tested models.

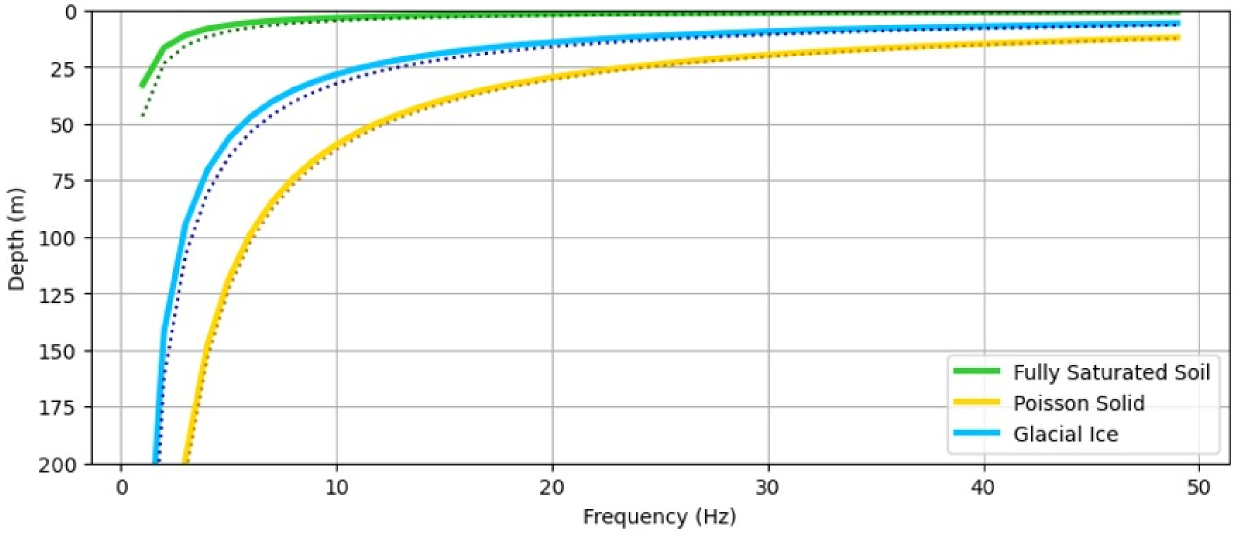

Figure 4.3 Frequency-dependent depths at which Rayleigh-wave particle motion change from retrograde to prograde for a fully saturated soil profile (green) (Yang, 2005), a Poisson's solid (yellow) (Ammon *et al.*, 2020), and glacial ice (blue) based on parameters estimated for the Saskatchewan Glacier (Stevens *et al.*, 2023). Solid line are analytical solutions (Eqn. (4.5)), and dotted lines are approximated depths (Eqn. (4.6)) for all models. Table 4.1 lists associated material properties.

Table 4.1 Elastic properties for different subsurface media examined in our analytical models: a. fully saturated soil profile (Yang, 2005); b. Poisson solid (Ammon *et al.*, 2020); c1. ice layer derived from the Saskatchewan Glacier (Stevens *et al.*, 2023); c2. ice layer derived from the Greenland Ice Sheet (Walter *et al.*, 2015); c3. ice layer derived from Nathorst Land, Spitsbergen (Johansen *et al.*, 2011); d. firn layer derived from the Helheim Glacier, Greenland (Killingbeck *et al.*, 2020). Note that although some case studies report higher-precision values, we have rounded results to the nearest hundredth for consistency.

	Model	V_p (m s^{-1})	V_p/V_s	V_r/V_s
a	Fully Saturated Soil	1550	6.30	0.95
b	Poisson Solid	5800	1.73	0.92
c1	Ice (Saskatchewan Glacier)	3450	1.95	0.93
c2	Ice (Greenland Ice Sheet)	3870	2.10	—
c3	Ice (Spitsbergen)	3600	2.00	—
d	Firn (Helheim Glacier)	2900	2.23	—

The depth-dependent terms are eigenfunctions for which the phase velocity V_r is the eigenvalue (Aki & Richards, 2002). This is an important feature, as it provides a means of solving for V_r using the characteristic equation derived from the eigenproblem. For the homogeneous half-space model, the characteristic equation simplifies to

$$\frac{V_r^6}{V_s^6} - 8\frac{V_r^4}{V_s^4} + \left(24 - 16\frac{V_s^2}{V_p^2}\right)\frac{V_r^2}{V_s^2} + 16\left(\frac{V_s^2}{V_p^2} - 1\right) = 0. \tag{4.7}$$

We refer the reader to Ammon *et al.* (2020) for a digestible derivation of this equation starting from the potential field definitions of the stress tensor at the free surface. Note that Eqn. (4.7) is a cubic polynomial in V_r^2/V_s^2 and that solutions for V_r are highly sensitive to V_s, a fact that provides an opportunity to derive a $V_s(z)$ profile from the Rayleigh-wave data via inversion. Although there are multiple solutions for V_r, the solution is constrained by realistic V_p/V_s ratios. We visualize this constraint by plotting V_r/V_s versus V_p/V_s (Figure 4.4) and note the solution for a Poisson solid, fully saturated soil and several glacial estimates (Table 4.1) derived from published studies. Figure 4.4 suggests that glacial estimates of V_r/V_s are slightly higher than that of a Poisson solid.

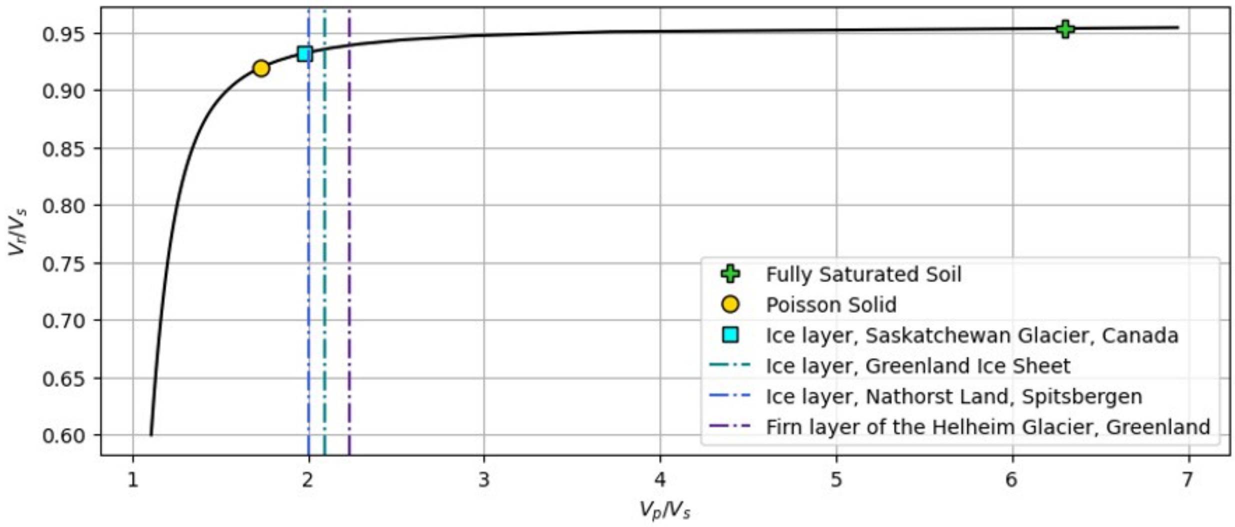

Figure 4.4 Rayleigh-wave characteristic equation (Eqn. (4.7)) represented as a relationship between V_p/V_s and V_r/V_s (black curve) with reference values for a saturated soil (green cross), Poisson solid (yellow circle), and glacial ice at the Saskatchewan Glacier (cyan square). V_p/V_s estimates of other glacial examples are plotted as vertical lines since V_r/V_s estimates are not mentioned in reference studies. Table 4.1 lists associated material properties.

4.3.3 Layering and Dispersion Effects

In a layered Earth, the Rayleigh-wave displacement and characteristic equations become more complex due to the introduction of a relationship between V_r and f. In an Earth model where velocities generally increase with depth, lower-frequency wave modes propagate deeper, interacting with faster velocities, and therefore arrive earlier than the higher-frequency modes. This velocity-dependence on frequency (i.e., $V_r(f)$) is called dispersion. We refer the reader to Ammon *et al.* (2020) for a comprehensive physical overview of dispersion phenomenon and to Aki & Richards (2002) for more advanced mathematical treatment. Whereas Eqns. (4.1) and (4.2) may be solved analytically for a homogeneous Earth model, Rayleigh-wave displacements and dispersion need to be calculated numerically for general layered Earth scenarios (Aki & Richards, 2002).

Each frequency in a propagating Rayleigh wave carries velocity information about a range of depths with variable sensitivity. At the high-frequency limit, λ is potentially much shorter than the thickness of the uppermost layer. That is, the wave displacement is entirely contained within that single layer and the effective velocity of this high-frequency component of the Rayleigh wave is dominantly controlled by properties of the uppermost layer. At longer wavelengths, the wave interacts with multiple layers at any given time and thus mapping V_r to a specific depth requires untangling the overlapping frequency-dependent sensitivities of Rayleigh-wave displacement to different depths.

Short of calculating velocity-dependent sensitivity kernels of the eigenfunctions, a reasonable assumption is that the Rayleigh-wave depth of investigation, h, is equal to a half wavelength, $\lambda/2$ (Park *et al.*, 1999). The minimum and maximum depths of investigation, respectively denoted h_{min} and h_{max}, are given by

$$h_{min} \approx \frac{\lambda_{min}}{2} \approx \frac{V_{r,min}}{2f_{max}} \approx \Delta r_x \tag{4.8}$$

and

$$h_{max} \approx \frac{\lambda_{max}}{2} \approx \frac{V_{r,max}}{2f_{min}} \approx \frac{L}{3} \text{ to } \frac{L}{2}, \tag{4.9}$$

where receiver spacing Δr_x and array length L control the shortest and longest wavelengths, λ_{min} and λ_{max}, measurable on an array. The recoverable wavelengths are themselves constrained by the Nyquist sampling theorem (de Lucena & Taioli, 2014; Socco & Strobbia, 2004).

Subsurface layering can act as waveguides that increase propagating wavefield complexity. As waves reflect and refract within these layers, only certain frequencies will align in a manner that produces coherent, stable oscillations, which manifest as higher-order modes. The limiting frequencies over which a higher-order mode exists are a function of layer thickness, depth, velocity contrasts, and propagating frequencies. The modes are distinguishable by their different dispersive behavior and dominant frequency ranges. Higher-order modes are particularly important for recovering complex models with velocity inversions (i.e., where a fast velocity material overlies a slow velocity medium). A low-velocity layer will bend the transmitted ray toward the normal and allow for high-frequency oscillations within this layer. Multi-mode analysis can be necessary for characterizing voids or unfrozen layers (e.g., at Spitsbergen in the Norwegian Arctic; Tsuji *et al.*, 2012) or firn-aquifer systems (e.g., at the Helheim Glacier in Greenland; Killingbeck *et al.*, 2018).

In a layer-over-half-space model, fundamental mode amplitudes are strongest. In layered media, the fundamental mode is strongest at lower frequency ranges (with the exact range dependent on layer thickness and velocities) and thus controls the maximum depth of investigation. Our investigations focus on fundamental-mode dispersion, although including higher-order modes would be a natural progression of this work.

4.4 Methods and Implementation

MASW dispersion analysis hinges on generating plots showing relative signal amplitude in $V_r - f$ space, commonly referred to as dispersion panels (DPs), in order to estimate V_r of the fundamental mode as a function f, or the dispersion curve (DC). To construct DPs for dispersion analysis, the seismic data are first organized into shotgathers of the form $D(d, t)$, where d represents the offset and t the recording time. Each gather contains all time-series traces recorded from a single shot, sorted by increasing offset. Each shot gather is then transformed to the frequency domain ($D(d, \omega)$) and subsequently normalized ($D_N(d, \omega)$) in both the offset and frequency dimensions (Park *et al.*, 1998) to minimize the influence of geometrical spreading and attenuation effects. The normalized amplitudes at each offset and frequency ideally are representative of dispersion effects. Through slant-stack processing (Ólafsdóttir *et al.*, 2018b), traces are move-out corrected, stacked, and normalized by the number of traces for a user-selected range of phase velocities and frequencies producing DPs ($D_S(V_r, \omega)$). DCs are picked along the (ideally continuous) peak-magnitude trend. We used the open-source *MASWaves* software package (Ólafsdóttir *et al.*, 2018b) to generate DPs and automatically pick DCs based on maximum amplitude.

A comprehensive analysis of surface-wave dispersion typically involves inverting these DCs to obtain V_s depth profiles which inform interpretations of subsurface structure and mechanical behavior. However, we focus on improving the forward problem by constructing accurate and reliable DCs that are an essential yet underexplored aspect in the MASW literature — especially in the context of cryospheric field experiments.

4.4.1 Design of DC Sensitivity Studies

The inversion of surface-wave dispersion data is a strongly ill-posed problem, largely due to the complex wave physics involved — complexities we have simplified in the above Theory section. As a result, the accurate extraction of DCs becomes critically important, particularly in glaciated environments where surveys are often constrained by limited array lengths, low receiver counts, shallow source penetration, and non-ideal (near-)surface conditions, such as crevassing. To systematically investigate these limitations, we design three synthetic studies.

The first simulates an ideal active-source survey, which features a long array and dense spatial sampling, over a simple two-layer model to establish best-practice data conditioning steps. The second study uses the same model but applies non-ideal survey designs to explore how acquisition geometry alone can limit the forward problem, even under optimal conditioning. In the third study, we simulate wave propagation through three variations of firn-aquifer models to test the robustness of our conditioning approach under more realistic near-surface complexity. All studies examine MC datasets, using both vertical (Z) and radial (R) component data. In the final study, we also develop an approach for integrating these components in an MC-MASW framework that enhances DC accuracy with minimal changes to field deployment or processing workflows.

The synthetic MC data were simulated with the open-source SOFI2D seismic modeling package (Bohlen *et al.*, 2016). For all experiments, a vertical impact source was simulated as an Ormsby wavelet with a flat frequency spectrum between 5 Hz and 30 Hz. For all studies, sources and receivers were positioned 1 m below the free surface. Because individual simulations had only positive offsets ($d > 0$), the horizontal-component data correspond to the radial R component for all source-receiver pairs. For field studies with non-uniform geophone orientation and for multi-azimuth acquisitions with directional (signed) offsets, rotating recorded data into a $R-T$ coordinate system would be a critical data preprocessing step.

4.4.2 Field Data Implementation

Building on the data conditioning strategies and MC analysis developed through the synthetic studies, we apply MC-MASW to a field dataset acquired on Saskatchewan Glacier (Stevens *et al.*, 2023, 2024). The raw 3-C field data were organized into shot-gathers using *ObsPy* (Beyreuther *et al.*, 2010). Although the horizontal components were predominantly parallel and orthogonal to the 2-D array axis we applied an $R-T$ rotation to correct for any minor misalignment. This rotation and other minor data refinement (e.g., time-shifts and noise filtering) were completed using the open-source *Seismic Unix* seismic processing software package (Stockwell Jr, 1999).

Unlike the controlled synthetic scenarios, the field data presented additional challenges due to ambient noise and other sources of variability. To address this, we combined multiple shot gathers to generate supergathers (Hesthammer & Løkkebø, 1997). This not only improved DC reliability but also enhanced the depth sensitivity of the MASW analysis, which will be discussed in detail in the presentation of results.

4.5 Results: DC Sensitivity Studies

We first present the results of three synthetic feasibility studies designed to assess DC sensitivity of MC data to data conditioning, acquisition geometry, and subsurface complexity. Each study isolates key factors that affect the accuracy and reliability of the forward problem in MC-MASW analysis.

4.5.1 Study 1: DC Sensitivity to Data Conditioning

This study aimed to identify data conditioning steps that enhance DP resolution and thereby improve the accuracy of DCs extracted from MC data. To achieve this, we simulated an MC experiment under ideal survey conditions (Figure 4.5) using an isotropic, elastic model representing a homogeneous ice layer overlying a bedrock half-space – conditions commonly observed in the ablation zones of mountain glaciers. Model properties are adapted from Stevens *et al.* (2023) at the Saskatchewan Glacier (see Table 4.2).

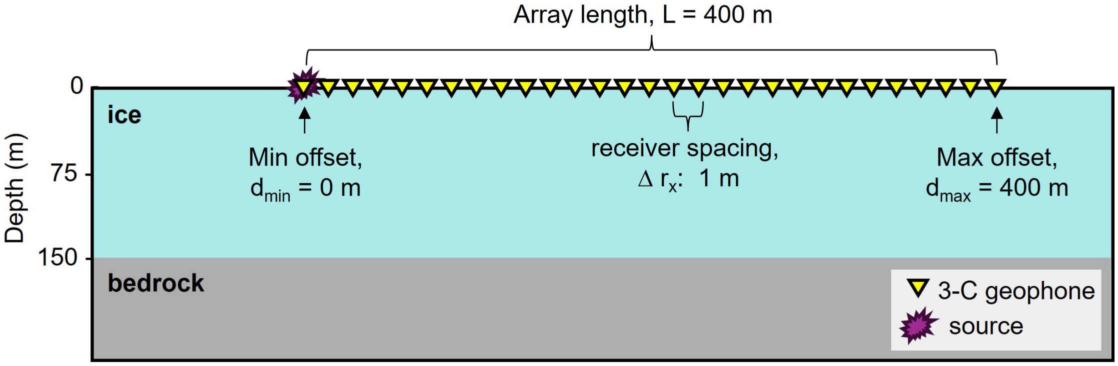

Figure 4.5 Model describing a homogeneous, isotropic, elastic ice layer of 150 m thickness overlying a bedrock half space. Table 4.2 presents the elastic model properties. The idealized acquisition has a dense 1 m receiver spacing and 400 m aperture. The sketched geometry is not to scale and approximates receiver placement for visual reference.

Table 4.2 Two-layer homogeneous ice-bedrock model elastic properties extracted from Stevens *et al.* (2023)

Layer	V_p (m s^{-1})	V_s (m s^{-1})	**Density** (ρ) (kg m^{-3})	**Thickness** (h) (m)
Ice	3500	1750	930	150
Bedrock	4000	2000	2600	∞

Figure 4.6 presents a representative example of the Z- and R-component synthetic data. The shot gathers (Figure 4.6a and Figure 4.6c) exhibit a strong Rayleigh-wave arrival with linear moveout (i.e., arrival time linearly increasing with offset d), and the direct P-wave arrival has higher raw amplitudes on the R component in comparison to those observed on the Z component. Using *MASWaves*, the shot gathers and relevant acquisition geometries (i.e., d_{min}, Δr_x, number of traces and orientation of offsets) were input to create DPs

(Figure 4.6b and Figure 4.6d). Z- and R-component DCs are automatically picked using the *MASWaves* algorithm at increments of 1 m s^{-1} for frequencies between 6 and 40 Hz.

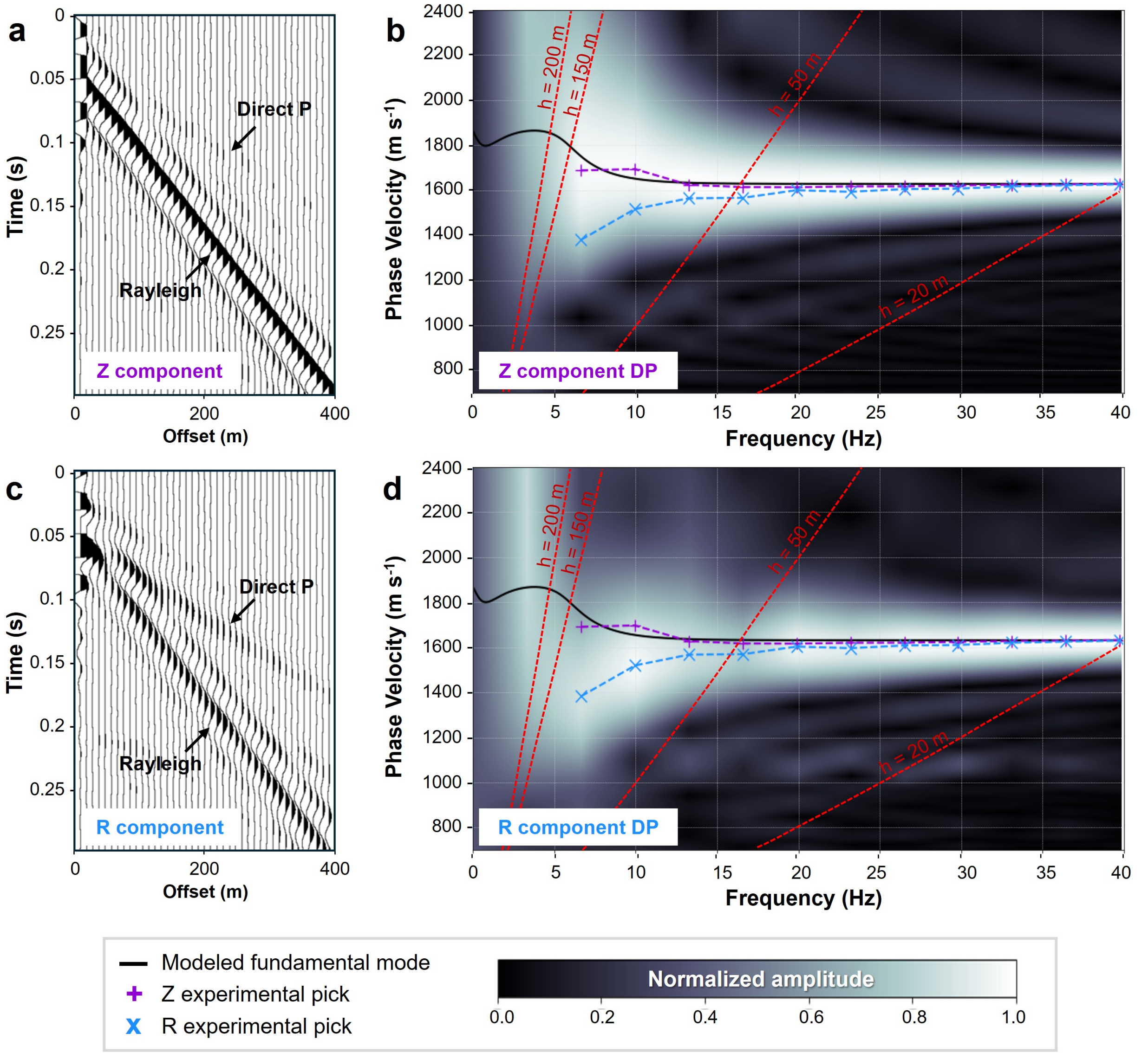

Figure 4.6 (a) Raw Z-component shot-gather data with corresponding (b) Z-component and (c) raw R-component shot-gather data with corresponding (d) R-component DP for the two-layer ice-bedrock model (Figure 4.5), with the numerically calculated DC for the fundamental model (black line). Every 10th trace is shown in the shot gathers for display purposes. Dashed red lines on DPs highlight the maximum wavelengths for resolving depths 20 m, 150 m, and 200 m; valid regions for picking experimental DCs for each depth range fall to the right of these lines. The experimental DCs for the Z- (purple) and R- (blue) components are displayed on both DPs. We note the DC complexity particularly for R and sub-10 Hz Z, which are not consistent with the numerical solution.

Given the known elastic model parameters and frequency range of interest, we calculated and plotted the numerical solutions for the fundamental (black line) mode using the open-source *disba* software package (Luu, 2021). Additionally, provided that the depth of investigation is related to V_r and f through Eqn. (4.9), we plot maximum wavelengths (red dashed lines) for resolving depths of 200 m (in bedrock), 150 m (ice-bedrock interface) and 20 m (in ice). Picked DCs at frequencies to the left of these depth-resolving relationships are unreliable. To the right of these lines, the depth-sensitivity of each frequency band varies according to the displacement eigenfunctions associated with the layered equivalent of Eqns. (4.1) and (4.2). Eqn. (4.9) also presents an approximation of the maximum depth of investigation based on array length. Given $L = 400$ m, we estimate $h_{max} = 133$ to 200 m which aligns with the low-frequency limit of observable strong amplitudes on the DPs (Figure 4.6b and Figure 4.6d).

For this synthetic model, the physics as implemented in the numerical solutions show that there is no observable dispersion at higher frequencies (over approximately 10 Hz) due to the homogeneity of the shallow ice layer. Above 20 Hz, the numerical solution of the fundamental mode (black line) is constant at 1670 m s^{-1} whereas the picked DC (herein referred to as experimental DC) averaged from the Z and R components is 1630 m s^{-1} with a 10 m s^{-1} discrepancy between the components.

The ice-bedrock layering generates dispersion in the $5 - 10$ Hz range indicative by the slope of the numerical solution. The DPs, though, are more complicated than theory suggests. Below 20 Hz, the resolution of the DPs declines as the high-amplitude band broadens and loses definition. Additionally at lower frequencies (below ~ 10 Hz), the Z- and R-component trends deviate from each other and the true solution. At 10 Hz, the difference between the experimental Z and R DCs is 180 m s^{-1} (>10% of the signal).

The numerical solutions are the vector-oriented solutions, i.e., they assume that particle displacement is calculated tangentially to the elliptical particle motion. To investigate why the Z- and R-component dispersion trends differ, we examine depth-sensitivities of the U_z

and U_x displacements, herein referred to as sensitivity kernels. In Figure 4.7, we compare $U_z(z)$ and $U_x(z)$ for the fundamental mode at discrete frequencies in the $5-40$ Hz band. Elliptical retrograde particle motion occurs where $U_x < 0$, $U_z > 0$, and $|U_z| > |U_x|$, then transitions to a prograde motion at depth. These depths can be identified by the R component data where $U_x = 0$ (solid arrows on Figure 4.7).

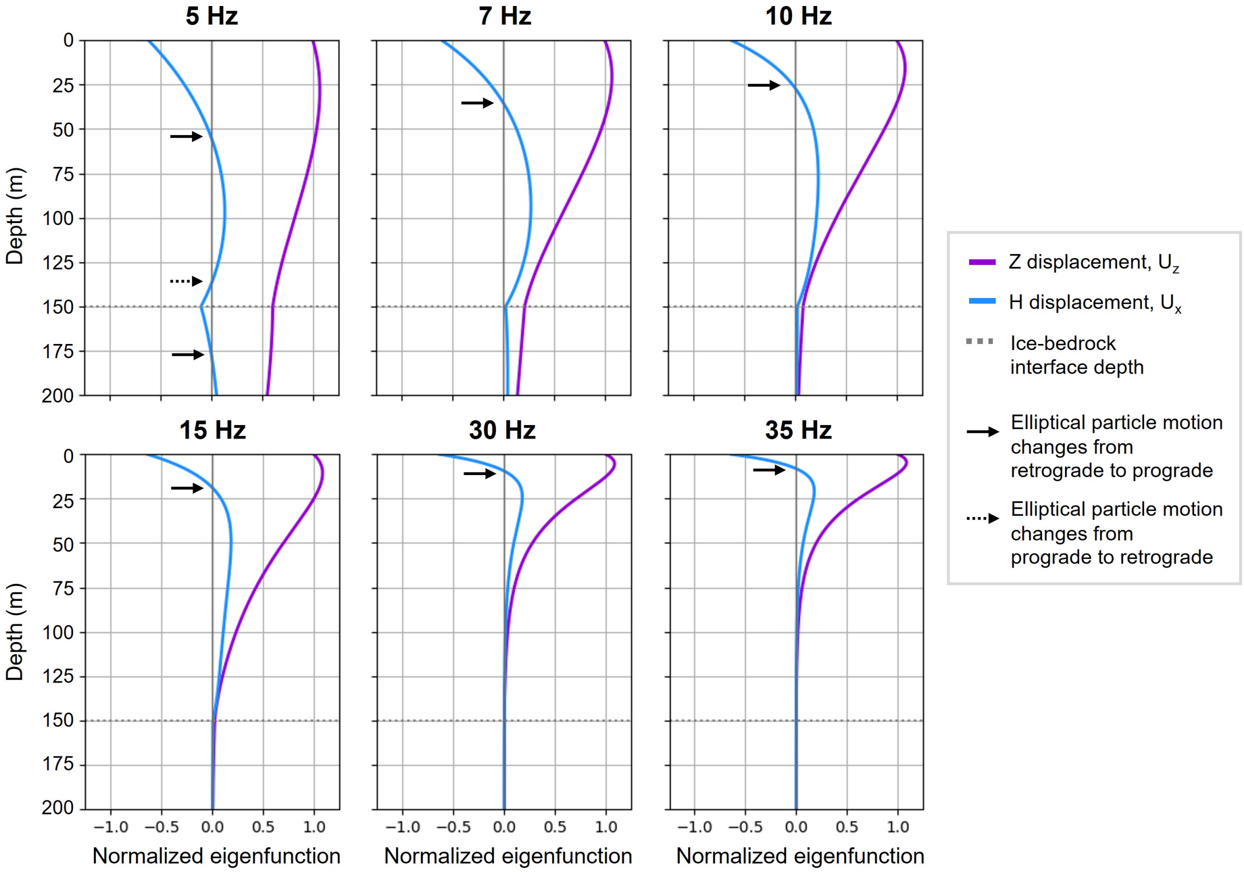

Figure 4.7 Monochromatic depth-sensitivity kernels for the homogeneous-ice over bedrock half-space model (Figure 4.5). Curves are the eigenfunctions (the layered-model equivalent of the third terms of Eqns. (4.1) and (4.2) normalized to $U_z(z=0)=1$) and represent the sensitivity of U_z (purple) and U_x (blue) to discrete model depths and wave frequencies. The dotted gray lines show the ice-bedrock interface depth for which only the $5-10$ Hz panels show non-zero U_z sensitivity and only $5-7$ Hz show non-zero U_x sensitivity.

The lowest frequency ($5-10$ Hz) components are most sensitive to the ice-bedrock interface at 150 m (dotted gray line). Above 10 Hz, the null Z- and R-component displacement at these depths indicate that the higher-frequency Rayleigh waves carry no information about the bedrock layer. Thus measuring dispersion at sub-10 Hz frequencies are critical for characterizing bedrock properties for this ice thickness.

There are two additional features of the 5 Hz U_x sensitivity kernel that provide important observational constraints on the system: (1) the second and third reversals in the sense of rotation at 130 and 175 m; and (2) an inflection point on U_x that occurs at the ice-bedrock interface (also observed with a smaller amplitude at 7 Hz). Our later analysis of a multi-layered system explores these observations in detail.

Effective data conditioning is crucial for constructing broadband, high-resolution DPs and facilitating accurate DC picks. Although data preprocessing is not always straightforward, two guiding principles apply for MASW purposes: (1) isolating the Rayleigh-wave mode; and (2) ensuring that each trace in the selected shot-gather window contains untruncated dispersive Rayleigh-wave energy. Furthermore, any noise-reduction effort applied to the MASW data input likely will improve experimental pick accuracy.

Below 20 Hz, R-component data are strongly affected by the direct P-wave arrival traveling sub-horizontally near the surface at 3500 m s^{-1}. We capture these arrivals in the shot gather (Figure 4.6c), and they cause substantial sub-20 Hz distortion of the corresponding DP (Figure 4.6d). Figure 4.8 shows the same data, but after removing the direct wave through frequency-wavenumber dip filtering. This filtering step improves DC generation for both Z- and R-components: at 10 Hz, the mean difference between experimental Z- and R-component picks (Figure 4.8d) is reduced from 180 m s^{-1} to 40 m s^{-1}, while the mean difference between the experimental picks and numerical solution is now reduced from 130 m s^{-1} to 60 m s^{-1}.

In field experiments, it is common practice to position a zero-offset ($d = 0$ m) receiver nearby the shot point to record time zero. This is critical information for windowing continuous geophone records into shot gathers. However, zero-offset data are often more complex close to the source point and, if used, can degrade dispersion curves. Ideally, shot-gather data should be windowed such that the full Rayleigh wavefield (including all possible dispersive effects) fall within the window selected to generate the DPs. Figure 4.9 shows the shot gather from Figure 4.8 after removing the near-offset traces (i.e., $d < 10$ m) and adjusting the panel window times to capture the full wavelet at all offsets.

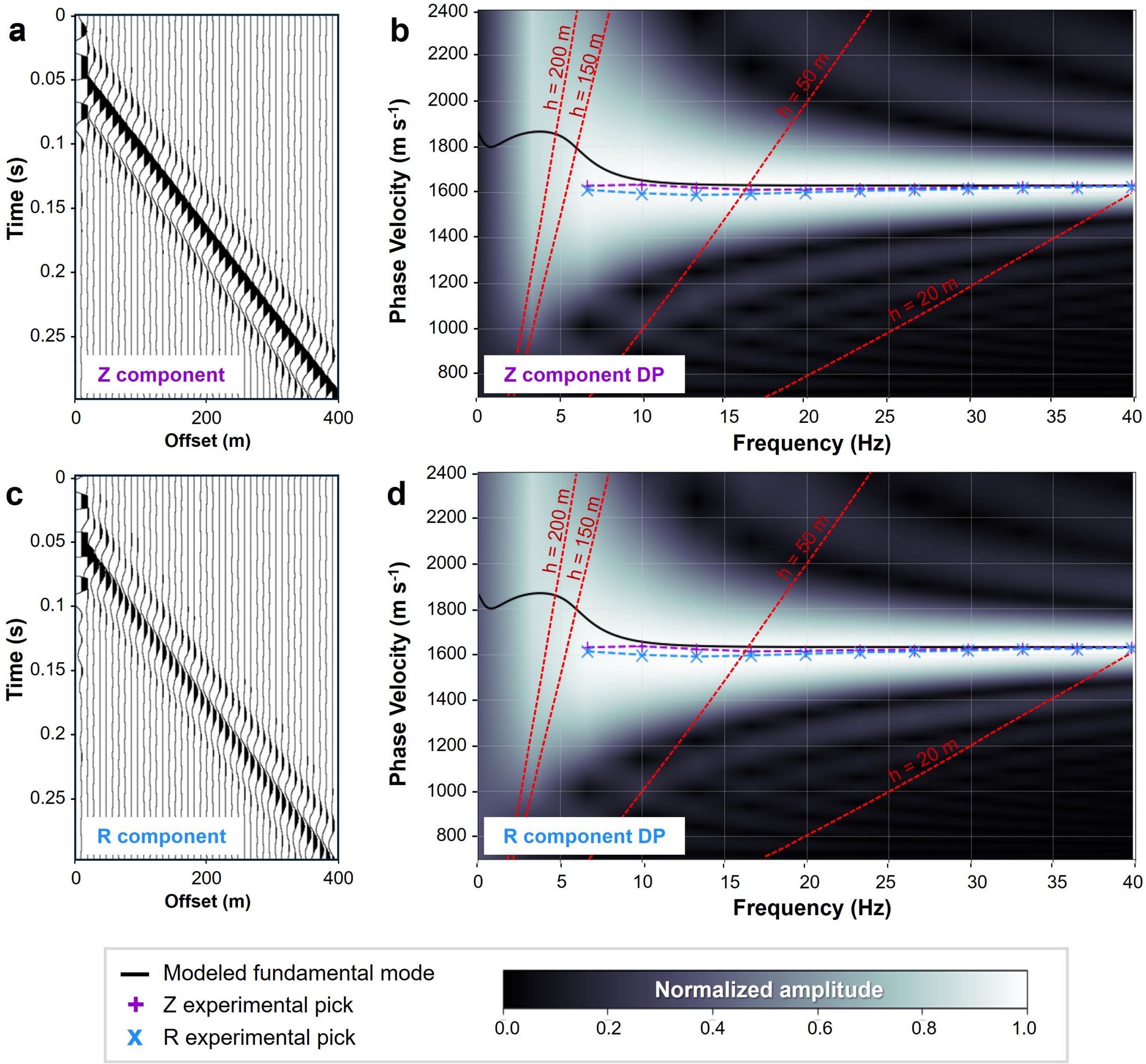

Figure 4.8 Conditioned shot gathers and DPs after removing the direct P-wave arrivals. See Figure 4.6 for descriptions of individual panels. Note the substantial improvement in the continuity of the R-component DP, with the mean Z- and R-component pick discrepancy reduced from 180 m s^{-1} to 40 m s^{-1}. Additionally, the Z- and R-component DCs are more closely aligned to the numerical solution (black line).

At 10 Hz, the discrepancy between experimental Z- and R-component picks and the mean difference between the experimental picks and the numerical solution are similar to the prior stage of removing the direct wave (Figure 4.9). However, the substantial value of this conditioning step is in improving DP resolution (i.e., stronger and more localized magnitudes). Below 5 Hz, the DP is abruptly truncated, which is accurate given that the Ormsby source wavelet used for simulation lacks frequencies below 5 Hz.

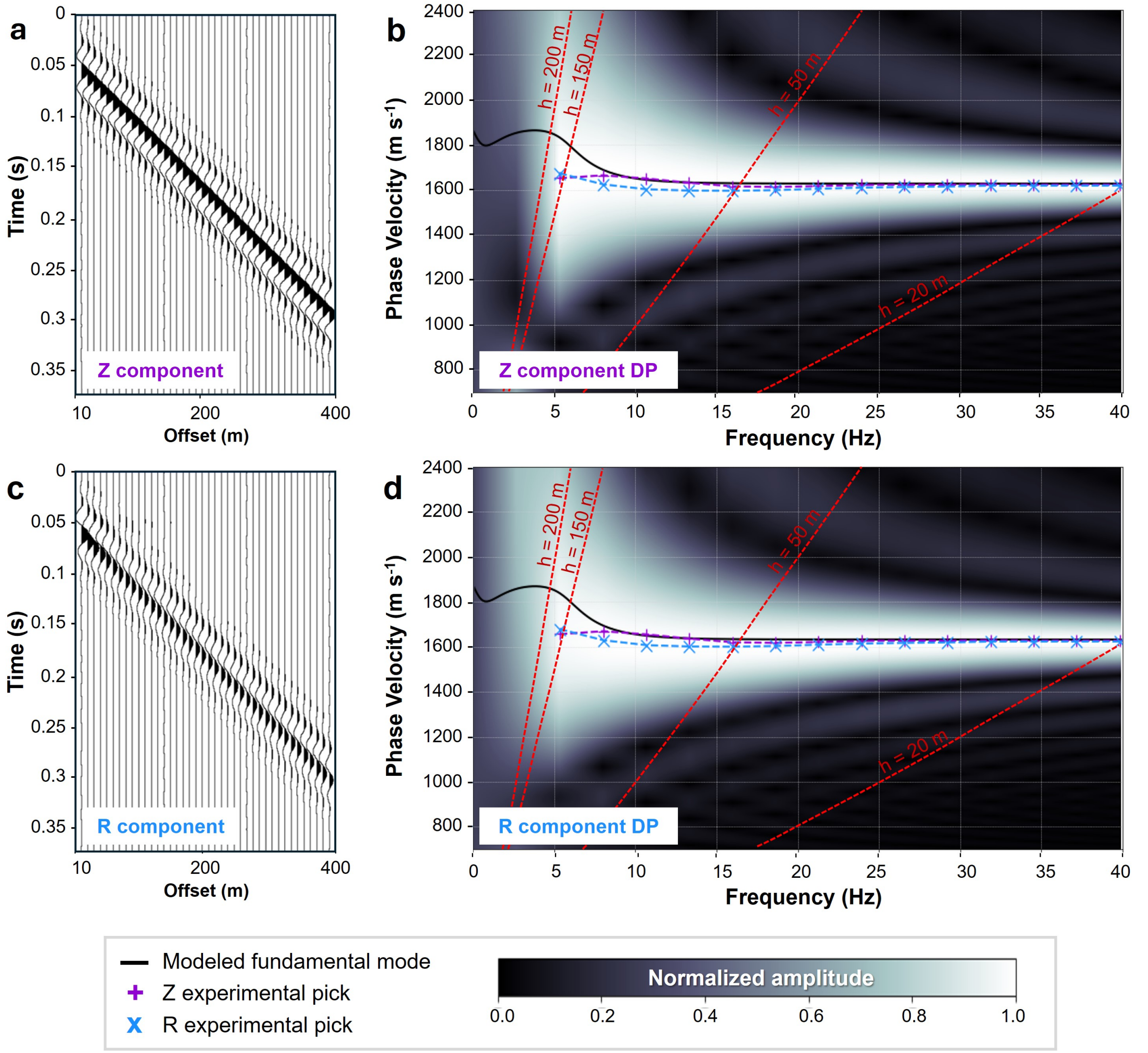

Figure 4.9 Conditioned shot gather data and DPs after removing the direct P-wave arrival and windowing out noisy near-offset traces to highlight the full Rayleigh-wave character at far offsets. See Figure 4.6 for descriptions of individual panels. We improved sub-10 Hz resolution of the DPs with appropriate data conditioning.

4.5.2 Study 2: DC Sensitivity to Acquisition Geometry

Practical limitations on survey design are often a restricting factor in geophysical field experiments. For example, active seismic experiments require transportation of a source (typically a sledgehammer), a base plate, and numerous geophones, and involve careful geophone deployment to ensure sufficient coupling and accurate positioning and potentially orientation, all of which can be challenging in glacial field conditions (Aster & Winberry, 2017). It is important to understand the practical limitations of survey design in order to make decisions about future field experiments or to improve the processing of existing data.

To illustrate the consequences of different survey designs, we modified the ideal acquisition described in Figure 4.5 in two independent ways: (1) shortening the array length, L, from 390 m to 190 m to represent a logistically constrained field location (e.g., crevasse fields limit array aperture); and (2) reducing the number of receivers from 400 to 40 stations and thereby increasing the spatial sampling interval, Δr_x, from 1 m to 10 m to represent a weight-limited field expedition (e.g., helicopter supported). Figure 4.10 illustrates the modified acquisitions, and Figure 4.11 presents the associated DPs generated from conditioned data after applying the direct-wave removal and offset-windowing steps that provide more reliable results.

The shorter array reduces DP resolution across all frequencies, with a more pronounced effect at lower frequencies (Figure 4.11a, Figure 4.11b). Additionally, the maximum depth of investigation is now restricted to between 63 m and 95 m according to Eqn. (4.9) and, although the experimental picks between 5 Hz and 10 Hz (for the R component in particular) may seem accurate, their alignment in this study is coincidental. In complex models where higher-order modes are needed to characterize low-velocity or thinner layers, the poor resolution caused by the short aperture can hinder the identification of separate modes, ultimately restricting the effectiveness of the MASW method.

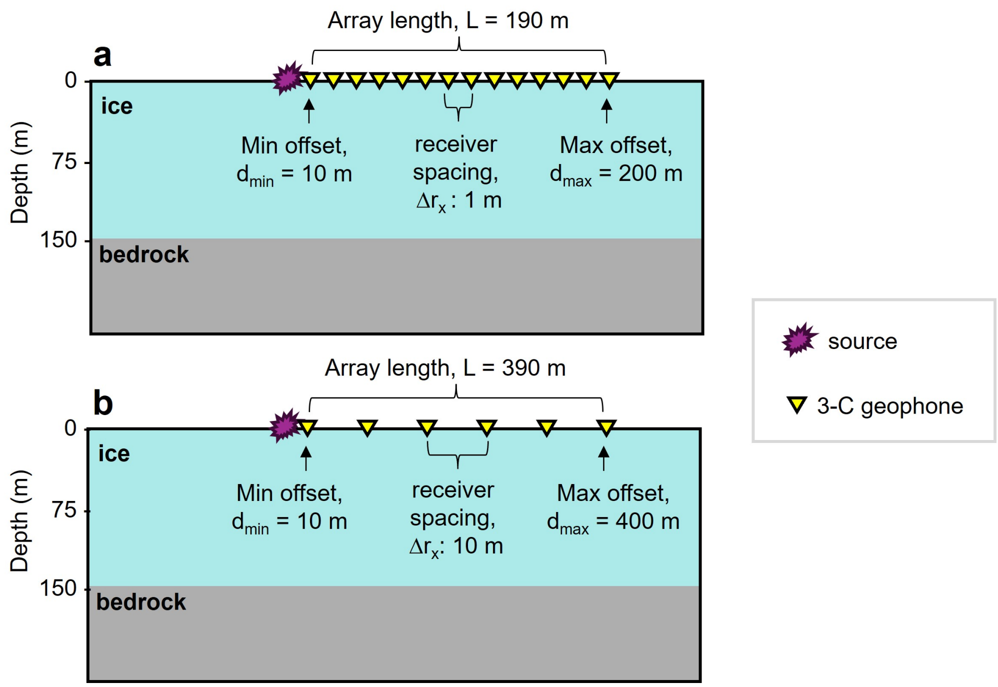

Figure 4.10 Two-layer ice-bedrock model described in Table 4.2 with two different acquisition experiments: (a) an aperture of $L = 190$ m (approximately half the length of the example described in Figure 4.5) and a receiver spacing of $\Delta r_x = 1$ m with the zero-offset receiver removed; and (b) an aperture of $L = 390$ m and a receiver spacing of $\Delta r_x = 10$ m. Not drawn to scale with the receiver placement only approximate for visual reference.

Greater receiver spacing (Figure 4.11c, Figure 4.11d) has less critical impact on DP resolution than a smaller-aperture survey. Larger receiver spacing primarily limits higher-frequency data according to Eqn. (4.8). In this experiment, however, 10 m-spacing is not a limiting factor for resolving the 150 m thick ice layer.

This first synthetic study has shown the impact that data conditioning steps and acquisition parameters have on estimating DCs, including the differential effect on Z-compared to R-component data. In these noise-free simulations, Z-component data are sufficient for MASW analysis; however, R-component data may offer more value than just boosting the data signal-to-noise ratio (SNR). We explore this below using data from more complex synthetic and field experiments.

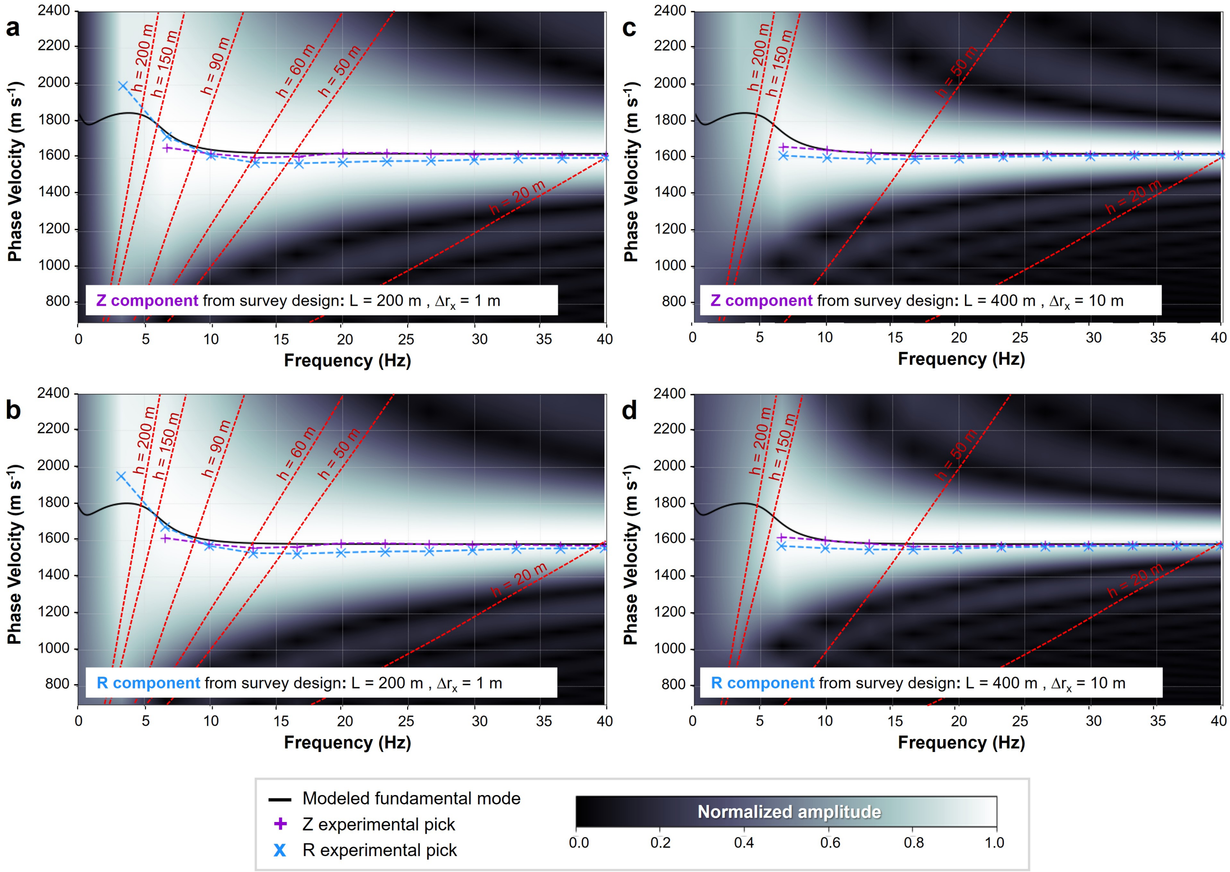

Figure 4.11 Z- and R-component dispersion panels from the two experiments described in Figure 4.10. We conditioned data by removing the direct P-wave arrival and windowing to capture the full Rayleigh-wave signal at all offsets. (a) Z- and (b) R-component dispersion panels for shorter aperture ($L = 190$ m) experiment with dense ($\Delta r_x = 1$ m) receiver sampling; The resulting dispersion panels are lower resolution compared to the those generated from the ideal acquisition (Figure 4.9). (c) Z- and (d) R-component dispersion panels for longer aperture experiment ($L = 390$ m) with sparse ($\Delta r_x = 10$ m) receiver sampling showing comparably lower data distortion than for the limited aperture case.

4.5.3 Study 3: DC Sensitivity to Shallow Complexity

We now seek to understand the value of well-conditioned MC data to characterizing more complex glacial environments such as a firn-aquifer system. Killingbeck *et al.* (2020) motivates the importance of these aquifers for evaluating water-storage capacity and understanding meltwater dynamics at the Helheim Glacier, Greenland. Using 1-C geophone data and a multi-modal Bayesian inversion approach constrained by radar and borehole measurements, they mapped the spatial and depth variations in V_s from which the aquifer thickness was interpreted. We use their results to build a four-layer elastic model for evaluating the effectiveness of an MC-MASW approach to velocity modeling.

Our “base” model (Figure 4.12a) consists of a 20 m firn layer overlying a 10 m-thick aquifer. For consistency with the previous investigation, we add bedrock at 150 m (much shallower than the true bed of Helheim Glacier). We also examine two model variations: (1) a “deep aquifer” model—an aquifer at 40 m with a thicker overlying firn layer (Figure 4.12b); and (2) a “thick aquifer” model—an aquifer twice as thick as the “base” model but with the top remaining at 20 m (Figure 4.12c).

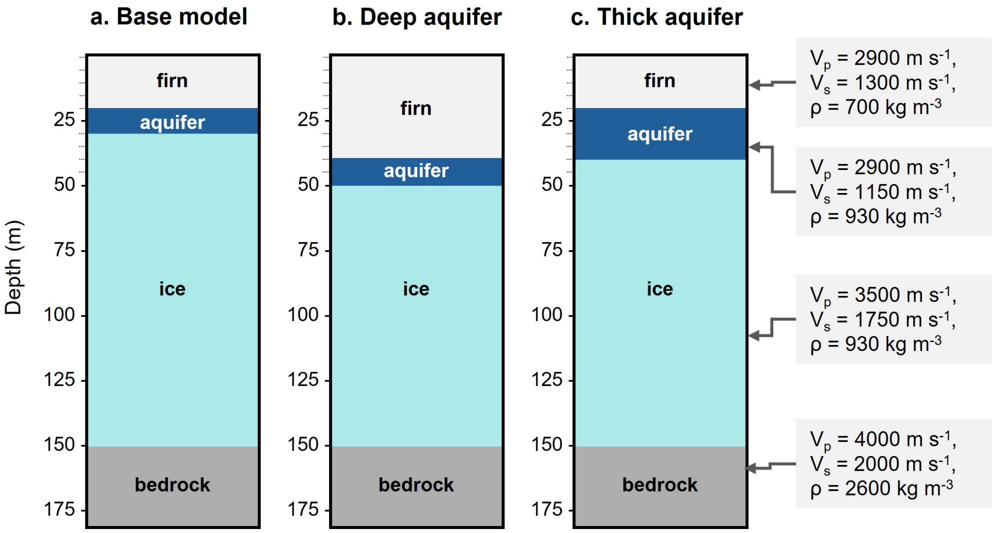

Figure 4.12 Firn-aquifer model variations for synthetic data generation. (a) “Base” model derived from Helheim Glacier seismic inversion results (Killingbeck *et al.*, 2020) with a 10 m thick aquifer overlain by 20 m of firn and a bedrock half-space imposed at 150 m depth. (b) “Deep Aquifer” model similar to (a) but with the firn layer extended to a depth of 40 m. (c) “Thick Aquifer” model similar to (a) but with the aquifer thickened to 20 m.

We simulated elastic shot-gather data using idealistic acquisition parameters: $\Delta r_x = 1$ m spacing and $L = 300$ m aperture. We condition the synthetic data by removing the near-offset traces (from 0 to10 m and effectively reducing L to 290 m) and direct arrivals and windowing appropriately to capture untruncated Rayleigh wave arrivals on each trace (Figure 4.13).

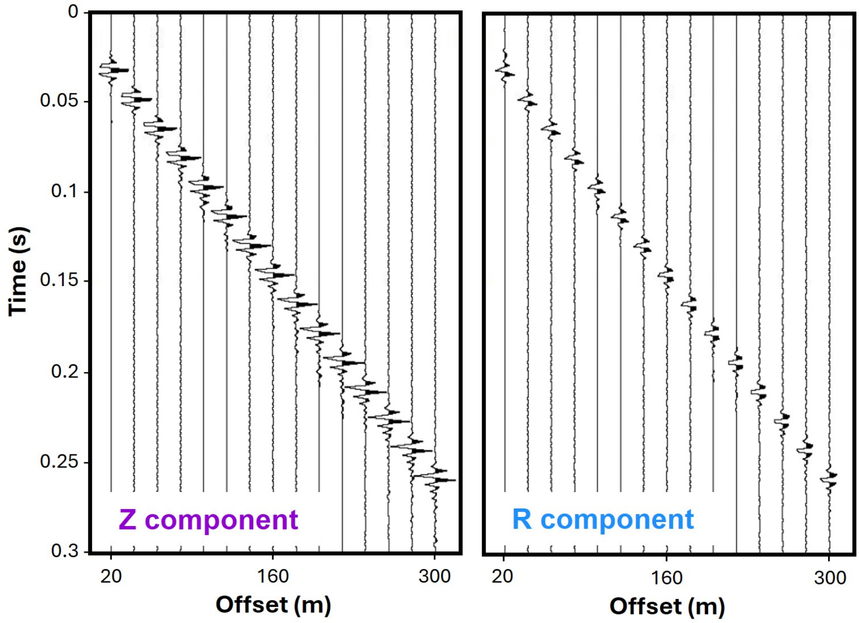

Figure 4.13 Conditioned Z- and R-component shot gathers for the “base” firn-aquifer model described in Figure 4.12a. Every 20th trace is plotted for offsets from 20 m to 300 m.

Figure 4.14 first compares the Z- and R-component numerical solutions for the fundamental mode of the three firn-aquifer models (Figure 4.14a), with separate comparisons of the experimental picks to the numerical solutions for each model (Figure 4.14b–d). The numerical solutions for the three models are quite similar and in particular, discerning between the deep (blue) and thick (pink) models would require high-resolution DPs and accurate experimental picks within the $8 - 20$ Hz range. Within this range, however, both the Z- and R-component experimental DCs (+ and x, respectively, on Figure 4.14b–d) significantly deviate from the numerical solution.

For all models, the Z-component DCs reveal a stronger gradient (indicative of dispersion) than the R-component DCs. To understand this phenomena, we examine the sensitivity kernels at different frequencies (Figure 4.15). We note that the U_z sensitivities (Figure 4.15a–g) are generally similar for all three models: for frequencies above 10 Hz, U_z is most sensitive (highest eigenfunction amplitude) to the shallow firn layer and under 10 Hz, U_z is more sensitive to deeper structure. The largest difference between models for

U_z are observed within $10 - 17$ Hz range. For all models, the strongest negative U_x sensitivities are at the surface and generally, the depths at which U_x sensitivity is maximum and positive are deeper than the corresponding U_z sensitivity. Additionally, the U_x kernels (Figure 4.15h–n) exhibit two characteristic signatures not observed on the U_z kernels: (1) 9.95 Hz and 13.27 Hz sensitivities show h_r changes per model at different frequencies; and (2) for all frequencies, there are inflection points in sensitivity that occur at depths (consistently at all frequencies) that correlate to the base of the aquifer (dotted lines).

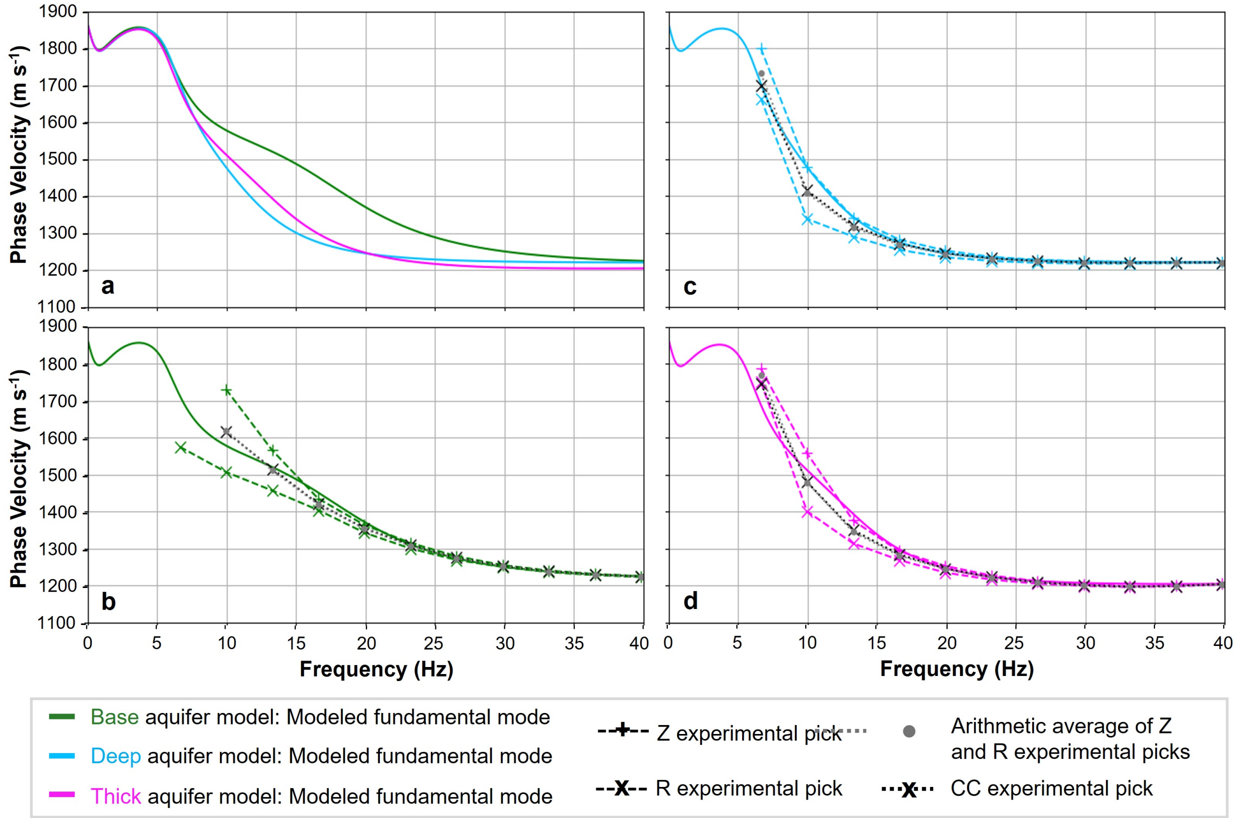

Figure 4.14 Numerical solutions and experimental DCs of the fundamental mode associated with the three models described in Figure 4.12. (a) Numerical solution of the fundamental DC for base (green), deep aquifer (cyan), and thick aquifer (magenta) models. Z- and R-component DCs for the (b) base, (c) deep aquifer, and (d) thick aquifer models, with experimental picks for Z- (plus symbols) and R-component (cross symbols), the arithmetic average of Z- and R-component phase velocity (grey circles), and the complex component (CC) of Z- and R- components (black cross symbols). Between 8 and 20 Hz, the variability of DCs for the three models suggests that accurate picks in this frequency band are important for mitigating the non-uniqueness of dispersion analysis and inversion.

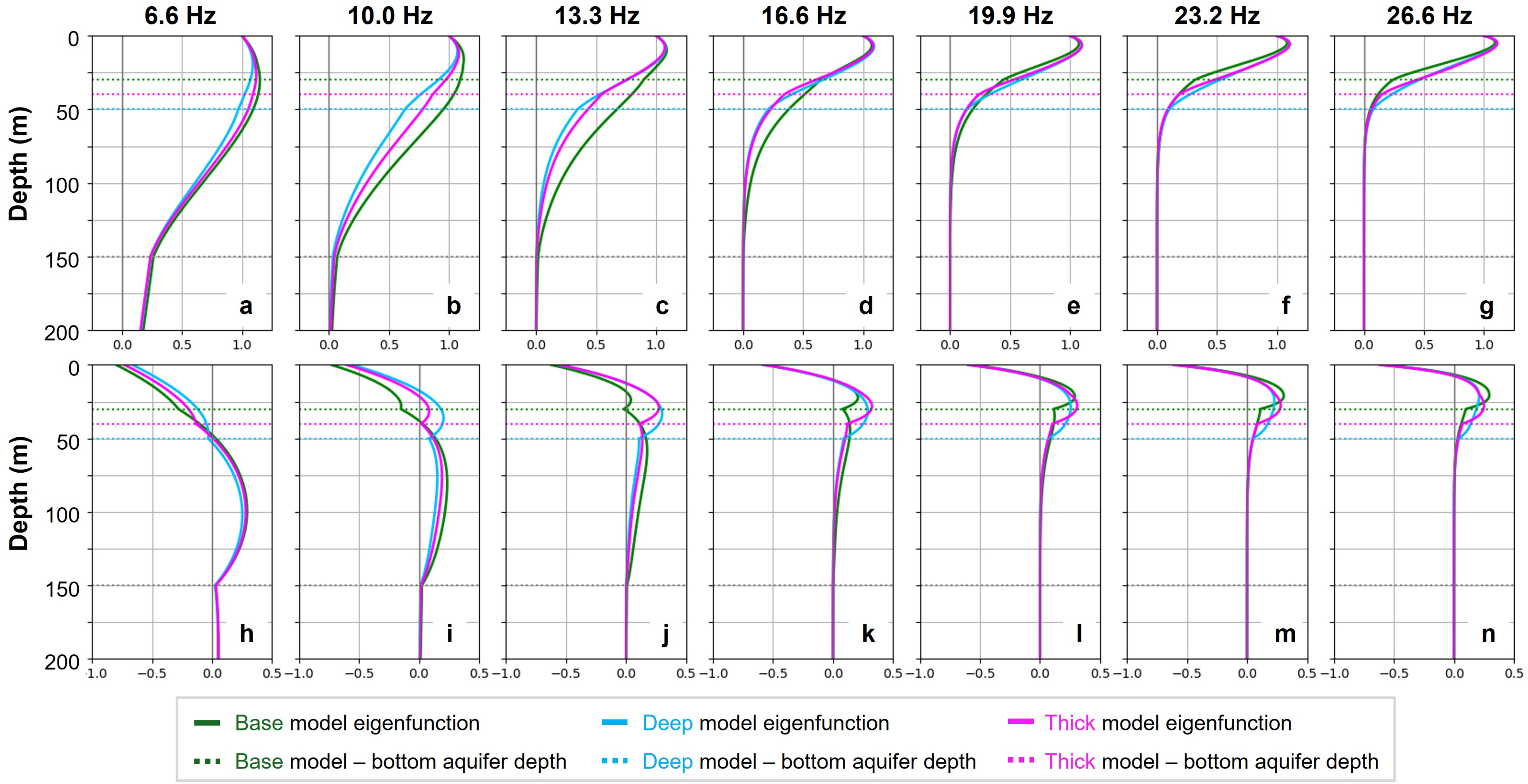

Figure 4.15 Depth sensitivity kernels for discrete frequencies of the three aquifer-firn experiments described in Figure 4.12. (a–g) U_z components. (h–n) U_x components. Depths of the bottom of aquifer are color coded for each model, and the depth of the ice-bedrock interface is shown with a dotted gray line at 150 m. The unique sensitivities of the U_x curves for each model motivate an opportunity for improving MASW inversion accuracy through use of MC data.

4.5.3.1 Combining MC data

To exploit the unique depth sensitivities of both U_z and U_x, we use a complex system to represent and combine the orthogonal components in the shot-gather domain. We calculate this complex component (CC) as

$$CC(d,t) = Z(d,t) + iR(d,t)\ . \tag{4.10}$$

Experimental picks for the CC component are plotted on Figure 4.14 for each respective firn model (black dotted lines with black crosses). Compared to the individual Z- and R-component picks, the CC picks very closely track the numerical solutions for all models. We also calculate an arithmetic mean of the Z and R experimental picks (gray dotted lines with gray dots) where there is no implicit account for orthogonality and each component is equally weighted. For these idealistic experiments the CC picks and arithmetic averages are almost identical with the exception of the 6 Hz pick (near the low frequency acquisition limit) on the "deep-" and "thick-aquifer" experiments where the CC picks are slightly more accurate.

We observed that the Z- and R-component DCs differ due to their variable depth sensitivities. For all the firn-aquifer models examined, the R-component DC picks tend to be lower than those from the Z component and an arithmetic average offered a more representative solution. Although not a concern in these ideal synthetic experiments, where DPs are poor resolution, this averaging may additionally help mitigate SNR-related picking errors. Moreover, our proposed CC summation method, which honors the orthogonal nature of the components, may outperform the arithmetic averaging as it potentially better exploits the unique depth sensitivities inherent to each displacement component. We evaluate this hypothesis and apply other insights derived from the synthetic studies to a MC field dataset acquired on the Saskatchewan Glacier in the Canadian Rocky Mountains.

4.6 Results: Field Experiment on Saskatchewan Glacier

This section evaluates the effectiveness of MC dispersion analysis under real-world conditions using a dataset acquired at the Saskatchewan Glacier, Canadian Rocky Mountain Region (Figure 4.16a). We assess data conditioning workflows and techniques for integrating Z- and R-component data amid the complexities of field seismic surveys, including constraints on array length, limited receiver coverage, and imperfect data quality.

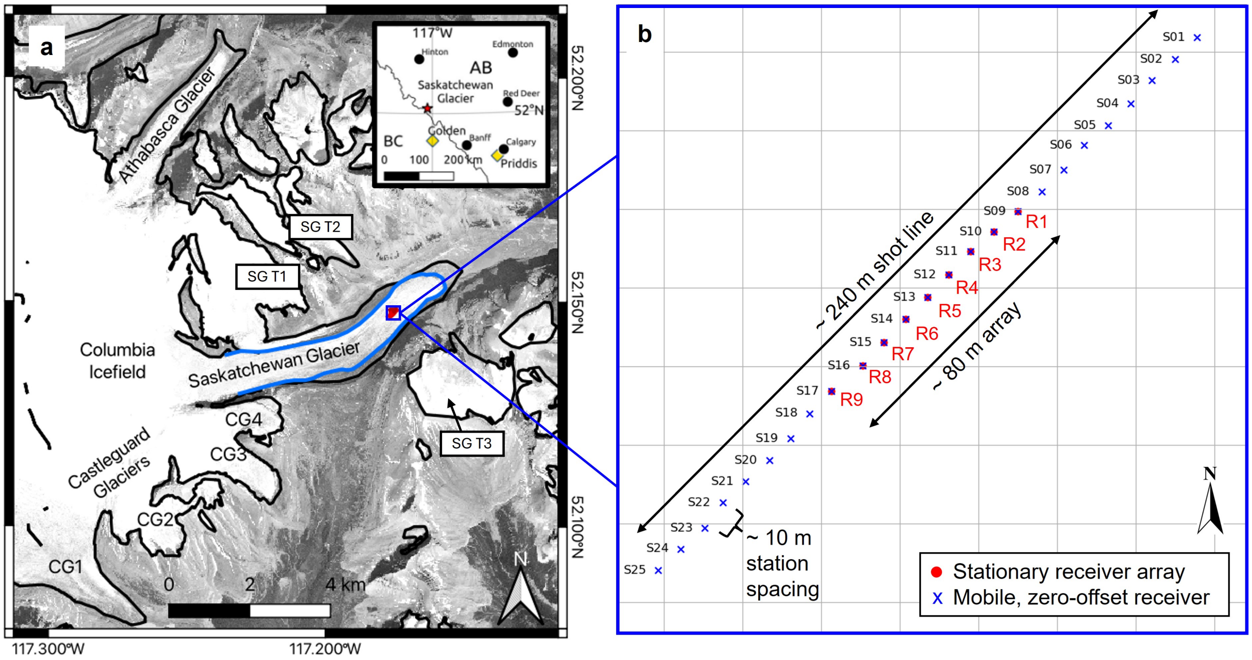

Figure 4.16 (a) Saskatchewan Glacier location in the Canadian Rocky Mountains, Canada (see inset map). Basemap imagery: Orthorectified 4-band PlanetScope scene accessed via Planet.com (b) Geometry of the active-source seismic experiment conducted in the ablation zone involving a stationary array of nine 3-C geophones (R1-R9) linearly spaced at 10 m to form an array of aperture $L = 80$ m. Source station locations S01-S25, also spaced 10 m apart, are shown as blue Xs.

4.6.1 Survey Details

In August 2019, Stevens *et al.* (2023) acquired a 2-D active-seismic survey on the Saskatchewan Glacier (Figure 4.16a) to supplement other geophysical investigations focused on basal ice dynamics. The acquisition used nine 3-C geophones (R1 to R9) spaced

$\Delta r_x = 10$ m apart forming a linear array of $L = 80$ m aperture oriented along the glacier's centerline. A sledgehammer impacting a metal plate served as a seismic energy source at 25 station locations (S01 to S25) distributed over a 240 m span centered on the array with a maximum two-sided offset of $d_{max} = 160$ m. A tenth 3-C geophone was moved to every source station to record the excitation time of each shot. These acquisition geometry details are plotted in Figure 4.16b.

4.6.2 Data Conditioning

In Figure 4.17 we show an example of raw Z- and R-component shot gathers from station S02. We note the presence of a noisy zero-offset trace and the absence of traces at receivers R2 and R9 for both gathers. These data issues reflect the inherent challenges in field experiments arising due to equipment malfunction. Without managing data errors appropriately, the Z- and R-component DPs are inaccurately complex and noisy as demonstrated in Figure 4.18a–b which were generated after removing the zero-offset trace.

In Figure 4.18c–d, e–f, and g–h, we muted the direct wave and inserted zero traces at missing trace locations prior to constructing the DPs for shots at stations S02, S05, and S09, respectively. This substantially improved the quality of the DPs (compare S02 results in Figure 4.18c–d with Figure 4.17a–b); however, the infilled zero traces imposed a beat-like signature on the DPs.A more optimal conditioning approach would be to infill the missing traces with representative non-zero data. This can be achieved through interpolation between traces; however, a simpler approach is to use supergather processing (Hesthammer & Løkkebø, 1997), which provides additional benefits to the dispersion analysis, as described next.

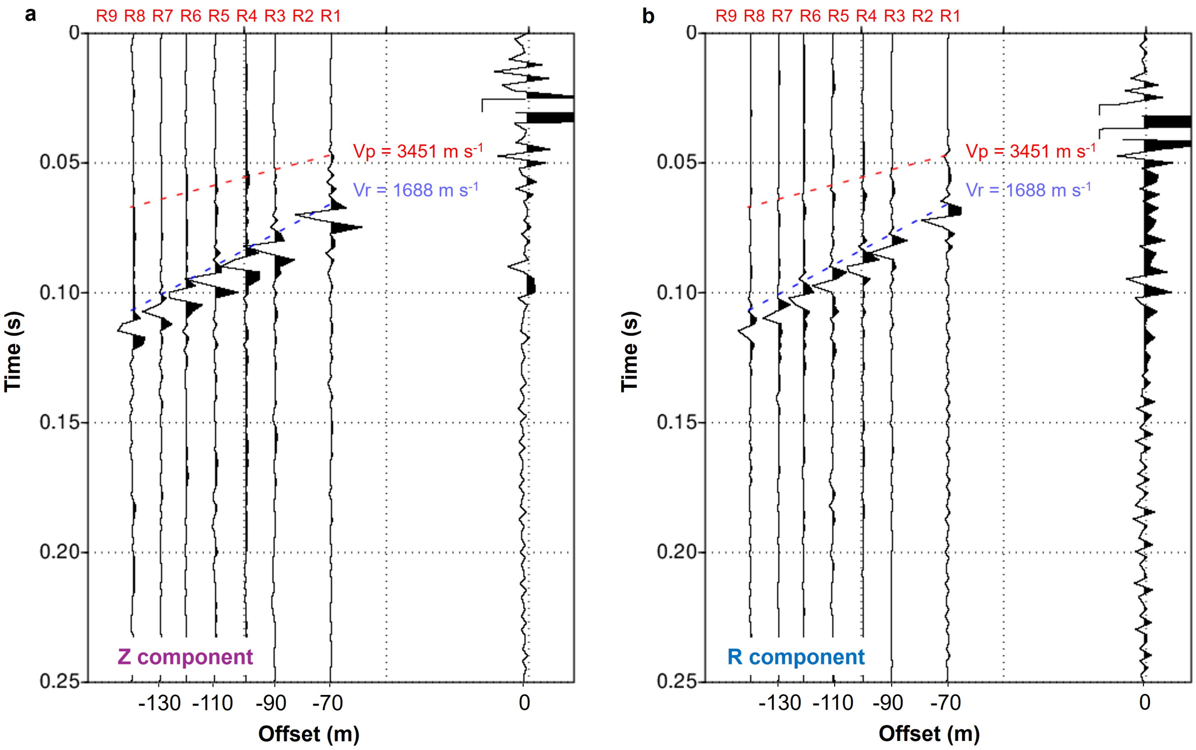

Figure 4.17 (a) Raw Z- and (b) R-component shot-gather data for station S02. The zero-offset trace recorded by the mobile geophone is used to window the continuously recorded data on geophones R1-R9 into shot gathers. V_p and V_r moveout velocities calculated by Stevens *et al.* (2023) are plotted. Note the missing traces at R2 and R9. Additionally, direct P-wave arrival is weaker on the Z- versus the R-component because of the predominantly horizontal particle motion. Strong Rayleigh wave energy is recorded on both components.

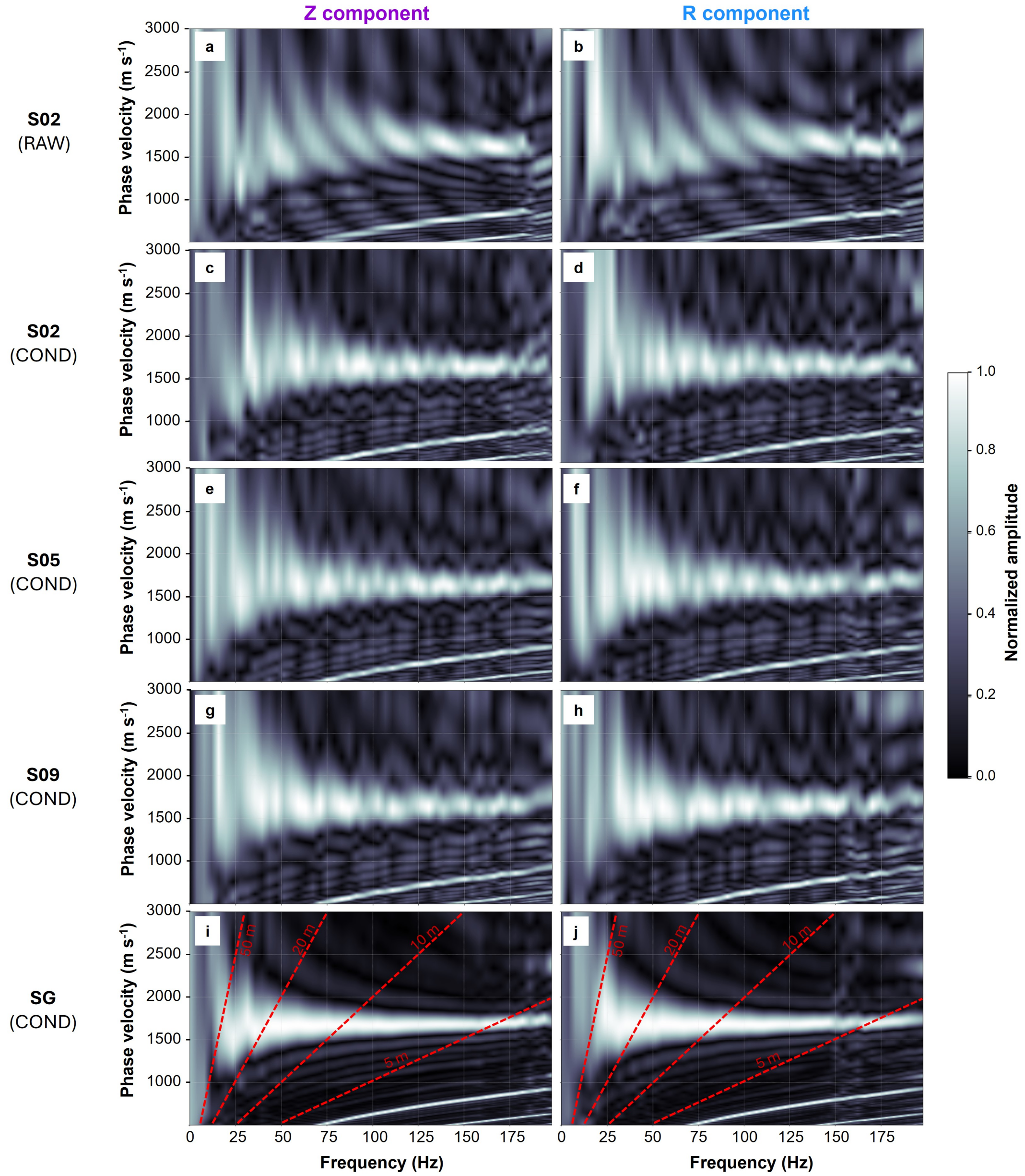

Figure 4.18 Raw (a) Z- and (b) R-component DPs for the S02 shot gathers shown in Figure 4.17. Conditioned (c) Z- and (d) R-component DPs corresponding to (a) and (b) after removing the zero-offset traces, muting the direct wave, and infilling missing traces with a zeroed trace. Conditioned (e) Z- and (f) R-component DPs at station S05 and (g) Z- and (h) R-component for station S09. Conditioned (i) Z- and (j) R-component supergather DPs combining S02, S05, and S09 shot-gather data. The conditioned individual shots produce consistent DCs although a beat-like signature is imposed as a result of the zeroed infill trace and no interpolation. The supergather DC infills missing offsets and extends the effective array aperture producing higher-resolution DPs.

4.6.3 Supergather Processing

Supergather processing provides a means to infill missing offset traces (Hesthammer & Løkkebø, 1997) but an additional benefit for our application is that it extends effective aperture thereby improving low-frequency content in the dispersion data. To build a supergather from several shots, each gather is first windowed to align traces of the same offsets by applying time-shifts as necessary to each shot gather. The time-shifted gathers stacked by averaging traces at similar offsets. Figure 4.19 illustrates the supergather approach where the Z-component gathers at stations S02, S05, and S09 are time-aligned (Figure 4.19a) and then stacked (Figure 4.19b). The resulting effective supergather aperture is $L = 130$ m (i.e., 50 m longer than the stationary receiver array) with no missing trace information. Figure 4.18i and j show the Z- and R-component DPs, respectively, constructed from the S02, S05, and S09 supergathers. The resolution of the resulting DPs is substantially improved compared to the single-gather DPs (Figure 4.18c–h) leading to higher confidence experimental picks.

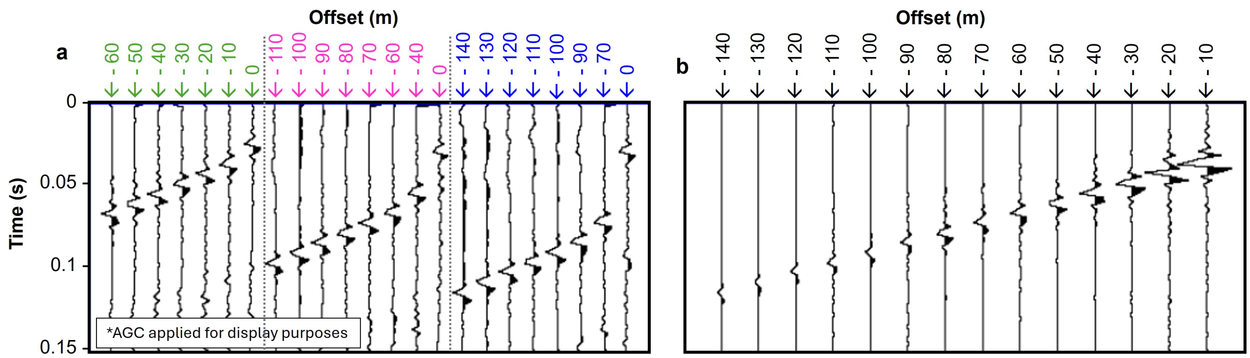

Figure 4.19 (a) Time-aligned Z-component shot gathers for stations S02 (blue), S05 (pink), and S09 (green) with differing offset ranges (x-axis labels). (b) Supergather produced from stacking the three shots in (a) based on similar offsets thus increasing the effective array aperture to $L = 130$ m and infilling missing offset traces without interpolation.

4.6.4 Dispersion Analysis

We generate the DP from the CC summation of the Z- and R-component supergathers (Figure 4.20a) and compare the experimental DC picks of the Z, R, and CC components with the arithmetic average of the Z- and R-component data (Figure 4.20b). The largest differences are observed sub-50 Hz. Generally, the combination methods (CC and average) result in smoother DCs versus the single-component picks.

The average and CC picks are similar between $40 - 150$ Hz and the differences observed outside this range could result from higher DC uncertainty due to poorer DP resolution. Following observations from the four-layer synthetic study, near the limiting acquisition frequencies we might expect the CC picks to be more reliable. This is possibly a rationale for the smoother CC DC trend between $25 - 40$ Hz versus that of the average.

An alternate method for reducing experimental pick uncertainties is presented by Ólafsdóttir *et al.* (2018a) and included in the *MASWaves* software. This approach calculates a mean DC from individual DP picks by averaging over user-defined, logarithmically spaced wavelength bins.

Using the conditioned S02, S05, and S09 panels presented in Figure 4.18, we perform this weighted-mean DC approach and compare the experimental picks to those of the arithmetic-mean- and CC-supergather DPs (Figure 4.20b). The bandwidths over which experimental picks can be reliably identified are similar between all three approaches. The *MASWaves* weighted-mean DC picks under 50 Hz fluctuate substantially, suggesting low confidence in the results. Above 50 Hz, these experimental DCs are flat with lower V_r values than those of the arithmetic average or CC component. We note that the weighted-mean DC picks in this range are highly sensitive to the selected bin window.

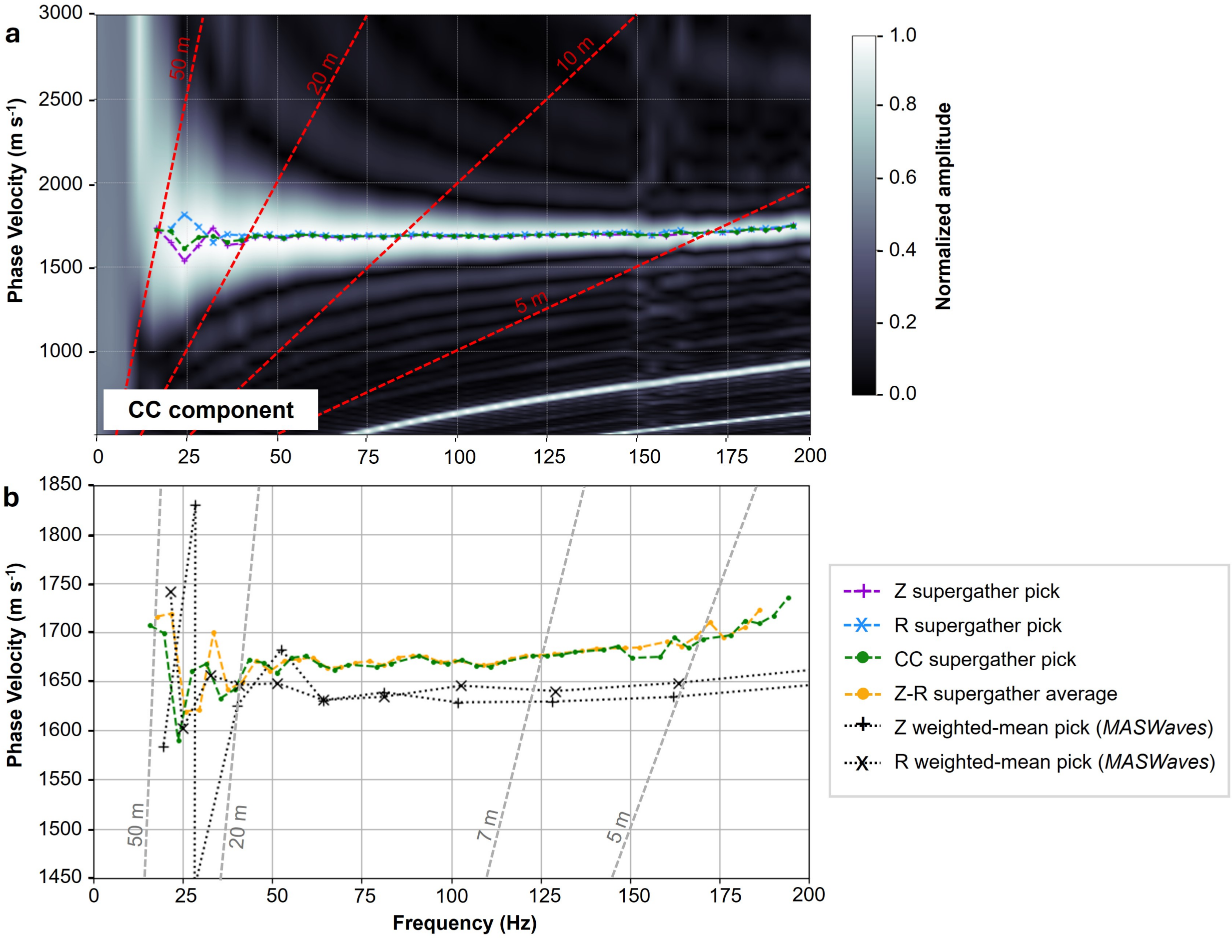

Figure 4.20 (a) Dispersion panel derived from CC supergather from shots 02, 05 and 09. (b) Comparison of experimental dispersion curve picks from CC supergather (dashed black line) and individual Z- and R-components (+ and x symbols, respectively), the arithmetic mean (black dots), and the weighted-mean picks calculated from the internal *MASWaves* algorithm (dark and light purple for Z and R components, respectively). All picks were made on the respective DC panels (Figure 4.18) using the standard picking algorithm in the *MASWaves* software. There is little evidence of dispersion and the experimental picks suggest an average $V_r = 1670$ m s^{-1} between 40 and 165 Hz.

Qualitative Interpretation

We first consider the resolution limitations of the survey, noting that the empirical estimates presented in the Theory section have been validated for typical ice velocities. For an array length of $L = 130$ m, the maximum resolvable depth is approximately 43–65 m (Eqn. 4.9), which is insufficient for detecting a bedrock interface expected at depths greater than 100 m (Stevens *et al.*, 2023). This depth range aligns with the 20 Hz low-frequency limit of the DCs presented in Figure 4.18b. Similarly, the minimum resolvable depth, estimated at 5 m for a receiver spacing of 10 m (Eqn. 4.8), is consistent with the inability to make reliable picks above $\sim$ 165 Hz. This is evidenced by the observable increase in noise on the DP (Figure 4.18a) and the apparent increase in V_r with frequency on the DC which are both likely due to aliasing.

High-confidence picks between 40 Hz and 165 Hz on the CC supergather yield a mean V_r value of 1670 ± 10 m s^{-1}, suggesting that the ice column is potentially vertically homogeneous between 5 m to 20 m. This estimate is fairly similar to the linear moveout velocity of 1690 m s^{-1} reported by Stevens *et al.* (2023). Notably, this interpretation of apparent homogeneity is drawn from a single supergather using only a small subset of shots from a 60 m active-source seismic spread. In cases where subsurface conditions are unknown, qualitative DP analyses can quickly indicate whether a uniform ice velocity assumption is reasonable (based on consistency with empirical velocity estimates or linear moveout) and whether inversion is necessary to resolve vertical layering inferred from observed V_r–f gradients in the panel.

Inversion is not only essential for mapping phase-velocity trends into V_s–depth profiles, but it may also help constrain reasonable solutions in frequency ranges where dispersion picks are uncertain and qualitative analysis is limited. In our case, the 20 Hz to 40 Hz band is sensitive to depths of approximately 20 m to 50 m exhibits more variable picks, with a mean phase velocity of 1650 ± 30 m s^{-1}. This could indicate a slight decrease in velocity with depth, although the trend may also reflect noise or errors in the pick estimates. A formal inversion may help determine whether these variations are attributable to a plausible subsurface model or whether they are simply artifacts of lower signal-to-noise conditions at these frequencies.

4.7 Discussion

The feasibility studies presented herein highlight the subtle differences in DCs arising from different preprocessing methods and subsurface layer complexity. These results underscore the inherent non-uniqueness of dispersion analysis and inversion, a challenge well-documented in prior studies. For example, de Lucena & Taioli (2014) conducted a detailed synthetic investigation into dispersion curve sensitivities, emphasizing the importance of inversion parametrization and initial model choice. With a focus on active-seismic glacial experiments, our study emphasizes improving the forward problem through acquisition strategies, appropriate data conditioning, and leveraging MC datasets.

4.7.1 Acquisition Design Recommendations

We demonstrate that prioritizing array aperture over receiver spacing is judicious for Rayleigh-wave dispersion analysis, enhancing both the depth of investigation and DP resolution. For instance, with a setup of ten geophones targeting a firn aquifer with a top depth of 40 m, setting the receiver spacing to half the shallowest depth of investigation (20 m in this case) will suffice and the receiver array can be as long as 180 m. To further optimize offset coverage, a denser shot spacing can be employed. For example, at 20 m receiver spacing, initiating shots every 10 m enables acquisition at offsets of 10 m intervals.

4.7.2 Supergathers and Data Conditioning

Supergathers aggregate Rayleigh-wave data from multiple shot locations to enhance signal quality, infill missing traces, and extend effective array aperture and thereby the depth of investigation. Although alternative methods such as the weighted-mean calculation presented by Ólafsdóttir *et al.* (2018a) offer results with frequency bandwidth similar to the supergather approach, the DC picks exhibit higher uncertainty, greater variance, and an increased dependence on the particular window selected for data binning and averaging. Beyond increasing SNR and improving picking confidence, supergathers inherently infill missing offsets and reduce (or obviate) the need for data interpolation.

A common drawback across all methods is that, in areas with lateral heterogeneity or structural complexity, spatial averaging of data points can obscure subtle subsurface features and reduce the accuracy of derived models. As such, the choice of processing strategy should be guided by the specific scientific objectives and the expected scale of variability. In surface wave analysis, DPs inherently average over the array aperture, making the trace mixing introduced by supergathers generally acceptable. However, a specific caveat with the supergather approach is that any misalignment of zero-offset traces can mask fine dispersive characteristics, underscoring the importance of applying appropriate timing corrections.

4.7.3 Horizontal-Component Contributions

The Z- and R-component data acquire orthogonal particle motions of Rayleigh waves. By leveraging both, the complete elliptical particle motion of Rayleigh waves can be reconstructed. At a fundamental level, we have identified two key mechanisms through which the R-component Rayleigh-wave energy enhances dispersion analysis. First, the R component provides an additional dataset for capturing dispersion at the same locations as the Z component, thereby increasing the accuracy of experimental picks by increasing the overall data volume. Although phase shifts between the Z- and R-component data complicate direct stacking, averaging the individual experimental picks from both components can yield more reliable results. This approach mitigates the impact of erroneous picks that may arise from poor SNR, improving the robustness of dispersion analysis. Second, R-component data exhibit complementary sensitivity to subsurface layering, offering insights into layered media indiscernible from Z-component data alone. We have observed that the depth at which the sense of elliptical particle motion reverse varies with different layer complexity and, at low frequencies, there are potentially multiple depths at which the sense of motion reverses direction. In addition, where strong V_s variations exist (e.g., at the ice-bedrock or firn-aquifer-ice interfaces), we observe inflection points on the U_x-depth sensitivity kernel that indicate localized narrowing or widening of the particle motion ellipticity. Moreover, these are sharpest at the frequencies exhibiting the strongest Rayleigh-wave dispersion effects (Lay & Wallace, 1995) and are thus functions of the depth and $V_s(z)$ contrast of subsurface velocity layering.

These sensitivities of the horizontal Rayleigh-wave displacement underscore the critical role of the R component in advancing the accuracy of MASW inversion using active-source seismic investigations. Finger & Löer (2024) noted the correlation between the extrema of ellipticity to sudden velocity changes and demonstrated its utility in $V_s(z)$ profiling using ambient seismic data. This motivates the integration of ellipticity information in active-seismic MASW to further improve the modeling of near-surface V_s structure.

4.8 Conclusions

Our feasibility studies provide actionable insights for glaciologists, offering guidance on survey design and data conditioning to enhance data quality. We highlight the advantage of longer receiver arrays on the quality of dispersion curves and validate rule-of-thumb approximations for the minimum and maximum depths of investigation as well as the depth of elliptical rotation reversal in glacial regimes in comparison to those of shallow soil models and Poisson solids. Furthermore, we outline critical data conditioning steps for enhancing Rayleigh-wave dispersion analysis. Key procedures include removing the zero-offset trace and windowing shot gathers to avoid truncating the Rayleigh-wave arrivals on all traces. When using multi-component data, rotating data to radial-transverse coordinates and muting the direct wave also are important steps. Interpolating or infilling missing traces (often unavoidable in field experiments) is critical for generating accurate dispersion curves. Using field data from the Saskatchewan Glacier, we demonstrate how building supergathers (under reasonable assumptions of lateral homogeneity) can be effective for infilling missing traces while improving dispersion-panel (and therefore dispersion-curve) resolution by increasing the effective array aperture.

Using multi-layered firn-aquifer models, we demonstrate how MC geophone records can improve the detection of englacial structures. Averaging experimental picks from the radial and vertical components can mitigate errors associated with low signal-to-noise ratios. Our depth-sensitivity analysis, though, reveals that the horizontal displacement of elliptical particle motion contains complementary information not captured by the vertical component data alone. Integrating horizontal displacement data in an MC-MASW analysis potentially could help differentiate aquifer thickness and depth, beyond the ability of single vertical-component geophone analysis.

4.9 Data Availability

Synthetic glacial datasets and models are available on GitHub (https://github.com/samara-melody/MC-MASW), alongside relevant processing scripts. We refer the reader to Stevens *et al.* (2023) and their accompanied supplemental material for information regarding accessibility of the Saskatchewan Glacier field datasets.

4.10 Acknowledgments

The Mines Geophysics Department, Mines Glaciology Laboratory and Center for Wave Phenomena each supported the author's research through scholarship. The author gives special thanks to H. Verboncoeur and N. Punithan for insightful discussions and shared domain knowledge.

Analyses in this work were conducted using a range of open-source software packages. We acknowledge the efforts of the developers and contributors who advance accessible tools for scientific research. We used the software *MASWaves* (Ólafsdóttir *et al.*, 2018b) for dispersion curve forward modeling and analysis and *disba* for numerical modeling (Luu, 2021). We carried out seismic data processing using *ObsPy* (Beyreuther *et al.*, 2010) for field data in MiniSEED format and *Seismic Unix* for SEGY-formatted data (Stockwell Jr, 1999). Additional numerical and symbolic computations, as well as data visualization, were supported by Python libraries including *NumPy* (Harris *et al.*, 2020), *SymPy* (Meurer *et al.*, 2017), *pandas* (McKinney, 2010) and *Matplotlib* (Hunter, 2007).

CHAPTER 5

IMPROVING SHEAR-WAVE VELOCITY MODELING USING MULTI-COMPONENT DISPERSION DATA FROM LIMITED-COVERAGE GLACIAL EXPERIMENTS

S. Garvey[1], J. Shragge[1], M. Siegfried[1]

5.1 Abstract

The quality and utility of active-source seismic data in glaciological field settings are often compromised by suboptimal acquisition conditions, commonly stemming from factors such as weight-limited expeditions and difficult terrain. While many seismic velocity modeling approaches are affected by these data quality and/or density limitations, multi-channel analysis of (Rayleigh) surface-wave (MASW) dispersion data remains among the most practical under these constraints. Still, sparse and short 2-D glacial seismic experiments using single, often vertical-component (SC) geophones, limit the reliability of dispersion picks and reduce the accuracy of inverted S-wave velocity (V_s) models. Given the elliptical particle motion of Rayleigh waves, we show that incorporating multicomponent (MC) data from three-component geophones into MASW provides a practical and effective improvement for seismic characterization in these settings. In synthetic experiments, MC-MASW resolves distinct V_s–depth structures for firn–aquifer models that appear indistinguishable using SC data alone, by leveraging the complementary depth sensitivities of the vertical and horizontal components of Rayleigh wave motion. Field results further demonstrate that MC-based inversions applied to both individual shot gathers and supergathers yield lower misfits and more stable V_s solutions than SC-MASW, even in relatively uniform glacier ice, due to enhanced signal quality. Overall, adopting an MC-MASW workflow enables more reliable V_s estimation in glaciological experiments without significantly increasing acquisition effort or cost.

---

[1] Department of Geophysics, Colorado School of Mines, Golden, CO 80401, U.S.A.

5.2 Introduction

Estimating ice thickness, internal structure, and subglacial topography is fundamental to understanding the flow dynamics of glacial systems (e.g., Sharp, 1954). These properties are typically inferred from geophysical surveys using ice-penetrating radar and/or seismic methods. Although radar provides high-resolution imaging of shallow structural features, seismic data complement these analyses by resolving mechanical rather than dielectric contrasts (such as in firn–aquifer systems that are often unresolvable with radar alone) and in some instances, by increasing the depth of investigation (e.g., Booth *et al.*, 2013; Brisbourne *et al.*, 2019; Godio & Rege, 2015; King *et al.*, 2007; Navarro *et al.*, 2005).

Seismic methods are sensitive to contrasts in elastic impedance, which depend on variations in compressional (V_p) and shear (V_s) wave velocities, as well as density (ρ). Active-source seismic experiments, which use controlled sources generating energy with frequencies predominantly between 5 and 100 Hz (Aster & Winberry, 2017), are well-suited for resolving englacial layering or, at minimum, estimating bulk ice thickness. Some passive experiments (e.g., Chaput *et al.*, 2022) can achieve similar results, though they are more commonly applied to detect ice movement and glacial earthquakes at lower frequencies (Podolskiy & Walter, 2016). Active-source experiments are often conducted in support of broader glacier dynamics studies, and detailed discussion of seismic workflows is relatively uncommon. Only a few specialized studies explicitly address methodological design and strategies for improving the use of active-source methods in glacial settings (e.g., Agnew *et al.*, 2023; Kuehn *et al.*, 2024; Tsuji *et al.*, 2012; Veitch *et al.*, 2021; Zechmann *et al.*, 2018). In most of these studies, as well as in others where active-source surveys are used in a supporting role, seismic velocities are modeled using first-arrival travel-time tomography, where direct or refracted P-wave arrivals are used to estimate a V_p model. This estimate is then often combined with empirical or assumed relationships to infer V_s and ρ.

Targeting direct P-wave arrivals is the most straightforward approach, where a near-surface V_p is estimated by measuring the linear moveout of the wave as it travels along the surface (e.g., Yilmaz, 2001). This method is exemplified by Stevens *et al.* (2023) at the Saskatchewan Glacier in the Canadian Rocky Mountains. However, because the direct P wave is most sensitive to the shallowest layer, the resulting V_p estimate primarily depends on near-surface properties and provides limited insight into deeper subsurface structure. This approach is best suited to settings where limited vertical heterogeneity is expected.

Alternatively, refraction tomography analyzes head waves traveling along refracting interfaces within the ice column (Yilmaz, 2001), enabling V_p-depth profiling that reveals layering associated with changes in the elastic properties of the ice (e.g., Agnew *et al.*, 2023; Church *et al.*, 2019; Kuehn *et al.*, 2024). Refraction techniques, though, are insensitive to "hidden" layers that are too thin to produce distinct first arrivals, and to "blind" layers in which low-velocity materials do not generate refracted waves (Kearey *et al.*, 2013). In glaciated environments, these limitations become particularly important in the context of firn aquifers (with V_s values lower than overlying firn or underlying ice)–features whose seismic signatures can be subtle and difficult to isolate.

The accuracy and depth of investigation of refraction surveys additionally depend strongly on survey aperture, source-receiver spacing, and data quality (Kearey *et al.*, 2013). It is generally recommended that the array length be at least two to three times the target depth of investigation (Yilmaz, 2001) as this method relies on waves traveling along deeper interfaces before returning to the surface. In glacial field settings, however, logistical constraints such as weight-limited expeditions and poor surface navigability often restrict the scale and design of seismic arrays (Aster & Winberry, 2017). Achieving a sufficiently long array with a limited number of receivers requires sparse spacing, which increases vulnerability to noise and reduces the visibility of thin layers. Conversely, denser arrays improve signal-to-noise ratios and vertical resolution but can limit the achievable depth of investigation, sometimes falling below the critical distance needed to observe refracted waves. These practical trade-offs complicate the design of glacial refraction experiments aimed at resolving both shallow and deep structures.

An alternative approach to velocity-depth profiling is to exploit the dispersive behavior of (Rayleigh) surface waves in response to subsurface layering. In contrast to the other methods discussed, the corresponding objective is to directly invert for V_s depth profiles and estimate V_p indirectly through empirical relationships or, if possible, via complementary methods within the same acquisition design. The typical experimental setup resembles that of a refraction survey, using an array of multiple usually single-component (SC) receivers that measure particle motion along a single orientation. Traditionally, these are vertical-component sensors, although a horizontal-component experiment would also be considered SC if only one directional component were recorded.

One methodology that is effectively applied in these seismic survey scenarios is known as multichannel analysis of surface waves (MASW) (Park *et al.*, 1999) and offers two key advantages in glaciological settings over refraction surveys: (1) Rayleigh waves can be observed at short offsets (though longer offsets benefit deeper investigations); and (2) they are sensitive to thin layers and low-velocity zones such as water-bearing strata (Foti *et al.*, 2018). The main disadvantage is the limited depth of investigation compared to refraction surveys because depth penetration is primarily controlled by the low-frequency limit of the data, which itself depends on survey aperture, data quality, and frequency spectrum of source energy. Although SC-MASW has been applied in some glacial studies (Killingbeck *et al.*, 2018; Kuehn *et al.*, 2024; Tsuji *et al.*, 2012), its use remains relatively limited, perhaps due to perceived data quality challenges and the simplicity of V_p modeling approaches, from which V_s can be inferred using empirical relationships.

Accurate V_s-depth modeling using surface-wave dispersion data depends on reliably extracting the Rayleigh-wave phase velocity-frequency trend (i.e., the dispersion curve, DC) from the seismic data and applying an inversion method that appropriately constrains the problem without oversimplifying the solution space. Chapter 4 addressed the challenge of DC extraction by showing that dispersion picks can be improved by combining well-conditioned SC shot gathers (the vertical Z and inline horizontal R components) using a complex component (CC) summation approach. This CC-component produced higher-resolution dispersion panels (DPs), from which DCs are more reliably extracted. In Chapter 4, we also identified two scenarios where these improvements were particularly beneficial: (1) layered subsurface environments; and (2) generally noisy field data.

Here we examine whether the improvements in DC quality of each scenario lead to better MC-MASW inversion outcomes. To explore the layered subsurface case, we build on the investigation of the firn-aquifer systems in Chapter 4 motivated by the growing interest in these perennial water storage features over the past decade (e.g., The Firn Symposium Team, 2024). We use synthetic models (as we are unaware of publicly available 3-C data from known firn–aquifer regions) to evaluate whether MC-MASW improves both the V_s and interface depth estimates the firn–aquifer interface layer compared to traditional SC-MASW. To explore the noisy field data scenario, we use the 3-C dataset from the Saskatchewan Glacier, acquired by Stevens *et al.* (2023) and also analyzed in Chapter 4. We examine whether the CC-component DCs, derived from both single shot gathers and supergathers, stabilize and improve the misfits of the inverse solution.

We begin by reviewing the relevant theory for forward modeling and inversion of Rayleigh-wave dispersion data, building upon the foundation laid in Chapter 4. Next, we briefly describe and justify the inversion parameterization applied to both the synthetic and field studies. The synthetic study is presented first, starting with a description of the dataset followed by the results. The field study follows the same structure, with the dataset introduced before the results. Throughout the chapter, we reference supplemental studies in Section 5.11 that explore the sensitivity of inversion solutions to parameterization and constraints. These findings are integrated into our discussion, where we evaluate the effectiveness of the MC-MASW approach for velocity modeling of englacial structures using practical, sparse, short-aperture 2-D seismic surveys. Our conclusions provide practical guidance for designing, conducting, and interpreting MC surface-wave experiments aimed at V_s-depth profiling in glacial environments.

5.3 Theory

Rayleigh-wave dispersion occurs because different frequencies have different penetration depths; lower frequencies sample deeper structures, whereas higher frequencies are confined to shallower layers. As a result, the Rayleigh-wave phase velocity (V_r) varies with frequency (f) because of subsurface variations in V_s (and to lesser degrees in V_p and ρ). The resulting f–V_r trend represents the DC, which can be inverted to estimate a localized one-dimensional (1-D) V_s–depth profile.

This section outlines the three main components of MASW analysis and inversion: (1) the numerical prediction of the theoretical dispersion curve DC_{theo}; (2) the forward problem of constructing DPs from the seismic record and extracting experimental dispersion curves DC_{exp}; and (3) the inverse problem that uses both DC_{theo} and DC_{exp} to estimate V_s depth profiles.

5.3.1 Forward Problem: Theoretical Dispersion Curves

In layered media, Rayleigh waves propagate along the surface with a frequency-dependent phase velocity V_r, a dispersive property governed by the Rayleigh wave equation. Here, we provide a high-level overview of Rayleigh wave mechanics; see Buchen & Ben-Hador (1996) and Aki & Richards (2002) for more detailed derivations.

Following Equation 4 of Buchen & Ben-Hador (1996), Rayleigh-wave motion in a given layer j can be expressed using a displacement-stress vector $y_j(z)$ formulated as the product of four matrices (Figure 5.1): a rigidity matrix M_j; a velocity matrix P_j; an eigenfunction matrix E_j; and an amplitude vector a_j. Matrices M_j and P_j incorporate the elastic properties of the layer, whereas a_j represents the amplitudes of the four wave modes present at each interface (i.e., the up- and down-going P and SV waves). Matrix E_j controls how the wave motion varies with depth, z, within the layer and is uniquely determined by the elastic velocities of that layer.

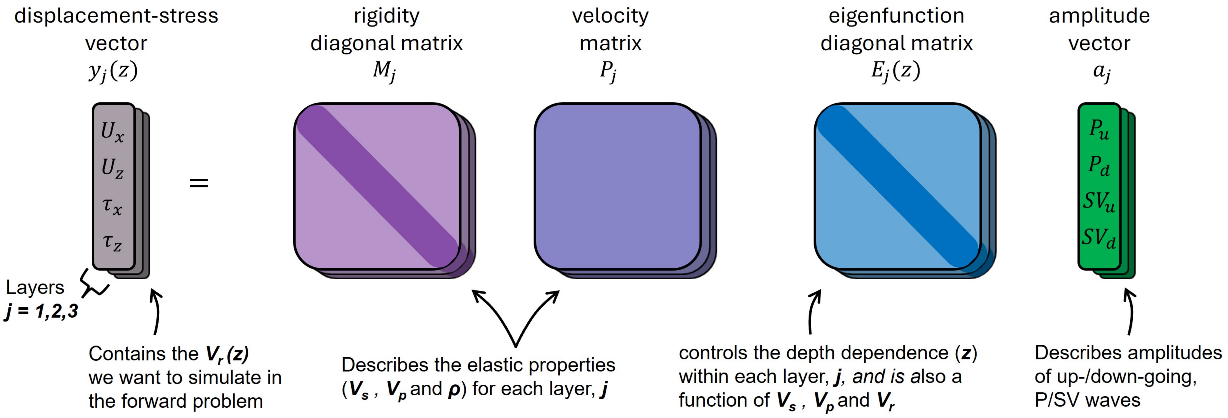

Figure 5.1 Description of the Rayleigh-wave displacement-stress vector following the nomenclature of Buchen & Ben-Hador (1996). Note that the eigenfunction, $E(z)$ solely controls the depth dependence within any layer, j.

Using propagator theory in combination with appropriate interface and boundary conditions, one can construct a complex matrix equation that characterizes wave propagation through a vertically heterogeneous medium. This leads to an eigenvalue problem in which the Rayleigh-wave phase velocity V_r acts as the eigenvalue. The resulting condition that the determinant of the system matrix must vanish defines the characteristic equation for Rayleigh waves, which yields the theoretical dispersion relation $DC_{theo} = D(\omega, V_r(z))$, where $\omega = 2\pi f$ is angular frequency.

Various formulations exist for constructing the system matrix and applying boundary conditions; Buchen & Ben-Hador (1996) provides a comparison of these approaches. Our inversion implementation via the *MASWaves* software package (Ólafsdóttir *et al.*, 2018b) uses the stiffness matrix method. Otherwise, we use *disba* software package (Luu, 2021), which employs the fast delta-matrix method for calculating numerical solutions in standalone analyses.

5.3.2 Forward Problem: Experimental Dispersion Curves

Quantifying the dispersion relation from seismic trace data requires decomposing the time-series signals into their frequency components. The *MASWaves* implementation follows the method of Park *et al.* (1998) in using slant-stacking of Fourier-transformed shot-gather seismic trace data. We describe the process visually in Figure 5.2. Let $D(x_j, t)$ represent the seismic response at source-receiver offset x_j and time t, recorded from a source shot indexed by j (Figure 5.2-a1). When transformed into the frequency domain via Fourier transform (Figure 5.2-a2), the data become a complex function of angular frequency ω:

$$D(x_j, \omega) = |D(x_j, \omega)| e^{-i\Phi_j}. \tag{5.1}$$

This representation contains terms associated with the phase Φ_j and magnitude $|D(x_j, \omega)|$. The latter incorporates amplitude variations due to factors such as geometrical spreading and energy loss. If the data are normalized to unity, then only the phase term is retained as:

$$D_{norm}(x_j, \omega) = e^{-i\Phi_j}, \tag{5.2}$$

where $e^{-i\Phi_j}$ encodes the dispersive behavior because

$$\Phi_j = \frac{\omega(V_r) x_j}{V_r}. \tag{5.3}$$

The velocity dependence of different frequency components manifests as a systematic phase shift across the array and can be directly extracted (as shown in Figure 5.2-a3) from the frequency-domain signal via:

$$\Phi_j = \arctan\left(\frac{\mathrm{Im}[D]}{\mathrm{Re}[D]}\right).$$

Although we parse the signal into phase and frequency components, these values are insufficient to resolve V_r (via Eqn. (5.3)) unless the velocity dependence on frequency is accurately modeled or validated. Our approach to resolving this ambiguity invokes a slant-stacking operation. A coherency measure is defined by integrating the product of the normalized data and the conjugate of the test phase:

$$D_{norm}(\omega, \Phi_{\text{test},j}) = \int D_N(x_j, \omega) e^{i\Phi_{\text{test},j}} \, \mathrm{d}x. \tag{5.4}$$

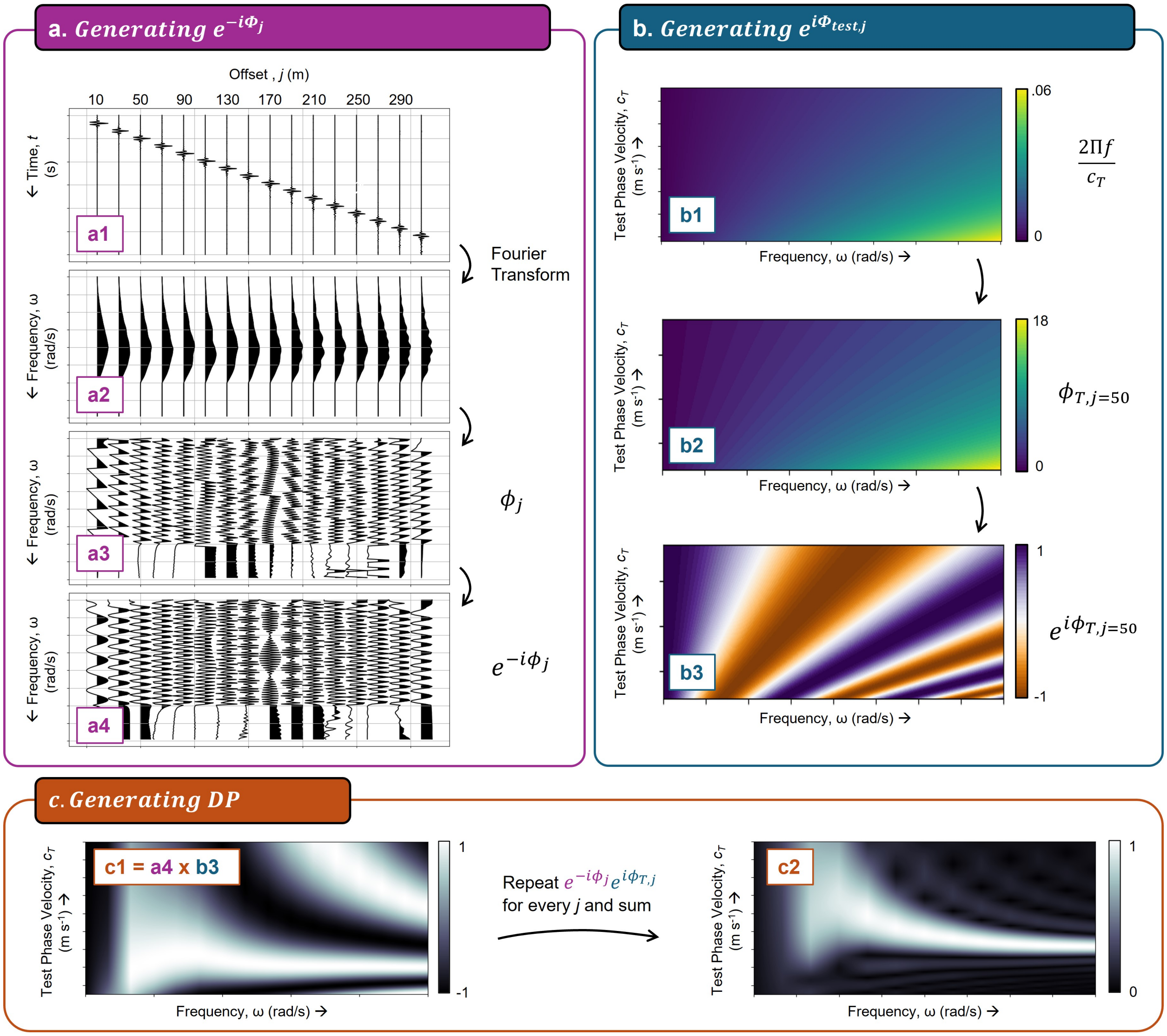

Figure 5.2 Overview of the process used to generate dispersion panels (DPs) from shot-gather seismic data for extracting experimental dispersion curves (DCs). (a) Steps involved in calculating the first exponential term, derived from the complex phase of the frequency-transformed shot-gather. Every 20th trace is shown for clarity in all sub-panels. Sub-panel (a1) shows the input shot gather, $D(x_j, t)$; (a2) the frequency-domain representation of the input shot gather, $D(x_j, f)$; (a3) the extracted phase for each trace, ϕ_j; and (a4) the first exponential term, $\exp(i\phi_j)$. (b) Construction of the second exponential term computed from a range of test phase velocities c_T and frequencies. Sub-panel (b1) shows the computed matrix of $\frac{2\pi f}{c_T}$ for various c_T and f; (b2) the offset-scaled version of this matrix for a representative trace at $j = 50$; and (b3) the second exponential term, $\exp(-i\frac{2\pi f x_j}{c_T})$, shown for $j = 50$. (c) Generating the final DP by (c1) computing the product of the two exponential terms for each offset; and (c2) stacking the result across offset.

This integral evaluates the similarity between the observed and test phase; that is, when the exponential terms align, the integrand is maximized (or, ideally, unity as D_{norm} is normalized) and this means that the $V_{r,\text{test}}$ is physically plausible at that frequency. By assuming a trial velocity $V_{r,\text{test}}$ and exploring a range of frequencies present in the data, one can compute a hypothetical phase (Figure 5.2-b1, Figure 5.2-b2) :

$$\Phi_{\text{test},j} = \frac{\omega x_j}{V_{r,\text{test}}},$$

and calculate $e^{i\Phi_{\text{test},j}}$ (Figure 5.2-b3).

Repeating this analysis over all offsets (Figure 5.2-c1) and stacking the functions of f and V_r (Figure 5.2-c2) generates a dispersion panel (DP) from which the dispersion curve (DC) can be identified using the maximum values. Each "slant" (i.e., test velocity versus offset) represents a plane wave and the amplitudes are normalized by trace number prior to "stacking" the f-V_r panel.

5.3.3 Inverse Problem: Estimating V_s-Depth Models

We implement a deterministic inversion approach to estimate V_s depth profiles from surface-wave dispersion data using *MASWaves*. The main inversion workflow steps are highlighted in Figure 5.3. We provide a brief overview here and refer the reader to Ólafsdóttir *et al.* (2018b) for a more detailed description of the algorithm and implementation.

A DC_{exp} extracted from a DP in the frequency domain is first converted to functions of wavelength λ yielding the observed dataset $d_{obs}(V_r, \lambda)$ used as input into the inversion. An initial 1-D model is then defined by a set number of layers each with an estimated thickness h, and elastic parameters V_s, V_p and ρ. From this model, the DC_{theo} is computed and likewise converted to $d_{calc}(V_r, \lambda)$. Next, the difference between d_{obs} and d_{calc} is quantified using a least-squares misfit function, ϵ. For each iteration, N, a trial misfit ϵ_{test} is computed and compared to the current minimum misfit ϵ_{DC}. If $\epsilon_{test} < \epsilon_{DC}$, or if $N = 1$ (i.e., the first iteration, for which no prior misfit exists), the current best model is updated with the trial parameters; otherwise, the original model is retained.

To efficiently explore the model space and reduce the likelihood of becoming trapped in local minima, a Monte Carlo-based update strategy is employed. New candidate models are generated by randomly perturbing V_s and/or h within user-defined bounds, controlled by the perturbation parameters b_s and b_h. Each of the user-defined number of inversion runs proceeds iteratively through the workflow in Figure 5.3 until either a maximum number of iterations is reached or the misfit ϵ falls below a specified threshold. Additional hyperparameters influence the efficiency and accuracy of the inversion; these are discussed in more detail Section 5.4.

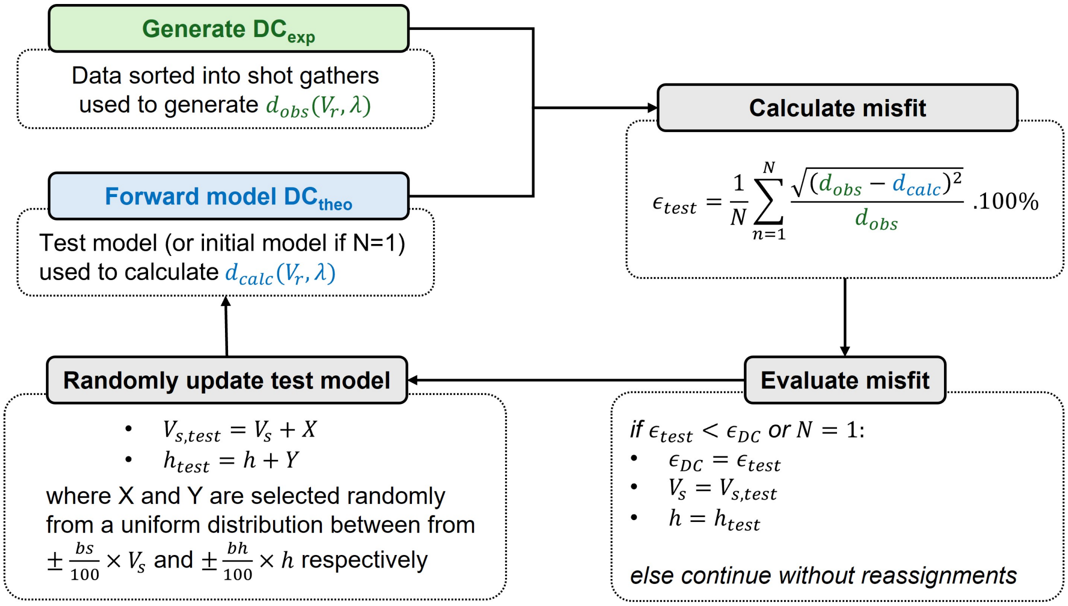

Note the following user-defined parameters:

- *Initial model*
- *Number of runs i.e. each new run starts from the initial model*
- *Number of iterations per run, N*
- *Sampling constraints, bs and bh*
- *Other hyperparameters: e.g. model and data constraints*

Figure 5.3 Overview of the deterministic inversion workflow implemented in *MASWaves*, which incorporates Monte Carlo sampling for model updates. For a more detailed description of the algorithm, we refer the reader to Ólafsdóttir *et al.* (2018b).

5.4 Inversion Parameterization

Deterministic inversion is fundamentally non-unique (e.g., Foti *et al.*, 2018); as a result, even with exact input data, a range of physically distinct model solutions can be obtained. This is illustrated in Figure 5.12 of the supplemental study in Section 5.11.1, and motivates our decision to include the solutions from exact input data in the synthetic firn-aquifer studies as a reference for the upper bound of "best-case" outcomes.

Since the goal of these studies is to compare the performance of SC- and MC-MASW approaches, we use relatively tight inversion constraints in the synthetic experiments (i.e. carefully tuned based on the exact-data experiment, but still not over-engineered). For the field data, such control is naturally more limited, though we still aim to keep the solution space as compact as practical through conservative parameterization. The supplemental material in Section 5.11 contains details on the specific inversion parameters, including choice of initial model, model constraints (such as V_p/V_s ratios and reversal flags), and hyperparameters (e.g. number of runs in Section 5.11.2) of the Monte-Carlo sampling scheme and inversion.

5.5 Synthetic Study: Firn-Aquifer Structures

Firn-aquifers are perennial water storage layers that may play a critical role in the ice sheet dynamics of Greenland (e.g., Forster *et al.*, 2014; Koenig *et al.*, 2014) and Antarctic (e.g., Di Biase *et al.*, 2024). Recent research on these systems has grown and involves coupled hydrological and mechanical models that depend on accurately delineating both the lateral extent and thickness of the aquifer (The Firn Symposium Team, 2024). A series of investigations on the Greenland Ice Sheet, following the initial discoveries using firn cores and radar sounding (Forster *et al.*, 2014; Koenig *et al.*, 2014), highlight the progression of geophysical efforts to characterize these features. In 2017, Montgomery *et al.* (2017) conducted a single-component (1-C, vertical) active-source experiment at Helheim Glacier and, using refraction tomography, quantified both deep ice structure and near-surface firn-aquifer thickness along the central flow line. Subsequently, Chu *et al.* (2018) explored the potential of deep-ice radar sounding for mapping more broadly, including the extent and changes in thickness of the aquifer in the near surface. Building on these efforts, Killingbeck *et al.* (2018) completed a joint inversion analysis combining borehole, radar, and seismic data to better delineate firn–aquifer systems within the larger ice-structural features. Our goal is to investigate how MC data could further enhance such efforts with a focused assessment on employing MC data in the MASW inversion scheme.

We develop three variations of a firn-aquifer system for our assessment. The "base" model is derived from the velocity model solution presented in Killingbeck *et al.* (2020) at Helheim Glacier, Greenland, with the exception that we impose a hard bedrock layer at 150 m depth. This modification allowed us to study the contribution of the low-frequency, long-wavelength information, relative to the higher-frequency, short-wavelength data that are predominantly sensitive to the firn-aquifer. In the second "deep" and third "thick" models, aquifer depth and thickness are doubled, respectively, relative to the base scenario. Table 5.1 summarizes the model geometries and properties for each layer. For an illustration we refer the reader to Figure 4.12.

Table 5.1 Firn-aquifer model variations for synthetic data generation. (a) "Base" model derived from Helheim Glacier seismic inversion results (Killingbeck *et al.*, 2020) with a 10 m thick aquifer overlain by 20 m of firn and a bedrock half-space imposed at 150 m depth. (b) "Deep Aquifer" model similar to (a) but with the firn layer extended to a depth of 40 m. (c) "Thick Aquifer" model similar to (a) but with the aquifer thickened to 20 m.

Layer	V_p (m s^{-1})	V_s (m s^{-1})	ρ (kg m^{-3})	V_p/V_s	**Base Aquifer**		**Deep Aquifer**		**Thick Aquifer**	
					z_{top} (m)	h (m)	z_{top} (m)	h (m)	z_{top} (m)	h (m)
Firn	2900	1300	700	2.23	0	20	0	40	0	20
Aquifer	2900	1150	930	2.52	20	10	40	10	20	20
Ice	3500	1750	930	2.00	30	120	50	100	40	110
Bedrock	4000	2000	2600	2.00	150	∞	150	∞	150	∞

We simulated Z- and X-component shot gather data using the open-source *SOFI2D* seismic modeling package (Bohlen *et al.*, 2016). Because the simulations used only positive offsets ($d > 0$ m), the horizontal X-component data effectively represent the radial R component for all source–receiver pairs. A vertical impact source was modeled in all experiments using an Ormsby wavelet with a flat frequency spectrum between 5 and 30 Hz. Sources and receivers were positioned 1 m below the free surface in all cases.

We simulated elastic shot-gather data using idealistic acquisition parameters: $\Delta r_x = 1$ m spacing and $L = 300$ m aperture. Following best-practices developed in Chapter 4, we condition the synthetic data by removing the near-offset traces (from 0 to 10 m, which effectively reduced L to 290 m) and direct arrivals and windowing appropriately to capture untruncated Rayleigh wave arrivals on each trace.

We compute DPs separately for the Z and R components (columns 1 and 2 of Figure 5.4) for each firn-aquifer model. Additionally, we construct a complex component (CC) to better represent the vector displacement of the elliptical particle motion by summing the orthogonal Z- and R-component gathers in a complex system following Eqn. 4.10. We generate corresponding DPs for each model (column 3 in Figure 5.4).

The work in Chapter 4 demonstrated that the CC-component potentially captures the unique depth-dependent sensitivities of both the vertical and horizontal particle displacements of Rayleigh waves. However, this benefit can only be exploited if the picked CC DC_{exp} is representative of the true glaciological structure. To visualize this, we transform these DC_{exp} into the input data format $d_{obs}(V_r, \lambda)$ and plot these in Figure 5.5a, Figure 5.5c, and Figure 5.5e for all components for the base, deep, and thick scenarios, respectively. We also plot the exact data for comparison (in black). Figure 5.5b, Figure 5.5d, and Figure 5.5f show the shortest Euclidean distances between each d_{obs} and the exact data, treated as a continuous curve. We note that there are intervals in which the CC component shows notably lower misfit to the exact data than the Z component, although the opposite also occurs in other intervals. We seek to explore how these observations affect the inverse solutions and determine whether the CC component ultimately provides a more accurate inverse solution for each scenario.

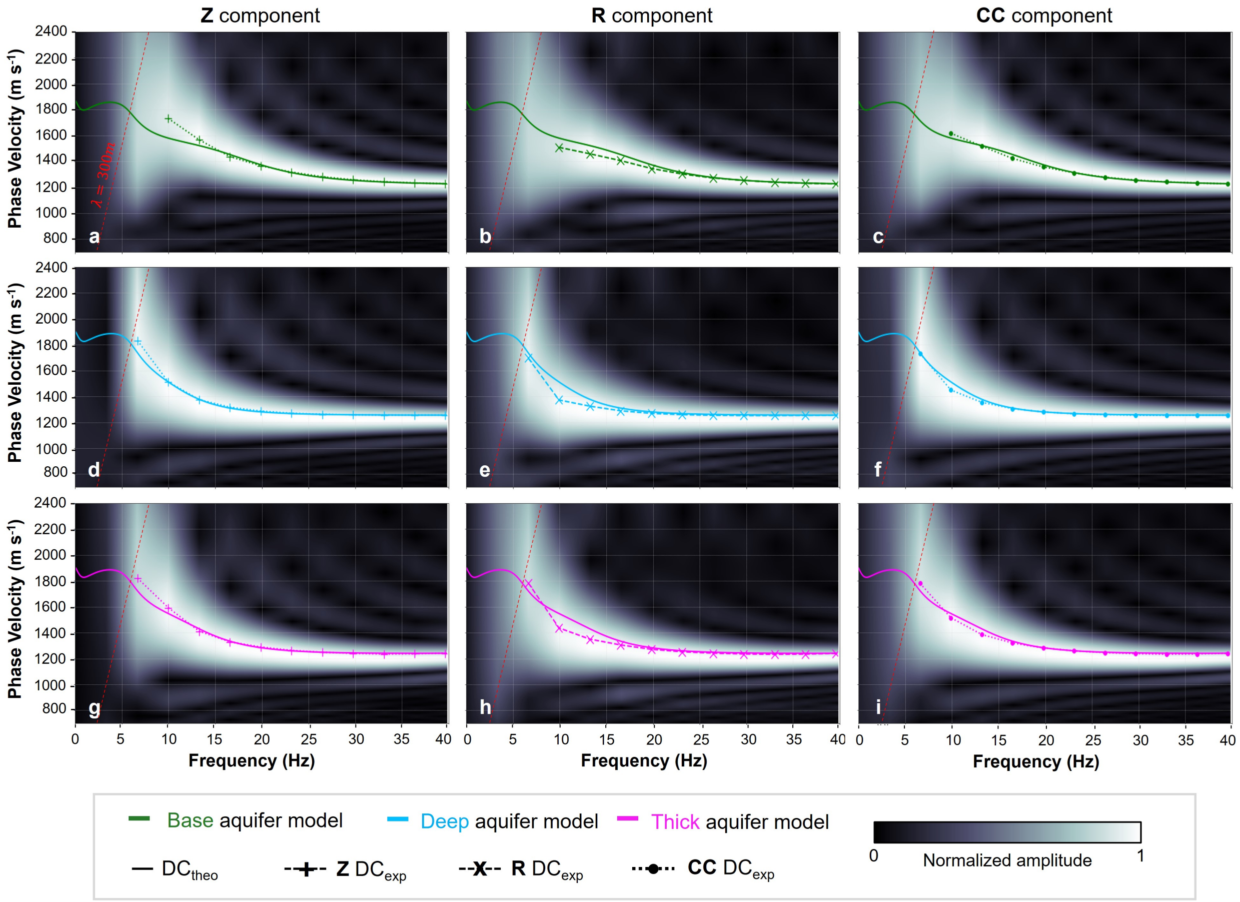

Figure 5.4 DPs for Z, R and CC components for each of the three firn-aquifer models: (a-c) base firn-aquifer model (d-e) deep aquifer model (g-i) thick aquifer model. Z-, R-and CC-component DC_{exp} are represented as plus, cross and dot markers, respectively. DC_{theo} for each of the three firn-aquifer models are plotted as solid curves. Dashed red lines on all DPs highlight the maximum resolvable wavelength of 300 m based on the array aperture.

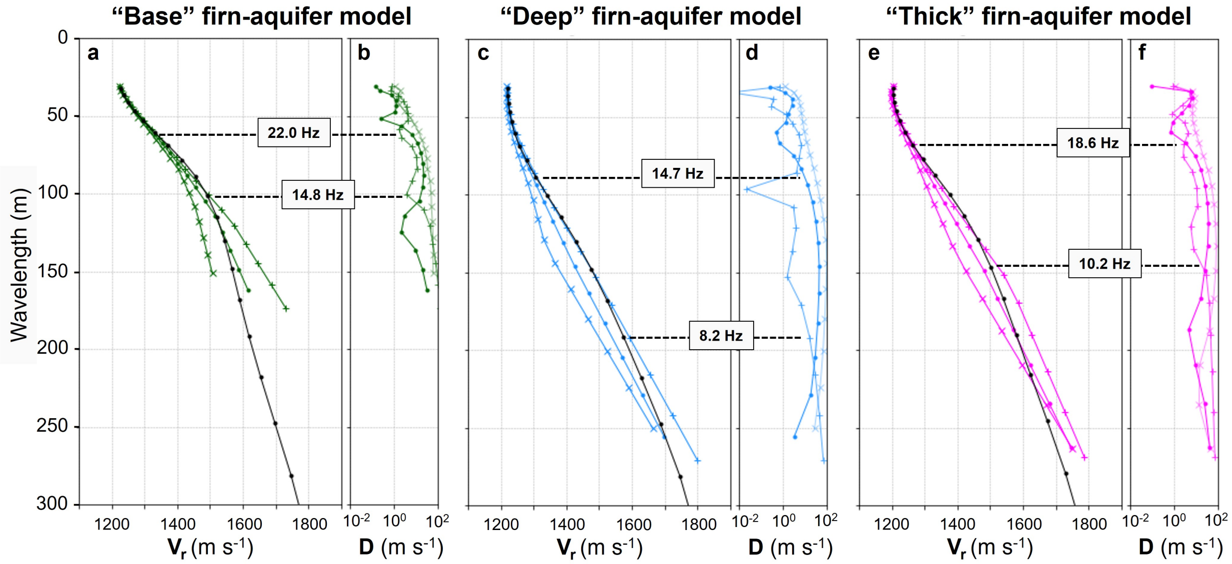

Figure 5.5 (a, c and e) Comparison of the Z-, R- and CC-component data (d_{obs}) for each firn-aquifer model (colored lines) alongside the exact data (d_{theo}) plotted in black. (b, d and f) Shortest Euclidean distance, D, between the point extractions of the Z-, R- and CC-component data and the exact data curve treated as a continuous curve. Points plotted along the exact-data curve are the data points used for the exact-data experiments. Annotated frequencies are those at which the component producing the smallest D switches, usually between the Z and CC components.

5.5.1 Results

We present the results of the synthetic studies, focusing on the median model solutions calculated from the individual solutions falling between the 10th and 90th percentiles of data misfit. The supplemental experiment described in Section 5.11.3 justifies why these median solutions provide an appropriate basis for our comparative analyses. Having used the exact data to guide the parameterization, we run the exact-data experiment for each scenario and present the model solutions in the first column of Figure 5.6. The median solutions of each experiment (solid curves in Figure 5.6a, Figure 5.6e, and Figure 5.6i for the base, deep, and thick scenarios, respectively) match the true model of each (dotted black curves), and these results serve as a benchmark for evaluating the inversions using the component datasets.

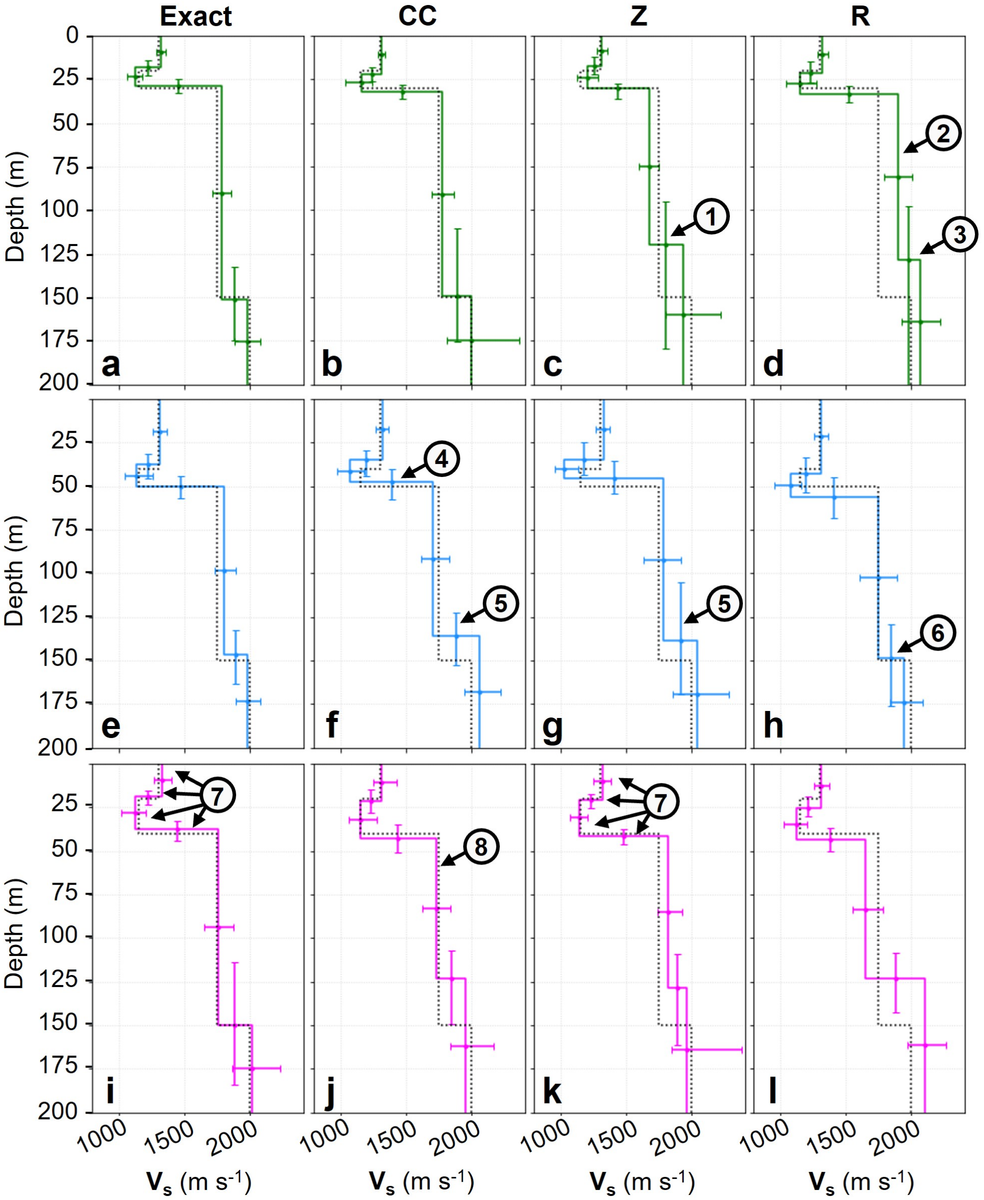

Figure 5.6 Comparison of the median solutions for (a-d) base, (e-h) deep, and (i-l) thick firn-aquifer models each using the true data (left-most column) and the *CC*-, *Z*-, and *R*-component data in the subsequent columns.

Base Model Scenario

We begin by presenting results for the base scenario experiment using single-component data (Z and R) and the combined CC component. The CC-component solution (Figure 5.6b) is comparable to that obtained using the exact data (Figure 5.6a) and outperforms the single-component approaches (Figure 5.6c and Figure 5.6d) at all depths, accurately characterizing both the firn–aquifer V_s-depth profile and the deeper ice and bedrock structures. The less accurate Z-component result at depth (Figure 5.6c, annotation #1) is likely linked to inaccurate long-wavelength information in the d_{obs} (Figure 5.5b), stemming from poor low-frequency picks in the DC_{exp} (Figure 5.4a). Similarly, the R-component experiment poorly recovers the ice and bedrock structures (Figure 5.6d, annotations #2 and #3, respectively). This is likely due to the lack of long-wavelength content in the d_{obs} (Figure 5.5b, where the data are truncated around 150 m), again resulting from poor low-frequency DC_{exp} picks (Figure 5.4c).

This noteworthy CC-component result is obtained despite the fact that a significant range of data points (between roughly 14.8 and 22.0 Hz, as observed in Figure 5.5b) are less accurate than those of the Z component. To understand why this occurs, we examine the depth-sensitivity kernels of Rayleigh-wave displacement for discrete frequencies (Figure 5.7a–Figure 5.7g). Below 10 Hz (Figure 5.7a), the Rayleigh-wave vertical particle displacement U_z exhibits increased sensitivity to the ice–bedrock interface, and above approximately 15 Hz, horizontal displacement U_x sensitivity is roughly maintained while U_z sensitivity decreases with frequency (highlighted by black arrows in Figure 5.7e–Figure 5.7g). Because the CC-component data capture the sensitivities of both U_z and U_x and remain sufficiently accurate at frequencies outside the 14.8–22.0 Hz range, the inversion produces an accurate solution despite the poorer data quality in the central frequency band.

Deep Model Scenario

In the deep model scenario, we first note that the firn-aquifer interface and aquifer velocity are poorly resolved in all component experiments. Otherwise, the CC inversion (Figure 5.6f) performs marginally better than the single-component inversions (Figure 5.6g–h), particularly in resolving the aquifer-ice interface (annotation #4) and in generally producing smaller error bounds around the deeper structure (annotation #5). The apparent improvement in resolving the aquifer-ice interface is not a fully convincing argument, as the error bounds in the CC- and Z- component results remain comparable. In contrast, the stronger performance at greater depths represents a more robust improvement and can be linked to the contribution of the R-component data since, when inverted alone (Figure 5.5d), R-component data effectively resolve the ice–bedrock interface (annotation #6), albeit with slightly larger error bounds.

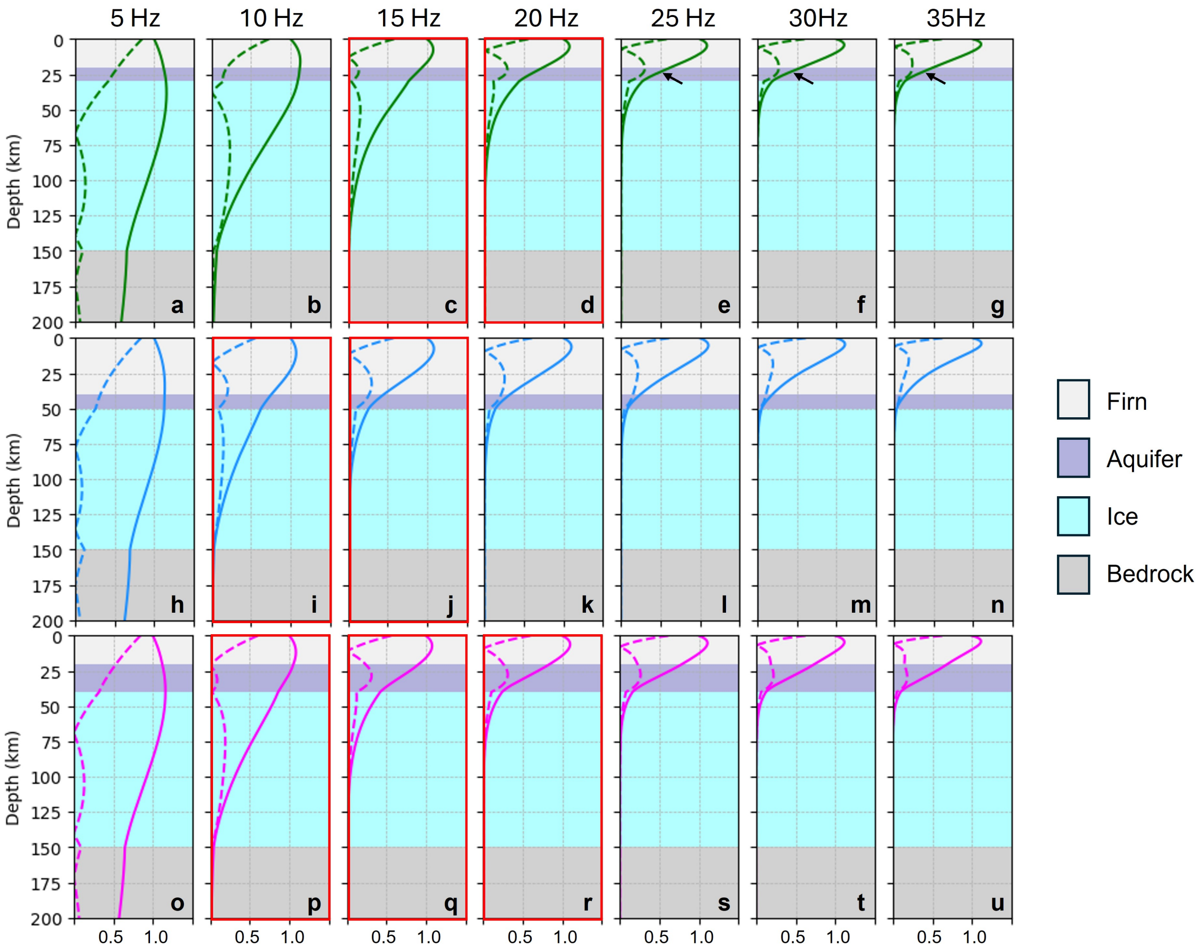

Figure 5.7 Comparison of the depth sensitivity of the vertical and horizontal Rayleigh-wave particle displacements U_z and U_x (plotted as solid and dashed curves, respectively) for the (a–g) base, (h–n) deep, and (o–u) thick firn-aquifer models, for discrete frequencies ranging from 5 Hz (leftmost column) to 35 Hz (rightmost column). Each kernel is plotted on a background shaded to indicate the material present at that depth. Panels highlighted with red boxes are affiliated with observations where the Z-component data appear more accurate than the CC-component data in Figure 5.5.

We again critically assess these results based on the principle that the ability of the components to resolve subsurface structures depends on both the accuracy of their picked DC_{exp} and their frequency-dependent depth sensitivities. The sub-10 Hz U_z and U_x data are most sensitive to the ice–bedrock interface (Figure 5.7h–i), though this range also exhibits high sensitivity to the firn-aquifer interface, particularly in U_z. This frequency range is most accurately picked in the CC data, as evident from Figure 5.5d, where the longer-wavelength CC-component data (below the 8.2 Hz marker) exhibit the lowest misfit. This not only improves the sensitivity and therefore the detectability of the deep ice-bedrock interface, but also contributes to the accurate mapping of the shallower aquifer-ice interface.

Thick Model Scenario

In the thick model scenario, the CC component (Figure 5.5j) is marginally outperformed in the shallow region by the Z component (Figure 5.5k, annotation #7). The Z-component experiment resolves the firn, firn-aquifer interface, aquifer, and aquifer-ice interface with accuracies and uncertainty estimates comparable to those in the exact-data experiment (Figure 5.5i, annotation #7). However, the CC-component experiment should not be discounted as it also resolves these properties and interfaces with similar accuracy, albeit with slightly larger error bounds in the shallow region. Additionally, it successfully captures V_s in the column (annotation #8). The R component performs worst when used alone.

These outcomes can be better understood by examining the frequency-dependent sensitivities. Between 10–20 Hz (Figure 5.7q and Figure 5.7r), strong U_x sensitivity to the aquifer is observed; however, this sensitivity is not reflected in the CC- or R-component experiments as the data for both components within this mid-frequency range are less accurate and deviate more strongly from the exact data (see Figure 5.5f, between the 10.2–18.6 Hz markers). Outside this range, sufficient sensitivity to the aquifer from both U_z and U_x drives the solution, resulting in accurate firn–aquifer structure estimates for the Z-

and CC-component experiments. Below 10 Hz where the U_z sensitivities to ice-bedrock interface are strongest (e.g., Figure 5.7o), the CC-component data are most accurate (Figure 5.5f), thus enabling the accurate ice-velocity solution in comparison to that of the Z-component experiment. It is possible that although there may also be sensitivity to the ice–bedrock depth at this frequency, the inverse problem remains predominantly controlled by the strong sensitivity to the shallow regions (e.g., Figure 5.5p), thereby resulting in poor ice–bedrock resolution.

5.5.2 Key Insights

In all model scenarios, we observe that there exists a mid-frequency band (approximately 10–20 Hz) where the Z-component data are as or more accurate than the CC-component data. These frequency ranges are highlighted in red boxes in Figure 5.7. Outside these intervals, particularly in the base and thick scenarios, there is sufficient combined U_z and U_x sensitivity to the aquifer to enable accurate solutions from the CC inversion. Within these mid-frequency ranges, the Z component can at times achieve comparable performance as seen in the thick scenario; however, it also carries the risk of poorer performance as exemplified in the base scenario. The deep scenario is particularly notable in that sensitivity to the firn-aquifer interface is concentrated around a narrow range near 10 Hz, where both the CC and Z components exhibit similar data accuracies and perform comparably, though both show limitations in resolving the aquifer structure.

Importantly, in all scenarios, the CC component is never outperformed in a manner that would render it a less favorable choice; at worst, it performs on par with the single Z-component inversion. Although R-component data have an increased sensitivity to certain shallow aquifer structures, they lack sufficient sensitivity to simultaneously resolve deeper structures. Therefore, the CC-component inversion offers a robust approach for characterizing V_s depth profiles across a wide range of depths in all cases evaluated.

An important caveat of our synthetic experiments is that they may be considered a best-case scenario: the inversion was carefully parameterized using information derived from the true model, and the observed data were extracted from effectively noise-free synthetic shot gathers. This approach allows us to evaluate the potential advantages of the CC component, but it does not fully capture the challenges that arise in practical field applications, where data often are noisy and subsurface structures are not precisely known.

5.6 Field Study: Alpine Glacier

To evaluate the performance of our MC-MASW approach under realistic field conditions, we apply it to a MC field experiment conducted by Stevens *et al.* (2023) in the ablation zone of the Saskatchewan Glacier (Figure 5.8a). This alpine glacier is assumed to have a relatively homogeneous seismic velocity structure above bedrock, making it a suitable site for assessing the signal-to-noise ratio (SNR) improvement offered by the CC component at the level of individual shot gathers and with supergather processing (Hesthammer & Løkkebø, 1997). In the latter case, we also examine whether the extended aperture improves lower-frequency picks that better constrain bedrock depth in either the single-component or CC-component DCs.

The 2-D seismic survey was oriented along the glacier's centerline and employed nine 3-C geophones (R1 to R9), placed at 10 m spacing to form an 80 m linear array (Figure 5.8b). A sledgehammer striking a metal plate served as the seismic source at 25 shot locations (S01 to S25) distributed across a 240 m line centered on the receiver array. A tenth 3-C geophone was used as a mobile receiver and co-located with each shot to record excitation times.

Data from receivers R2 and R9 were unavailable for our study, resulting in missing offsets for certain shots as illustrated in Figure 5.8c. For example, shot #1 lacks the 90 m and 160 m offset traces, while shot #2 is missing the 80 m and 90 m traces. Each individual shot gather spans a reduced array length of 70 m due to the missing R9 data at the end of the stationary receiver array.

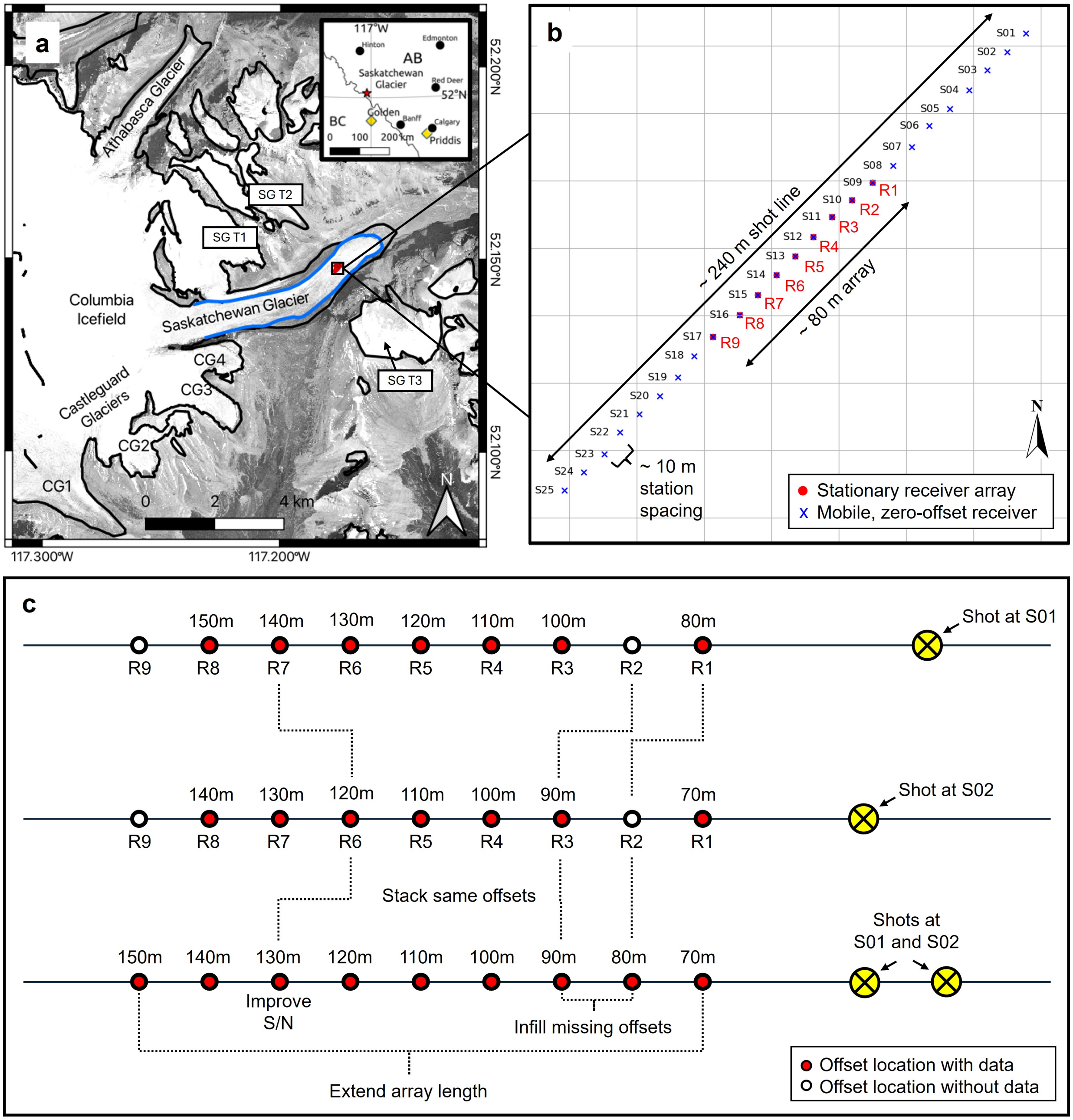

Figure 5.8 (a) Saskatchewan Glacier location in the Canadian Rocky Mountains, Canada (see inset map). Basemap is orthorectified 4-band PlanetScope imagery accessed via Planet.com. (b) Geometry of the active-source seismic experiment conducted in the ablation zone involving a stationary array of nine 3-C geophones (R1-R9) linearly spaced at 10 m to form an array of aperture $L = 80$ m. Source station locations S01-S25, also spaced 10 m apart, are shown as blue Xs. (c) Description of the offset coverage and array length for shots #1, #2, and a supergather generated from both #1 and #2.

The supergather approach provides a natural mechanism to infill missing offsets by stacking multiple shots that share common offsets (Hesthammer & Løkkebø, 1997) and enhances SNR where offset data overlap (Shragge *et al.*, 2021). Moreover, it effectively extends the data aperture and thus improves the low-frequency content of extracted dispersion data. For instance, stacking shots#1 and #2 yields an 80 m array spanning offsets from 70 m to 150 m (Figure 5.8c).

In Figure 5.9, we show the DPs constructed from the Z, R, and CC components for each of four experiments. The first and second experiments (Figure 5.9a–c and Figure 5.9d–f, respectively) compare the DPs from two single shot gathers at locations S01 and S02. The third experiment (Figure 5.9g–Figure 5.9i) is a low-fold supergather built from these two individual shots but trimmed to match the 70 m aperture ($80 - 150$ m offset) of the single-shot experiments. The fourth experiment is a high-fold supergather composed of shot locations S01 through S08 and with a 140 m aperture ($10 - 150$ m offset).

Although the DPs are plotted up to 100 Hz, estimates of the recoverable wavelengths are constrained by the Nyquist sampling theorem (de Lucena & Taioli, 2014; Socco & Strobbia, 2004); these bounds ideally should guide the selection of data points used to construct the DC_{exp} curves. In the Saskatchewan experiment, where the receiver spacing is 10 m, the shortest resolvable wavelength is 20 m. In noisy field data, the Nyquist-based estimate of the longest recoverable wavelength may be optimistic. For arrays with 70 m aperture (in the first through third experiments) and 140 m (high-fold supergather experiment), the corresponding longest recoverable wavelengths are approximately 140 m and 280 m, respectively. Under noisy conditions, a more conservative approach involves sampling at twice the Nyquist rate, meaning that wavelengths equal in length to the array are well sampled and can be recovered with high confidence.

In Figure 5.9, automatic picks of the high-amplitude DC trend generated by the internal *MASWaves* algorithm are shown as colored dots. From these, a subset was selected as the DC_{exp} curves used for inversion. These picks, plotted as crosses, were initially chosen within the expected lower and conservative upper wavelength limits of the experiment. However, in the single-shot-gather and low-fold supergather experiments, some noisier picks at the lower-frequency end of this range on the Z and R components were manually removed to stabilize the inversion. This subjective conditioning was not necessary for any of the CC component experiments.

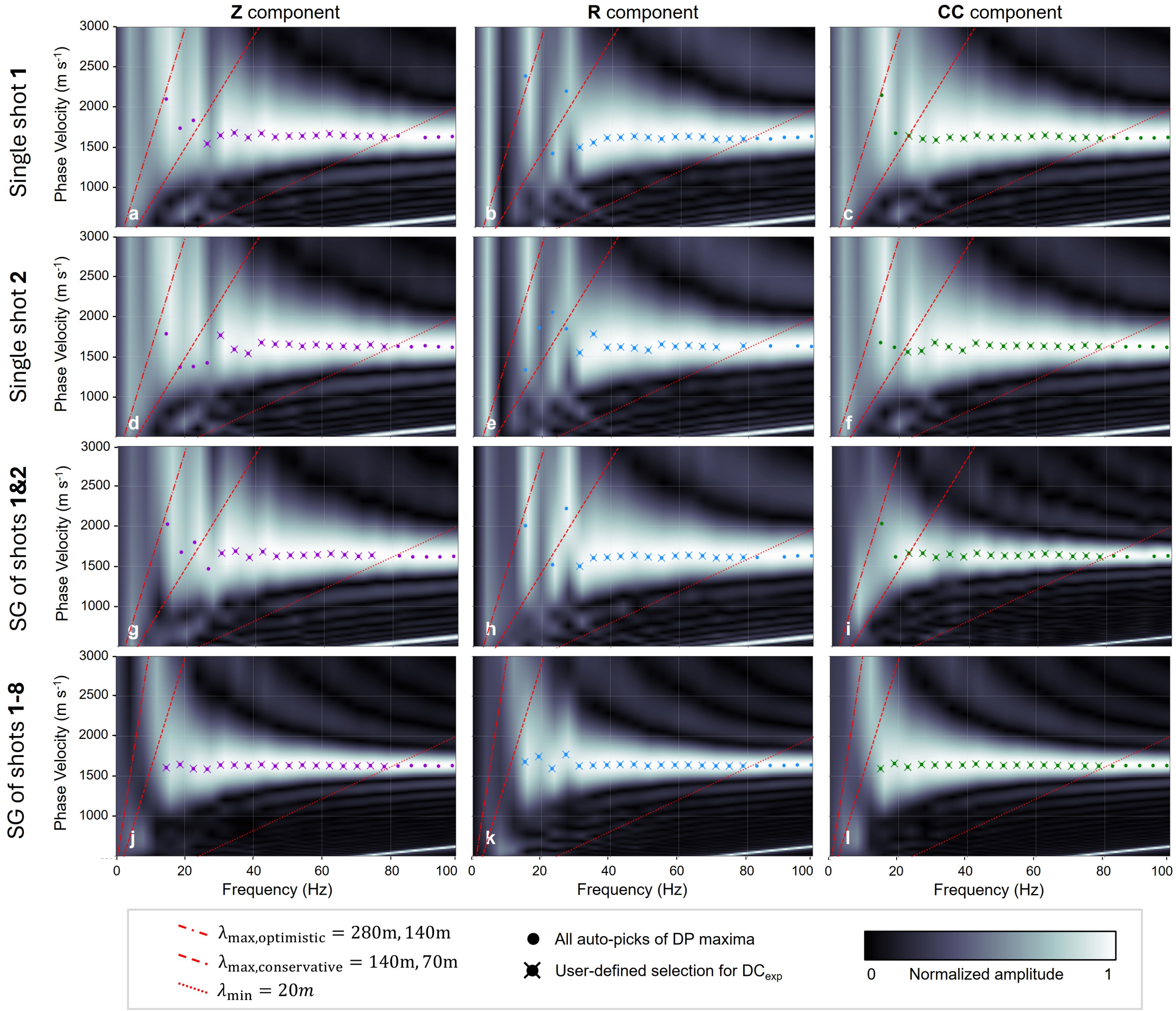

Figure 5.9 DPs for Z-, R- and CC-components for four experiments: (a–c) shot gather at location S01; (d–e) shot gather at location S02; (g–i) supergather of shots at locations S01 and S02; and (j–l) supergather of shots at locations S01 through S08. All auto-picks selected by the internal *MASWaves* algorithm are plotted as dots; however only a few of these picks (crosses) are used to represent the DC_{exp} input into inversion. This is primarily based on the expected lower and conservative upper wavelength limits of the experiment based on survey design. In some cases, manual de-selection of picks on the Z and R components was necessary at low frequencies to stabilize the inverse solution.

5.6.1 Results

To evaluate the field study, we consider both the median model solutions within the 10th to 90th percentile range of data misfit, alongside the full spectrum of solutions. This discussion focuses primarily on the V_s estimates of the shallow ice layer, because inversion sensitivities to both bedrock depth and V_s are strongly influenced by the accuracy of the low-frequency dispersion data. For each experiment, the DC_{exp} provides little to no reliable coverage of the low-frequency range, which is critical for resolving bedrock properties.

Single-shot-gather Experiments

The results for the Z, R, and CC components for the two single-shot experiments are shown in Figure 5.10. For these experiments, it is important to first note a key caveat: the Z and R components required manual adjustment of dispersion picks at the low-frequency end (Figure 5.9) to stabilize the inversion. These adjustments introduce an element of subjectivity into the SC-MASW experiments that is not required in the MC-MASW case. This manual step improved inversion stability, but it reduced the depth sensitivity of the SC-MASW results by excluding long-wavelength information. For instance, in Figure 5.10a and Figure 5.10b, the Z- and R-component models terminate around 60 m, whereas the CC-component results in Figure 5.10 extend to 70 m, which is a conservative estimate of the maximum resolvable depth for this experiment.

Assuming laterally homogeneous ice between S01 and S02, and considering the 10 m shot spacing negligible relative to the 70–150 m offset spread (Figure 5.8c), we expect that the shallow V_s structure should remain consistent across these two single-shot-gather experiments. This expectation is confirmed in the CC-component results (Figure 5.10c, Figure 5.10f), which show a shallow V_s difference of only 5 m s^{-1} (1751 m s^{-1} for the S01 experiment (Figure 5.10c) compared to 1756 m s^{-1} for the S02 experiment (Figure 5.10f). In contrast, the Z and R components yield less consistent estimates, with velocity differences of approximately 10 m s^{-1} and 20 m s^{-1}, respectively.

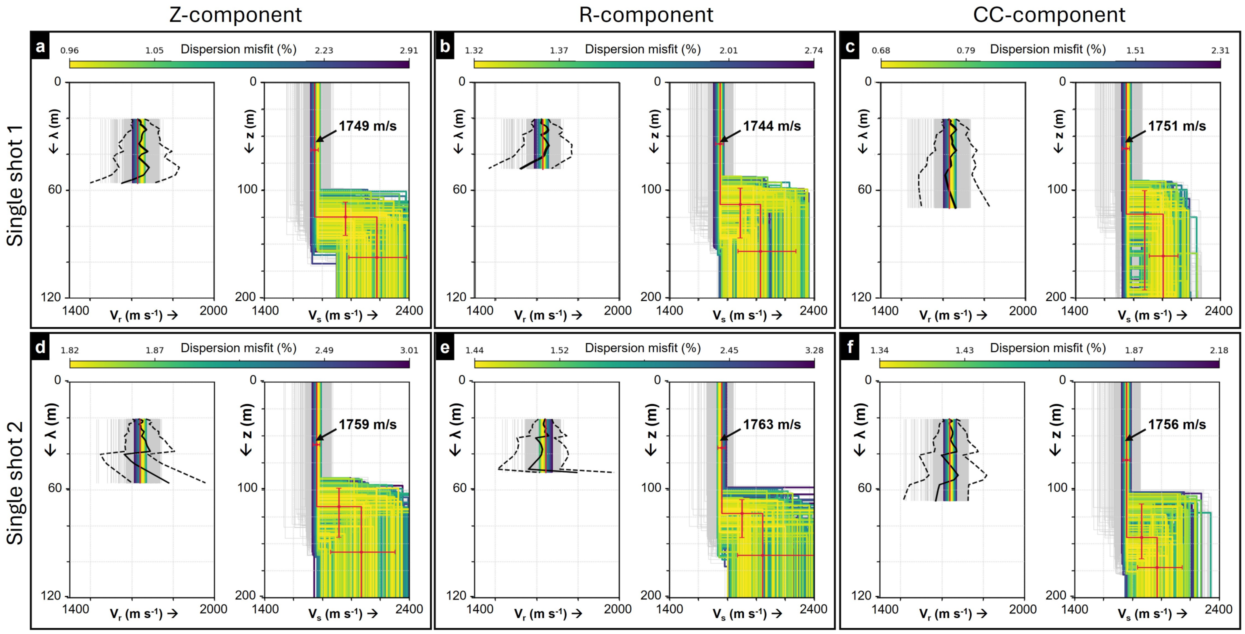

Figure 5.10 Results for two single-shot experiments (at station location 1 and 2) using the Z (left), R (middle), and CC (right) data: (a–c) input dispersion data generated from shot location S01; (d–e) input dispersion data generated from shot location S02; The left subplot of each panel shows the d_{calc} for each model solution that is plotted in the right subplot. The solutions are colored by the dispersion misfit where the misfit to d_{obs} (solid black curve) falls within depth-varying error bounds (dashed black curves). Solutions beyond this range are plotted in gray. Red lines in both subplots indicate the median solution, calculated from models with misfits within the 10th to 90th percentile range.

Overall, the MC-MASW experiment produces more consistent shallow ice V_s estimates between these neighboring single-shot experiments and yields lower dispersion misfits, highlighting its robustness even when compared to SC-MASW results aided by manual pick adjustments.

Low-fold Supergather Experiment

The results for the Z, R, and CC components in the low-fold supergather experiment (comprising shot locations 1 and 2, referenced as SG12) are shown in Figure 5.11a–c. As observed in the single-shot experiments, the SG12 Z- and R-component results remained unstable. Although stacking improved the SNR somewhat, manual removal of noisy picks was still required within the expected range of resolvable wavelengths.

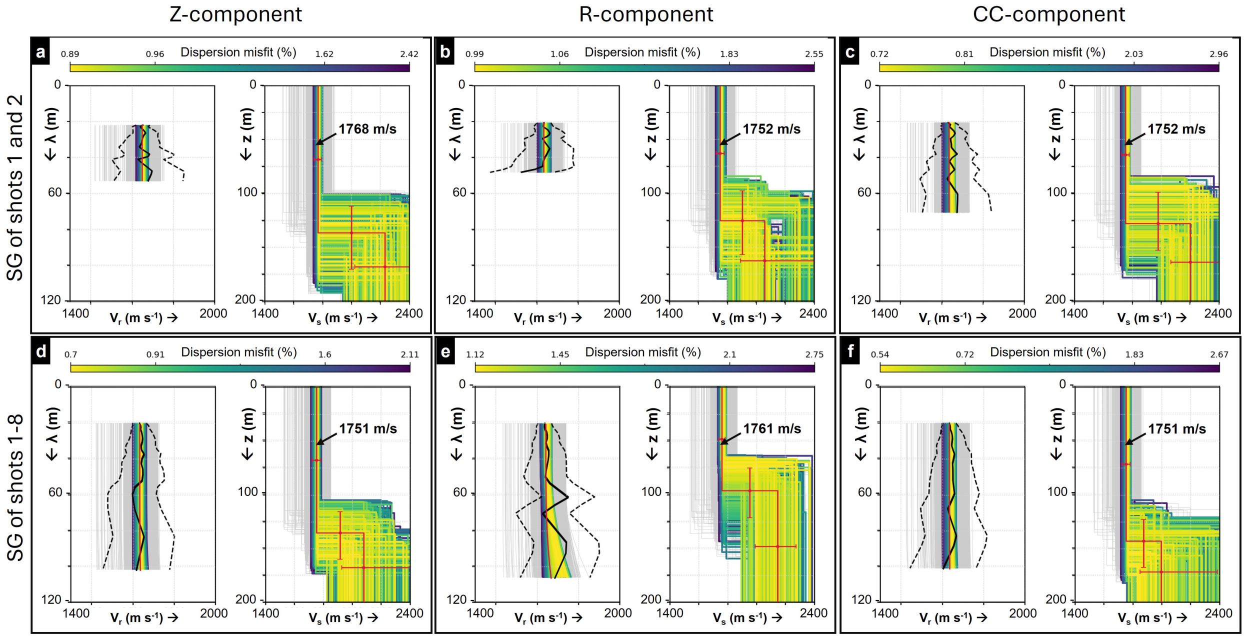

Figure 5.11 Results for two supergather experiments using the Z (left), R (middle), and CC (right) data: (g–i) input dispersion data generated from a low-fold supergather of shots at locations S01 and S02; and (j–l) input dispersion data generated from a high-fold supergather of shots at locations S01 through S08. Refer to Figure 5.10 for descriptions of subplots.

The R-component SG12 inversion (Figure 5.11b) estimated an englacial V_s of 1752 m s^{-1}, close to the average of the single-shot-gather results although the manual data conditioning limited the maximum usable wavelength to 50 m. Although this constraint does not affect the present model solutions given the ice's thickness and homogeneity, it could pose challenges in settings with more complex englacial structure.

In contrast to the R-component results, Z component SG12 solutions were outside the V_s range established by the single-shot-gather experiments. That is, although Z-component experiments for the S01 (Figure 5.10a) and S02 (Figure 5.10d) experiments yielded V_s estimates of 1749 m s^{-1}, and 1759 m s^{-1}, respectively, the SG12 result (Figure 5.11a) increased to 1768 m s^{-1}, nearly doubling the range of Z-component solutions observed between the two shot locations.

Without requiring manual data conditioning, the SG12 CC component outperformed the single-component inversions, producing a stable and plausible V_s estimate of 1752 m s^{-1} (Figure 5.11c), well within the range defined by the CC single-shot experiments. It also preserved the full depth sensitivity of the data and maintained lower misfit values than either of the SC-MASW results.

High-fold Supergather

With a high-fold supergather (SG1–8) comprising shot locations S01 through S08, SNRs improved noticeably across all components. All picks between the minimum and maximum resolvable wavelengths were retained, although the R-component experiment (Figure 5.11e) might have benefited from the manual removal of some low-frequency noisy picks. The resulting Z- and CC-component inversions (Figure 5.11d and Figure 5.11f, respectively), however, yielded identical V_s solutions of the ice at 1751 m s^{-1}.

This convergence between the Z and CC results under high fold suggests that, with sufficient stacking, the relative advantage of the CC component may diminish. Nonetheless, it remains notable that the CC component continues to exhibit a lower misfit.

5.6.2 Key Insights

Across all acquisition scales (single-shot-gather, low-fold, and high-fold supergathers), the CC component consistently produced stable V_s estimates for the ice column at Saskatchewan Glacier between $1751 - 1755$ m s^{-1}, with data misfits lower than those from the corresponding SC-MASW experiments. High-fold stacking substantially improved the quality of the Z-component data, removing the need for manual conditioning and yielding a V_s estimate within the range observed in the CC-component experiments. The R-component experiments, however, always required manual removal of noisy low-frequency picks, which limited the usable wavelength range. Although the remaining data still produced reasonable V_s estimates for the 150 m thick homogeneous ice, the reduction in depth sensitivity is not ideal, especially in more complex subsurface settings.

Overall, all four experiments highlight the comparative resilience of the CC processing enabled by 3-C data collection and its lower sensitivity to noise that typically affects the Z and R components.

Our concluding estimate of $V_s = 1751 - 1755$ m s^{-1} provides a more localized and direct measurement of shear-wave velocity compared to values derived empirically from P-wave linear moveout analysis. With P-wave moveout analysis, results and associated uncertainties are sensitive to the assumed V_p/V_s ratio. For instance, applying a commonly accepted Antarctic V_p/V_s ratio of 1.95 (Smith *et al.*, 2015) yields an estimate of $V_s = 1740 \pm 168$ m s^{-1} (Stevens *et al.*, 2023). In Stevens *et al.* (2024), this ratio was updated to 1.943 ± 0.003 using Wadati analysis of passive seismic data, resulting in a revised V_s estimate of 1776 ± 33 m s^{-1}. Although this update significantly reduces the uncertainty, our approach yields even lower error margins. Moreover, because our V_s values are measured directly from the same local 2-D array used to calculate V_p, they better reflect the specific ice conditions at the site. Using the reported $V_p = 3451 \pm 60$ m s^{-1} from Stevens *et al.* (2023, 2024), our results imply a local V_p/V_s ratio of approximately 1.97 for the Saskatchewan Glacier.

5.7 Discussion

The results of our main synthetic studies, supported by the supplemental experiment described in Section 5.11.1, emphasize the importance of careful inversion setup to obtain stable and reliable subsurface models. Even modest variations in model parameterization or data treatment can introduce substantial biases or instabilities. This sensitivity is particularly problematic in experiments where prior knowledge is limited, such as our field study, which makes tuning the inversion more challenging. Deterministic inversion frameworks provide little flexibility for internally optimizing these hyperparameters (e.g., Sambridge *et al.*, 2013), leaving limited opportunity to improve the model outcomes.

A further limitation of deterministic inversion is the absence of explicit uncertainty quantification (e.g., Bodin & Sambridge, 2009; Tarantola *et al.*, 1982). Individual inversion runs can produce highly variable solutions even with ideal data and parameterization (as demonstrated in the supplemental Section 5.11.1), and this variability is amplified when model parameterization is suboptimal or data constraints are weak. In these circumstances, relying solely on the median model can be misleading, as it may obscure the range of plausible subsurface structures. Without explicit representation of model variability, deterministic methods risk imparting a false sense of confidence in the final results. To realize the full potential of MC dispersion measurements, future research should focus on developing and applying probabilistic (e.g., Tarantola *et al.*, 1982) and trans-dimensional inversion algorithms (e.g., Bodin & Sambridge, 2009; Killingbeck *et al.*, 2018; Sambridge *et al.*, 2013) that deliver more insightful and reliable subsurface characterizations by explicitly incorporating uncertainty quantification and robust hyperparameter tuning.

5.8 Conclusion

We presented an MC-MASW workflow that serves as a practical and cost-effective extension to traditional MASW approaches. Our MC-MASW processing and inversion pipeline enables more reliable and detailed subsurface characterization in glacier settings without substantially increasing acquisition effort or scale. This advancement has important implications for improving geophysical investigations of glacier structure, dynamics, and hydrology under challenging field conditions. By leveraging the complementary depth sensitivities of the vertical and horizontal components of Rayleigh-wave particle motion recorded on 3-C geophones, layered V_s depth profiles can be modeled with greater accuracy. Our results demonstrate that firn-aquifer systems, which are difficult to distinguish using SC data alone, are more clearly resolved with the inclusion of MC data. Field data further validate the benefits of the MC-MASW approach, consistently yielding lower misfits and more stable V_s solutions compared to SC-MASW. In these cases, the improvements stem primarily from enhanced signal quality provided by the additional horizontal-component information. Finally, our results underscore the importance of robust inversion strategies to fully exploit the increased information content of MC datasets. We recommend future research efforts focus on the application of probabilistic and trans-dimensional inversion algorithms to further enhance model reliability and uncertainty quantification.

5.9 Data Availability

Synthetic glacial datasets and models are available on GitHub (https://github.com/samara-melody/MC-MASW), alongside relevant processing scripts. We refer the reader to Stevens *et al.* (2023) and their accompanied supplemental material for information regarding accessibility of the Saskatchewan Glacier field datasets.

5.10 Acknowledgments

The Mines Geophysics Department, the Mines Glaciology Laboratory, and the Center for Wave Phenomena supported this research through scholarship. We are especially grateful to Dr. Luke Zoet (University of Wisconsin–Madison), Dr. Dougal Hansen (Washington University), and Dr. Nathan Stevens (University of Washington) for providing access to the Saskatchewan dataset and for their generous discussions during the early stages of this work.

This study relied on a range of open-source software packages, and we gratefully acknowledge the developers and contributors who make these tools available to the scientific community. Synthetic data were simulated using *SOFI2D* (Bohlen *et al.*, 2016). The software *MASWaves* (Ólafsdóttir *et al.*, 2018b) was used for dispersion curve forward modeling and analysis, and *disba* was employed for numerical modeling (Luu, 2021). Seismic data processing was carried out with *ObsPy* (Beyreuther *et al.*, 2010) for MiniSEED-formatted data and *Seismic Unix* for SEGY/SU-formatted data (Stockwell Jr, 1999). Additional numerical and symbolic computations, as well as data visualization, were supported by Python libraries including *NumPy* (Harris *et al.*, 2020), *SymPy* (Meurer *et al.*, 2017), *pandas* (McKinney, 2010), and *Matplotlib* (Hunter, 2007).

5.11 Supplemental: Experiments to Validate MASW Inversion Results

This supplemental material addresses three overarching themes:

1. Inversion Ill-posedness – An exact-data experiment based on the “base” firn–aquifer scenario is used to establish an upper bound on the accuracy of the inverse solution.
2. Inversion Hyper-parameterization – The “base” scenario is used to motivate the choice of the number of inversion runs.
3. Median Model Representation – The “base” scenario is further used to evaluate whether the median model provides a reliable representative solution.

5.11.1 Inversion Ill-Posedness

Deterministic inversion is fundamentally non-unique (e.g., Foti *et al.*, 2018); consequently, even with exact input data (ranging from 5 to 40 Hz), a range of physically distinct model solutions can be produced. Figure 5.12 illustrates this behavior for the exact data derived from the ”base” firn-aquifer scenario. We ran the inversion 100 times with 200 iterations per run; further parameterization details, although important, are deferred to Section 5.11.2.

The median-model solution (green curve in Figure 5.12a) closely approximates the true velocity profile (dotted black curve in Figure 5.12a). However, among the five best-fitting solutions (Figure 5.12b) based on lowest data misfit, one stands out as clearly inaccurate. The orange model, despite a low misfit of 0.219%, completely fails to resolve the aquifer layer. This example underscores the inherent non-uniqueness of deterministic inversion and highlights the value of Monte Carlo simulations in addressing this issue. By incorporating a statistical perspective on the ensemble of solutions, such simulations support a more robust estimate, as demonstrated here using the calculated median curve.

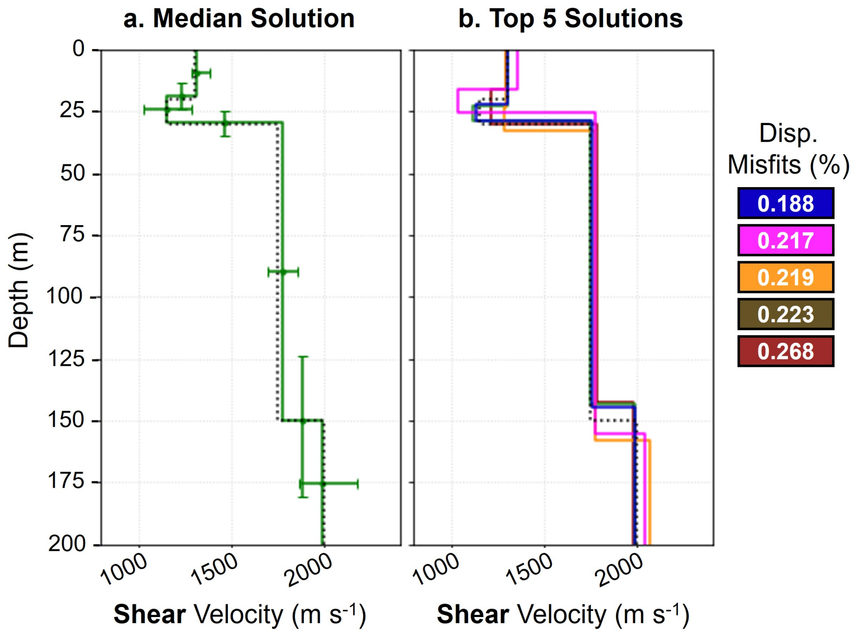

Figure 5.12 Results of an inversion test where the exact data is used as input in the inversion (i.e., the numerically calculated DC_{theo} is treated as d_{obs}). (a) Median model solution for 100 runs, with 200 iterations per run (in green), versus the true solution plotted as a dotted black curve. The error bounds are calculated from the solutions ranking between the 10th and 90th percentiles. (b) Top five solutions based on lowest data misfits, which are color-coded by the misfit percentages. We note that the yellow model solution, despite having a low misfit, does not resolve the aquifer layer and, as such, emphasizes the non-uniqueness of the inverse problem.

5.11.2 Inversion Hyper-Parameterization

In *MASWaves*, the number of iterations and the number of Monte Carlo simulations are the primary hyperparameters governing the inversion. Iteration counts can be reasonably determined from rate-of-convergence plots. In this supplemental study, we motivate our choice of six runs, which were used in the analyses presented in the main text.

It should be noted that the results presented here for the “base” firn-aquifer scenario come from a different execution of the inversion (with all parameters held constant) than those shown in the main text. Although exact replication is not expected in a Monte Carlo framework, the consistency between these results and those in the main text demonstrates the reliability of our overall findings.

Figure 5.13 shows the median solutions for Z, R, and CC components across two inversion setups: six runs (upper row of subplots) and 100 runs (lower row). The median solutions are computed from the subset of models whose data misfits fall between the 10th and 90th percentiles of all inversion results.

All six experiments in Figure 5.13 show consistently low data misfits, with the median d_{calc} (green curves in the left subplots), closely tracking d_{obs} (solid black curves). Although the Z-component misfit may appear slightly higher, direct comparisons risk over-interpretation especially since the d_{obs} vary between each component, and we have noted the inaccuracy of the Z and R components at low frequencies and therefore longer wavelengths in the main text (Figure 5.4).

Model solution accuracy is highest in the CC component experiments, where the median $V_s(z)$ profile (green curve, right subplots in Figure 5.13) closely matches the true model (dotted black curves) for both the six-run and 100-run experiments. Although all six experiments recover near-accurate $V_s(z)$ solutions in the firn-aquifer region, the single-component inversions (Z and R) poorly resolve the deeper ice and bedrock structure.

Of particular concern in the single-component approaches is when the true model values for either ice or bedrock V_s or the ice-bedrock interface lie near the edges of the associated uncertainty bounds (refer to purple arrow annotations on Figure 5.13. This indicates low confidence in the corresponding median estimates and invites speculation about the individual model solutions from which the medians were calculated. This is explored in Section 5.11.3.

5.11.3 Median Model Representation

We focus on the six-run experiments to assess the robustness of individual solutions and the reliability of the median. The consistency between the 6- and 100-run results lends credibility to this smaller set, suggesting that the outcomes from just six runs provide a reasonable approximation of the broader distribution of model solutions (Figure 5.13).

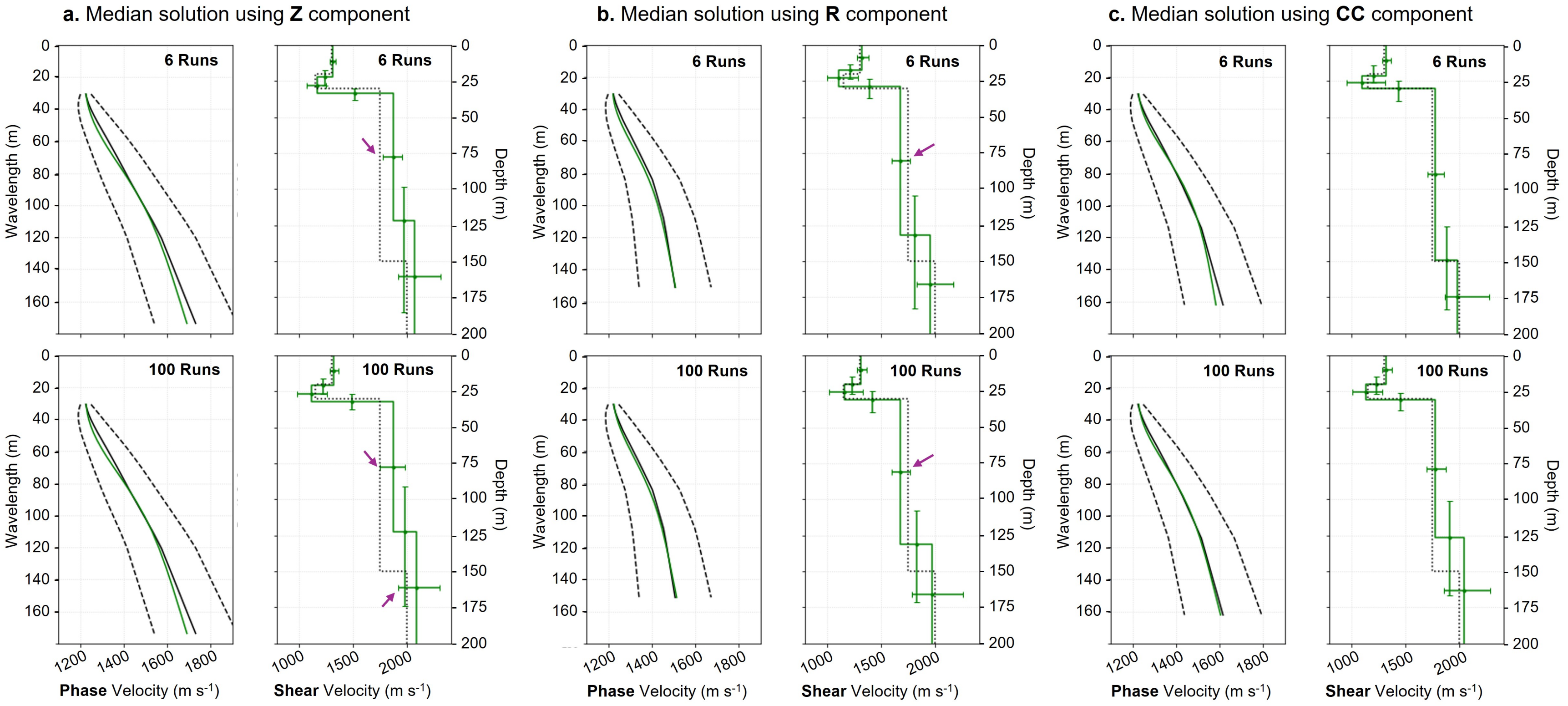

a. Median solution using **Z** component

b. Median solution using **R** component

c. Median solution using **CC** component

Figure 5.13 Comparison of the median solutions from six inversion runs using (a) *CC*-, (b) *Z*-, and (c) *R*-component dispersion data. The *CC* component, constructed by combining complementary *Z* and *R* data, yields the most accurate estimate of the subsurface structure. See Figure 5.12 for subplot descriptions and line definitions.

Figure 5.14 through Figure 5.16 show the model solutions and associated data misfits for each iteration within each of the six inversion runs. The lines are color-coded by the data misfit percentage, illustrating clear convergence toward low-misfit solutions as each run progresses. In the R- and CC-component experiments (Figure 5.15 and Figure 5.16, respectively), five out of six runs successfully recover the firn aquifer layer. Anomalous results, such as run #4 in the R experiment or run #5 in the CC experiment, appear sporadically but exert minimal influence on the overall median solution, as evidenced by the accurate prediction of the firn-aquifer structure in both the R- and CC-component experiments (Figure 5.13).

Following the observation made on the median solution of the six-run Z-component experiment, we note that each of the comprising individual runs shown in Figure 5.14 reasonably recovers the firn aquifer, but struggles to resolve the deeper ice and bedrock layers. In some cases, such as runs #3, #5, and #6, we recovered a three-layer system with the bedrock layer missing entirely. This limitation is likely related to inaccurate long-wavelength information in the d_{obs} stemming from poor low-frequency picks in the DC_{exp}. The R-component experiments exhibit similar poor resolution at depth, now due to less long-wavelength content in the d_{obs} (truncating around 150 m), again resulting from poor low-frequency DC_{exp} picks.

In contrast to the single-component experiments, the combined CC component more reliably recovered both the firn aquifer and deeper structures, with solutions closely aligning with the true model. In general, the V_s of the deep ice structure is well resolved across all individual CC runs (Figure 5.16). Most of the uncertainty is concentrated around the ice-bedrock interface and the bedrock V_s. The median estimates for both the interface depth and bedrock V_s in Figure 5.13 are fairly accurate, though they are associated with broader uncertainty bounds.

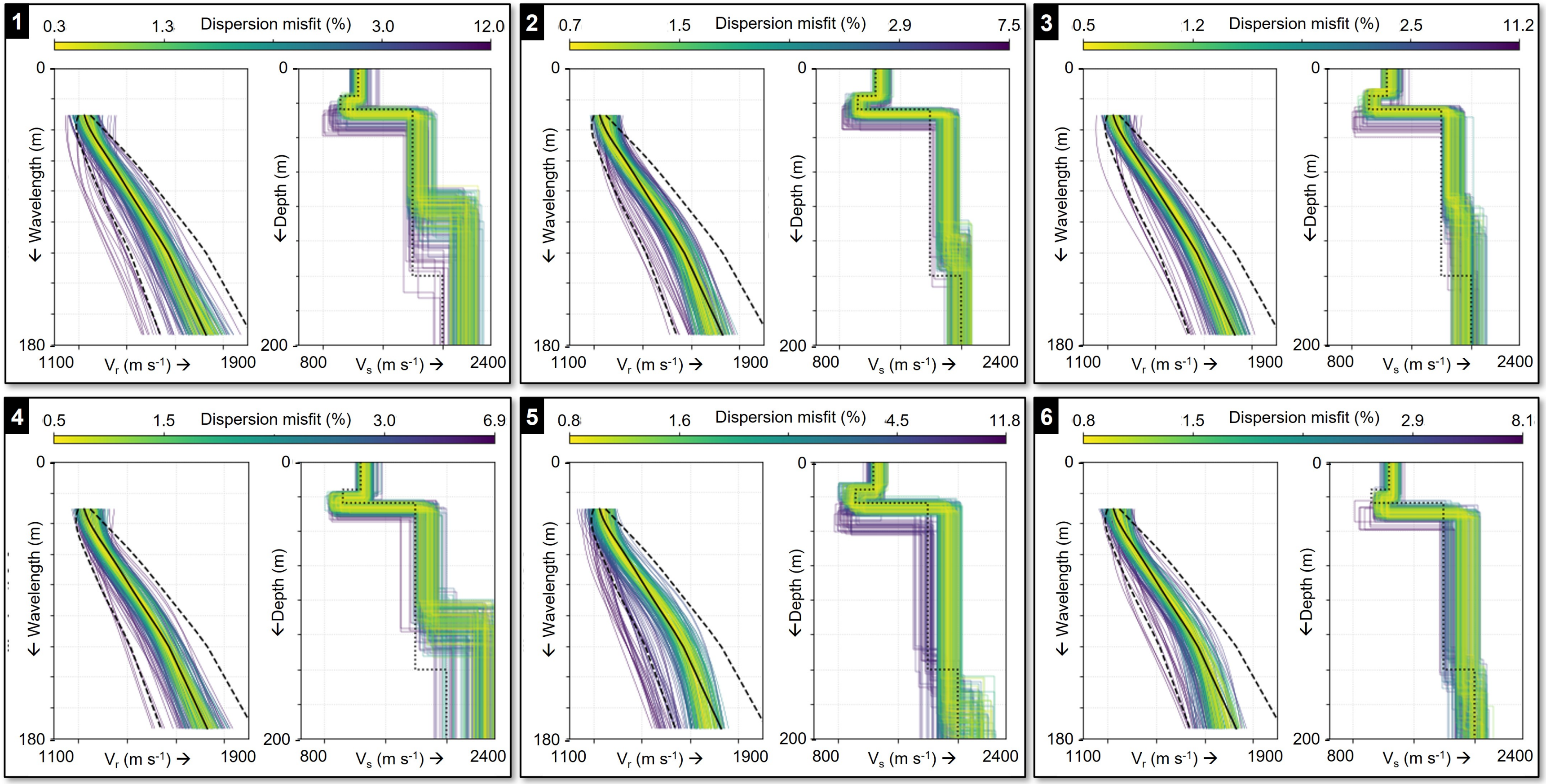

Figure 5.14 Results (curves colored by data misfit) from six inversion runs using the Z data as input. Although most runs recover a firn aquifer layer, the deeper ice and bedrock layers are poorly resolved. This suggests that although longer-wavelength information necessary for resolving these depths is present in d_{obs}, it does not accurately represent the true dispersion behavior, as can be confirmed by comparing DC_{exp} to DC_{theo} in Figure 5.4. All solutions converge at data misfit values ranging from 0.3% to 0.8%. See Figure 5.12 for subplot descriptions and line definitions.

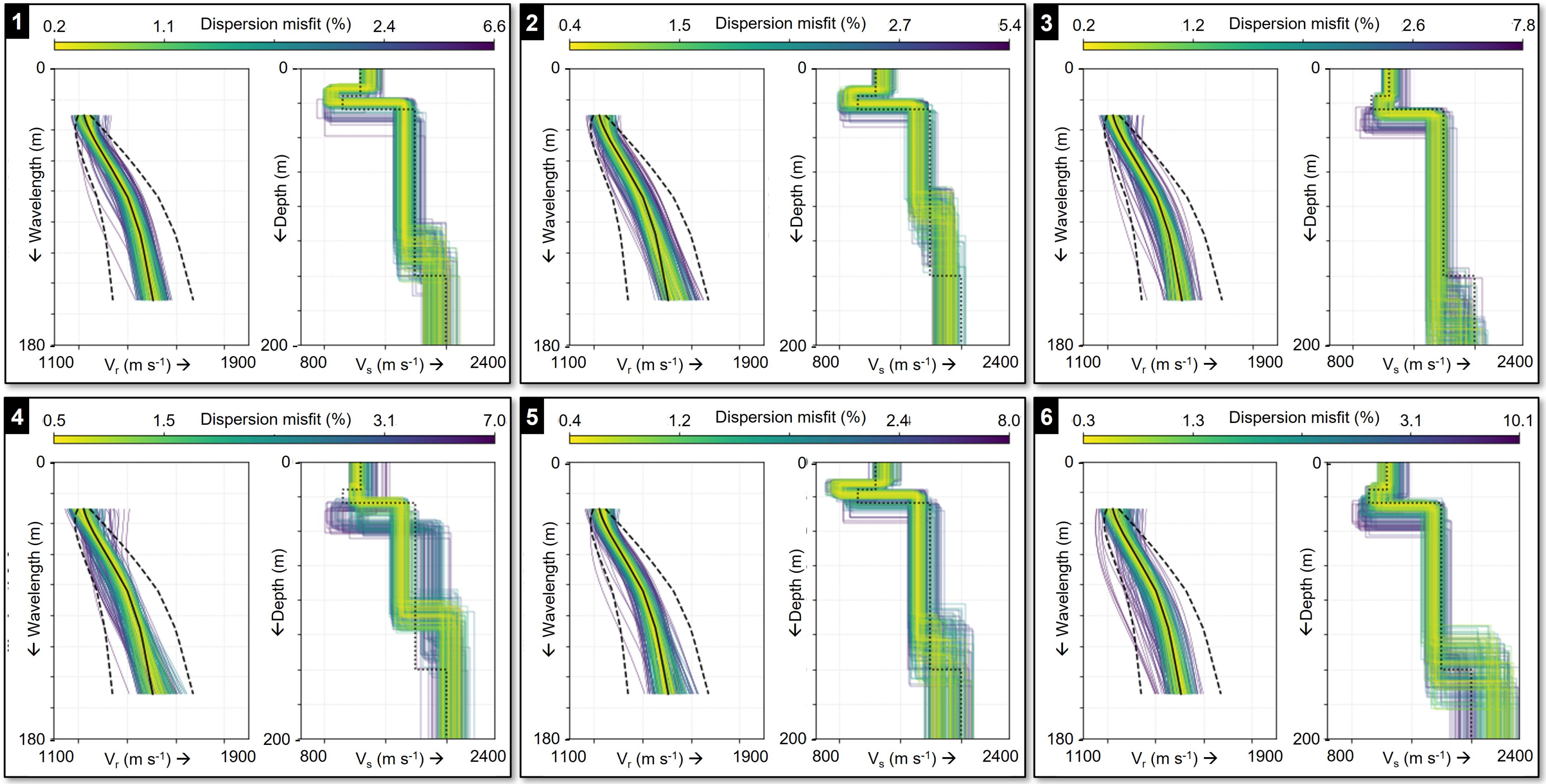

Figure 5.15 Results (curves colored by data misfit) from six inversion runs using the R data as input. Similar to the observations made in the CC-component experiment (Figure 5.16), five out of six runs recover a firn aquifer layer. In this experiment, however, the deeper ice and bedrock layers are poorly resolved, as in the Z-component experiment. Compared to the Z-component results, this is likely due to the d_obs capturing very little long-wavelength (above 150 m) information which stems from the DC_{exp} of Figure 5.4b. All solutions converge at data misfit values ranging from 0.2% to 0.5%. See Figure 5.14 for subplot descriptions and line definitions.

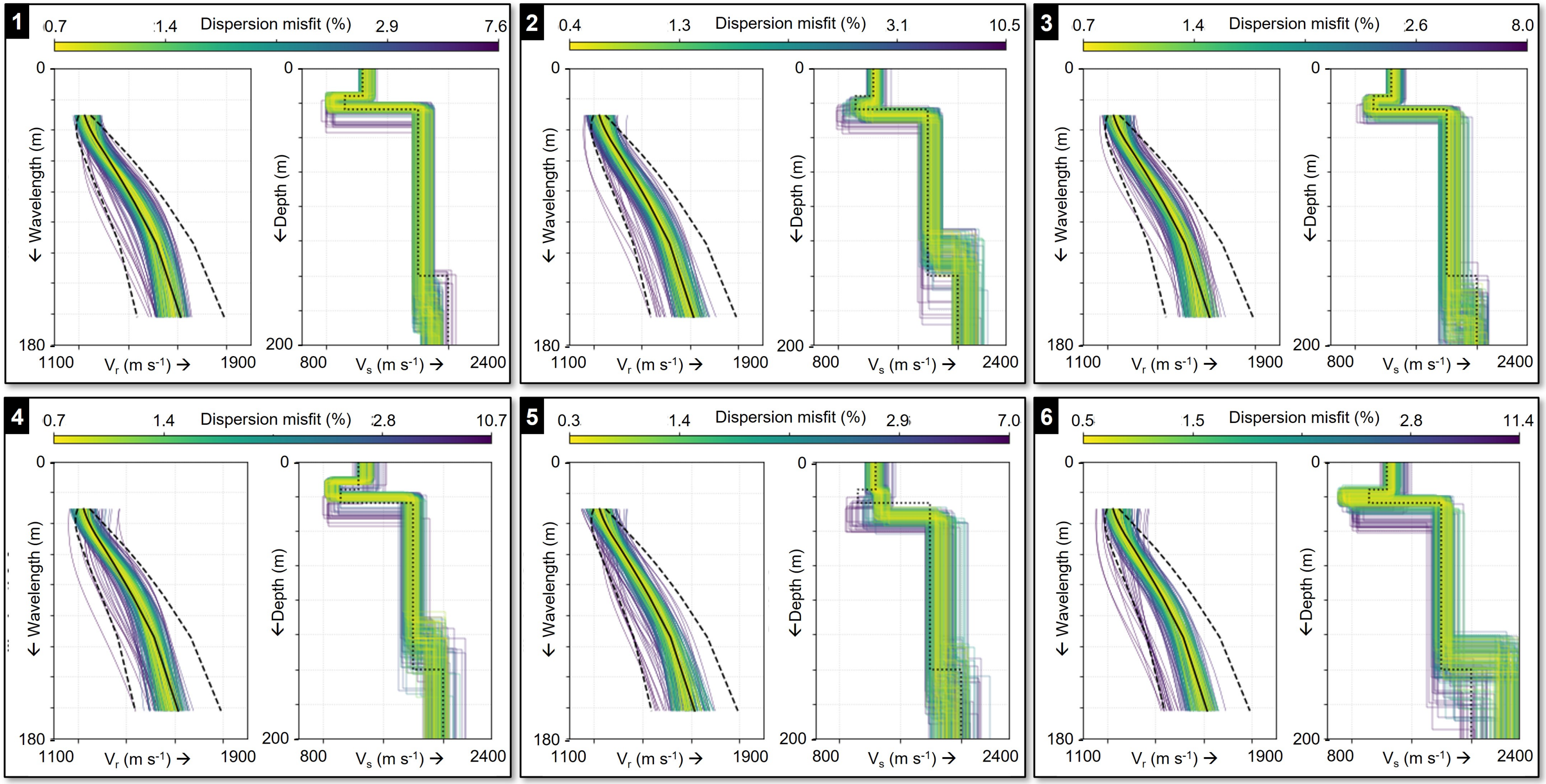

Figure 5.16 Results (curves colored by data misfit) from six inversion runs using the *CC* data as input. Most runs recover a firn aquifer layer, with the exception of run #5, despite the low misfit. Although such anomalous solutions can occur across any of the experiments in this study, they exert minimal influence on the median solution, as seen in both the six- and 100-run results in Figure 5.13. The deep ice V_s structure is generally well resolved across all runs, with most uncertainty concentrated near the ice-bedrock interface and in the bedrock V_s. Still, the median estimates for both parameters are reasonably accurate, albeit with broad uncertainty bounds. All solutions converge at data misfit values between 0.3% and 0.7%. See Figure 5.14 for subplot descriptions and line definitions.

CHAPTER 6

MAXIMIZING THE VALUE OF MULTI-COMPONENT SEISMIC DATA WITH ROBUST INVERSION APPROACHES

S. Garvey[1], J. Shragge[1], M. Siegfried[1]

6.1 Abstract

Rayleigh waves recorded on the radial-horizontal (R) component of geophones are sensitive to subsurface velocity structure and layering in ways that differ from vertical (Z) component data. Honoring the ellipticity of Rayleigh wave particle motion, a complex component (CC) is derived to better represent the vector-displacement which improves the accuracy of extracted dispersion curve (DC) data. Harnessing the finer-scale details of CC DCs, however, requires sufficiently adaptive algorithms, particularly in regions of complex or poorly understood geology. This study evaluates the capability of trans-dimensional Bayesian (TDB) inversion, compared with traditional deterministic multi-channel analysis of surface waves (MASW), to fully exploit CC dispersion data for depth-dependent shear-wave velocity modeling ($V_s(z)$) in a polythermal glacial environment.

We apply both MASW and TDB inversion to a multi-component (MC) seismic experiment on Slakbreen Glacier, Svalbard, to examine how prior assumptions about layering and noise sensitivity influence solution outcomes. A central limitation of MASW is the need to impose constrained model parameterizations to mitigate non-uniqueness and instability. In contrast, TDB inversion avoids such constraints, including the need to predefine the number of layers or explicitly flag low-velocity zones, and provides quantitative probability distributions for solutions of layering, $V_s(z)$, and data noise.

Our findings demonstrate that TDB inversions not only leverage the subtle yet critical improvements of CC DCs over MASW inversions, but also quantify the lower noise levels

---

[1] Department of Geophysics, Colorado School of Mines, Golden, CO 80401, U.S.A.

in the CC component relative to the Z and R components, highlighting that its value lies in both enhanced sensitivity and signal-to-noise characteristics. Additionally, we reveal ice layering at Slakbreen Glacier that plausibly marks the transition from cold to warm ice expected in a polythermal glacier. Interpretation of the CC-TDB results indicates that this transition ($V_s = 1772$ m s^{-1} to $V_s = 1661$ m s^{-1}) occurs at a depth of 94 m, followed by a transition from warm ice to bedrock ($V_s = 2116$ m s^{-1}) between 118 and 138 m.

6.2 Introduction

The shear-wave velocity (V_s) structure of near-surface formations strongly influences Rayleigh-wave propagation, particularly affecting their phase velocities (V_r) and dispersion (i.e., frequency-dependent phase velocity variations, $V_r(f)$) characteristics (Aki & Richards, 2002). Because of this sensitivity, inversion of Rayleigh-wave dispersion data has become a widely used approach for estimating V_s-depth profiles ($V_s(z)$). The inverse problem, however, is ill-posed, as the relationship between Rayleigh-wave dispersion and the V_s material property is strongly non-linear and requires careful numerical treatment.

Rayleigh waves propagate along the Earth's surface with elliptical particle motion. In multi-component (MC) seismic experiments using three-component (3-C) geophones, this particle motion is partially recorded on both the vertical (Z) and radial-horizontal (R) components, which can be combined using a complex system honoring their orthogonality as introduced in Chapter 4. The resulting complex-component (CC) representation of the Rayleigh wave signal produces higher accuracy dispersion curve (DC) data which subsequently benefits the inverse solution in terms of accuracy, stability, and uniqueness.

This MC approach is demonstrated in Chapter 5 using a deterministic inversion, known as multichannel analysis of surface waves (MASW). Introduced by Park *et al.* (1998), MASW has become popular due to its relatively straightforward implementation (Foti *et al.*, 2018) and the availability of open-source platforms such as *MASWaves* (Ólafsdóttir *et al.*, 2018b). Although MASW has been successfully applied in some glacial seismology studies (e.g., Killingbeck *et al.*, 2018; Kuehn *et al.*, 2024; Tsuji *et al.*, 2012), its broader application appears limited. This may be because the inverse problem is ill-posed, and even minor variations in model parameterization or data processing workflow can introduce significant biases or instabilities in the MASW inversion (evidenced in Chapter 5 and associated supplemental material). Reliable inversion results depend on prior knowledge of subsurface elastic layering to guide parameterization, which is often unavailable in glacial studies where radar methods are more commonly used. In addition, deterministic inversion does not provide explicit uncertainty quantification (e.g., Bodin & Sambridge, 2009; Tarantola *et al.*, 1982), so even when a Monte Carlo approach is applied with ideal data and parameterization, individual trials can yield variable solutions (Refer to experiment S5.1, Section 5.11). Suboptimal parameterization and weak data constraints further amplify this variability, underscoring the assertion that MASW may be less dependable in complex or poorly constrained glacial environments.

Unlike deterministic methods, which typically yield a single "best-fit" solution and may underrepresent model ambiguity, Bayesian approaches aim to explore the full solution space by employing a probabilistic framework that allows explicit quantification of uncertainty (Bodin & Sambridge, 2009; Tarantola *et al.*, 1982). A particularly valuable extension for geoscience applications is transdimensional Bayesian (TDB) inversion, which uses a variational inference strategy to treat the number of layers (and therefore the number of model parameters) as unknown rather than fixed a priori (Sambridge *et al.*, 2013). This approach minimizes risks associated with rigidly fixing model parameterization, which can produce biased or misleading results (Gao & Lekić, 2018). By allowing model complexity to adapt to the data, TDB inversion enables a more data-driven analysis of surface-wave dispersion, potentially making better use of the sensitivities inherent in MC data.

In this study, we compare the utility of TDB and MASW in leveraging the CC-DC data derived from an explosive-source multi-component experiment at the polythermal Slakbreen Glacier, Svalbard. We first outline the key elements of each inversion approach to provide the necessary background for interpreting the solutions. We then introduce the

MC experiment, describing how the CC-component data was generated and conditioned. We present the MASW results first, then the TDB results, and conclude with a discussion of the glacier's thermal regime to validate the CC-TDB solutions.

6.3 Comparison of Inversion Methods

In this section, we frame the inversion problem in the context of the MASW and TDB strategies employed. We review each method at a high level to facilitate comparison, generally following the flow of the inversion process. For algorithmic details, readers are referred to Ólafsdóttir *et al.* (2018b) and Magrini *et al.* (2025), which describe the open-source software packages used in this study (*MASWaves* and *BayesBay*).

Rayleigh-wave dispersion occurs because different frequencies penetrate to different depths: high frequencies are most sensitive to near-surface features, whereas low frequencies extend that sensitivity to deeper structures. Because V_s varies with depth (i.e., $V_s(z)$), the phase velocity as a function of frequency, $V_r(f)$, referred to as the dispersion curve (DC), is sensitive to the $V_s(z)$ profile. This relationship between $V_r(f)$ and $V_s(z)$ is strongly non-linear, making the inverse problem inherently ill-posed and requiring numerical forward modeling to compute theoretical DCs as well as stochastic sampling to robustly explore the model space. Both MASW and TDB employ these strategies with the objective of finding a model, m, whose theoretical DC (DC_{theo}) closely matches the observed DC (DC_{obs}).

Figure 6.1 presents the key elements of the MASW and TDB inversions. In both schemes, the workflow involves:

(a) defining a set of fixed parameters held constant throughout the inversion,

(b) defining the free model parameters to be solved for,

(c) calculating DC_{theo} based on the current proposed model m' (initially selected from (a) and (b), or updated from the previous iteration),

(d) calculating the misfit between DC_{theo} and DC_{obs},

(e) evaluating whether m' should replace the current model m, and

(f) proposing a new model m' based on m.

The primary distinction between the two inversions lies in the mechanics: how the model parameter spaces are defined (fixed versus free), how data similarity is measured, and the rules governing model acceptance, rejection, and updating.

6.3.1 Model Parameterization and Prior Assumptions

Model parameterization differs significantly between the two approaches. In MASW V_p and ρ are fixed, whereas TDB uses a forward function dependent on V_s but allows V_p and ρ to be recalculated at each iteration following the model update (Figure 6.1a). In both inversions, V_p and ρ not considered free parameters as they are not being optimized each iteration. The $V_s(z)$ is the common free Earth parameter for both MASW and TDB, although the depth solution is handled differently in each inversion.

In MASW, the number of layers (k) is a fixed hyperparameter (Figure 6.1a) that allows for layer thickness, h to be treated as free parameter (Figure 6.1b). In contrast, TDB explores solutions of k dynamically through a stochastic strategy facilitated by reversible-jump Markov Chain Monte Carlo (rj-MCMC) (Green, 1995), which is discussed in Section 6.3.3.

Another key fixed hyperparameter in MASW is the number of anticipated V_s reversals, which determines whether the inversion allows low-velocity layers in the candidate models m' (Figure 6.1a). While permitting reversals broadens the solution space, we observe that in settings without true low-velocity layers this flexibility may introduce instability and yield misleading results. In contrast, TDB inversion, implemented through the rj-MCMC framework and a Voronoi partitioning strategy (discussed in Section 6.3.4), naturally explores models with or without reversals (Figure 6.1b). In the Bayesian framework, the preference for simpler solutions (parsimony) reduces unnecessary complexity, allowing the inversion to remain stable across a broad model solution space.

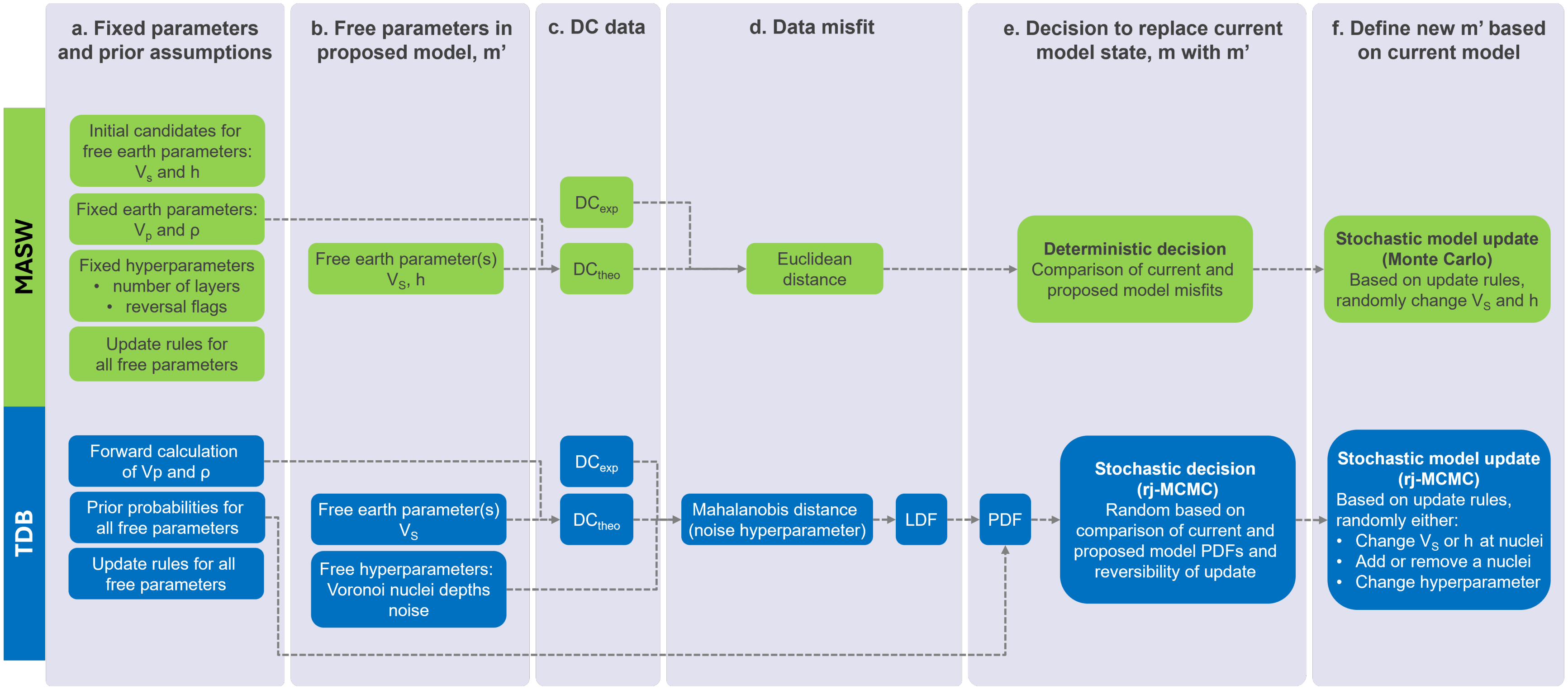

Figure 6.1 Key elements of the MASW (green workflow) and TDB (blue workflow) inversions. Both approaches involve proposing a new model m', evaluating whether it should replace the current model m, and, if accepted, using it to generate the next m'. The main distinction lies in the inversion mechanics: the definition of parameter spaces (fixed versus free in (a) and (b), respectively), the method of measuring data similarity (c and d), and the rules for model acceptance, rejection, and updating (e and f).

Additionally, the Bayesian approach requires prior probability distributions for each free Earth and hyperparameter. In our implementation, we assume uniform prior distributions between user-defined upper and lower bounds so as not to bias the solution. These bounds also define the limits of the model space, which are similarly pre-defined in MASW. In Figure 6.1a, we group these boundary definitions as part of the update rules that govern the overall sampling and iteration scheme of both inversions.

6.3.2 Data Misfit and Noise Quantification

In both inversions, we forward modeled Earth parameters to generate DC_{calc}, which we then compared with DC_{obs} (Figure 6.1c). In MASW, this comparison is evaluated using a least-squares (Euclidean) misfit function, whereas in TDB the misfit is more commonly expressed through the Mahalanobis distance (Figure 6.1d) which accounts for correlated data, such as the trend between phase velocity and frequency (McLachlan, 1999).

Noise is not directly accounted for in the MASW workflow; instead, it is often mitigated during preprocessing through steps such as down-sampling, filtering, or stacking. In contrast, TDB more formally incorporates uncertainty within the inversion, requiring an estimate of a data covariance (noise) matrix in the Mahalanobis distance calculation. In TDB, accurate noise quantification is particularly critical, as mischaracterization can bias model complexity outcomes Bodin *et al.* (2012). Following the approach and cautions of Bodin *et al.* (2012), we treated noise as a free hyperparameter (Figure 6.1b) to be approximated through inversion.

Since TDB is a Bayesian formulation, the misfit is expressed probabilistically via the likelihood density function (LDF), which in our implementation is approximated by a Gaussian distribution. This is multiplied by the prior probabilities of each free hyper- and Earth parameter to produce a posterior density distribution (PDF).

6.3.3 Evaluation of Candidate Models

A core distinction between MASW and TDB inversions lies in how candidate models are evaluated (Figure 6.1e). In MASW, model selection is deterministic: a candidate model is accepted if it yields a lower Euclidean misfit than the current state. In contrast, TDB evaluates candidate models probabilistically by comparing their PDFs, together with aspects of reversibility and stochasticity, all embedded within the rj-MCMC framework outlined below.

The rj-MCMC strategy foundational to TDB extends the traditional MCMC algorithm, specifically the Metropolis-Hastings (MH) formulation (Green & Hastie, 2009). In a standard MCMC approach, a series of candidate solutions are generated following Markov chain rules, and as the target probability distribution of solutions (PDF in a Bayesian application) becomes stationary (i.e., relatively unchanging with each iteration), samples from the PDF of each model parameter are drawn using Monte Carlo rules. To ensure that the chain will converge to the correct PDF, MCMC algorithms must satisfy the detailed balance condition: the probability of moving from m to m' is equal to the probability of moving from m' to m (proposal ratio). This concept of 'reversibility' prevents chains from systematically favoring certain updates over others and is implemented either implicitly or explicitly depending on the specific algorithm. In the Metropolis–Hastings formulation, this criterion is embedded in an acceptance probability that governs whether a proposed model update is accepted or rejected. The acceptance probability is a product of the proposal ratio and the ratio of posteriors between m' and m, which plays a role analogous to the misfit measure used in MASW. The acceptance probability introduces an element of randomness, allowing a "worse" model to be accepted, which helps the algorithm explore the full model space.

The rj-MCMC modifies the acceptance probability to account for the potential change in dimensionality inherent to TDB. Invoking a model update in which k is altered changes the total number of model parameters (model dimensionality). When this occurs, the detailed balance condition must be satisfied across jumps in dimensionality. However, because a dimensionality change alters the parameter space, the density distribution becomes biased and requires correction. In rj-MCMC, this is achieved by scaling the acceptance probability with a Jacobian term, ensuring reversible jumps and that the PDFs of all free parameters converge to the stationary target distribution.

6.3.4 Model Space Discretizations and Updates

Changing the number of layers using rj-MCMC is facilitated by a flexible Voronoi partitioning strategy, where each partition (layer) is associated with a Voronoi nucleus with assigned free Earth parameters. The boundaries between layers correspond to equidistant surfaces between adjacent nuclei. Proposed model updates can involve changing the properties of a nucleus, adding or removing nuclei (thereby changing the number of layers), or adjusting hyperparameters that control model smoothness or data noise levels (Figure 6.1f).

Unlike adaptive TDB discretization, MASW uses an a priori fixed model discretization (Figure 6.1a) that involves changing the free Earth parameters of a layer to update a model. To facilitate more complete exploration of the solution space and partially mitigate trapping in local minima, a Monte Carlo strategy is employed in the *MASWaves* implementation (Figure 6.1f), which introduces random perturbations of the free Earth parameters within user-defined bounds.

6.3.5 Implementation and Post-Inversion Analysis

Each inversion proceeds iteratively until reaching a user-defined maximum number of iterations. In a single MASW run, each sequential candidate model is designed to reduce the misfit, so the “best” fit final model is that having the lowest misfit. In contrast, in a single Markov chain of TDB, misfit is not necessarily reduced sequentially, and the “best” model is not automatically the final one. Instead, all models in the stationary distribution produce reasonably low data misfits and lie within the user-defined bounds of the model solution space. Evaluating the resulting PDFs of each free parameter therefore provides criteria alternative to data misfit for selecting a “best” model.

Across multiple runs, the “best” models identified by MASW can vary substantially, reflecting the fact that the method often explores only a narrow portion of the solution space, with different runs sampling regions that may not even overlap. This variability persists even though each run begins from the same user-defined initial model, underscoring the sensitivity of MASW to its starting conditions. Conversely, TDB demonstrates greater consistency across runs because it is designed to explore the solution space more comprehensively. This is facilitated in part by the random selection of the initial model within the predefined bounds of the model space, which allows each run to access a broader range of possible solutions rather than being confined to a single starting point.

Comparisons of MASW results across runs can lead to misleading statistical summaries, since the “best” models from different runs may be so disparate that aggregate measures, such as the median V_s, do not correspond to any physically plausible individual model. By contrast, TDB provides a more reliable framework for assessing model variability because it evaluates full posterior distributions across chains, enabling statistical measures that are grounded in the probability structure of the solution space rather than in potentially inconsistent sets of final models.

6.4 Svalbard Dataset

In March 2025, the University Centre in Svalbard (UNIS) hosted an Arctic Seismic Exploration course led by researchers from the University of Bergen and funded through an Equinor research venture. As part of the course, an explosive-source 3-C seismic experiment was conducted at the Slakbreen Glacier, Svalbard (Figure 6.2). This survey was part of a broader geophysical investigation that also employed radar and distributed acoustic sensing to study the englacial structures of the polythermal glacier expected to have thermal ice layering likely of cold ice (below the melting point) overlies a layer of temperate ice at the melting point (Pälli, 2003). The 2 km 3-C experiment was oriented along the glacier centerline in the ablation zone. Explosive sources were excited every 12.5 m (Figure 6.2c) and seismic data were recorded on 24 3-C geophones with a 10 Hz natural frequency deployed between shot points 107 and 119 at a 6.25 m spacing (Figure 6.2c). The horizontal components of the 3-C geophones were oriented East and South, an unconventional setup that required modified pre-processing to rotate the data into radial (R) and transverse (T) components and to preserve the expected phase relationships between wave modes on the Z- and R-components.

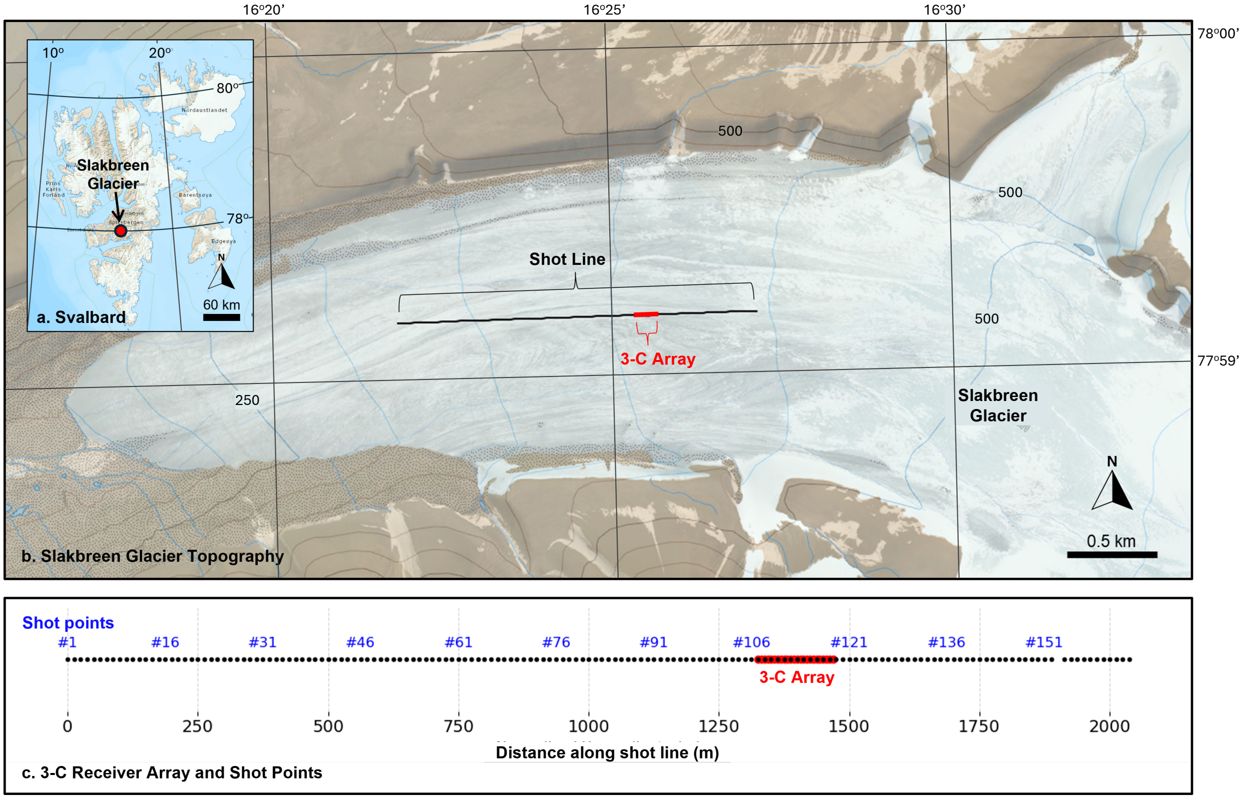

Figure 6.2 Overview of the Slakbreen Glacier seismic experiment. (a) Location of Slakbreen within Svalbard. (b) Site map of the Slakbreen Glacier area with elevation contours (meters) and location of 3-C experiment overlaid on satellite imagery from `https://toposvalbard.npolar.no/`. (c) Layout of the 3-C seismic experiment showing the source-receiver acquisition geometry.

Figure 6.3 shows raw Z- and R-component shot gathers from shot location 91 (plotted in Figure 6.2c) displayed on equivalent amplitude scales. The surface Rayleigh-wave energy appears of comparable strength on each but with a 90° phase difference, whereas the direct

P wave is more prominent on R, albeit with opposite polarity. Noise and null traces are present on both gathers but differ in position and character. A weak reflection event is also visible on both components, possibly originating from depths near the bedrock.

Following the approach of Chapter 4, we constructed a supergather from shot locations 1 to 101 on the western side of the 3-C array to boost SNR, infill missing trace information, and maximize depth of investigation by extending the receiver array length. Figure 6.4 shows the Z-, R-, and CC-component supergathers plotted on equivalent amplitude scales, with specific wave modes annotated on the Z-component gather. The CC component is a complex-valued signal; to visualize the gather, the absolute value of the complex signal is taken and the sign is reassigned based on the Z-component polarity. In Figure 6.4c, a few locations are annotated where the Rayleigh-wave signal is visually enhanced, while other modes, such as the direct and reflected waves, are slightly diminished because they do not conform to the phase shift between Z and R on which the complex summation is based.

In Figure 6.5a, we show the dispersion panel (DP) constructed from the CC-component supergather in Figure 6.4c, together with the fundamental DC_{obs} curves from the corresponding Z, R, and CC DPs between 8 and 60 Hz. These picks fall well within the measurable range of frequencies given the acquisition geometry of 6.25 m receiver spacing and an array length of $\sim$ 1400 m. We transformed these picks to V_r versus wavelength (Figure 6.5b), which served as the data representation input into the inversions. The most substantial differences between the three components are observed at wavelengths over $\sim$ 160 m.

Data were sub-sampled to 50 points for input into the MASW and TDB inversions to improve computational stability and speed. Section 6.11 details the inversion algorithm parameterizations.

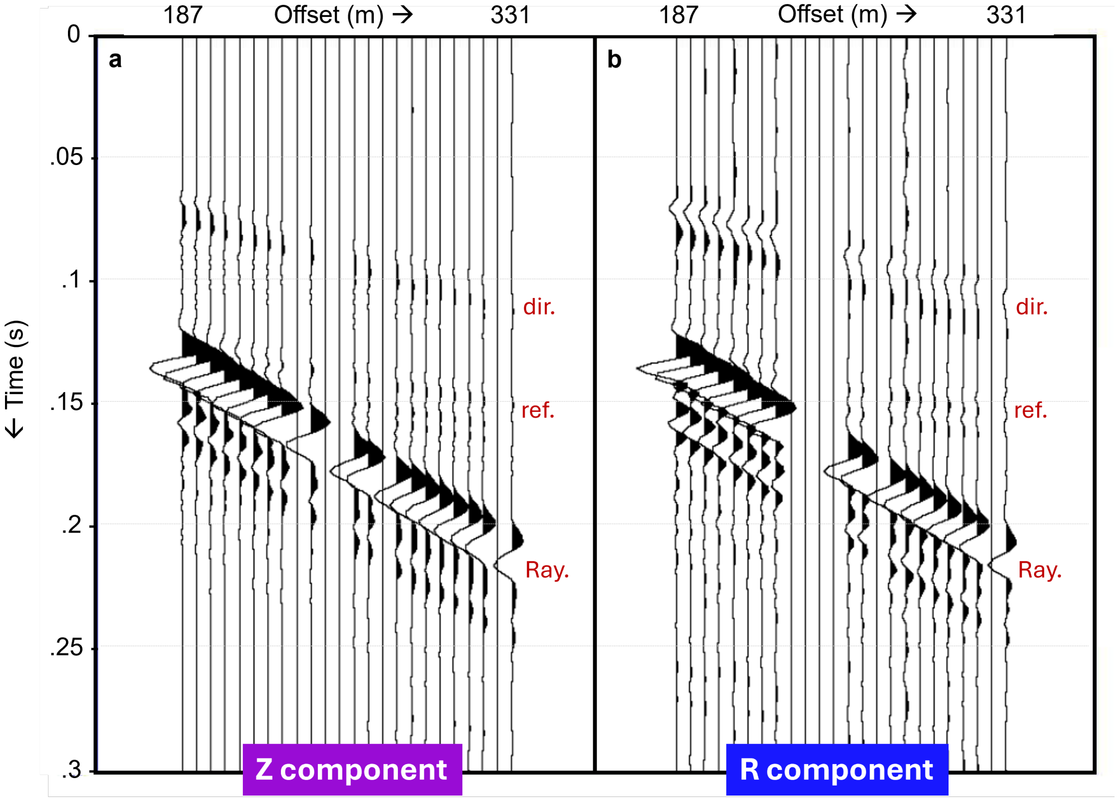

Figure 6.3 Raw Z- and R-component shot gathers from shot location 91 (plotted in Figure 6.2c) shown on equivalent amplitude scales. Surface Rayleigh-wave energy (annotated "Ray.") is equally strong on both components, whereas the direct wave (annotated annotated "dir.") appears stronger on R. A weak reflection (annotated "ref.") is also observed on both components.

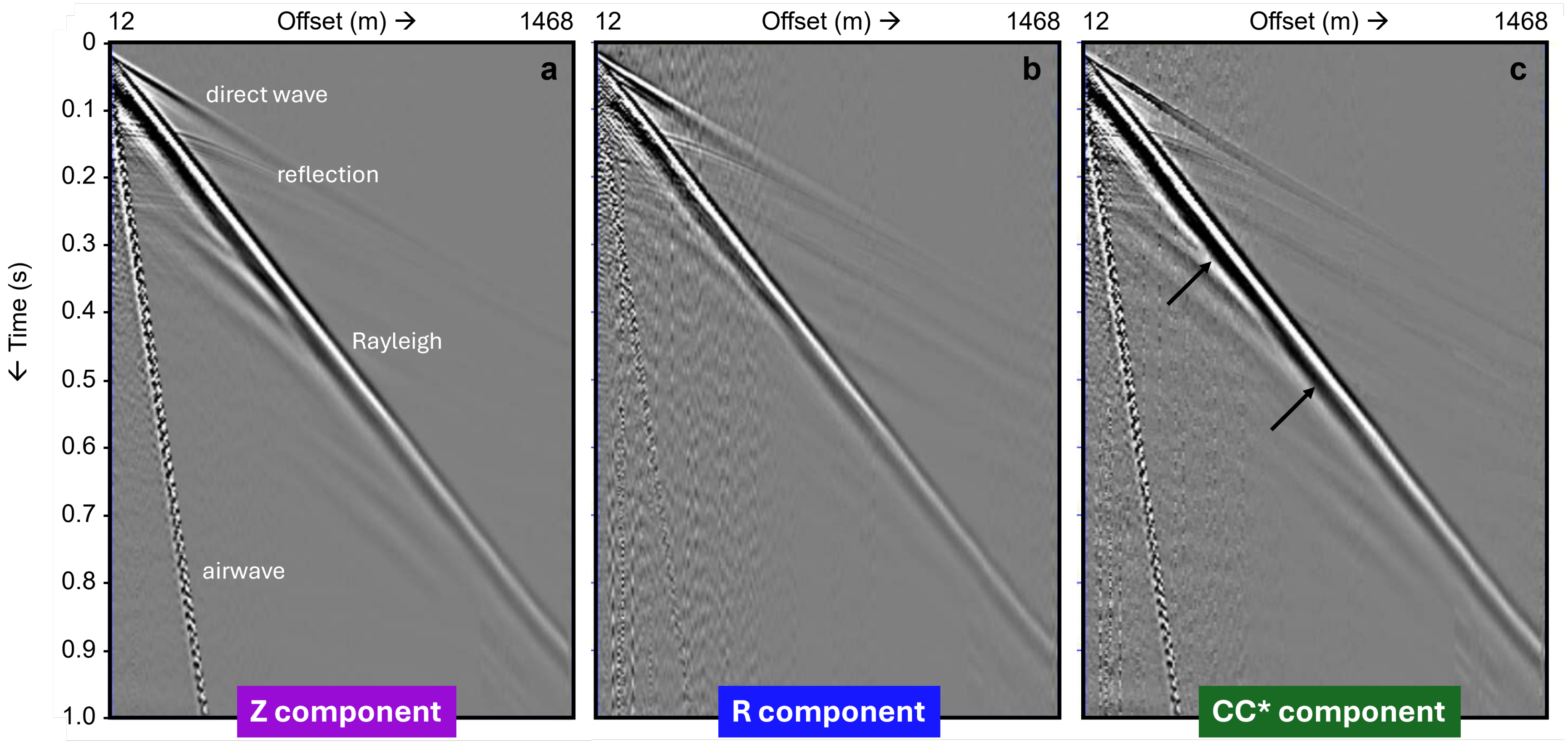

Figure 6.4 (a) Z-, (b) R-, and (c) CC^*-component supergathers constructed from shots 1 to 101 on the western side of the 3-C array (refer to Figure 6.2c). As the CC component is a complex-valued signal, the CC^* gather is visualized by taking the the absolute value of the complex signal and reassigning polarity based on that of the Z-component. All gathers are plotted on equivalent amplitude scales, with specific wave modes annotated on the Z-component gather. The CC representation enhances the Rayleigh-wave signal (black arrows annotated on the CC gather), whereas wave modes that are not recorded with a 90° phase shift between the Z and R components are slightly diminished by the summation.

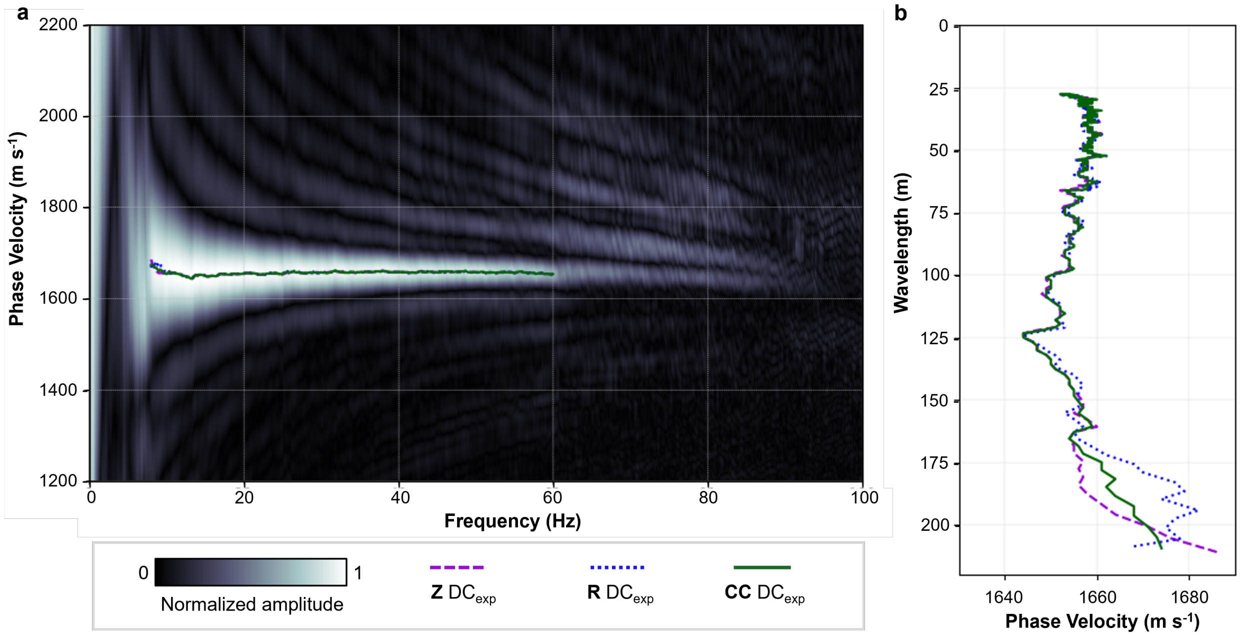

Figure 6.5 (a) Dispersion panel for the CC component, based on a supergather constructed from 101 shot gathers acquired on the western side of the 3-C array. DC_{obs} picks from this panel are plotted in green between 8 and 60 Hz and, for comparison, the equivalent Z- and R-component picks are plotted in blue and purple, respectively. (b) Comparison of all three components DC_{obs} picks transformed to plots of V_r versus wavelength, the representation of the data used as input for inversion.

6.5 MASW Results

We first present MASW inversion results using only the CC component to illustrate sensitivities to fixed parameters discussed previously (Figure 6.1a). These parameters include the velocity reversal flag and the initial model, which for these experiments consisted of two ice layers with equal Earth parameters over bedrock. The results are summarized in Figure 6.6, where each row corresponds to an experiment and the three columns display, for that experiment: (1) the initial model; (2) the observed data, the calculated data from each iteration colored by misfit percentage, and the median calculated between the 10th and 90th percentiles of the results; and (3) the model solutions from each iteration colored by misfit percentage along with the median solution. In experiment #1 (Figure 6.1a1—a3), velocity reversals are not allowed, whereas in experiment #2 (Figure

6.1b1—b3), the reversal flag is enabled. In experiment #3 (Figure 6.1c1—c3), the initial model from experiment #2 is modified so that the internal interface between the two ice layers is shifted shallower by 40 m.

Both experiments #1 and #2 yield reasonable median solutions (red curves in Figure 6.6a3 and b3), as the calculated median data (red curves in Figure 6.6a2 and b2) closely match the observed data (black curves). However, the models differ notably: experiment #1 shows an increasing velocity profile with depth, whereas experiment #2 resolves a low-velocity zone as the second layer. Misfits are slightly lower in #2 (as low as 0.1%) compared to #1 (as low as 0.18%), giving a small preference to solution #2.

The credibility of experiment #2 is influenced by the choice of initial model parameterization. In experiment #3, the depth of the internal ice interface is shifted from 100 m to 60 m, and though the initial $V_s(z)$ profiles are unchanged (Figure 6.6b1 and c1), the results are substantially different. The model from experiment #3 shows a thicker low-velocity second layer than in experiment #2, although the misfits remain similar. Notably, the error bar associated with the top-depth of the low-velocity layer is narrower in experiment #3, whereas in #2 the error bars for this interface are biased shallower, suggesting that results of #3 may better reflect the true structure.

The varying results of experiments #1 through #3 underscore the constrained solution space imposed by MASW parameterization, and the rationalizations based on misfits and median error bars exemplify the need to speculate within the limited uncertainty quantification the method provides.

The aforementioned limitations of MASW also restrict comparisons between experiments conducted with the CC component and the single-components. In Figure 6.7, the CC experiment was re-run alongside equivalent inversions using the individual Z and R components from which CC was constructed. The CC experiment produced a slightly lower data misfit of 0.1% versus the single-component cases (0.15%). Interface depths are similar across all median solutions (red curves in Figure 6.7a2, b2, and c2).

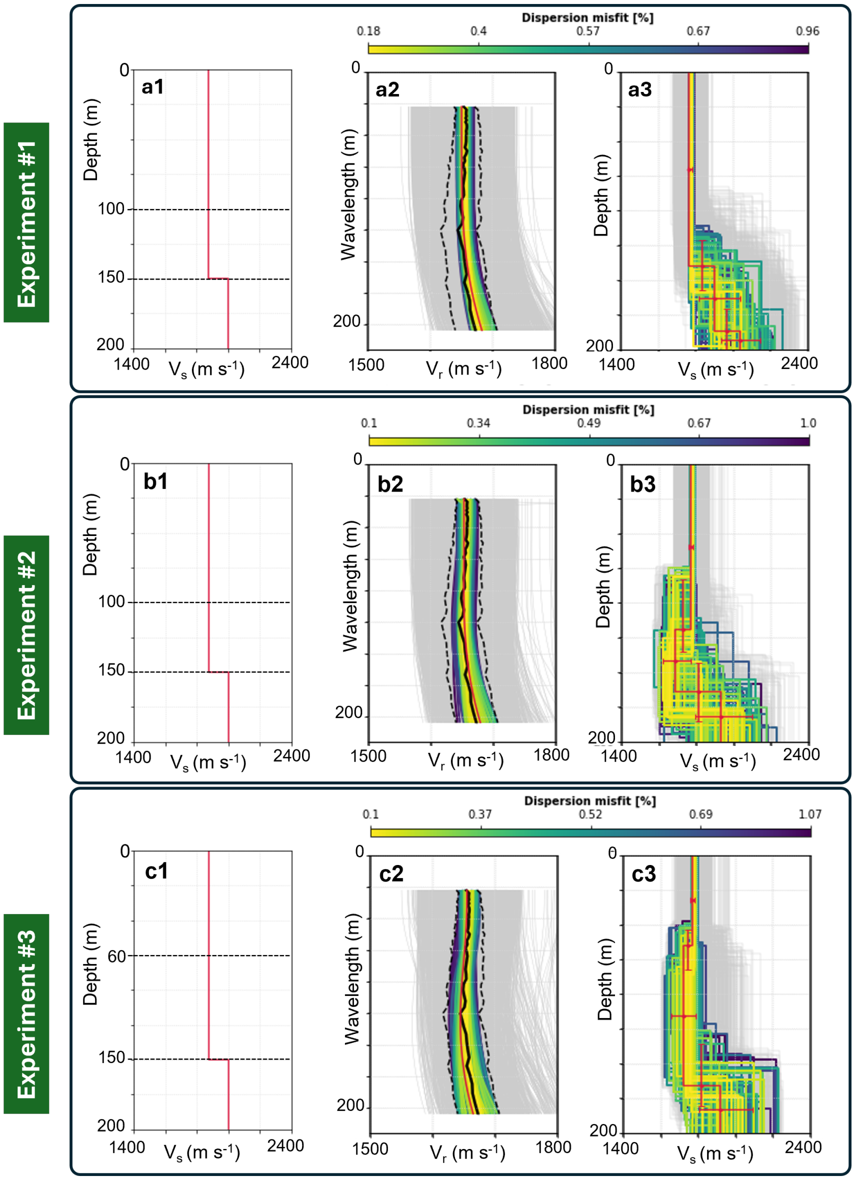

Figure 6.6 Results of three MASW inversion experiments, shown by row. (a, b) The initial model consists of two ice layers with identical elastic properties over bedrock; in (b) the reversal flag allows a low-velocity layer. (b, c) Both include a low-velocity layer, but the internal ice boundary is shifted from 100 m in (b) to 60 m in (c). Columns show: (1) initial model, (2) observed data (solid black), error bounds (dashed black), calculated data from each iteration (colored by misfit percentage), and the median between the 10th and 90th percentiles (solid red), and (3) model solutions from each iteration (colored by misfit percentage) with the median solution (solid red).

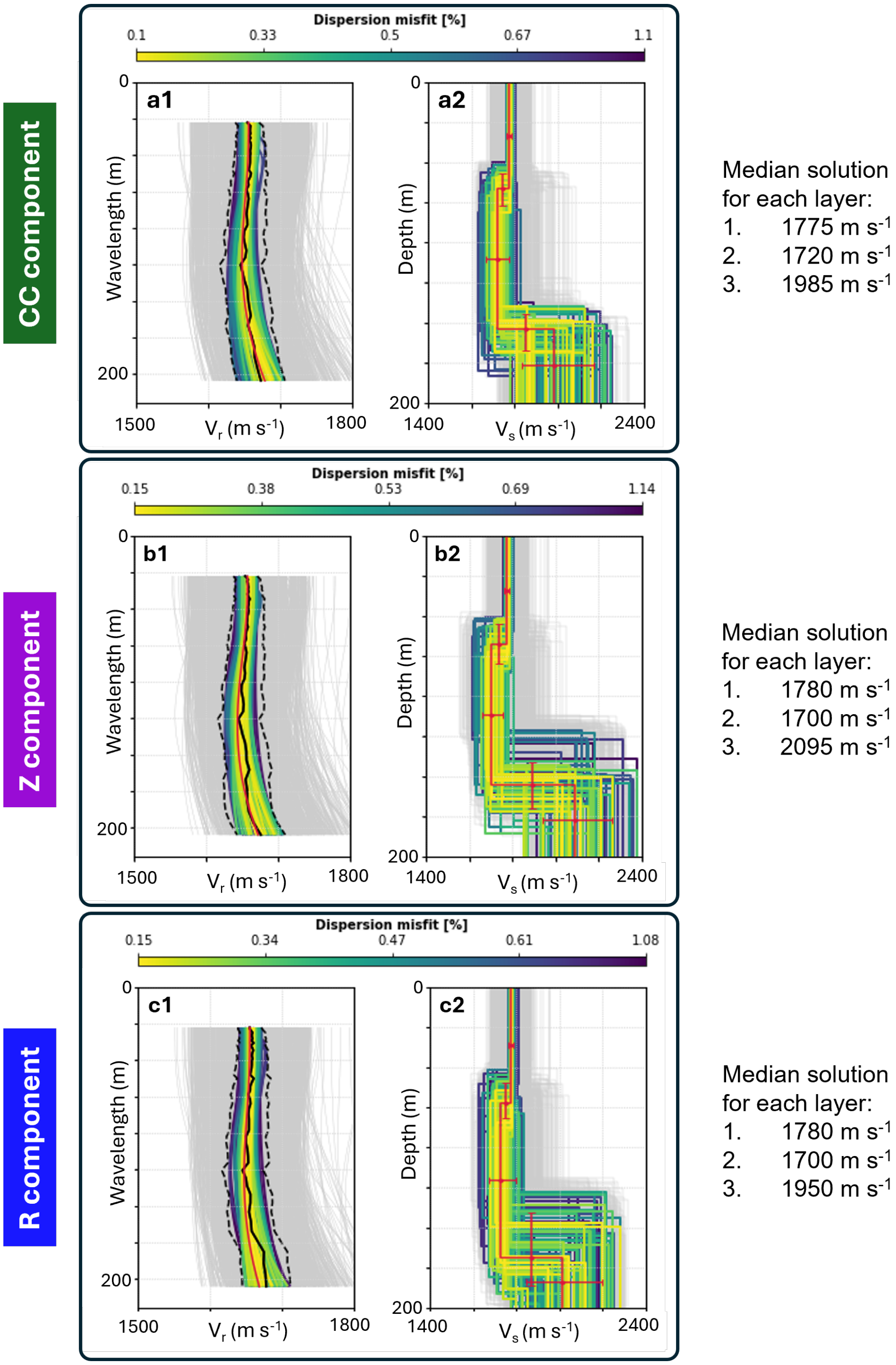

Median solution for each layer:
1. 1775 m s^{-1}
2. 1720 m s^{-1}
3. 1985 m s^{-1}

Median solution for each layer:
1. 1780 m s^{-1}
2. 1700 m s^{-1}
3. 2095 m s^{-1}

Median solution for each layer:
1. 1780 m s^{-1}
2. 1700 m s^{-1}
3. 1950 m s^{-1}

Figure 6.7 Results of three MASW inversion experiments using (a) *CC*-, (b) *Z*-, and (c) *R*-component data. All experiments use the same parameterization as experiment #3 in Figure 6.6. See Figure 6.6 for descriptions of the individual plots. The median solution for each of the three predefined layers is shown on the right for each experiment.

The first-layer V_s values differ by approximately 5 m s^{-1} between the CC (1775 m s^{-1}) and Z (1780 m s^{-1}) solutions. The second and third layers show larger differences, roughly 20 m s^{-1} and 110 m s^{-1}, respectively, with the CC results exhibiting weaker velocity contrasts and producing a $V_s(z)$ profile of reduced structural complexity. Specifically, the CC solution gives $V_s = 1720$ m s^{-1} for the low-velocity layer and 1985 m s^{-1} for deepest layer.

6.6 TDB Results

The MASW experiments highlighted the limitations of a deterministic inversion, in which plausible model solutions were assessed primarily through data misfits and sensitivity tests, providing a semi-quantitative perspective. In contrast, we apply a TDB inversion to the same Svalbard dataset (Figure 6.5), where the number of layers and noise assumptions are now treated as free hyperparameters optimized within the inversion.

In Figure 6.8, we show the model solutions from three experiments using the CC-, Z-, and R-component data. The median solutions of the shallowest ice layer are consistent across all three components at 1770 m s^{-1}. The shallow R-component solution now aligns with the CC and Z results, unlike in the MASW inversion, likely reflecting the explicit noise handling in the TDB methodology.

Without enforcing a low-velocity layer condition, all three median solutions resolve a low-velocity zone that is fairly consistent across components, with V_s values of 1660 m s^{-1} for both the CC and Z components and 1655 m s^{-1} for the R component. These values are generally lower than those obtained from the corresponding MASW inversions.

The V_s estimates for the deepest resolvable layer, likely corresponding to bedrock, differ notably across components. At this depth, we note that the SC solutions are especially sensitive to parameterization though each parameterization choice produces repeatable outcomes, with subsampling to 50 data points likely contributing to their stability. The Z-component yields a sharp interface solution consistent with hard bedrock of 3125 m s^{-1} and the R-component median solution is more complex, showing a gradual increase to

2260 m s^{-1} followed by a secondary low-velocity zone. The *CC* median solution indicates a bedrock velocity of 2115 m s^{-1} producing an overall V_s–depth profile with reduced structural complexity compared to SC solutions — an observation that is consistent with those drawn from the MASW experiments.

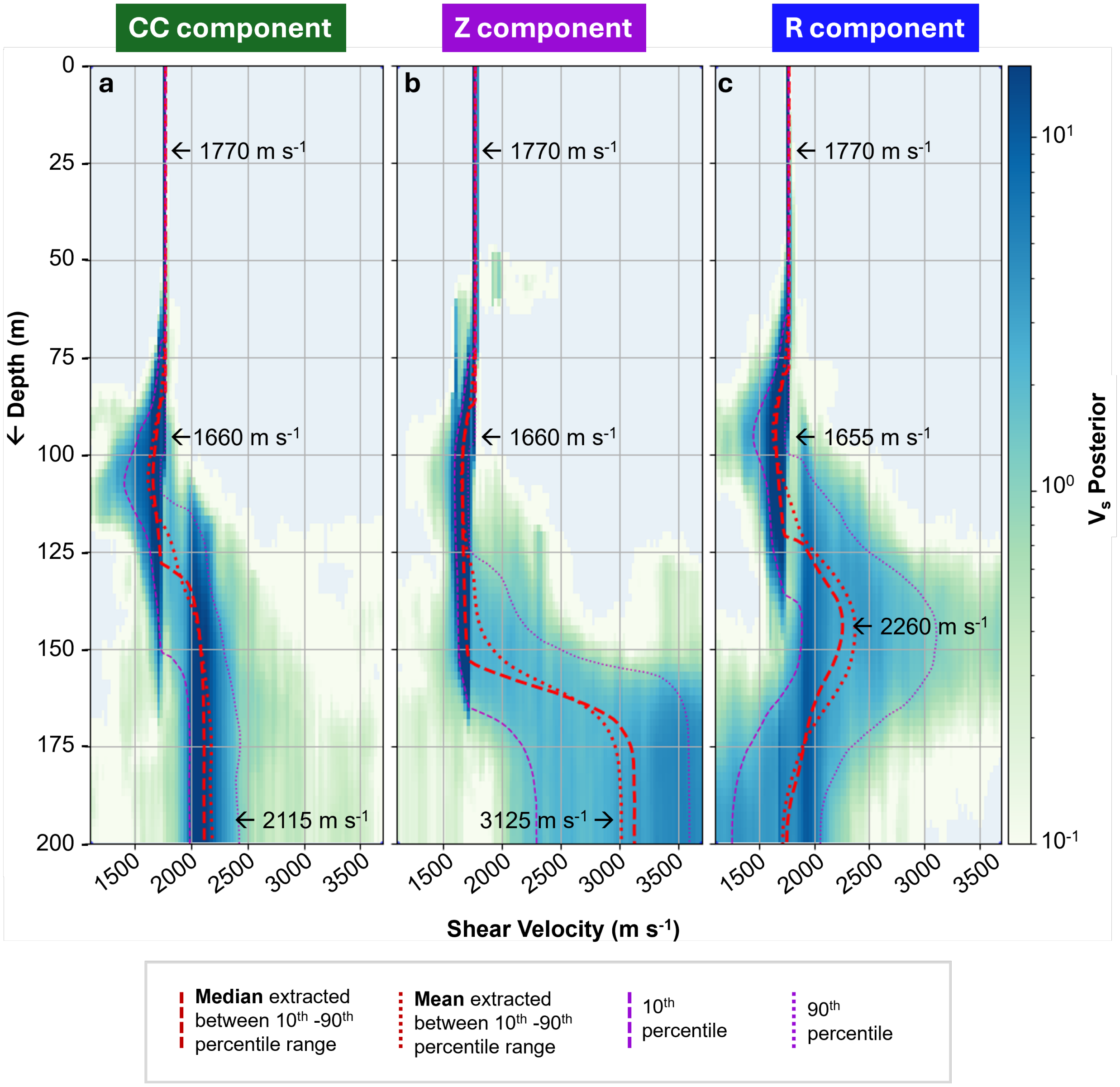

Figure 6.8 Model solutions of three TDB inversion experiments using the (a) *CC*-, (b) *Z*-, and (c) *R*-component data. All experiments share similar parameterization with the exception of the noise window which was lower for the *CC* experiment.

The CC and Z experiments estimate the top of the low-velocity zone at approximately 94 m, whereas the R experiment indicates a slightly shallower depth of 84 m. This is more clearly illustrated in Figure 6.9a, which compares the median solutions. The top of the bedrock shows the greatest variability, with the Z component producing a solution roughly 20 m deeper than the CC and R solutions.

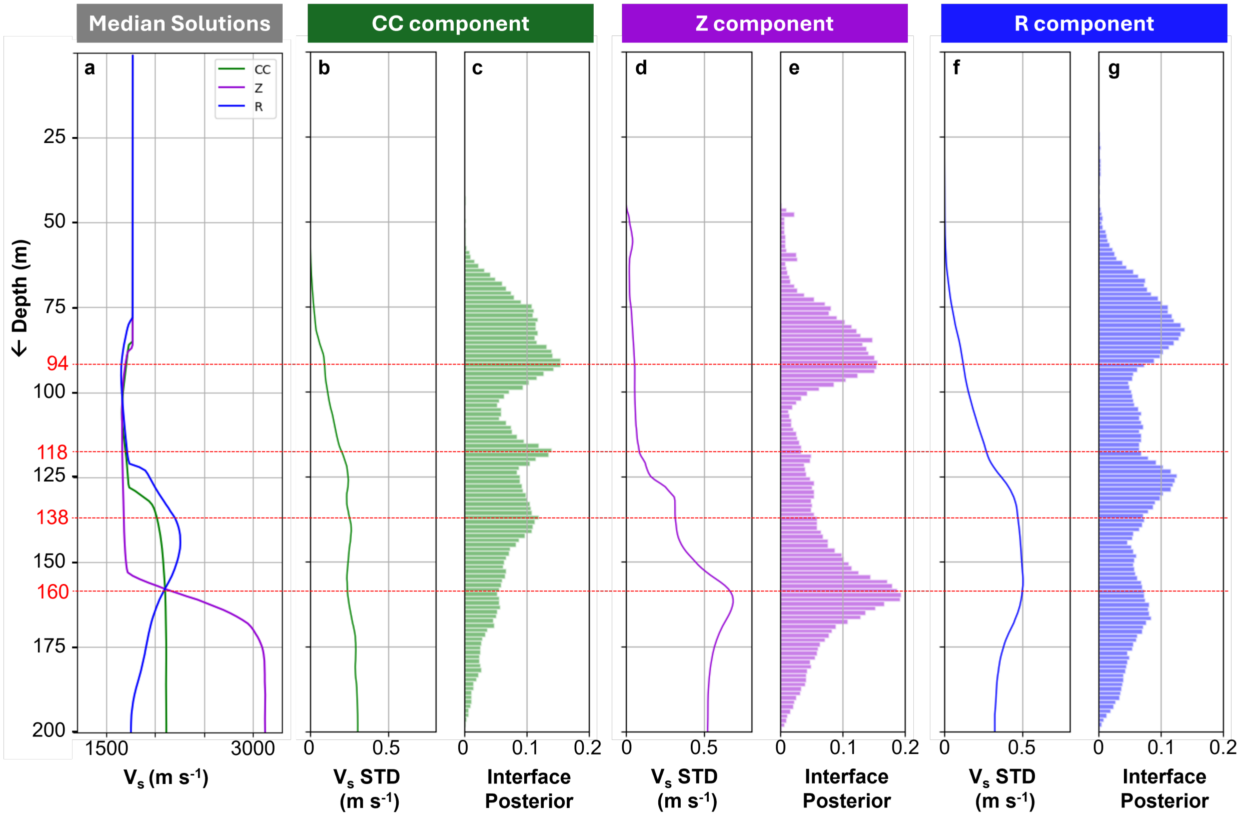

Figure 6.9 (a) Comparison of median model solutions and the (b,c) CC-, (d,e) Z-, and (f,g) R-component TBD results, where panels, (b), (d), and (f) are the standard deviation of the depth-dependent V_s posterior for each component experiment and (c), (e), and (g) are the depth-dependent posterior distributions of interface solutions for each component experiment. Red horizontal lines indicate depths where the interface posteriors are high for either the CC or Z solutions. The R component posterior is not evaluated due to the unreliability of its complex model solution (Figure 6.8).

Evaluating posterior distributions is a key advantage of the Bayesian approach. In Figure 6.9b—g, the standard deviations (STD) of the $V_s(z)$ solutions and interface posteriors are shown for each of the three component experiments. Although the Z component exhibits a strongly peaked posterior at 160 m (Figure 6.9e), the increased V_s STD at these depths (over 500 m s^{-1} in Figure 6.9d) warrants caution in interpreting this result. In contrast, the CC-component interface posterior in Figure 6.9c reveals two well-resolved depth interfaces at 118 m and 138 m, and the median CC solution in Figure 6.9a appears to average these two depths. The V_s STD of the CC solution are similar at both depths, around 300 m s^{-1} (Figure 6.9b), and not necessarily biasing toward either depth interface. This may suggest a bi-modal posterior distribution for the inferred bedrock depth rather than distinct geological layers.

To aid interpretation of the median solutions and depth-dependent posteriors, we examine the free-hyperparameter posteriors in Figure 6.10. Panels a–c compare the observed dispersion curves (DC_{obs}) with the range of calculated curves (DC_{calc}) in all iterations for each experiment. Similar levels of agreement are observed in all experiments, reflecting the explicit treatment of data noise as a free hyperparameter in the inversion. Panels d–f show the prior and posterior distributions of the noise parameter for each experiment. The uniform noise priors are component-specific, informed by the observations of Bodin *et al.* (2012), who noted that constraining the noise for each dataset facilitates more effective exploration of other model parameters. The CC component exhibits a lower noise posterior than the SC datasets, highlighting the improvement in SNR achieved through the MC approach. Finally, panels g–i present the posterior solutions for k, supporting the two conclusions drawn from the median V_s solutions and depth-dependent posteriors: (1) that the CC yields structurally simpler and reasonable solutions, strongly favoring three-layer models (Figure 6.10g); and (2) that the bi-modal interface posterior likely represents two alternative options for bedrock depth rather than a more complex four-layer model.

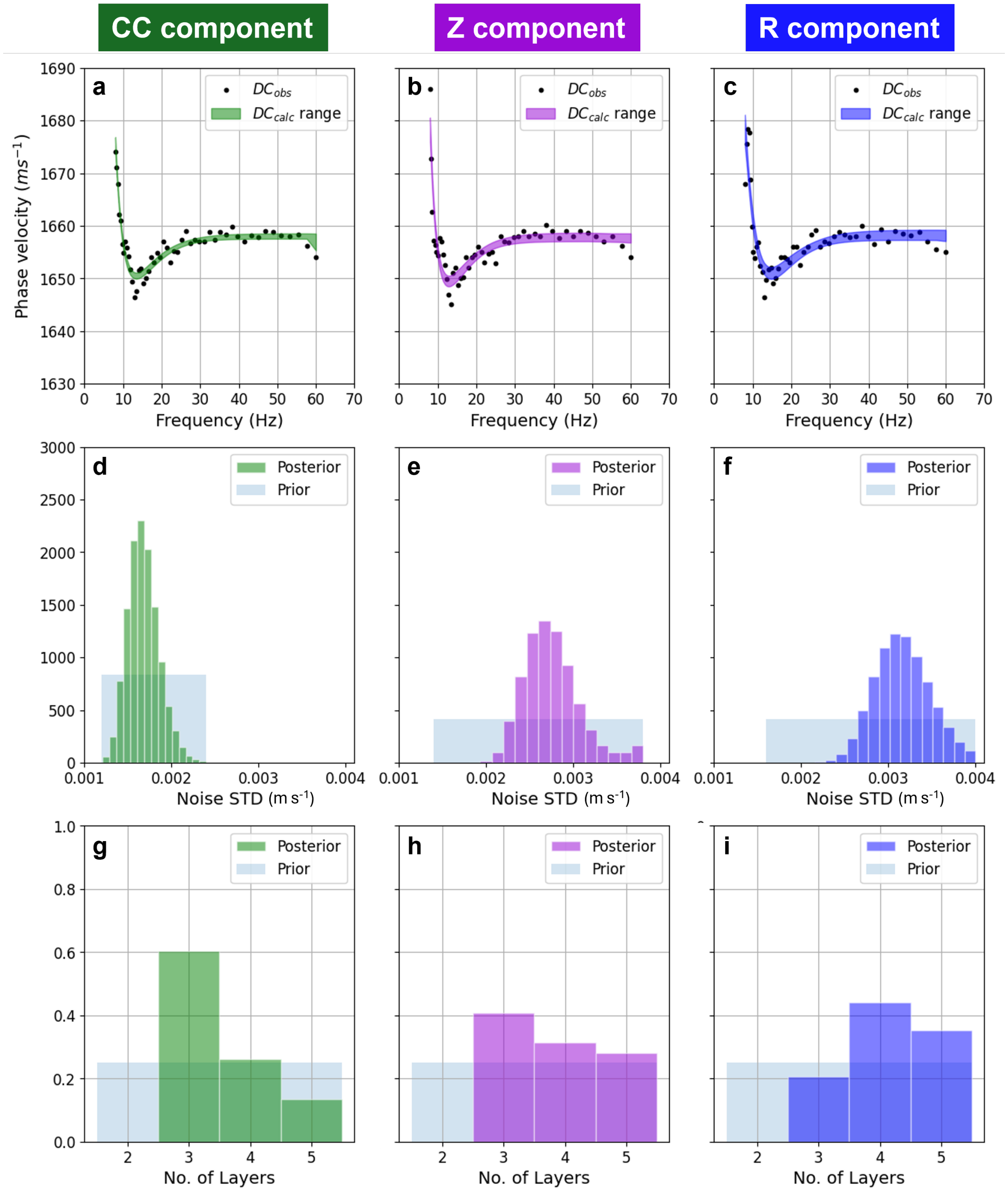

Figure 6.10 Comparison of DC_{obs} (colored points) with the range of DC_{calc} for all accepted solutions in our experiments using (a) CC-, (b) Z-, and (c) R-component. Prior (uniform) and posterior distributions for noise levels in each of the (d) CC-, (e) Z-, and (f) R-component experiments. Data misfits are comparable across all experiments due to the treatment of noise as a free hyperparameter in the TDB inversion. The CC component exhibits the lowest estimated noise level among the three components. Number of layers in the prior and posterior model distributions for the (g) CC-, (h) Z-, and (i) R-component experiments

6.7 Interpretation of Slakbreen Glacier Structure

We ground-truth the CC- and Z-component solutions, focusing on the low-velocity zone and the presumed bedrock, by comparing them with velocity profiles from analogous polythermal glaciers in Svalbard: Bakaninbreen (Smith *et al.*, 2002) and Lovenbreen (King *et al.*, 2008). Figure 6.11a shows their locations relative to Slakbreen. In both case studies, V_p-depth profiles were primarily derived from a combination of first-arrival tomography, empirical estimates of the temperature dependence of V_p (Kohnen, 1974), borehole temperature measurements, and coincident radar imaging. We convert our CC- and Z-component median solutions to V_p-depth profiles, assuming $V_p/V_s = 2.0$ for glacial ice (Aster & Winberry, 2017), and compare them with the analog glaciers in Figure 6.11b. We neglect snow and firn layers of the analog studies.

At both Bakaninbreen and Lovenbreen glaciers, the low-velocity zones, starting at approximately 52 m and 120 m depths, respectively, were interpreted as temperate ice underlying colder ice. The refraction approaches in both case studies cannot resolve these layers, and both authors assume a V_s value of 3630 m s^{-1} based on measurements acquired beneath West Antarctic ice streams (Atre & Bentley, 1993). In cold ice, both studies derived the temperature dependence of seismic velocity through empirical measurements following from Kohnen (1974). In temperate ice, however, the relationship remains unclear, and the estimates from Atre & Bentley (1993) were assumed as bulk values until bedrock.

In contrast, our surface-wave inversion directly resolves the minimum V_s of the low-velocity layer at 1660 m s^{-1} (see the CC- and Z-component solutions in Figure 6.8), which corresponds to $V_p = 3320$ m s^{-1} assuming $V_p/V_s = 2.0$. The gradient of velocity change from likely cold ice to this warmer ice compares reasonably with those observed at Bakaninbreen and Lovenbreen glaciers (indicated by the blue arrow annotations in Figure 6.11b). We also observe a notable gradient in both the CC- and Z-component solutions as the warm ice transitions into sub-glacial material, although the CC and Z solutions vary considerably between the two components at these subglacial depths.

Whereas characterizing subglacial material was a primary objective of the two reference studies, our focus is narrower: we aim to validate the plausible range of sub-glacial V_s solutions derived from the TDB inversion, given the strong divergence between the CC and Z components at these depths. To this end, we adopt the highest reported V_p at depth for both analog glaciers (4850 m s^{-1}, King *et al.* 2008) to evaluate the extremity of plausible solutions. We note that the Z-component solution is unrealistically high, whereas the CC-component solution suggests softer sub-glacial material than this maximum reported value at 4230 m s^{-1}.

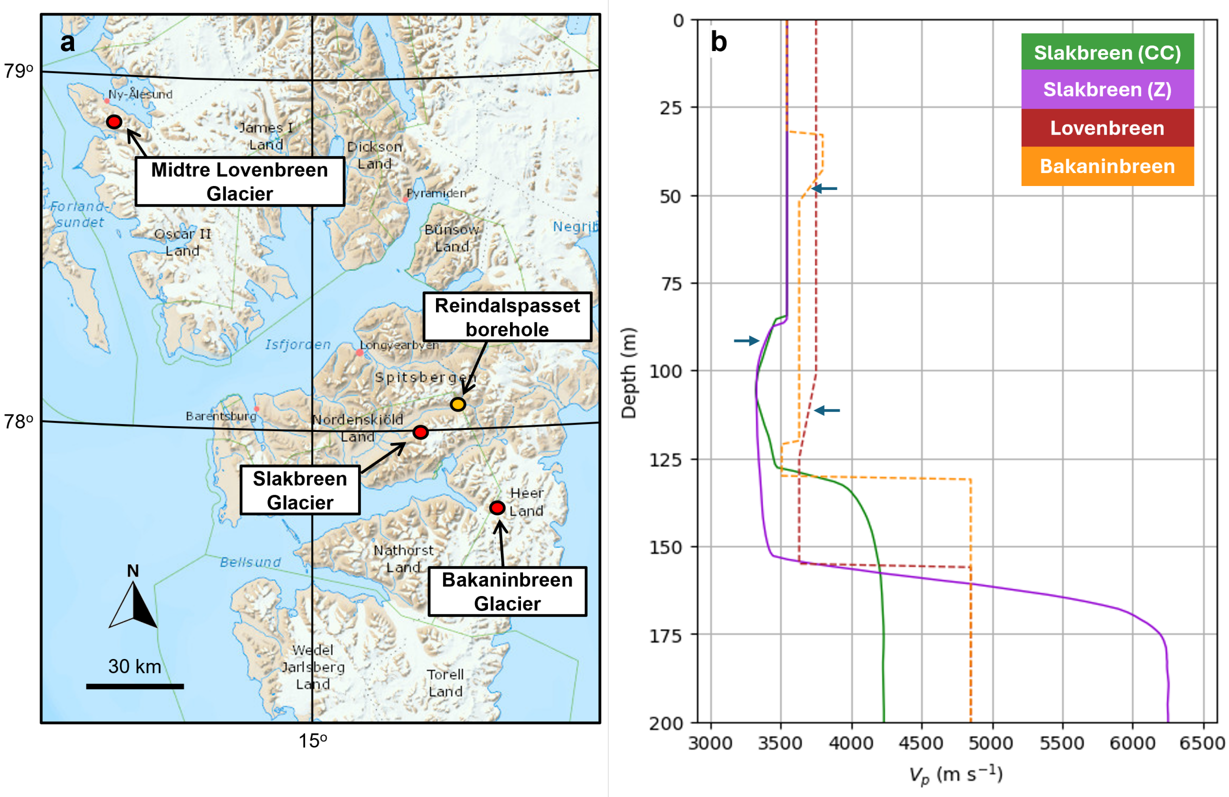

Figure 6.11 (a) Locations of the two polythermal glacier case studies (Bakaninbreen and Lovenbreen) and the density logged exploration well at Reindalspasset relative to the Slakbreen field site. (b) Comparison of V_p profiles: median solutions from the Slakbreen CC- and Z-component data, converted assuming $V_p/V_s = 2.0$ for glacial ice (Aster & Winberry, 2017), alongside V_p models from Lovenbreen (King *et al.*, 2008) and Bakaninbreen (Smith *et al.*, 2002). Blue arrows annotate the transition from cold to warmer ice in each solution.

Both King *et al.* (2008) and Smith *et al.* (2002) produced crossplots of V_p versus bulk density (i.e., acoustic impedance estimates) for a range of likely subglacial materials in Svalbard. For our study site at Slakbreen, we might assume a bulk density of approximately 2600 kg m^{-3}, based on measurements from a drilling exploration well roughly 13 km away at Reindalspasset (Nuus *et al.*, 2025) (Figure 6.11a); however, we caution that this value may not be fully transferable to Slakbreen. Using the $V_p = 4230$ m s^{-1} value from the CC component, we calculate the acoustic impedance as $\sim 1.10 \times 10^7$ $\mathrm{kg} \cdot \mathrm{m}^{-2} \cdot \mathrm{s}^{-1}$, which suggests a hard bedrock material. If the density at Slakbreen is in fact lower, the re-calculated acoustic impedance could instead indicate permafrost.

6.8 Conclusion

We used a MC explosive-source experiment on Slakbreen Glacier, Svalbard to compare MASW and TDB inversion of Rayleigh-wave dispersion data for estimating V_s structure. The results highlight the sensitivity of MASW inversions to model parameterization, with the CC component showing clear improvements in misfit reduction. In contrast, the TDB median solution effectively extracts information from the CC component even under relatively unconstrained priors that can cause MASW to miss key internal structures, such as the thermal transition. Across all components, the TDB median solutions reveal a persistent low-velocity zone, interpreted as the transition from cold, stiff ice above to warmer, softer ice below, consistent with a polythermal ice transition. The transition from this low-velocity zone to bedrock is best constrained in the CC-component experiment, owing to the improved accuracy of low-frequency Rayleigh-wave dispersion data obtained by integrating MC information.

6.9 Data Availability

The datasets generated and/or analyzed during this study are owned by the UNIS Arctic Seismic Exploration course administration. Access requests can be directed to the course organizers.

6.10 Acknowledgments

We gratefully acknowledge the University Centre in Svalbard (UNIS), the students of the Arctic Seismic Exploration course, and researchers from the University of Bergen for granting permission to use the seismic data acquired at Slakbreen Glacier. We also thank Equinor for supporting the course through their research venture funding, and Bent Ole Ruud for facilitating data transfer and addressing related questions.

This study also relied on a range of open-source software packages, and we are grateful to the developers and contributors who make these tools available to the scientific community. We used *MASWaves* (Ólafsdóttir *et al.*, 2018b) for dispersion curve forward modeling and analysis, and both *MASWaves* and *BayesBay* (Magrini *et al.*, 2025) for inversion, with *disba* (Luu, 2021) employed for numerical forward modeling within the *BayesBay* framework. Seismic data processing was carried out using *Seismic Unix* (Stockwell Jr, 1999). Additional numerical and symbolic computations, as well as data visualization, were supported by Python libraries including *NumPy* (Harris *et al.*, 2020), *SymPy* (Meurer *et al.*, 2017), *pandas* (McKinney, 2010), and *Matplotlib* (Hunter, 2007).

6.11 Supplemental: Inversion Parameterizations for Slakbreen Experiments

This supplemental material summarizes the parameterization used in both the multichannel analysis of surface waves (MASW) and the trans-dimensional Bayesian (TDB) inversion.

6.11.1 MASW Parameterization

For the MASW inversions, different initial model parameterizations and reversal flags (on or off) were compared, while all other search parameters and priors were held constant. Details of the parameterizations are provided below.

Initial Model

A three layer initial model was used for all MASW experiments, though the depth of the ice interface differ for experiment #1 and #2 (Table 6.1) versus #3 (Table 6.2) described in Section 6.5 of the main text.

Table 6.1 Initial model for experiments #1 and #2 in Section 6.5.

Layer	Thickness [m]	V_s [m s^{-1}]	Density [kg/m^3]	V_p [m s^{-1}]
1	100	1875	930	3750
2	50	1875	930	3750
3 (half-space)	–	2000	2600	4000

Table 6.2 Initial model for experiment #3 in Section 6.5.

Layer	Thickness [m]	V_s [m s^{-1}]	Density [kg/m^3]	V_p [m s^{-1}]
1	60	1875	930	3750
2	90	1875	930	3750
3 (half-space)	–	2000	2600	4000

Reversal Flag

In experiment #1 (Section 6.5), the inversion was not allowed to search for low-velocity layers; in all other MASW experiments, the flag was enabled.

Forward Modeling

The range of test phase velocity over which the forward modeling was computed was defined between 1200 and 3000 m s^{-1}, with an increment of 100 m s^{-1}.

Updating Shear-Wave Velocity

The shear-wave velocity (V_s) of a given layer is updated by adding a random perturbation drawn from a uniform distribution between $\pm\frac{bs}{100} \times V_s$, where $bs = 5$.

Updating Layer Thickness

The layer thickness (h) perturbation is drawn from a uniform distribution between $\pm\frac{bh}{100} \times h_s$, where $bh = 10$.

Inversion Implementation

For each experiment, the Monte Carlo adapted MASW inversion was run 6 times each performing 200 iterations.

Post Processing

Upper and lower bounds were constructed around the observed data, increasing gradually with depth from ±1% at the shallowest point to ±2% at the deepest.

6.11.2 TDB Parameterization

For the TDB inversion, all experiments were parameterized similarly with the exception of the data noise which vary per component experiment. Details of the parameterizations are provided below.

Voronoi Positions

We used a uniform prior for Voronoi nuclei locations, allowing positions between 0 and 200 m depth. Nuclei perturbations followed a Gaussian distribution with a standard deviation of 1 m.

Shear Velocity Model Space

V_s was bounded between $1100 - 3700$ m s^{-1} at all depths between $0 - 300$ m and perturbations were drawn from a Gaussian distribution with a 5 m s^{-1} standard deviation.

Trans-Dimensional Parameters

The number of Voronoi nuclei was treated as a free parameter with a uniform prior, constrained to vary between 2 and 5 layers.

Phase Velocity Data Noise

Observational noise was modeled using a uniform prior of $1.2 - 2.4$ m s^{-1} for the CC experiment, $1.4 - 3.8$ m s^{-1} for Z, and $1.6 - 4.0$ m s^{-1} for R. In all experiments, perturbations were applied using a Gaussian distribution with a 0.5 m s^{-1} standard deviation.

Forward Modeling

Forward modeling of fundamental Rayleigh-wave dispersion was performed using the open-source package *Disba* (Luu, 2021). In all cases, we assumed a V_p/V_s ratio of 2.1 to estimate P-wave velocity and assigned a constant density profile of 2200 kg m^{-3}. The frequency range of the observed data range were used to guide the test phase velocities.

Inversion Implementation

The reversible-jump Markov Chain Monte Carlo (rjMCMC) inversion was run with 20 parallel chains, each performing 800,000 iterations. The first 300,000 iterations of each chain were discarded as burn-in, and model states were saved every 200 iterations.

CHAPTER 7

CONCLUSION

Advancing subsurface characterization, particularly in complex geological settings, requires exploiting the dimensionality of seismic data afforded by multi-component (MC) seismology. The individual studies comprising this dissertation are motivated by the assertion that deploying three-component (3-C) receivers or ocean-bottom nodes (OBN) entails only incremental cost and effort compared to single-component (SC) acquisition systems. As a result, recording horizontal (H-component) data is increasingly feasible, and I demonstrate that its value extends beyond shear (S) waves, capturing additional wave modes such as compressional (P) and surface (Rayleigh) waves with higher density and improved resolution, which complement vertical, Z-component imaging and velocity model building.

The useful components of the wavefield vary by geological problem, and consequently the benefits of active-source MC experiments differ between domains. A classic example is surface waves which are treated as noise in deep-earth investigations (i.e., ground roll) but provide valuable information for constructing high-resolution shear-wave velocity (V_s) models in near-surface studies. Drawing on applications across domains and scales, from production-scale oil and gas exploration to localized glacial studies, this work provides both disciplinary depth and broader insights into the effective use of MC seismic techniques.

Each study addresses the same two overarching questions: what are the tangible benefits of MC data for specific project objectives? and how can processing and interpretation workflows ensure that all component sensitivities are properly accounted for? The findings are summarized below in terms of domain-specific conclusions.

7.1 Oil and Gas Exploration

In oil and gas exploration, large-scale, high-density SC surveys often provide sufficient resolution and accuracy for subsurface characterization, so MC methods must demonstrate clear added value to justify their use. OBN acquisitions provide this opportunity by enabling four-component (pressure and three displacement) recordings at the seafloor. We demonstrate that the inline H displacement components capture not only S-wave information but also reflected P waves (HPP data) with relatively high signal, enabled by the complexity of the subsurface and the density of the array.

7.1.1 Contributions of HPP data to Imaging

In Chapter 3, we show that HPP data can improve reflector focusing and continuity in imaging complex subsurface structures, particularly in areas where vertical-component reflected P-wave (ZPP) illumination is weak. These improvements are most notable in shallow and dipping layers as well as in sub-salt regions. Enhanced shallow illumination is valuable for seafloor engineering, including mapping potential hazards, while improved sub-salt imaging is critical because the stratigraphic layers juxtaposed against salt bodies frequently host prolific reservoirs.

More specifically, we show that in relatively simple layered geometries, the strength of the HPP signal generally depends on the target depth and dip relative to the receiver depth and offset. It often exhibits an inverse relationship with ZPP signals: when the P-wave signal of a reflector is strongest on the H component, it tends to be weakest on the Z component. In more complex sub-salt areas, sparse ZPP illumination and inter-salt multiples increase the complexity of ZPP images. By contrast, these multiples appear weaker and with opposite polarities on the radial (R) horizontal component, highlighting the complementary value of HPP data.

7.1.2 HPP Sensitivities and Processing Considerations

We also make critical observations regarding signed-offset polarization and illumination biases in HPP data compared to ZPP data. Although rotation to RPP is commonly used to remove offset bias, this approach assumes that layers are parallel to the recording surface. As a result, strongly dipping interfaces appear with opposite polarities on negative versus positive offsets, which can cause destructive interference if stacked across signed offsets. Additionally, HPP illumination of dipping beds varies between signed offsets regardless of the coordinate system (X or R), with beds dipping in the source-to-receiver direction being best illuminated by receivers on the downdip side of the source. These fundamental behaviors of HPP data have direct implications for the integration of MC components in tomography, shallow velocity model building, and elastic full-waveform imaging, but also acquisition if contributions of HPP illumination are to be maximized.

7.1.3 Suggestions for Future Work

The immediate next steps for extending this synthetic work should focus on applying the current acoustic experiments to elastic datasets and incorporating free-surface effects, building on the understanding of HPP illumination, particularly given the observed signed-offset biases that are likely to persist in elastic media. Exploring vector-based migration techniques could then account for amplitude variations with emergence angle and better exploit signed-offset HPP signals. Addressing multiples also represents a research opportunity, as polarity differences between ZPP and HPP data may be leveraged for improved multiple suppression. Finally, analyzing field OBN datasets is essential to confirm and quantify the tangible advantages of HPP data for velocity model building and full-waveform inversion, moving beyond synthetic predictions to real-world impact.

7.2 Glacial Seismology

Active-source glacial seismic surveys face persistent challenges due to typically sparse receiver arrays and weaker active sources compared to conventional exploration settings.

These constraints reduce data quality and limit the resolution of subsurface models. Our work demonstrates how MC acquisitions can mitigate some of these limitations. At a basic level, wave modes recorded on each component can be stacked to enhance signal-to-noise ratios. More importantly, MC data can exploit the unique and complementary sensitivities of the same wave modes recorded on the Z and R components. We apply this approach to Rayleigh-wave dispersion analysis, demonstrating improved solutions for V_s-depth profiles through ice and into shallow bedrock.

7.2.1 Contributions of CC-Rayleigh-wave Data to V_s-Depth Profiling

We introduce a method that better captures the vector-displacement of Rayleigh wave particle motion by combining the orthogonal Z- and R-component gathers using a complex system., This complex-component (CC) produces more accurate and stable inversion results for the two tested inversion approaches — via multi-channel analysis of surface waves (MASW; Chapters 5 and 6) and trans-dimensional Bayesian (TDB) inversion (Chapter 6) — and demonstrates effectiveness across diverse geologic settings:

1. Firn-aquifer scenarios, explored in Chapters 4 and 5 using synthetic models to distinguish between aquifers of varying thicknesses and depths, which exhibit subtly different dispersion characteristics.

2. The homogeneous alpine Saskatchewan Glacier, Canadian Rocky Mountains (Chapters 4 and 5), where improved SNR of the Rayleigh-wave signal in the gather enhanced the quality of dispersion curves and stabilized inversion results.

3. The polythermal valley glacier, Slakbreen, Svalbard (Chapters 6), where results indicate a potential new application of Rayleigh-wave dispersion analysis for characterizing thermally sensitive V_s layering in polythermal glaciers.

7.2.2 *CC* Sensitivities and Acquisition/Processing Considerations

In Chapter 4, we discuss the sensitivities of R-component data to subsurface layering, revealing features that are indiscernible from Z-component data alone. Observed behaviors include multiple depths where the Rayleigh-wave displacement on the R component changes sign, indicating reversals in the direction of elliptical particle motion, as well as localized narrowing or widening of particle motion ellipticity, particularly at strong V_s contrasts such as the ice-bedrock or firn-aquifer-ice interfaces.

Chapter 4 also provides recommendations for acquisition design and data conditioning to optimally leverage the CC-component approach. Prioritizing array aperture over receiver spacing improves depth of investigation and dispersion panel resolution, whereas adjusting the shot spacing ensures adequate offset coverage. Chapter 6 highlights that the CC method relies on the R component exhibiting the expected 90° phase rotation relative to Z; deviations from standard acquisition coordinates (e.g., North–East or X–Y) may require modifications to R–T rotation procedures. Additionally, constructing supergathers from multiple shots enhances signal quality, extends array aperture, improves depth of investigation, reduces uncertainty in dispersion-curve picking and inherently infills missing offsets, minimizing the need for interpolation.

7.2.3 Suggestions for Future Work

A major caveat of the general MASW approach for Rayleigh-wave dispersion analysis is that achieving sensitivity to greater depths requires longer array lengths, which inherently introduces spatial averaging. The CC component may improve data quality sufficiently to enable the use of low-fold supergathers. With this in mind, one promising direction is to explore a strategy in which the 1-D V_s profile is constructed progressively: beginning with shallow information from a short array and then incrementally extending depth sensitivity by building fold into the supergather.

Additionally, this work has focused primarily on the fundamental mode of Rayleigh waves; however, higher-order modes will inevitably be generated where strong layering is present. These modes are expected to have stronger expression on the H components, potentially offering even greater benefit from CC recordings.

Finally, the CC-component opens opportunities for joint inversion with complementary datasets, such as Love waves on the T-component, passive HV spectral ratios, or receiver functions that better constrain depth. A transdimensional Bayesian framework offers a natural way to integrate these data, as it can account for the distinct sensitivities and noise characteristics of each.

7.3 Broader Contributions

Nearly a decade has passed since the last comprehensive review of active-source MC seismology, highlighting the need for an updated synthesis of the field — particularly given the expanding computational and acquisition capabilities that now make MC concepts increasingly relevant. A secondary, but important, objective of this dissertation was to provide such an update (Chapter 1), tracing the evolution of active-source MC strategies from early studies focused on isolating specific S-wave attributes to approaches gradually integrated into full-waveform imaging methods.

Complementary to this goal is the facilitation of critical knowledge transfer between application domains — an exchange often limited in profit-driven industry or less accessible academic spaces. Chapter 2 reviews and defines concepts that support this transfer, and in each study, relevant wavefield theory is presented in a manner accessible to a broad geophysical audience while maintaining links to the underlying mathematical framework.

7.4 Summary and Outlook

We have demonstrated that body P- and surface Rayleigh waves recorded on the H component of geophones and OBNs are sensitive to subsurface velocity structure and layering in ways that differ from Z-component data. Critically, these H-component signals can be exploited to reduce uncertainties inherent in traditional Z-component approaches, providing a path toward more robust and detailed subsurface characterization.

Collectively, the studies of this dissertation underscore the importance of evaluating the sensitivities of all seismic components prior to joint analysis or processing of multi-component (MC) data. We have shown that the unique sensitivities of H-component data contribute to solution accuracy, uniqueness, and stability, despite being weaker than those observed on Z-component recordings. To fully harness H-component information in joint workflows without masking from Z-component signals or noise, each component must be carefully weighted, whether the data are combined prior to processing, as in the CC component of Rayleigh wave signals (Chapter 4), or jointly processed using full-waveform methods.

Furthermore, algorithms should be sufficiently adaptive to exploit the finer-scale details of MC datasets while mitigating issues related to ill-posedness. Traditional workflows, such as Kirchhoff migration for P-wave imaging (Garvey *et al.*, 2025) and deterministic MASW inversion for S-wave velocity modeling (Chapter 5), allow detailed interrogation of individual components but rely on strong constraints, including acoustic synthetic datasets and restrictive parameterizations. These constraints limit applicability in complex or poorly understood geologic settings and hinder full exploitation of MC data, a limitation particularly evident when comparing deterministic MASW with trans-dimensional Bayesian (TDB) inversion of Rayleigh-wave dispersion data in Chapter 6.

Collectively, these findings highlight the broader potential of H-component data to enhance subsurface characterization and motivate future studies that systematically integrate multi-component sensitivities into advanced workflows. They also provide a positive outlook for active-source MC seismology, particularly as improvements in computational and acquisition technologies continue to expand the possibilities for detailed, high-resolution imaging.

REFERENCES

Agnew, RS, Clark, RA, Booth, AD, Brisbourne, AM, & Smith, AM. 2023. Measuring seismic attenuation in polar firn: method and application to Korff Ice Rise, West Antarctica. *Journal of Glaciology*, **69**(278), 2075–2086.

Aki, K, & Richards, PG. 2002. *Quantitative Seismology.* University Science Books.

Alfaro, R, Secker, S, Zamboni, E, Guitton, A, Cozzens, AJ, Henderson, N, Nechayuk, V, Jenkerson, M, Johnson, G, & Karran, J. 2023. Marine vibrator milestone: a pilot seismic survey. *Page D011S012R006 of: Offshore Technology Conference Brasil.* Offshore Technology Conference.

Alford, RM. 2005. *Shear data in the presence of azimuthal anisotropy: Dilley, Texas.* Society of Exploration Geophysicists.

Ammon, CJ, Velasco, AA, Lay, T, & Wallace, TC. 2020. *Foundations of Modern Global Seismology.* Academic Press.

Arrowsmith, SJ, Trugman, DT, MacCarthy, J, Bergen, KJ, Lumley, D, & Magnani, MB. 2022. Big data seismology. *Reviews of Geophysics*, **60**(2), e2021RG000769.

Aster, RC, & Winberry, JP. 2017. Glacial Seismology. *Reports on Progress in Physics*, **80**(12), 126801.

Ata, E, Olson, R, Mosher, CC, Shaw, S, & Betterly, S. 2013. A look at converted waves from an OBN test survey. *In: SEG International Exposition and Annual Meeting.* Society of Exploration Geophysicists.

Atre, SR, & Bentley, CR. 1993. Laterally varying basal conditions beneath Ice Streams B and C, West Antarctica. *Journal of Glaciology*, **39**(133), 507–514.

Babcock, E, & Bradford, J. 2014. Quantifying the basal conditions of a mountain glacier using a targeted full-waveform inversion: Bench Glacier, Alaska, USA. *Journal of Glaciology*, **60**(224), 1221–1231.

Backus, MM, Murray, PE, Hardage, BA, & Graebner, RJ. 2006. High-resolution multicomponent seismic imaging of deepwater gas-hydrate systems. *The Leading Edge*, **25**(5), 578–596.

Barzegar, M, Blanks, S, Sainsbury, BA, & Timms, W. 2022. MEMS technology and applications in geotechnical monitoring: a review. *Measurement Science and Technology*, **33**(5), 052001.

Bennett, MR. 2022. *Our Dynamic Earth: A Primer*. Cham: Springer International Publishing.

Beyreuther, M, Barsch, R, Krischer, L, Megies, T, Behr, Y, & Wassermann, J. 2010. ObsPy: a Python toolbox for seismology. *Seismological Research Letters*, **81**(3), 530–533.

Bleistein, N. 1986. Two-and-one-half dimensional in-plane wave propagation. *Geophysical prospecting*, **34**(5), 686–703.

Bleistein, N, Cohen, JK, & Hagin, FG. 1987. Two and one-half dimensional Born inversion with an arbitrary reference. *GEOPHYSICS*, **52**(1), 26–36.

Bodin, T, & Sambridge, M. 2009. Seismic tomography with the reversible jump algorithm. *Geophysical Journal International*, **178**(3), 1411–1436.

Bodin, T, Sambridge, M, Tkalčić, H, Arroucau, P, Gallagher, K, & Rawlinson, N. 2012. Transdimensional inversion of receiver functions and surface wave dispersion. *Journal of Geophysical Research: Solid Earth*, **117**(B2).

Bohlen, T, De Nil, D, Köhn, D, & Jetschny, S. 2016. SOFI2D seismic modeling with finite differences: 2D—elastic and viscoelastic version. *user guide*. Accessed: 2024-03-01.

Booth, AD, Mercer, A, Clark, R, Murray, T, Jansson, P, & Axtell, C. 2013. A comparison of seismic and radar methods to establish the thickness and density of glacier snow cover. *Annals of Glaciology*, **54**(64), 73–82.

Bostock, MG. 2002. Kirchhoff-approximate inversion of teleseismic wavefields. *Geophysical Journal International*, **149**(3), 787–795.

Brisbourne, AM, Martin, C, Smith, AM, Baird, AF, Kendall, JM, & Kingslake, J. 2019. Constraining recent ice flow history at Korff Ice Rise, West Antarctica, using radar and seismic measurements of ice fabric. *Journal of Geophysical Research: Earth Surface*, **124**(1), 175–194.

Bucha, V. 2021. Kirchhoff pre-stack depth scalar migration in a simple triclinic velocity model for three-component P, S1, S2 and converted waves. *Geophysical Prospecting*, **69**(2), 269–288.

Buchen, PW, & Ben-Hador, R. 1996. Free-mode surface-wave computations. *Geophysical Journal International*, **124**(3), 869–887.

Cafarelli, B, Randazzo, S, Campbell, S, Sobreira, JFF, Guimaraes, MAG, Rodriguez, C, Johann, P, & Theodoro, C. 2006. Ultra-deepwater 4-C offshore Brazil. *The Leading Edge*, **25**(4), 474–477.

Caldwell, J. 1999. Marine multicomponent seismology. *The Leading Edge*, **18**(11), 1274–1282.

Casasanta, L, & Gray, SH. 2015. PS imaging of ocean-bottom data. *The Leading Edge*, **34**(4), 414–420.

Chaput, J, Aster, R, Karplus, M, & Nakata, N. 2022. Ambient high-frequency seismic surface waves in the firn column of central west Antarctica. *Journal of Glaciology*, **68**(270), 785–798.

Cherry Jr, JT. 1962. The azimuthal and polar radiation patterns obtained from a horizontal stress applied at the surface of an elastic half space. *Bulletin of the Seismological Society of America*, **52**(1), 27–36.

Cho, Y, Solano, CP, Kimbro, J, Yang, Y, Plessix, R, & Matson, K. 2022. Influence of shear velocity on elastic full-waveform inversion: Gulf of Mexico case study using multicomponent ocean-bottom node data. *Geophysics*, **87**(5), R391–R400.

Chopra, S, & Stewart, R. 2010. Introduction to this special section: multicomponent seismic. *The Leading Edge*, **29**(10), 1210–1211.

Chu, W, Schroeder, DM, & Siegfried, MR. 2018. Retrieval of englacial firn aquifer thickness from ice-penetrating radar sounding in southeastern Greenland. *Geophysical Research Letters*, **45**(21), 11–770.

Church, G, Bauder, A, Grab, M, Rabenstein, L, Singh, S, & Maurer, H. 2019. Detecting and characterising an englacial conduit network within a temperate Swiss glacier using active seismic, ground penetrating radar and borehole analysis. *Annals of Glaciology*, **60**(79), 193–205.

Crice, D. 2005. MASW, the wave of the future editorial. *Journal of Environmental & Engineering Geophysics*, **10**(2), 77–79.

Damasceno, A, Tura, A, & Simmons, JL. 2021. The added value of joint PP–PS inversion for reservoir characterization: a case study using Jubarte PRM seismic data (offshore Brazil). *Geophysical Prospecting*, **70**(1), 121–134.

Daves, J, & Simmons, JL. 2018. Shear-wave reflection signal recovery through Horizontal-geophone azimuth estimation. *Pages 1–5 of: 80th EAGE Conference and Exhibition 2018*, vol. 2018. European Association of Geoscientists & Engineers.

Davis, TL, Benson, RD, Roche, SL, & Talky, D. 1997. 4-D, 3-C seismology and dynamic reservoir characterization — a geophysical renaissance. *Pages 880–882 of: SEG Technical Program Expanded Abstracts 1997.* Society of Exploration Geophysicists.

de Lucena, RF, & Taioli, F. 2014. Rayleigh wave modeling: a study of dispersion curve sensitivity and methodology for calculating an initial model to be included in an inversion algorithm. *Journal of Applied Geophysics*, **108**, 140–151.

Dellinger, JA, Clarke, RA, & Gutowski, PR. 2002. Three-dimensional vector infidelity correction by general linear transform. *Pages cp–5 of: 64th EAGE Conference & Exhibition.* European Association of Geoscientists & Engineers.

Dhelie, PE, Danielsen, V, Haugen, JA, Davenne, E, Straith, KR, Roodaki, A, Peiro, M, Fotsoh, A, Gao, W, Masmoudi, N, *et al.* 2022. High-resolution FWI of converted-wave data — a case study from the Edvard Grieg field. *Page D011S042R003 of: SEG International Exposition and Annual Meeting.* Society of Exploration Geophysicists.

Di Biase, V, Munneke, PK, Veldhuijsen, SBM, de Roda Husman, S, van den Broeke, MR, Noël, B, Buth, LG, & Wouters, B. 2024. Probability of Firn Aquifer Presence in Antarctica by Combining Remote Sensing and Regional Climate Model Data. *Geophysical Research Letters*, **51**(15), e2024GL109367. e2024GL109367 2024GL109367.

Dillon, PB. 1990. A Comparison Between Kirchhoff and GRT Migration on VSP Data. *Geophysical Prospecting*, **38**(7), 757–777.

Farfour, M, & Yoon, WJ. 2016. A review on multicomponent seismology: a potential seismic application for reservoir characterization. *Journal of Advanced Research*, **7**(3), 515–524.

Fehler, M, & Keliher, PJ. 2011. *SEAM Phase 1: challenges of subsalt imaging in tertiary basins, with emphasis on deepwater Gulf of Mexico.* Society of Exploration Geophysicists.

Finger, C, & Löer, K. 2024. Depth of sudden velocity changes derived from multi-mode Rayleigh waves. *Journal of Geophysical Research: Solid Earth*, **129**(3), e2023JB028322.

Forster, RR, Box, JE, Van Den Broeke, MR, Miège, C, Burgess, EW, Van Angelen, JH, Lenaerts, JTM, Koenig, LS, Paden, J, Lewis, C, *et al.* 2014. Extensive liquid meltwater storage in firn within the Greenland ice sheet. *Nature Geoscience*, **7**(2), 95–98.

Foti, S, Lai, CG, Rix, GJ, & Strobbia, C. 2014. *Surface wave methods for near-surface site characterization.* CRC press.

Foti, S, Hollender, F, Garofalo, F, Albarello, D, Asten, M, Bard, PY, Comina, C, Cornou, C, Cox, B, Di Giulio, G, *et al.* 2018. Guidelines for the good practice of surface wave analysis: a product of the InterPACIFIC project. *Bulletin of Earthquake Engineering*, **16**, 2367–2420.

Gaiser, JE. 1998. Compensating OBC data for variations in geophone coupling. *Pages 1429–1432 of: 68th Annual International Meeting, SEG, Expanded Abstracts.* Abstract.

Gaiser, JE. 1999. Applications for vector coordinate systems of 3-D converted-wave data. *The Leading Edge*, **18**(11), 1290–1300.

Gaiser, JE. 2016. *3C seismic and VSP: converted waves and vector wavefield applications.* Society of Exploration Geophysicists.

Gao, C, & Lekić, V. 2018. Consequences of parametrization choices in surface wave inversion: insights from transdimensional Bayesian methods. *Geophysical Journal International*, **215**(2), 1037–1063.

Garvey, SM, Simmons, JL, & Calderón-Macías, C. 2025. Contributions of the Horizontal OBN Components to P-wave Imaging. *Interpretation*, **13**(3), 1–39.

Gherasim, M, Hoelting, C, & Marfurt, K. 2005. 3-D VSP elastic Kirchhoff pre-stack depth migration—Vinton Dome, Louisiana. *Pages 2649–2652 of: SEG Technical Program Expanded Abstracts 2005.* Society of Exploration Geophysicists.

Godio, A, & Rege, RB. 2015. The mechanical properties of snow and ice of an alpine glacier inferred by integrating seismic and GPR methods. *Journal of Applied Geophysics*, **115**, 92–99.

Green, PJ. 1995. Reversible jump Markov chain Monte Carlo computation and Bayesian model determination. *Biometrika*, **82**(4), 711–732.

Green, PJ, & Hastie, DI. 2009. Reversible jump MCMC. *Genetics*, **155**(3), 1391–1403.

Guan, P, Shao, C, Jiao, Y, Zhang, G, Li, B, Zhou, J, & Huang, P. 2021. 3-D multi-component reverse time migration method for tunnel seismic data. *Sensors*, **21**(9), 3244.

Hardage, BA, DeAngelo, MV, Murray, PE, & Sava, D. 2011. *Multicomponent seismic technology.* Society of Exploration Geophysicists.

Hardage, BA, DeAngelo, M, Sava, D, Wagner, D, Murray, P, Sullivan, C, Simmons, JL, Ebrom, D, Roche, S, & Zhou, R. 2014. Introduction to special section: multicomponent seismic interpretation. *Interpretation*, **2**(2), SEi–SEii.

Harris, CR, Millman, KJ, van der Walt, SJ, Gommers, R, Virtanen, P, Cournapeau, D, Wieser, E, Taylor, J, Berg, S, Smith, NJ, Kern, R, Picus, M, Hoyer, S, van Kerkwijk, MH, Brett, M, Haldane, A, Fernández del Río, J, Wiebe, M, Peterson, P, Gérard-Marchant, P, Sheppard, K, Reddy, T, Weckesser, W, Abbasi, H, Gohlke, C, & Oliphant, TE. 2020. Array programming with NumPy. *Nature*, **585**(7825), 357–362.

Harris, JB, Smolkin, DE, Butler, DT III, & Galicki, SJ. 2009. Shallow shear-wave seismic characterization of a Pleistocene gravel deposit, Yazoo County, Mississippi. *Pages 579–585 of: Symposium on the Application of Geophysics to Engineering and Environmental Problems 2009.*

Häusler, M, Schmelzbach, C, & Sollberger, D. 2018. The Galperin source: a novel efficient multicomponent seismic source. *Geophysics*, **83**(6), P19–P27.

Hesthammer, J, & Løkkebø, SM. 1997. Combining seismic surveys to improve data quality. *First Break*, **15**(4).

Hokstad, K. 2000. Multicomponent kirchhoff migration. *Geophysics*, **65**(3), 861–873.

Holden, J, Fritz, D, Bukola, O, McLeman, J, Refaat, R, Page, C, Brunelliere, J, Sioni, S, Mitra, A, & Lu, X. 2016. Sparse nodes and shallow water-PS imaging challenges on the Alwyn north field. *Pages 1–5 of: 78th EAGE Conference and Exhibition 2016*, vol. 2016. European Association of Geoscientists & Engineers.

Hou, A, & Marfurt, KJ. 2002. Multicomponent prestack depth migration by scalar wavefield extrapolation. *Geophysics*, **67**(6), 1886–1894.

Huang, Y, Mao, J, Sheng, J, Perz, M, He, Y, Hao, F, Liu, F, Wang, B, Yong, SL, Chaikin, D, Ramirez, AC, Hart, M, & Roende, H. 2023. Toward high-fidelity imaging: dynamic matching FWI and its applications. *The Leading Edge*, **42**(2), 124–132.

Hunter, JD. 2007. Matplotlib: a 2D graphics environment. *Computing in Science & Engineering*, **9**(3), 90–95.

Ibs-von Seht, M, & Wohlenberg, J. 1999. Microtremor measurements used to map thickness of soft sediments. *Bulletin of the Seismological Society of America*, **89**(1), 250–259.

Igel, H. 2017. *Computational seismology: a practical introduction.* Oxford University Press.

Jennings, J, & Ronen, S. 2017. Simultaneous source deblending with the radiality and source-similarity attributes. *Pages SEG–2017 of: SEG International Exposition and Annual Meeting.* Society of Exploration Geophysicists.

Jílek, P, & Červený, V. 1996. Radiation patterns of point sources situated close to structural interfaces and to the earth's surface. *Pure and Applied Geophysics*, **148**(1), 175–225.

Johansen, TA, Ruud, BE, Bakke, NE, Riste, P, Johannessen, EP, & Henningsen, T. 2011. Seismic profiling on Arctic glaciers. *First Break*, **29**(2).

Karus, EV, Ryabinkin, LA, Rapoport, MB, Galperin, EI, Teplitskiy, VA, Demidenko, YB, & Mustafayev, KA. 1975. Detailed investigations of geological structures by seismic well surveys. *Pages 247–257 of: World Petroleum Congress Proceedings.*

Kearey, P, Brooks, M, & Hill, I. 2013. *An introduction to geophysical exploration.* John Wiley & Sons.

Killingbeck, SF, Livermore, PW, Booth, AD, & West, LJ. 2018. Multimodal layered transdimensional inversion of seismic dispersion curves with depth constraints. *Geochemistry, Geophysics, Geosystems*, **19**(12), 4957–4971.

Killingbeck, SF, Schmerr, NC, Montgomery, LN, Booth, AD, Livermore, PW, Guandique, J, Miller, OL, Burdick, S, Forster, RR, Koenig, LS, *et al.* 2020. Integrated borehole, radar, and seismic velocity analysis reveals dynamic spatial variations within a firn aquifer in southeast Greenland. *Geophysical Research Letters*, **47**(18), e2020GL089335.

King, EC, Woodward, J, & Smith, AM. 2007. Seismic and radar observations of subglacial bed forms beneath the onset zone of Rutford Ice Stream, Antarctica. *Journal of Glaciology*, **53**(183), 665–672.

King, EC, Smith, AM, Murray, T, & Stuart, GW. 2008. Glacier-bed characteristics of midtre Lovénbreen, Svalbard, from high-resolution seismic and radar surveying. *Journal of Glaciology*, **54**(184), 145–156.

Koenig, LS, Miège, C, Forster, RR, & Brucker, L. 2014. Initial in situ measurements of perennial meltwater storage in the Greenland firn aquifer. *Geophysical Research Letters*, **41**(1), 81–85.

Kohnen, H. 1974. The temperature dependence of seismic waves in ice. *Journal of Glaciology*, **13**(67), 144–147.

Koller, MG, Chatelain, JL, Guillier, B, Duval, AM, Atakan, K, Lacave, C, Bard, PY, & participants, SESAME. 2004. Practical user guideline and software for the implementation of the H/V ratio technique on ambient vibrations: measuring conditions, processing method and results interpretation. *In: 13th World Conference on Earthquake Engineering.*

Kuehn, T, Holt, JW, Johnson, R, & Meng, T. 2024. Active Seismic Refraction, Reflection, and Surface-Wave Surveys in Thick Debris-Covered Glacial Environments. *Journal of Geophysical Research: Earth Surface*, **129**(1), e2023JF007304.

Kuo, JT, & Dai, T. 1984. Kirchhoff elastic wave migration for the case noncoincident source and receiver. *Geophysics*, **49**(8), 1223–1238.

Laws, RM, Halliday, D, Hopperstad, JF, Gerez, D, Supawala, M, Özbek, A, Murray, T, & Kragh, E. 2019. Marine vibrators: the new phase of seismic exploration. *Geophysical Prospecting*, **67**(6-Geophysical Instrumentation and Acquisition), 1443–1471.

Lay, T, & Wallace, TC. 1995. *Modern Global Seismology*. Elsevier.

Li, XY, & Zhang, YG. 2011. Seismic reservoir characterization: how can multicomponent data help? *Journal of Geophysics and Engineering*, **8**(2), 123–141.

Li, Y, Gu, Y, Zhang, Y, Wang, Y, Yu, G, & Xu, M. 2024. What extra information can be provided by multi-component seismic data: a case study of 2D3C prospecting of a copper–molybdenum mine in inner Mongolia, China. *Minerals*, **14**(7), 689.

Liner, CL. 2012. *Elements of seismic dispersion: a somewhat practical guide to frequency-dependent phenomena*. Society of Exploration Geophysicists.

Liu, Y, & Simmons, JL. 2025. Depth imaging of multicomponent seismic data through the application of 2D full-waveform inversion to P-and SH-wave data: SEAM II Barrett model study. *Geophysical Prospecting*, **73**(3), 795–811.

Liu, Z. 1993. A Kirchhoff approach to seismic modeling and prestack depth migration. *Pages 888–891 of: SEG Technical Program Expanded Abstracts 1993*. Society of Exploration Geophysicists.

Lou, M, Zhang, Y, & Pham, LD. 2001. Shear-wave splitting and fracture orientation analysis from PS waves-examples from synthetic and field OBC data. *Pages SEG–2001 of: SEG International Exposition and Annual Meeting*. Society of Exploration Geophysicists.

Louboutin, M, Lange, M, Luporini, F, Kukreja, N, Witte, PA, Herrmann, FJ, Velesko, P, & Gorman, GJ. 2019. Devito (v3.1.0): an embedded domain-specific language for finite differences and geophysical exploration. *Geoscientific Model Development*, **12**(3), 1165–1187.

Luporini, F, Louboutin, M, Lange, M, Kukreja, N, Witte, P, Hückelheim, J, Yount, C, Kelly, PHJ, Herrmann, FJ, & Gorman, GJ. 2020. Architecture and performance of Devito, a system for atomated stencil computation. *ACM Trans. Math. Softw.*, **46**(1).

Luu, K. 2021. *DISBA: Numba-accelerated computation of surface wave dispersion.* Accessed: 2024-04-01.

Magrini, F, He, J, & Sambridge, M. 2025. BayesBay: a versatile Bayesian inversion framework written in Python. *Seismological Research Letters*, **96**(3), 2052–2064.

Majer, EL. 1978 (05). *Seismological investigations in geothermal regions.* Tech. rept. California Univ., Berkeley (USA). Lawrence Berkeley Lab.

Martin, GS, Larsen, S, & Marfurt, K. 2002. Marmousi-2: an updated model for the investigation of AVO in structurally complex areas. *In: 2002 SEG Annual Meeting.* OnePetro.

Masmoudi, N, Ratcliffe, A, Wang, M, Xie, Y, & Wang, T. 2021. A practical implementation of converted-wave reflection full-waveform inversion. *Pages 1–5 of: 82nd EAGE Annual Conference & Exhibition*, vol. 2021. European Association of Geoscientists & Engineers.

McKinney, W. 2010. Data structures for statistical computing in Python. *Pages 51–56 of: Proceedings of the 9th Python in Science Conference.*

McLachlan, GJ. 1999. Mahalanobis distance. *Resonance*, **4**(6), 20–26.

Mei, J, Zhang, Z, Lin, F, Huang, R, Wang, P, & Mifflin, C. 2019. Sparse nodes for velocity: learnings from Atlantis OBN full-waveform inversion test. *Page D043S125R004 of: SEG International Exposition and Annual Meeting.* Society of Exploration Geophysicists.

Meurer, A, Smith, CP, Paprocki, M, Čertík, O, Kirpichev, SB, Rocklin, M, Kumar, AMiT, Ivanov, S, Moore, JK, Singh, S, Rathnayake, T, Vig, S, Granger, BE, Muller, RP, Bonazzi, F, Gupta, H, Vats, S, Johansson, F, Pedregosa, F, Curry, MJ, Terrel, AR, Roučka, Š, Saboo, A, Fernando, I, Kulal, S, Cimrman, R, & Scopatz, A. 2017. SymPy: symbolic computing in Python. *PeerJ Computer Science*, **3**(Jan.), e103.

Miller, GF, & Pursey, H. 1954. The field and radiation impedance of mechanical radiators on the free surface of a semi-infinite isotropic solid. *Proceedings of the Royal Society of London. Series A. Mathematical and Physical Sciences*, **223**(1155), 521–541.

Millet, F, Bodin, T, & Rondenay, S. 2019. Multimode 3-D Kirchhoff migration of receiver functions at continental scale. *Journal of Geophysical Research: Solid Earth*, **124**(8), 8953–8980.

Montgomery, LN, Schmerr, N, Burdick, S, Forster, RR, Koenig, L, Legchenko, A, Ligtenberg, S, Miège, C, Miller, OL, & Solomon, DK. 2017. Investigation of firn aquifer structure in southeastern Greenland using active source seismology. *Frontiers in Earth Science*, **5**, 10.

Nahm, JW, & Duhon, MP. 2003. Interpretation and practical applications of 4C-3D seismic data, East Cameron gas fields, Gulf of Mexico. *The Leading Edge*, **22**(4), 300–309.

Navarro, FJ, Macheret, YY, & Benjumea, B. 2005. Application of radar and seismic methods for the investigation of temperate glaciers. *Journal of Applied Geophysics*, **57**(3), 193–211.

Nuus, MH, Fuchs, S, Smyrak-Sikora, AA, Kubutat, T, & Senger, K. 2025. *Thermal Conductivity and Heat Flow Modeling of Petroleum Exploration and Research Wells Onshore Svalbard*. https://ssrn.com/abstract=5396091. Preprint, not peer-reviewed.

Ólafsdóttir, EA, Bessason, B, & Erlingsson, S. 2018a. Combination of dispersion curves from MASW measurements. *Soil Dynamics and Earthquake Engineering*, **113**, 473–487. Accessed: 2024-05-01.

Ólafsdóttir, EA, Erlingsson, S, & Bessason, B. 2018b. Open software for analysis of MASW data. *In: Proceedings of the 16th European Conference on Earthquake Engineering*. Accessed: 2024-05-01.

Omar, S. 2018. *Multicomponent seismic analysis for velocity variations with azimuth related to horizontal transverse isotropy*. Colorado School of Mines.

Pälli, A. 2003. *Polythermal glacier studies in Svalbard determined by ground-penetrating radar*. University of Oulu.

Park, CB, Miller, RD, & Xia, J. 1998. Imaging dispersion curves of surface waves on multi-channel record. *Pages 1377–1380 of: SEG technical program expanded abstracts 1998*. Society of Exploration Geophysicists.

Park, CB, Miller, RD, & Xia, J. 1999. Multichannel analysis of surface waves. *Geophysics*, **64**(3), 800–808.

Pearce, E, Booth, A, Rost, S, Sava, P, Brisbourne, A, Jones, I, & Hubbard, B. 2021. Full Waveform Inversion (FWI) for glaciological seismic data - Improving the seismic characterisation of glacier firn. *Pages EGU21–916 of: EGU General Assembly Conference Abstracts*. EGU General Assembly Conference Abstracts.

Pertuz, T, & Malehmir, A. 2023. Ultrahigh-resolution 9C seismic survey in a landslide prone area in southwest of Sweden. *Geophysical Journal International*, **235**(3), 2094–2106.

Picotti, S, Francese, R, Giorgi, M, Pettenati, F, & Carcione, JM. 2017. Estimation of glacier thicknesses and basal properties using the horizontal-to-vertical component spectral ratio (HVSR) technique from passive seismic data. *Journal of Glaciology*, **63**(238), 229–248.

Podolskiy, EA, & Walter, F. 2016. Cryoseismology. *Reviews of Geophysics*, **54**(4), 708–758.

Preiswerk, LE, Michel, C, Walter, F, & Fäh, D. 2019. Effects of geometry on the seismic wavefield of Alpine glaciers. *Annals of Glaciology*, **60**(79), 112–124.

Redpath, BB. 1973. *Seismic refraction exploration for engineering site investigations.* Tech. rept. Army Engineer Waterways Experiment Station.

Rocha, D, Tanushev, N, & Sava, P. 2016. Acoustic wavefield imaging using the energy norm. *GEOPHYSICS*, **81**(4), S151–S163.

Rocha, Daniel, & Sava, Paul. 2018. Elastic least-squares reverse time migration using the energy norm. *Geophysics*, **83**(3), S237–S248.

Rodgers, PW. 1968. The response of the horizontal pendulum seismometer to Rayleigh and Love waves, tilt, and free oscillations of the Earth. *Bulletin of the Seismological Society of America*, **58**(5), 1385–1406.

Sambridge, M, Bodin, T, Gallagher, K, & Tkalčić, H. 2013. Transdimensional inference in the geosciences. *Philosophical Transactions of the Royal Society A: Mathematical, Physical and Engineering Sciences*, **371**(1984), 20110547.

Schalkwijk, KM, Wapenaar, CPA, & Verschuur, DJ. 2003. Adaptive decomposition of multicomponent ocean-bottom seismic data into downgoing and upgoing P-and S-waves. *Geophysics*, **68**(3), 1091–1102.

Seher, T, Masoomzadeh, H, Ren, Y, Baldock, S, & Wang, B. 2022. Deconvolution of upgoing and downgoing wavefields: a data example from the NOAKA OBN experiment. *Pages 2807–2811 of: Second International Meeting for Applied Geoscience & Energy.* Society of Exploration Geophysicists and American Association of Petroleum Geologists.

Sharp, RP. 1954. Glacier flow: a review. *Geological society of America bulletin*, **65**(9), 821–838.

Sheriff, RE. 2002. *Encyclopedic dictionary of applied geophysics.* Society of exploration geophysicists.

Shragge, J, Yang, J, Issa, Na, Roelens, M, Dentith, M, & Schediwy, S. 2021. Low-frequency ambient distributed acoustic sensing (DAS): case study from Perth, Australia. *Geophysical Journal International*, **226**(1), 564–581.

Simmons, JL, & Backus, M. 2001. Shear waves from 3-D–9-C seismic reflection data: have we been looking for signal in all the wrong places? *The Leading Edge*, **20**(6), 604–612.

Smith, AM. 1997. Variations in basal conditions on Rutford Ice Stream, West Antarctica. *Journal of Glaciology*, **43**(144), 245–255.

Smith, AM, Murray, T, Davison, BM, Clough, AF, Woodward, J, & Jiskoot, H. 2002. Late surge glacial conditions on Bakaninbreen, Svalbard, and implications for surge termination. *Journal of Geophysical Research: Solid Earth*, **107**(B8), ESE–1.

Smith, EC, Smith, AM, White, RS, Brisbourne, AM, & Pritchard, HD. 2015. Mapping the ice-bed interface characteristics of Rutford Ice Stream, West Antarctica, using microseismicity. *Journal of Geophysical Research: Earth Surface*, **120**(9), 1881–1894.

Snyder, DB, Cary, P, & Salisbury, M. 2009. 2D-3C high-resolution seismic data from the Abitibi Greenstone Belt, Canada. *Tectonophysics*, **472**(1), 226–237. Deep seismic profiling of the continents and their margins.

Socco, LV, & Strobbia, C. 2004. Surface-wave method for near-surface characterization: a tutorial. *Near Surface Geophysics*, **2**(4), 165–185.

Solano, CP, & Plessix, R. 2023. Can elastic waveform inversion benefit from inverting multicomponent data? *The Leading Edge*, **42**(3), 184–189.

Soubaras, R. 1996. Ocean bottom hydrophone and geophone processing. *Pages 24–27 of: SEG Technical Program Expanded Abstracts 1996*. Society of Exploration Geophysicists.

Stevens, NT, Roland, CJ, Zoet, LK, Alley, RB, Hansen, DD, & Schwans, E. 2023. Multi-decadal basal slip enhancement at Saskatchewan glacier, Canadian Rocky Mountains. *Journal of Glaciology*, **69**(273), 71–86.

Stevens, NT, Zoet, LK, Hansen, DD, Alley, RB, Roland, CJ, Schwans, E, & Shepherd, CS. 2024. Icequake insights on transient glacier slip mechanics near channelized subglacial drainage. *Earth and Planetary Science Letters*, **627**, 118513.

Stewart, R. 2009. *The measure of full motion: multicomponent seismic exploration and its value.* Society of Exploration Geophysicists. Pages 4243–4248.

Stockwell Jr, JW. 1999. The CWP/SU: Seismic Unix package. *Computers & Geosciences*, **25**(4), 415–419.

Stokoe, KH, & Rosenblad, BL. 1999 (05). Offshore geotechnical investigations with shear waves. *Pages OTC–10823–MS of: Offshore Technology Conference.*

Tarantola, A, Valette, B, *et al.* 1982. Inverse problems= quest for information. *Journal of geophysics*, **50**(1), 159–170.

Tatham, RH. 2002. Future directions of multicomponent seismic methods in the marine environment. *Pages OTC–14108 of: Offshore Technology Conference.* Offshore Technology Conference.

Tatham, RH, McCormack, MD, Neitzel, EB, & Winterstein, DF. 1991. *Multicomponent Seismology in Petroleum Exploration.* Society of Exploration Geophysicists.

The Firn Symposium Team. 2024. Firn on ice sheets. *Nature Reviews Earth & Environment*, **5**(2), 79–99.

Tsoflias, GP, Ivanov, J, Anandakrishnan, S, & Miller, R. 2008. Use of active source seismic surface waves in glaciology. *Pages cp–177 of: 21st EEGS Symposium on the Application of Geophysics to Engineering and Environmental Problems.* European Association of Geoscientists & Engineers.

Tsuji, T, Johansen, TA, Ruud, BO, Ikeda, T, & Matsuoka, T. 2012. Surface-wave analysis for identifying unfrozen zones in subglacial sediments. *Geophysics*, **77**(3), EN17–EN27.

Tura, A, Simmons, JL, Daneshvar, S, Copley, M, & Stitt, J. 2022. Improving reservoir characterization and time-lapse seismic through joint inversion of PP-and PS-wave seismic data. *Interpretation*, **10**(2), T341–T350.

Vardy, ME, Vanneste, M, Henstock, TJ, Clare, MA, Forsberg, CF, & Provenzano, G. 2017. State-of-the-art remote characterization of shallow marine sediments: the road to a fully integrated solution. *Near Surface Geophysics*, **15**(4), 387–402.

Veitch, SA, Karplus, M, Kaip, G, Gonzalez, LF, Amundson, JM, & Bartholomaus, TC. 2021. Ice thickness estimates of Lemon Creek Glacier, Alaska, from active-source seismic imaging. *Journal of Glaciology*, **67**(265), 824–832.

Vigh, D, Jiao, K, Watts, D, & Sun, D. 2014. Elastic full-waveform inversion application using multicomponent measurements of seismic data collection. *Geophysics*, **79**(2), R63–R77.

Waggoner, J, & Kristiansen, P. 2003. Using multicomponent seismic data to better understand reservoir characteristics. *Pages SPE–84569 of: SPE Annual Technical Conference and Exhibition?* Society of Petroleum Engineers.

Walter, F, Roux, P, Roeoesli, C, Lecointre, A, Kilb, D, & Roux, PF. 2015. Using glacier seismicity for phase velocity measurements and Green's function retrieval. *Geophysical Journal International*, **201**(3), 1722–1737.

Wang, Yi, Bale, R, Grion, S, & Holden, J. 2010. The ups and downs of ocean-bottom seismic processing: applications of wavefield separation and up-down deconvolution. *The Leading Edge*, **29**(10), 1258–1265.

Yan, J, & Sava, P. 2008. Isotropic angle-domain elastic reverse-time migration. *Geophysics*, **73**(6), S229–S239.

Yan, J, & Sava, P. 2009. Elastic wave-mode separation for VTI media. *Geophysics*, **74**(5), WB19–WB32.

Yang, C, Huang, Y, Liu, Z, Sheng, J, & Camarda, E. 2020. Shear wave noise attenuation and wavefield separation in curvelet domain. *Page D031S032R006 of: SEG International Exposition and Annual Meeting.* Society of Exploration Geophysicists.

Yang, J. 2005. Rayleigh surface waves in an idealised partially saturated soil. *Geotechnique*, **55**(5), 409–414.

Yang, RL. 1982 (11). The use of supercomputers in the search for oil. *Pages SPE–11258–MS of: SPE Eastern Regional Meeting.*

Yilmaz, Ö. 2001. *Seismic data analysis: processing, inversion, and interpretation of seismic data.* Society of exploration geophysicists.

Zechmann, JM, Booth, AD, Truffer, M, Gusmeroli, A, Amundson, JM, & Larsen, CF. 2018. Active seismic studies in valley glacier settings: strategies and limitations. *Journal of Glaciology*, **64**(247), 796–810.

Zhang, D, Tsingas, C, Ghamdi, AA, Huang, M, Jeong, W, Sliz, KK, Aldeghaither, SM, & Zahrani, SA. 2021. A review of OBN processing: challenges and solutions. *Journal of Geophysics and Engineering*, **18**(4), 492–502.

Zhao, BL. 2008. Application of multi-component seismic exploration in the exploration and production of lithologic gas reservoirs. *Petroleum Exploration and Development*, **35**(4), 397–412.

APPENDIX

COPYRIGHT PERMISSIONS FOR CHAPTER 3

A.1 Journal Permission

Permission to include modifications of the published manuscript in *Interpretation* (Chapter 3 of this dissertation) is shown in Figure A.1.

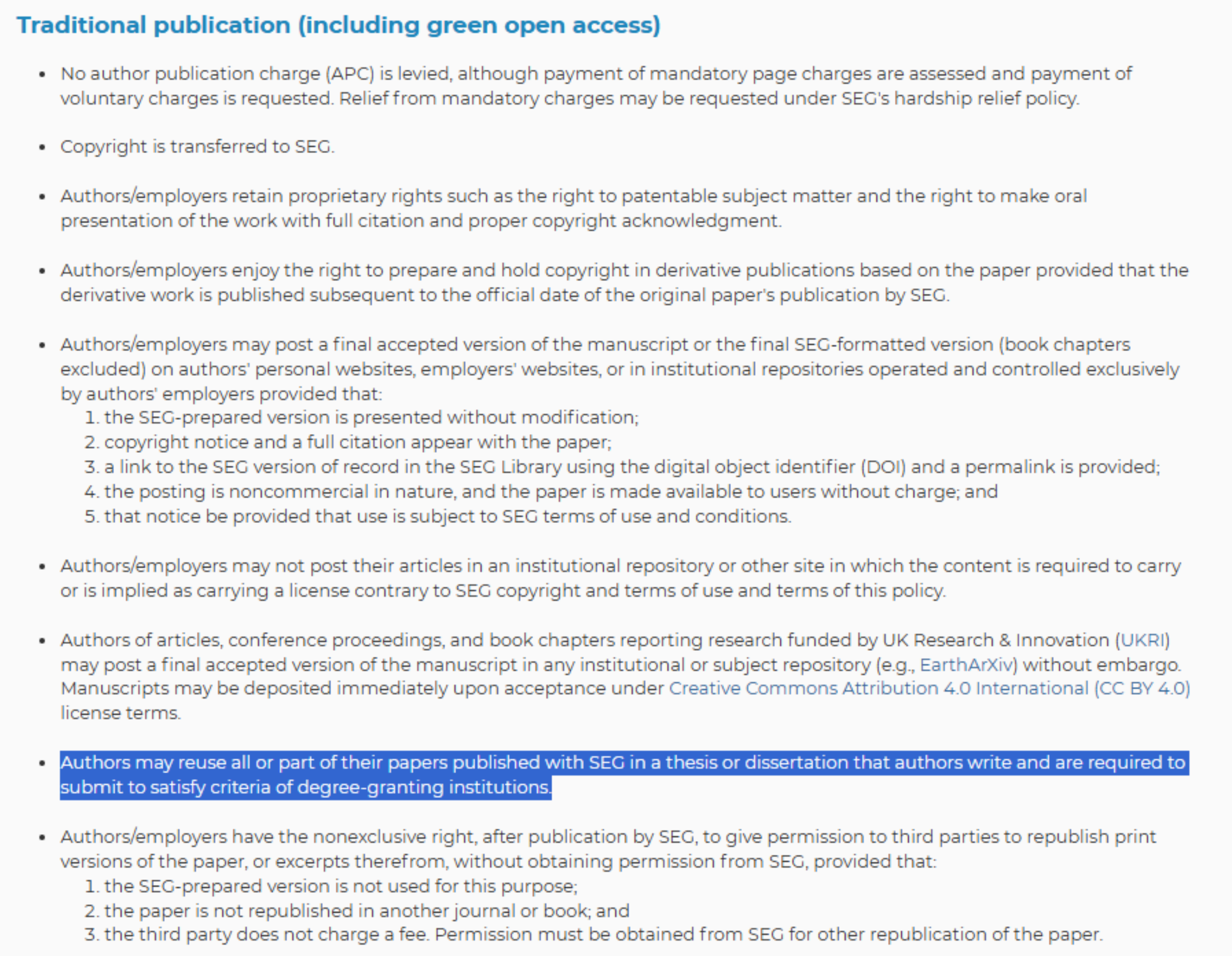

Traditional publication (including green open access)

- No author publication charge (APC) is levied, although payment of mandatory page charges are assessed and payment of voluntary charges is requested. Relief from mandatory charges may be requested under SEG's hardship relief policy.
- Copyright is transferred to SEG.
- Authors/employers retain proprietary rights such as the right to patentable subject matter and the right to make oral presentation of the work with full citation and proper copyright acknowledgment.
- Authors/employers enjoy the right to prepare and hold copyright in derivative publications based on the paper provided that the derivative work is published subsequent to the official date of the original paper's publication by SEG.
- Authors/employers may post a final accepted version of the manuscript or the final SEG-formatted version (book chapters excluded) on authors' personal websites, employers' websites, or in institutional repositories operated and controlled exclusively by authors' employers provided that:
    1. the SEG-prepared version is presented without modification;
    2. copyright notice and a full citation appear with the paper;
    3. a link to the SEG version of record in the SEG Library using the digital object identifier (DOI) and a permalink is provided;
    4. the posting is noncommercial in nature, and the paper is made available to users without charge; and
    5. that notice be provided that use is subject to SEG terms of use and conditions.
- Authors/employers may not post their articles in an institutional repository or other site in which the content is required to carry or is implied as carrying a license contrary to SEG copyright and terms of use and terms of this policy.
- Authors of articles, conference proceedings, and book chapters reporting research funded by UK Research & Innovation (UKRI) may post a final accepted version of the manuscript in any institutional or subject repository (e.g., EarthArXiv) without embargo. Manuscripts may be deposited immediately upon acceptance under Creative Commons Attribution 4.0 International (CC BY 4.0) license terms.
- Authors may reuse all or part of their papers published with SEG in a thesis or dissertation that authors write and are required to submit to satisfy criteria of degree-granting institutions.
- Authors/employers have the nonexclusive right, after publication by SEG, to give permission to third parties to republish print versions of the paper, or excerpts therefrom, without obtaining permission from SEG, provided that:
    1. the SEG-prepared version is not used for this purpose;
    2. the paper is not republished in another journal or book; and
    3. the third party does not charge a fee. Permission must be obtained from SEG for other republication of the paper.

Figure A.1 Reuse and Open-Access Policy of the Society of Exploration Geophysicists' Interpretation journal, acquired from https://library.seg.org/page/policies/open-access. The highlighted section indicates the permissions for reuse of the published manuscript for inclusion in this dissertation to meet degree requirements.

A.2 Journal Citation

Garvey, SM, Simmons, JL, & Calderón-Macías, C. 2025. Contributions of the Horizontal OBN Components to P-wave Imaging. *Interpretation*, **13**(3), 1–39.

A.3 Co-Author Permissions

Co-author permissions to include published manuscript from *Interpretation* as Chapter 3 of dissertation are shown in Figure A.2 and Figure A.3.

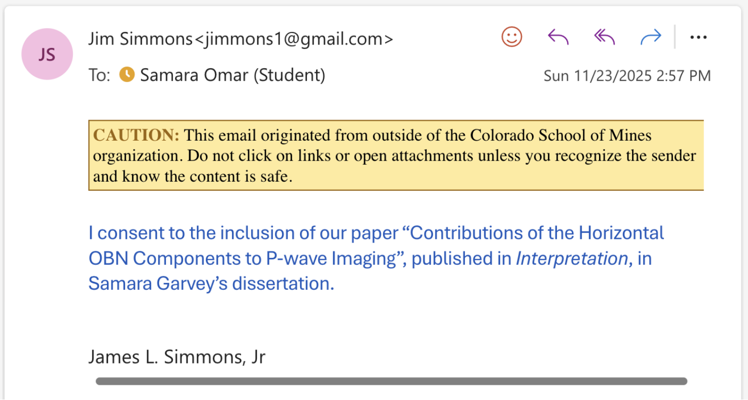

Jim Simmons<jimmons1@gmail.com>

To: Samara Omar (Student)

Sun 11/23/2025 2:57 PM

CAUTION: This email originated from outside of the Colorado School of Mines organization. Do not click on links or open attachments unless you recognize the sender and know the content is safe.

I consent to the inclusion of our paper "Contributions of the Horizontal OBN Components to P-wave Imaging", published in *Interpretation*, in Samara Garvey's dissertation.

James L. Simmons, Jr

Figure A.2 Email correspondence from Dr. Jim Simmons providing permission for the inclusion of our manuscript published in *Interpretation* within this dissertation.

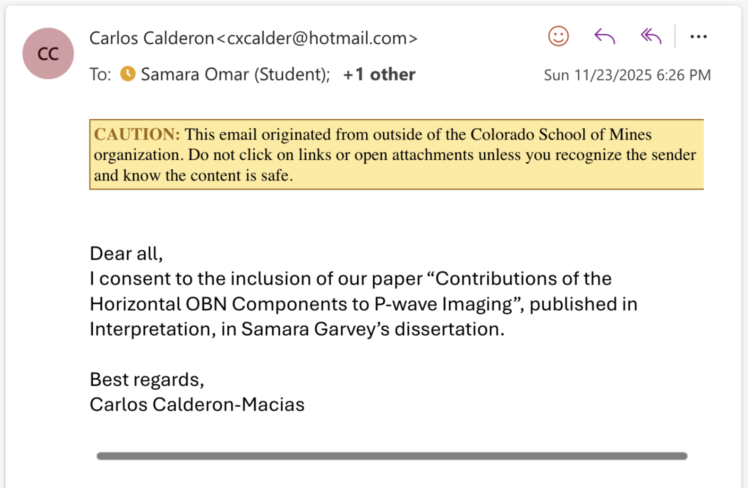

Carlos Calderon<cxcalder@hotmail.com>

To: Samara Omar (Student); **+1 other**

Sun 11/23/2025 6:26 PM

CAUTION: This email originated from outside of the Colorado School of Mines organization. Do not click on links or open attachments unless you recognize the sender and know the content is safe.

Dear all,
I consent to the inclusion of our paper "Contributions of the Horizontal OBN Components to P-wave Imaging", published in Interpretation, in Samara Garvey's dissertation.

Best regards,
Carlos Calderon-Macias

Figure A.3 Email correspondence from Dr. Carlos Calderón-Macías providing permission for the inclusion of our manuscript published in *Interpretation* within this dissertation.